JOURNAL OF CONDENSED MATTER NUCLEAR SCIENCE

Experiments and Methods in Cold Fusion

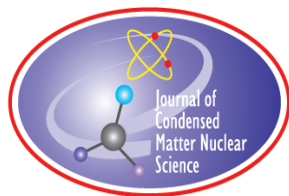# JOURNAL OF CONDENSED MATTER NUCLEAR SCIENCE

Experiments and Methods in Cold Fusion

JOURNAL OF CONDENSED MATTER NUCLEAR SCIENCE

Volume 20, October 2016

JOURNAL OF CONDENSED MATTER NUCLEAR SCIENCE

Volume 20   2016

CONTENTS

EDITORIAL

RESEARCH ARTICLES

Editorial

I am very proud of this new edition of the *Journal of Condensed Matter Nuclear Science*. This is proof of the increasing activity going on in this field. After years of denial by the scientific community, more and more scientists are now involved. There is still a long way to go, but we are on the right track. In this edition, we present both theoretical and experimental papers, which are important for this area of research to progress.

Sincerely,

Dr. Jean-Paul Biberian
(*Editor-in-Chief*)
October 2016

Research Article

Attempted Replication of Excess Heat in the Letts Dual-laser Experiment

Mason J. Guffey, Yang Tang and P.J. King*

ReResearch LLC, 3519 Jack Northrop Ave., Hawthorne, CA 90250, USA

Abstract

By attempting a nearly exact replication of prior published work, we test the claim that release of non-chemical excess heat from loaded palladium deuteride (PdD) can be triggered by the application of two laser beams with wavelengths selected at specific difference frequencies around 8, 15 and 20 THz. No significant excess heat events were observed in 231 laser triggered trials across 9 cathode runs. The average excess heat rate observed from all runs was 6.1 ± 21.6 mW with $\sim$10 W of input electrical power. We found no evidence of excess heat on the order of 100 mW reported by Letts. Calorimetry artifacts stemming from apparatus design issues often exceeded 100 mW and contributed to larger-than-desired uncertainties on individual excess heat measurements.
© 2016 ISCMNS. All rights reserved. ISSN 2227-3123

Keywords: Dual-laser experiment, Phonon, THz, Triggering

1. Introduction

The March 23, 1989 announcement by Martin Fleischmann and Stanley Pons of the possibility of nuclear fusion in an electrochemical system of heavy water (D_2O) and Pd generated worldwide interest [1–3]. Since then, small groups of researchers have been trying to replicate these claims without definitive success. Some experimental observations of anomalous heat effects (AHE) were made using calibrated calorimetry [4]. Others have claimed the correlated generation of He as a reaction byproduct [5], thus lending credence to the conjecture that a nuclear reaction may be taking place in the system.

Unfortunately, almost no published reports describe the specific steps necessary to independently reproduce claims of AHE reliably starting from commercially available materials and equipment. While preparation of the Pd cathode is proposed to be a crucial determinant of success [6], descriptions of specific cathode preparation procedures along with quantitative material properties are rare. Furthermore, there is no consensus within the research community about what kind of material preparation is required to observe the effect.

The dual-laser experiment (DLE) published by Dennis Letts [7,8] is a rare example of a report of AHE combined with sufficient documentation for a replication attempt. The reports of Letts et al. claim that a sufficiently prepared

---

*Corresponding author. E-mail: pjking@reresearch.net.

Pd cathode plated with Au will exhibit excess heat on the order of 100–300 mW in response to stimulation by two lasers having a frequency difference tuned to specific peaks in the THz range. These peaks coincide with phonon resonance frequencies of Pd, making the reports even more remarkable. Letts et al. [7,8] document the specific material preparation and measurement steps making a high fidelity replication attempt feasible. Letts claimed a 95% replication rate of AHE by following his protocol [8].

The DLE merits replication for another reason: the low energy nuclear reactions research community considers it an important result to build upon. For example, it provides experimental support for Peter Hagelstein's theoretical explanations of AHE, and it was referenced at least twice in oral presentations at the International Conference on Condensed Matter Nuclear Science (*ICCF-19*) in April 2015 [9,10].

This report describes our attempt to replicate the DLE, based on published reports and limited additional input from Letts. We did not observe the laser-triggered excess heat effects described by Letts et al. but we learned a lot about the experimental apparatus. We speculate on possible reasons for our different result, and suggest ways in which the DLE could be improved to make other replication attempts more straightforward.

2. Experiment

Letts concluded a 2015 publication [8] with the following:
   "The dual-laser experiments seem to support these conclusions:

   (1) Three specific beat frequencies will trigger excess power in a deuterated cathode.
   (2) Cathode fabrication, loading and laser application protocols enable excess power.
   (3) An external magnetic field is required and its affect (sic) is linear.
   (4) Polarization of the laser beams affects excess power.
   (5) Plating gold on the cathode surface after loading is required to produce excess power.
   (6) Higher cell temperature produces larger excess power and is exponential in effect.
   (7) The dual-laser effect is highly reproducible when protocols are followed."

Our experimental procedure was designed to closely replicate the protocol described in Letts JCMNS 2010, with additional input obtained via personal correspondence with Letts [11]

2.1. Materials preparation

Letts suggested that we use the 17-step procedure provided in his ASTI 2004 presentation [12] as our principal guide for cathode preparation. The 17 steps are summarized below:

Step 1 : The starting material was 0.5 mm thick palladium foil, *Alfa Aesar #11514* (99.9% purity metals basis). A piece of the material, ∼10 mm × 8 mm in size was cut from the foil with the use of a *Dremel rotary tool* with a *diamond wheel cutter* attachment.

Step 2 : This piece is polished using a polishing compound (*Custom Chemical Packaging Pol-Gel*, a rebranded version of the 10,000 grit Nicsand used in the original work) and the Dremel tool first with a metal and then with a fiber brush attachment. The polishing generally results in a mirror-like finish.

Step 3 : The resulting piece is rinsed in either tap or distilled water.

Step 4 : The piece is then annealed in a benchtop furnace (*Thermolyne type 1300*) to 750°C for 3 h, then allowed to cool in air overnight. This procedure and all subsequent annealing steps result in a blue-green surface sheen attributed to oxide.

Step 5 . Next the piece was etched in aqua regia (1:3 HNO_3:HCl) for 2–10 min. It was found that some degree of variability resulted from this procedure, in some instances completely removing the oxide layer and resulting in a speckled shiny surface, while in other instances the oxide coating was incompletely removed. In some instances the aqua regia was used after waiting a few hours as was the standard procedure known to the author, while in others it was used immediately after mixing on instructions from Letts [9].

Step 6 . After etching, the piece is washed in distilled water, then re-polished using the same procedure as above (Steps 2 and 3).

Step 7 : Repeat Step 6.

Step 8 . The piece is then cleaned in an ultrasonic bath with distilled water for 5 min, then...

Step 9 : ...annealed at 850°C for 2.5 h and allowed to cool overnight.

Step 10 : Afterwards, the piece is re-polished (resulting in the removal of the oxide film) and ...

Step 11 : ...ultrasonically cleaned in either 1:1 H_2O:IPA or a ∼15% solution of *Cole-Parmer ultrasonic compound remover* . The decision to use the former was based on the procedure's description of "compound remover", the latter was used based on the specific suggestion of Letts [9].

Step 12 : Next the piece was cold-rolled with a *Woodward Fab slip roller* cleaned with acetone prior to each use. Several passes through the roller (∼5–10) were necessary to achieve the target thickness of 250 μm specified in the procedure, verified with a set of calipers. The piece was rotated 90° each pass through the roller.

Step 13 : Subsequent to the rolling, the piece is polished, ...

Step 14 : ...ultrasonically cleaned (Step 8), ...

Step 15 : ...annealed at 850°C (Step 9), and

Step 16 : ...etched in aqua regia as described previously (Step 5).

Step 17 : The piece is then ready to be cut into 2–3 rectangular coupons 5 mm × 10 mm in size for use in the experiment.

The final wash applied to the sample varied between experiments, see Supplemental Information for details.

2.1.1. *Cathode material supplied by Letts*

For one experiment (DLER7), cathode material was supplied directly by Letts, from a batch that had successfully produced excess heat from the dual-laser effect in his May 2012 experiment. In two other runs (DLER10 and DLER11), the material was processed by us, except for the final etch (Step 16 above), which was performed by Letts. See Table 1 for experimental designations.

2.1.2. *Cathode material supplied by Coolescence LLC*

For experiment DLER17, the cathode material was supplied by Coolescence LLC. The foil sample was mechanically mounted in a PEEK (polyether ether ketone) assembly during measurement.
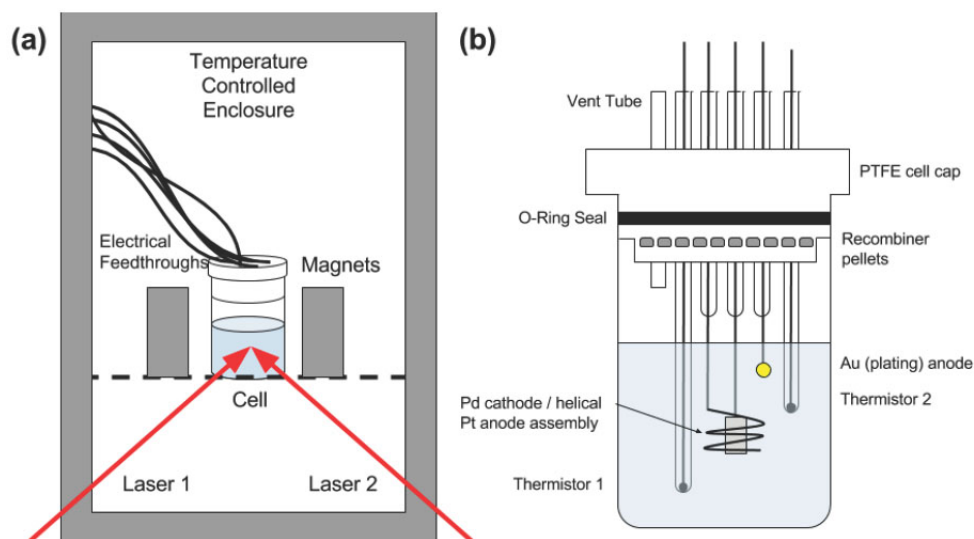
Figure 1. (a) A depiction of the entire apparatus. The cell and magnets rest on a wire frame grating of the temperature enclosure. See Supplementary Information for more details. (b) The measurement cell. For 4-wire resistance measurement, four additional wires were connected to cathode. These are omitted from the figure for clarity.

2.2. Setup description

Experiments were conducted in a custom-built, temperature controlled enclosure consisting of a modified commercial beverage cooler outfitted with a system of fans and baffles to circulate air, and a heating wire controlled with a Keysight E3632A power supply (see Supplemental Information). The enclosure temperature was determined from an average of either two or four thermistors located inside the enclosure, and a software-controlled PID loop controlled the heater wire voltage using this input.

The cell consisted of a 300 mL borosilicate lab beaker (Kimble KIMAX #14020) with a custom-built Teflon cell cap (see Fig 1 and Supplemental Information). Feedthroughs for temperature probes were constructed by taking 5 mm OD glass tubing (Ginsberg Scientific #5MMSLT-24) and sealing one end completely with a butane torch. Into these tubes were inserted *Measurement Specialties 44004RC* thermistors, and the back end of the tube was sealed with superglue. Feedthroughs for the three electrodes (the Pd cathode, and the Pt and Au anodes) were constructed as follows: First, a piece of 500 μm diameter Pt wire (Alfa Aesar #43288) was soldered onto Cu wire. Then one end of a piece of glass tubing was sealed around the Pt wire. Next, the wire was either laser-welded onto the Pd cathode, shaped into a coil for the Pt anode, or in the case of the Au anode a small bunch of Au wire (*Alfa Aesar #10968*) was melted onto the end of the Pt wire. A depiction of the entire apparatus (cell plus enclosure) is shown in Fig. 1.

Cell current was provided by a second Keysight E3632A power supply. The thermistors were measured with a digital multimeter/switch combination from National Instruments, models *PXI-4070* and *PXI-2503*. Temperature measurements were conducted using built-in LabVIEW routines for thermistor measurement at 10 kΩ range, which is the equivalent of a 2-wire resistance measurement as specified by National Instruments [13]. The PXI-2503 device switches the input to the PXI-4070 DMM between the thermistor leads. All data including cell current, cell voltage, and thermistor temperatures were recorded with *SignalExpress* every 10 s. This acquisition loop was maintained throughout the 2–3 week timeline for each run.

The feedthrough junctions were sealed at the top of the cell cap with Buna 008 O-rings. The cell was operated vented to the air through a tube, so that recombiner operation could be tested by immersing the end of the tube in water. During most runs this was not necessary, as significant electrolyte loss was not observed. Recombiner pellets consisting of platinum reduced onto alumina (*Alfa Aesar #89106*) were wedged into a groove cut into cell cap.

For most experiments, the electrolyte was 90 mL of 0.5 M LiOD made by dissolving Li metal pellets (*Sigma-Aldrich #499811*) into D_2O (99.9 atom %, *Sigma-Aldrich #151882*). For one experiment (DLER11) the electrolyte concentration was lowered to 0.1 M on the assumption that this might aid in the plating process.

The laser system employed consisted of two identical laser diode kits (*Thorlabs LTC-100B*). Each kit included a laser diode mount as well as current and temperature controllers. The laser wavelength of each diode was controlled by varying the case temperature using the supplied temperature controllers. The diodes employed varied based on the specific detuning frequencies being targeted, including Thorlabs models *HL6501MG* , *HL6750MG* and *HL6756MG* . "P" polarization was maintained for most experiments reported, as is summarized in Table 1.

2.3. Loading and resistance ratio

In accordance with procedures reported by Letts [7], electrolysis current was held at 50 mA for at least 120 h with an enclosure temperature setpoint of 15°C. For experiments DLER16B and DLER17, a stepped current protocol was used that consisted of 12+ h at 10 mA, and 4+ h each of 25, 50, 100, and 200 mA, as suggested by Coolescence LLC.

Certain experiments were performed with four additional laser welds connecting to the cathode with the purpose of measuring the resistance across the cathode using a 4-terminal AC resistance meter (*Hioki 3561*).

2.4. Data preparation

In order to use the system identification codes that fit a model differential equation to the dynamics of the calorimeter, we first interpolate all of the data onto a grid that is uniformly sampled at 10 s intervals. Although not essential, we then apply a 60 s low pass filter to the data to reduce the measurement noise. We believe that this degree of filtering is justifiable given that the calorimeter has a time constant on the order of 1800 s and as a result, for all real heat inputs, the calorimeter itself acts like a low pass filter with a time constant 30 times longer than the applied low pass filter. Nevertheless, we ran our analysis both with and without the 60 s low pass filter; the interpretation did not change.

2.5. Calibration

The main objective of calibration is to quantify the relationship between power input to the calorimeter and temperature measurements. Central to our calibration was to quantify the uncertainty in differences between measured and modeled temperature changes because these differences could be signatures of excess heat, but they could also be artifacts. We calibrated the system on a per-run basis, after loading and prior to gold plating and laser triggering, using the heat supplied by electrolytic current, i_{cell} in the absence of the laser trigger to excite the system and measure its thermal response.

The simplest model one can fit to the calorimeter's dynamic temperature measurements, $\Delta T(t)$, has one heat capacity, c and one thermal conductance, k:

$$d\Delta T/dt = -k\Delta T/c + Q_{in}/c. \tag{1}$$

$\Delta T(t)$ is the difference between the cell temperature and the inside temperature of the enclosure containing the calorimeter. The enclosure temperature during calibration was controlled at approximately 23°C, as was earlier done by Letts [7]. The input power, $Q_{in}(t)$, originates from the power applied to the cell. As is well known, an amount of

power $i_{\text{cell}}v_0$ goes into splitting water into oxygen and deuterium, which is then converted back into water at the recombiner; v_0 is the thermoneutral voltage, which for deuterium is approximately 1.53 V. Letts treats this power as leaving the system without reaching the cell temperature sensors [14]. We modeled the calorimeter power according to Letts' assumption that the recombiner power escapes without affecting the temperature sensor ($Q_{\text{in}}(t) = i_{\text{cell}}(v_{\text{cell}} - v_0)$) and also according to the "all power reaches the sensor" assumption: $Q_{\text{in}}(t) = i_{\text{cell}}v_{\text{cell}}$. For each of the seven cathode experiments that we calibrated, the latter analysis produced a better fit with the exception of DLER7 which was not significantly different. The results reported in this document analyze the data using $Q_{\text{in}}(t) = i_{\text{cell}}v_{\text{cell}}$

The calorimeter thermal parameters c and k were determined using the MATLAB System Identification Toolbox to fit a dynamic time series of temperature and power throughout a series of applied current transitions between 50 mA and 1.5 A that excite the thermal dynamics of the calorimeter. Data collection for the calibration phase of each experimental run took 1–2 days. Example fits to measurement data appear in Section 3. An example of fitting both with and without subtraction of the water splitting power is shown in the Linear Calibration section of the supplementary information.

2.6. Gold plating procedure

After calibration, Au plating onto the Pd surface was attempted by connecting the Au anode electrically in parallel with the Pt anode. Since this aspect of the procedure is incompletely described in Letts [7], several plating times were employed by various experiments (as low as 10 min and as high as ~14 h, corresponding with Letts' description [9]) with some laser trials performed after each plating attempt (see Table 1). The surface was usually observed to be black at the end of the experiment after the current was switched off; during operation, the bubble sheath around the cathode made the observation of the surface difficult.

2.7. Laser triggering

After the plating step, the electrical power applied to the cell was held constant and the temperature was allowed to stabilize; this established the first part of the baseline heat rate $Q_{\text{out,notrig}}$. A series of laser triggering trials was then conducted to establish triggered excess heat, $Q_{\text{out,trig}}$, followed by another period without laser stimulation, which established the second baseline portion of $Q_{\text{out,notrig}}$. The lasers were operated in a constant current mode, with their outputs kept to ~10 mW each. The beams incident on the sample were kept to ~1–2 mm in diameter, and mostly collimated over the ~60 cm distance between the diodes and the cathode. P polarization (parallel to plane of incidence) was maintained for most experiments, in correspondence with the protocol (see Fig. 2); alternate polarization configurations were tested a few times (see Table 1). Lasers were incident on the sample generally for 40 min to 1 h at a time; however, longer time periods of up to 3–4 h were tested as well.

2.8. Excess heat and uncertainty analysis

Excess heat attributable to the laser trigger is expressed by:

$$Q_{(\text{excess,trig})} = Q_{(\text{out,trig})} - Q_{(\text{out,notrig})}, \tag{2}$$

where $Q_{\text{out,notrig}}$ is the averaged output power when there is no trigger applied, and $Q_{\text{out,trig}}$ is the power flowing out of the calorimeter while the laser trigger is applied. In terms of temperature and conductance, k, this expression becomes:

$$Q_{\text{excess,trig}} = k(\Delta T_{\text{trig}} - \Delta T_{\text{notrig}}) = k(T_{\text{trig,cell}} - T_{\text{trig,surroundings}} - \Delta T_{\text{notrig}}). \tag{3}$$
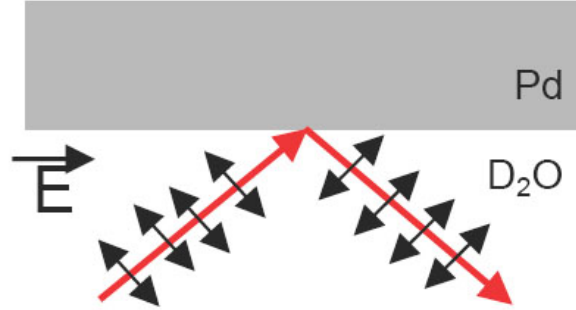
Figure 2. Schematic of "P" polarization used for most experiments.

If one assumes that the sources of uncertainty are uncorrelated, then the uncertainty associated with this computation, $\sigma_{Q\text{excess,trig}}$, is the 2-norm of the individual uncertainties:

$$\sigma_{Q\text{excess,trig}} = \sqrt{\sigma_1^2 + \sigma_2^2 + \sigma_3^2 + \sigma_4^2}, \tag{4}$$

where

$\sigma_1 = \sigma_k \left| \langle T_{\text{trig,cell}} - T_{\text{trig,surroundings}} - \Delta T_{\text{notrig}} \rangle_t \right|$ uncertainty in thermal conductance,

$\sigma_2 = k\sigma_{T_{\text{trig,cell}}}$ cell temperature variance during triger,

$\sigma_3 = k\sigma_{T_{\text{trig,surroundings}}}$ surroundings temperature variance during triger,

$\sigma_4 = k\sigma_{\Delta T_{\text{notrig}}}$ untriggered baseline temperature variance.

σ_k is the uncertainty in thermal conductance determined from the calorimeter calibration, and $\langle \rangle_t$ denotes a time averaged quantity. Note that this uncertainty estimate is not the most conservative. If we make no assumption about the correlation, then the total uncertainty is bounded by the 1-norm of the four uncertainties above:

$$\sigma_{Q\text{excess,bound}} \leq \sigma_1 + \sigma_2 + \sigma_3 + \sigma_4. \tag{5}$$

Typically the largest source of uncertainty is in σ_4, the establishment of a stable baseline before and after the application of the laser trigger as will be discussed in Section 3.

It is worth noting that the uncertainty analysis that we apply herein differs from that practiced by Hagelstein and Letts. They used the goodness-of-fit to an exponential relaxation time to model the triggered temperature rise in order to estimate the uncertainty of their excess power observations. Also, it is notable that the error bars on our results in Fig. 9 are larger than those in the comparable work by Hagelstein and Letts [17]. Details of the method used by Hagelstein and Letts were not provided; however, we make three observations: (1) typically, we see no triggered temperature rise, which makes use of the Hagelstein-Letts technique problematic. (2) The relaxation time model used by Hagelstein and Letts presumed that excess heat signatures appeared as a step change in the calorimeter. While this presumption may be appropriate for their dataset, that is not the case in the present work. (3) The detailed uncertainty estimation methods used by Hagelstein and Letts are not included in their publication. It is possible that some uncertainties in both the thermal parameters and the temperature measurements may not be fully accounted for in the Hagelstein Letts uncertainty estimation method.

Table 1.   Summary of experiments discussed in this manuscript.

Cathode run	LiOD conc. (M)	Plating times (h:min)			Approx. mag. field (G)	Polarization pairs tested*
		Sequence 1	Sequence 2	Sequence 3		
DLER5	0.497	0:10	0:55	4:55	200	PP & PS
DLER6	0.509	2:10	4:04	5:58	200	PP & PS
DLER7	0.519	2:04	3:56	14:35	200	PP
DLER8	0.5	6:19	4:40		200	PP
DLER10	0.446	2:00	6:18		200–500†	PP
DLER11	0.1	2:20			500	PP
DLER14	0.5	2:00			500	PP
DLER16B	0.5	6:43			500	PP
DLER17	0.5	8:21			500	PP

*Each letter corresponds to the polarization of light from a particular diode, P or S, corresponding to parallel and perpendicular to the plane of incidence respectively.

†Magnetic field was 200 G for loading phase, 500 G for laser experiments.

3. Results

In an attempt to demonstrate the open access to both experimental methods and raw data that is necessary for collegial and conclusory scientific progress, the raw data for the experiments in Table 1 and discussed below are available *here*.
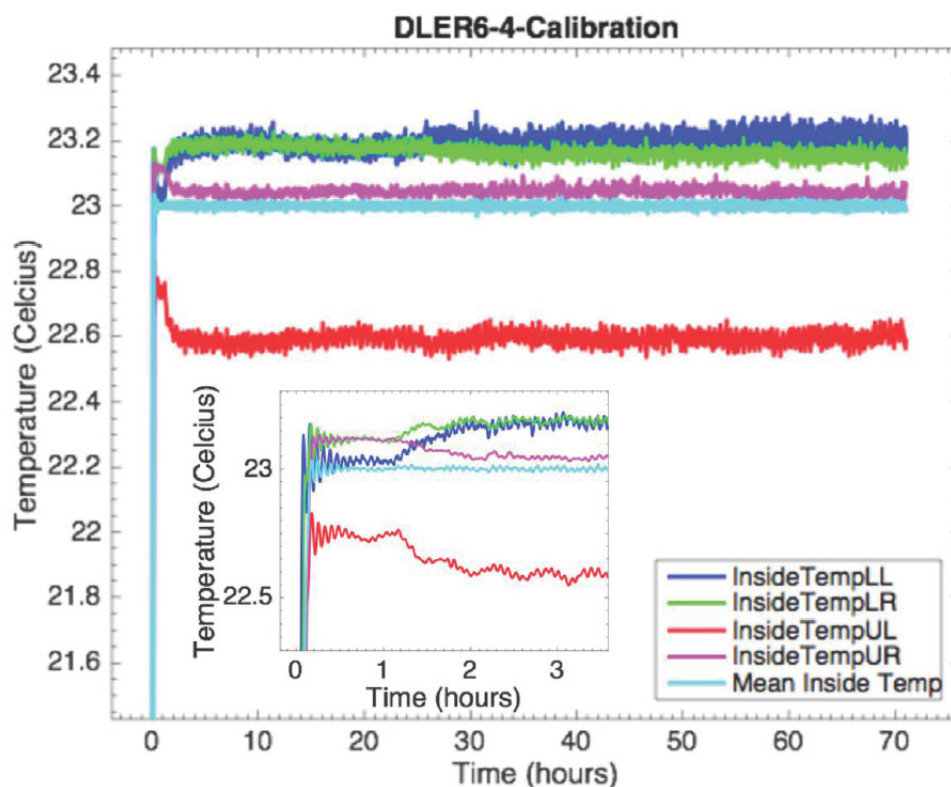
Figure 3.   Typical enclosure temperature stability. Inset shows early time stabilization period.
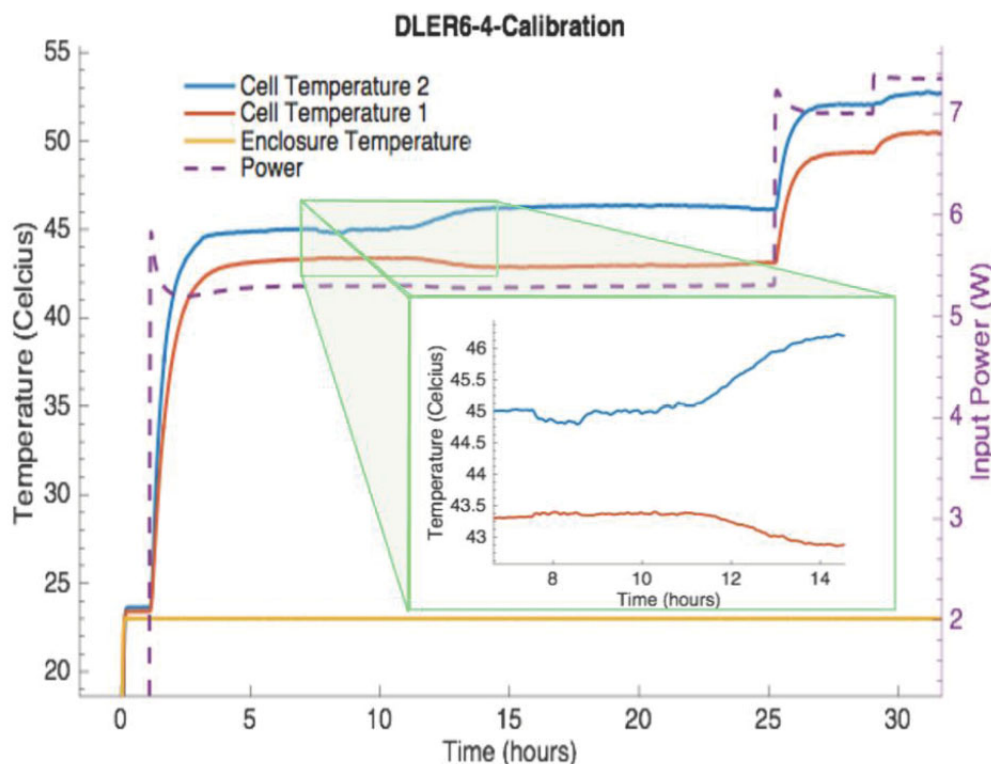
Figure 4. Example of anti-correlated electrolyte temperature sensing instability occurring during calibration period. Inset focuses on time period where instability occurs.

3.1. Materials preparation

The materials preparation end-points specified by Letts in his published works consist primarily of visual descriptions of the resulting surface after polishing, annealing, and etching. These were generally achieved in the present work. However, due to the inability to visually determine properties such as surface r.m.s. roughness, surface-based impurity concentration, oxide thickness after etching, or other potentially relevant material parameters, it is unclear whether our produced material matched that obtained by Letts in the original work by quantitative measures.

3.2. Enclosure temperature

Maintaining a constant enclosure temperature was essential for the calorimetry practiced in this experiment. A representative example of temperature measurements over a 70 h run is shown in Fig. 3.

The abbreviations LL, LR, UL, and UR refer to lower left, lower right upper left and upper right locations in the enclosure respectively. This dataset, which was typical, illustrated a number of important details. As shown in the inset, we saw that the control loop that stabilizes the enclosure temperature leveled out after several hours. Although likely adequate for this experiment, there remained a small oscillation at about 3.5 mHz (∼5 min period) which was undesirably close to the roughly 25 min thermal relaxation time of the calorimeter. Assuming that the source of these
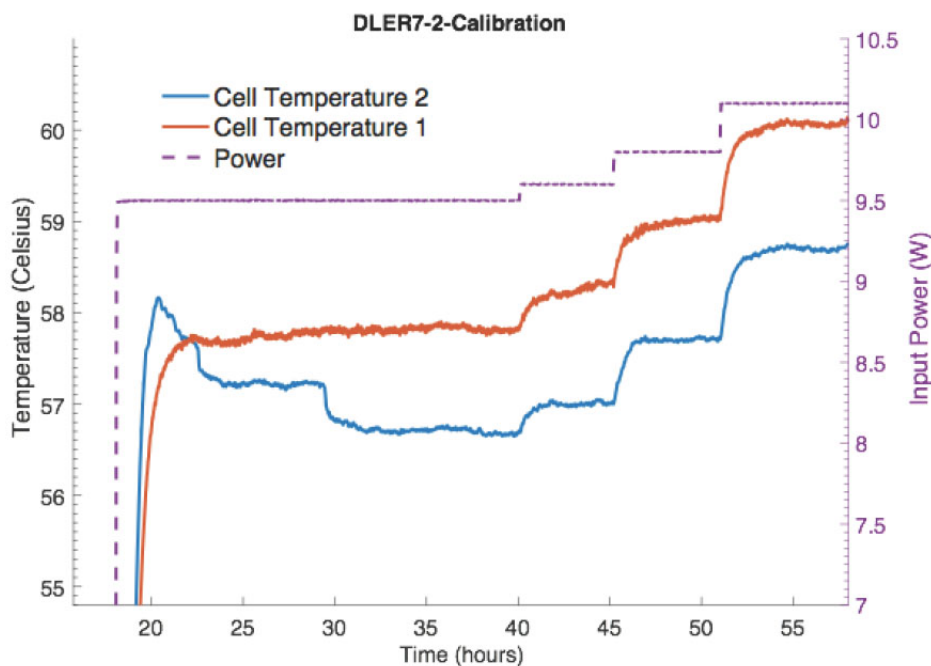
Figure 5. Example of single-thermistor temperature sensing instability.

fluctuations was the software-based PID loop controlling the enclosure temperature, a more judicious choice of the proportional, integral and derivative gain parameters might have eliminated the oscillation.

The four measurements agreed to within $0.8°$C when in equilibrium. The sensor data had a noise amplitude of on the order of $0.2°$C; The apparent increase in sensor noise at hour 25 correlated with an increase in applied cell power. The sensor noise appeared to not be completely correlated because the mean enclosure temperature was less noisy than the individually measured temperatures. Based on these findings, we used the time varying mean of all of the enclosure temperature measurements for data analysis purposes.

3.3. Electrolyte temperature sensing instability

All experiments analyzed showed evidence of temperature sensing instability. Such instability interfered directly with attempts to interpret temperature changes as anomalous heat. A representative example in Fig. 4 shows thermistor and power measurements before, during and after a plateau in applied power.

Between hour 10 and hour 15, while the input power and enclosure temperature were relatively stable, the two cell temperature measurements were not stable; they shifted *in opposite directions*. One plausible explanation is that the cap that holds the glass tubes containing both thermistors was tilting and causing thermistor 1 to move further from the electrodes and thermistor 2 to move closer to them. We note that the cap had an o-ring seal that was press-fit into the glass beaker. The magnitude of the temperature shift was about 0.5 and $1.2°$C for the first and second sensors, respectively.

Other observations of cell temperature sensing instability suggest that individual thermistors might have shifted position in the electrolyte during the runs, as shown in Fig. 5. In this example, between hours 19 and 40, under

Figure 6. Model fits to the two cell temperature readings obtained during run DLER7-2. Delta (°C) corresponds to temperature difference between cell and enclosure.

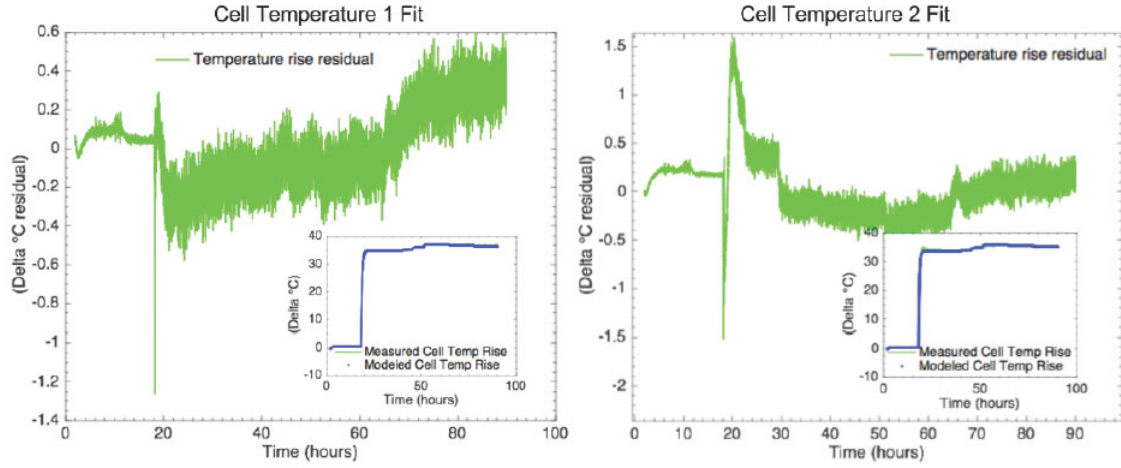constant applied power, the first thermistor rose monotonically as expected while the second thermistor fell about 1.5°C in several steps.

3.4. Calorimeter calibration observations

When the ordinary differential equation described in Section 2.5 was applied to calibration data we obtained values for the calorimeter's lumped parameter heat capacity, c, and thermal conductance, k, as well as the standard deviations for these parameters. The thermal conductance in particular was essential for the analysis of the laser trigger experiment because the input power during that experiment was held constant, and in steady state, the temperature rise of the calorimeter is $k\Delta T$.

Figure 6 shows the residual, $e_T = \Delta T_{\text{measured}} - \Delta T_{\text{modeled}}$, of the fit to cell temperatures 1 and 2 measured during run DLER7-2 (cathode run DLER7, data set 2), a portion of which is shown in Fig. 5. The insets of each plot show the measured and modeled temperatures overlaid, illustrating the importance of viewing residuals to assess the fit. The input data used for the fit is the power time series, $i_{\text{cell}}v_{\text{cell}}$. As expected, we obtained a better fit using cell temperature 1, which appeared to be more stable, particularly between hours 20 and 40 (note differences in scale). For each experimental run, we determined which sensor was more reliable based on the fit to the model. This sensor, 1 in the example provided, was used for analyzing the laser trigger experiments.

The difference between modeled and measured temperature provided an indication of calorimeter accuracy. The product ke_T of the temperature residual, e_T, and the thermal conductance during calibration is a direct measure of anomalous heat that arises from artifacts (mechanical, electrical, etc.) during calibration and is an indication of heat artifacts that could have arisen during experimentation. In all nine runs, we kept track of the largest heat artifacts that arose during each calibration; these ranged in magnitude from 0.13 to 0.46 W. Many of these artifacts appeared as brief disturbances to the thermometry during changes to the input power.

3.5. Attempts at excess heat observations

A representative time series of enclosure and cell temperatures and applied power is shown in Fig. 7. Triangles indicate the times at which laser triggers were applied, altered to a new difference frequency, and ended. The time series, which is over 70 h long, includes measurements on two separate days.

Figure 8 shows instantaneous excess heat measurements inferred from the temperature changes relative to the average baseline temperatures (plotted in gray) prior to and after each series of laser triggers. Each color change (blue, red, green, cyan, and magenta) indicates the application of a new difference frequency to the cathode. The horizontal bars above and below the excess heat measurements represent one standard deviation on the excess heat measurement at each laser difference frequency.

The laser power input was not observed, as it tended to be below the noise floor. The results of the laser trials of experiment DLER7-3 are summarized in Table 2. In both laser trial series, we observed that the excess heat rate baselines before and after the laser trials differed by 10's of mW. We attribute this to calorimeter drift, as referenced previously.

By far, the largest contribution to the excess heat measurement uncertainty is σ_4, the untriggered baseline temperature variance; this uncertainty ranged from about 15 to 21 mW. Clearly, a priority for any redesign of this experiment would be to stabilize the temperature measurements to establish a more accurate baseline. The next largest source of error is σ_2, cell temperature variance during trigger. This uncertainty contribution was as large as 18 mW. Note that we did not see evidence of an exponential rise upon triggering as reported in reference [7]. Had we observed such an exponential rise, this uncertainty term would have been modified by an accounting for an exponential fit to the output power. The next largest source of uncertainty is σ_3, the surroundings temperature variance during the trigger; this uncertainty contribution ranged up to about 8 mW. The smallest uncertainty contribution was from the uncertainty in the thermal conductance out of the calorimeter determined from the calibration of the calorimeter. This further illustrates
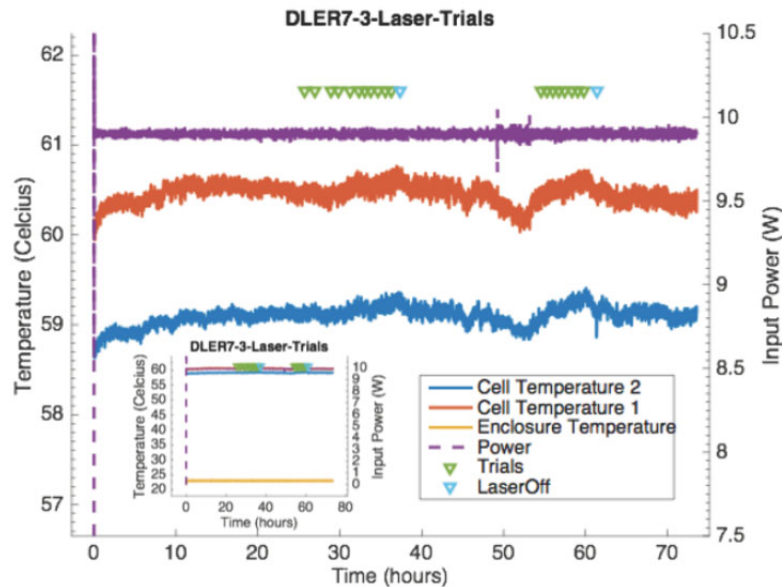
Figure 7. Representative laser trial data taken over a period of several days for experiment DLER7-3.
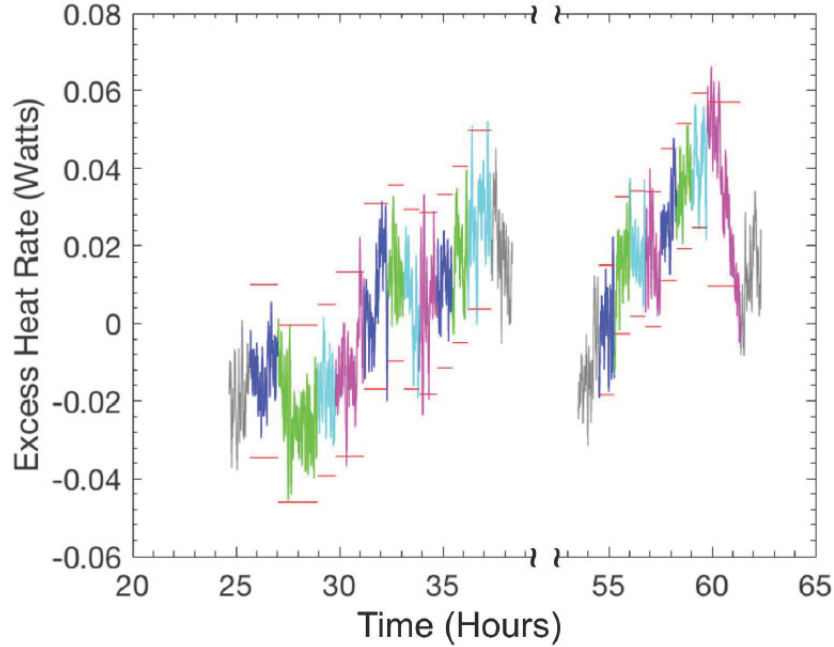
Figure 8. Calorimetric data analysis from Fig. 7, showing excess heat rate estimates including error bars. The figure depicts two separate dual-laser trials done over the course of two days. The gray plot portions bounding each trial are heat rate *without* laser irradiation. Different colors correspond to difference laser detuning frequencies. Red bars above and below the lines represent one standard deviation.

how a triggered excess heat experiment such as this is not very sensitive to the calibration method and is primarily affected by sensor stability.

A summary of excess heat rate as a function of difference frequency for all 231 laser triggered trials across nine cathode runs is shown in Fig. 9.

A rudimentary estimate of the average excess heat measured across all of the runs, and its uncertainty was obtained by averaging all the data and taking as the uncertainty the standard deviation of the excess heat measured during each laser trial. By this measure, the laser trials indicated an excess heat of 6.1 ± 21.6 mW. For comparison, the measurements reported in [7] are also shown in Fig. 9. Both datasets provided error bars on the measurements; however, as discussed in the methods section, the uncertainty analysis methods differ.

A histogram of the excess heat results measured at each laser triggered trial is shown in Fig. 10. We see that there is a very slight positive heat rate measurement of about 6 mW. It is possible that this is caused by the absorption of power from the laser trigger, although this is below the resolution of any one excess heat rate measurement.

Figures 9A and 10 show occasional observations approaching 100 mW of heat rate excess and heat rate deficit. It is worth noting that the largest magnitude heat rate observations are also those with the greatest measurement uncertainty. This phenomenon is depicted in Fig. 11. The slope of uncertainty vs. measurement is close to unity.

3.6. Resistance ratio measurements

Most of the attempts at resistance ratio measurements were met with experimental difficulty, making interpretation difficult. However, during run DLER17 the cathode was observed to achieve a resistance ratio (R/R) of 1.8, corre-

Table 2. Excess heat and uncertainty contributions calculated from run DLER7-3 (cathode run DLER7, data set 3).

Day	Trial	Frequency (THz)	Q_{excess} (W)	σ (W)	σ_1 (W)	σ_2 (W)	σ_3 (W)	σ_4 (W)
1	1	16.4	−0.012236	0.022379	0	0.006073	0.004456	0.021073
1	2	15.3	−0.023286	0.02285	0.000001	0.007163	0.005171	0.021073
1	3	14.5	−0.017147	0.02215	0.000001	0.005053	0.004585	0.021073
1	4	14.7	−0.010404	0.02383	0	0.009794	0.005278	0.021073
1	5	14.9	0.006955	0.023973	0	0.010341	0.004867	0.021073
1	6	15.1	0.012993	0.022735	0.000001	0.006131	0.005932	0.021073
1	7	15.3	0.006209	0.023202	0	0.008303	0.005033	0.021073
1	8	15.5	0.005101	0.023468	0	0.006869	0.007712	0.021073
1	9	15.7	0.010849	0.02237	0	0.005992	0.004518	0.021073
1	10	15.9	0.017819	0.022779	0.000001	0.007875	0.003573	0.021073
1	11	16.1	0.026829	0.023088	0.000001	0.00824	0.004591	0.021073
2	1	16.1	−0.001708	0.016825	0	0.005722	0.005195	0.014944
2	2	15.9	0.015012	0.017669	0.000001	0.008192	0.004662	0.014944
2	3	15.7	0.01806	0.016134	0.000001	0.004712	0.003842	0.014944
2	4	15.5	0.016601	0.017393	0.000001	0.006902	0.005616	0.014944
2	5	15.3	0.028174	0.017008	0.000001	0.006653	0.004654	0.014944
2	6	15.1	0.035451	0.01629	0.000001	0.005809	0.002881	0.014944
2	7	14.9	0.041971	0.017325	0.000002	0.00739	0.00471	0.014944
2	8	14.7	0.033394	0.023625	0.000001	0.017832	0.004103	0.014944

sponding to a D/Pd loading of ∼0.9.

4. Discussion

4.1. Impediments to replication

An objective of this experiment was to faithfully replicate the DLE as practiced by Letts. Given the importance of Letts' claims to the low energy nuclear reactions community, we recommend an in-person collaboration with him for those replicating his work. We estimate that it would take 2 months of his time to facilitate a definitive outcome.

It is worth noting that the DLE, if verified, represents a power source (up to 300 mW) that is approximately up to 4% of the applied electrical power (∼8 W). An effect of that scale has no immediate technological value as an energy source, even if an inexpensive source of Pd could be found. However, the scientific value of replication would be significant, given that such an effect is considered highly improbable by much of the physics community.

4.2. Apparatus replication fidelity

The make and model of much of the commercially available equipment, and the mechanical drawings for custom parts, used in our apparatus were either identical to Letts' original apparatus or altered with Letts' approval. We can therefore make some claims about the performance of the apparatus, and comment on the observation differences between ours and Letts' original experiment.

4.3. The importance of calibration method

A common calibration practice is to take several points from the steady state plateaus of temperature vs. power and produce a linear fit. While this approach provides a measure of calorimeter sensitivity in W/°C [15] we submit that this approach is inadequate for the purpose of establishing a calorimeter's propensity for heat artifacts. As shown in

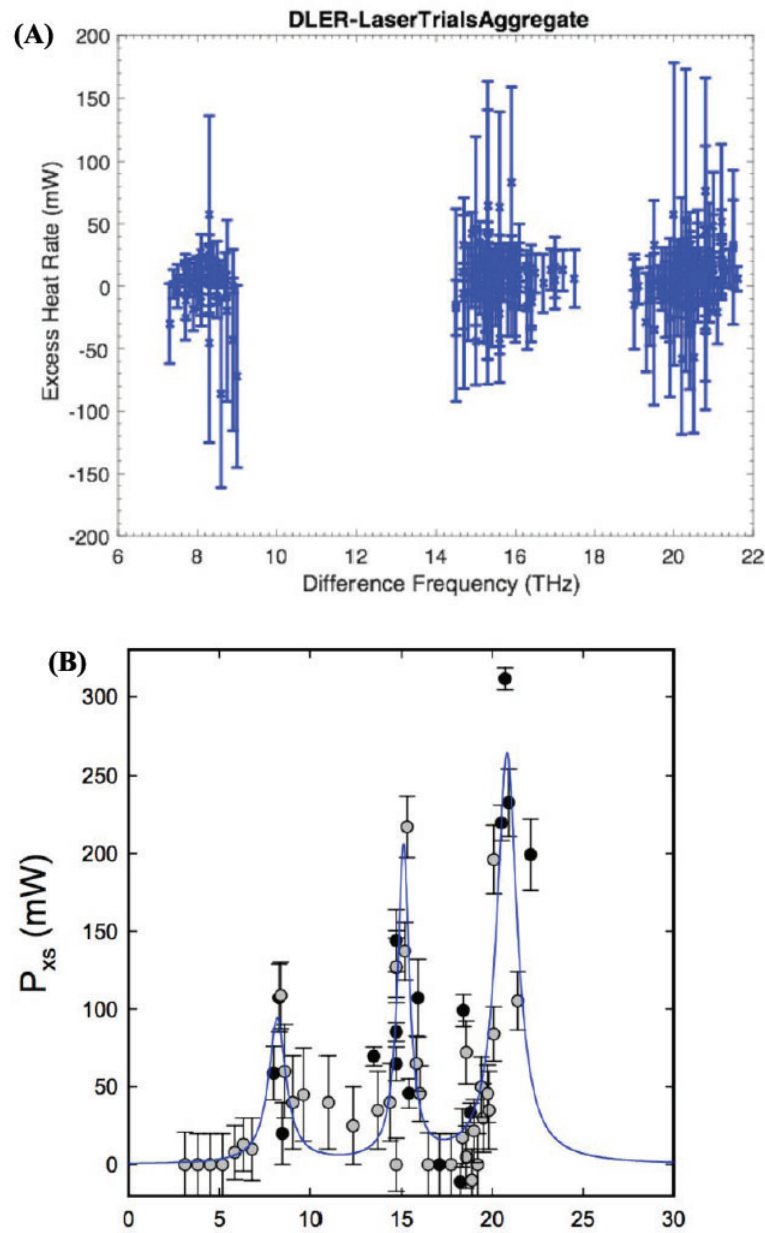**Figure 9.** (A) Aggregated calorimetric data obtained for all laser triggered trials discussed in this study. Error bars are 1 sigma standard deviations. (B) Letts' reports of excess heat as a function of detuning [7].

Fig. 6, a dynamic model fit to all of the data from a multi-day calibration run provides a more complete indication of the size of heat artifacts and the conditions where they occur.
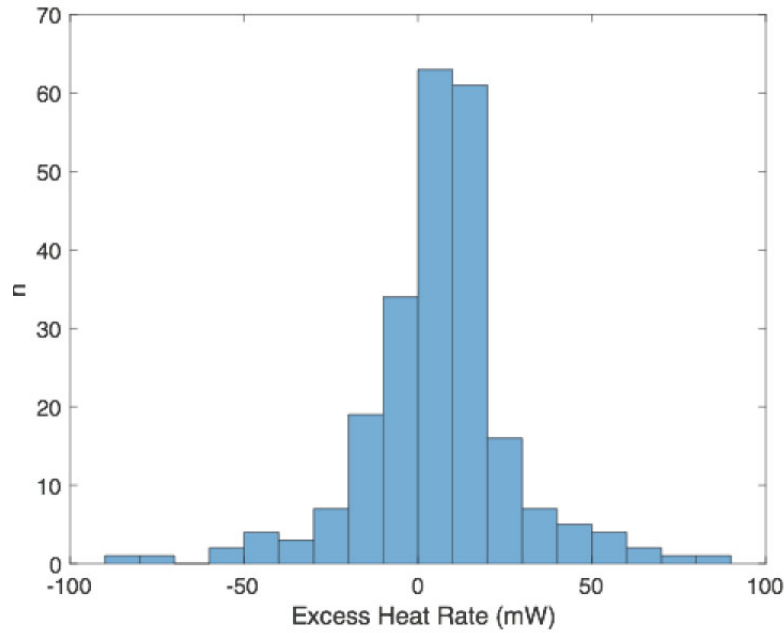
Figure 10. Histogram of all 231 laser triggered trial excess heat measurements.

Our data analysis differs in significant ways from data analysis [16] of the original DLE, for example Eq. (1) in this report is equivalent to the modeling of the calorimeter's relaxation time; however, what is different is our application of system identification to the complete calibration dataset instead of selected portions, and the examination of residuals. This procedure revealed myriad artifacts that one would typically address before attempting to detect excess heat, as discussed below. As discussed in the Supplemental Information, the quality of the fit using system identification tools did not find support for the assumption in [7] Eq. (2) that the power applied for water splitting can simply be subtracted from the input power. This suggests to us that heat from the recombiner is traveling into the electrolyte. Nevertheless, whether or not one analyzes the data using $Q_{\rm in}(t) = i_{\rm cell}(v_{\rm cell} - v_0)$ or $Q_{\rm in}(t) = i_{\rm cell}v_{\rm cell}$, this paper's overall conclusion regarding the observation of excess heat, and its uncertainty does not change appreciably. The two calibration methods produce two values for the thermal conductivity, k, to the surroundings that differ by about 30%; however, due to the differential nature of this triggered experiment, this results in a simple scaling of the result and would not cause a failure to observe excess heat were it present. The effect on the uncertainty is also scaled, as is readily observed inspection of the terms in the uncertainty analysis. For completeness, we ran all calibrations and analyses with $Q_{\rm in}(t) = i_{\rm cell}(v_{\rm cell} - v_0)$; instead of an excess heat result of 6.1 $\pm$ 21.6 mW, we obtained 4.6 $\pm$ 16.2 mW.

4.4. Temperature sensing artifacts

An important finding from the replicated apparatus is its inherent temperature sensing artifacts that produce artifactual signatures of excess heat. Our calibrations showed that the thermal conductance out of the calorimeter is about 270 mW/°C. We saw temperature shift artifacts that could be attributed to mechanical instability of the calorimeter cap that ranged from 0.5 to 1.2°C; artifacts this large correspond to heat artifacts on the order of 135–324 mW. It is worth
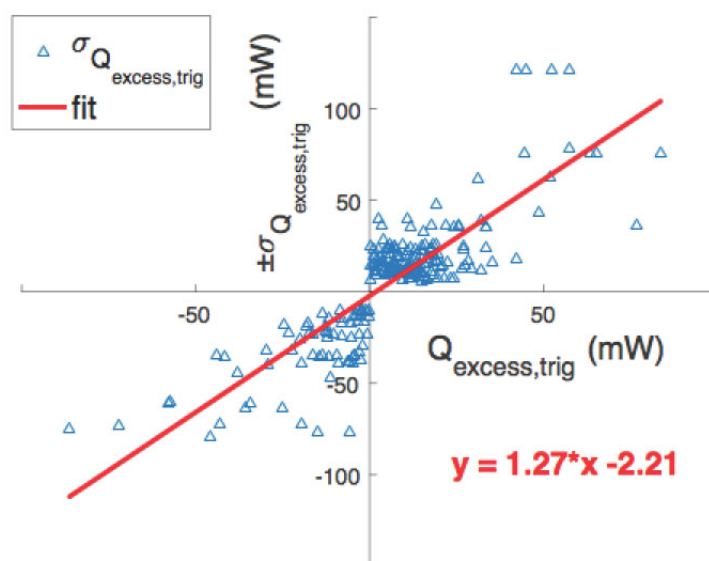
Figure 11.   Uncertainty in excess heat rate (signed) vs. excess heat rate.

noting that such artifacts are on the same order or larger than the excess heat observations reported in Letts' original experiment. It is hard to predict whether or when spurious movements of the thermistors will occur during any given attempt to trigger an excess heat effect; however, any credible claim of excess heat caused by an applied laser trigger should necessarily be done on an apparatus with demonstrably stable temperature sensing. One potential way to improve the temperature sensing stability would be to clamp the calorimeter cap in place and to ensure that all sensor mounts are supported at multiple points.

An additional potential source of spurious "excess" heat is variable recombiner function. Since the operating temperature of the experiment spans a range of ∼40°C and the behavior of the recombiner, as with any catalyst, should be expected to vary significantly with temperature, sudden exothermic bursts might be observed when recombiner pellets activate. Considering that our analysis shows the recombiner heat to be poorly separated from the electrolyte, care should be taken when interpreting excess heat events occurring during or shortly after major changes in cell temperature.

Not all of the temperature sensing artifacts observed by us could be explained by motion of the cell cap. For example, in Fig. 5, sensor 2 was observed to produce artifacts independently of sensor 1. This may be an indication of mechanical or electrical problems affecting only sensor 2. A 1.5°C artifact like the one shown above in Fig. 4 corresponds to a heat rate artifact of about 400 mW. With artifacts this large the calorimeter may not be well suited for precision calorimetry. The DLE attempts to trigger an excess heat event while running the calorimeter at constant power after a days-long phase comprising loading and plating. It was standard procedure to let the calorimeter stabilize at constant input power before applying the laser trigger. However, this can not guarantee that heat rate artifacts will not occur coincident with the laser trigger.

Given that the excess heat effect reported by Letts is up to a 4% effect (up to 300 mW out of 8 W), the calorimeter used to investigate such an effect would ideally be designed and confirmed to have no heat rate artifacts greater than about 10 mW. The authors believe that this is feasible; however, it would require a careful redesign of the calorimeter.

Electrical noise on the temperature sensors might also need to be reduced.

4.5. Electrolyte temperature non-uniformity

In one report of the DLE [17], the discrepancy between cell temperatures is said to be about 0.1°C or less; in our replication attempt, the discrepancy between the two cell temperature sensors was 20–30 times larger. Given the faithful replication of the parts used in this experiment, we find this difference noteworthy. Our observations spanning over four months of experiments show that the replicated apparatus has temperature differences within the electrolyte that span at least several °C. Neither our experiment, nor the Letts' original experiment stirred the electrolyte.

4.6. Venting

The original design of this experiment was vented to air through a small vent tube. The intent of this tube was to allow gas to escape when the recombiner was not functioning properly. In the original work, the method of submerging the exit-end of the tube in liquid was used to check for recombiner failure which would be expressed as bubbling. A concern with this approach is that a system open to air may take up and substitute light water for heavy water. Proton contamination, as this is called, has been raised as a possible failure mechanism because it is claimed [18] that hydrogen will go into Pd preferentially to deuterium.

4.7. Gold plating

In both the JCMNS 2010 as well as personal communication, Letts does not specify a particular plating time. The Current Science publication specifies plating in 10 min increments until the effect is observed. 10 min plating sequences were utilized early on in the experimental campaign (see Table 1), however, since no effect was observed, and with the guidance of the previous single laser work in which significantly longer plating times were employed, sequences as long as 14 h + were attempted. Bubbling and color change on the Au anode (from gold to red to black) over the course of a few hours were consistently observed during the plating process.

The resulting Au deposit in the original work is characterized only by its visual appearance. We replicated the Letts plating method which places the Pt and Au anodes in parallel with each other. A ramification of this is that the sum, but not the division, of current between the two anodes is unknown; this complicates our ability to know how much Au might have been applied to the cathode by Letts, and also how much plating may be occurring in our experiments. A suggested approach would sense current flowing from both anodes.

4.8. Heat measurements

Within the range of experimental uncertainty, the 231 excess heat measurements at each difference frequency were consistent with no excess heat triggered by the dual-laser stimulation. While it is impossible to disprove the claims of the Letts' original DLE, this work does refute the claim that results are highly reproducible [8] The quantity of laser triggered trials analyzed is 231 across 9 cathode runs, exceeding what is reported in the Letts' original DLE [7]

One question that might arise is whether each laser trial was of sufficient duration to trigger and sense an excess heat effect. We note that each dual-laser trigger was applied for a time longer than the thermal time constant, c/k, of the calorimeter which is about 30 min. Letts reported an excess heat response that is observed as rapidly as ∼5 min after laser triggering [7]

While outliers of 90 mW excess or absorbed heat were observed, these measurements had the least certainty. The excess heat measurements with the greatest certainty (smallest uncertainty) had the smallest magnitude of excess heat

rate (whether positive or negative). This trend is shown in Fig. 11. A validation of any cold fusion effect will need to show that the measured effect persists as the uncertainty of measurements is reduced; in this work, that was not observed.

5. Conclusions

In this work we attempted a high-fidelity replication of claims of excess heat triggered by dual-laser stimulation in an electrochemical system of palladium deuteride. We employed and described calorimeter calibration and error analysis methods that we believe are appropriate and adequate to the experimental objective. Despite having replicated Letts' original experimental design and protocol to the best of our ability, and conducting 231 attempts across 9 cathode runs, we did not observe evidence of laser-triggered excess heat events on the order of 100 mW reported by Letts. The average excess heat rate observed from all runs was 6.1 ± 21.6 mW with ~ 10 W of input electrical power.

However, several issues hampered our ability to replicate the work, including limited engagement with Letts (the author of the original DLE), the inability to directly compare material parameters of our cathodes with "successful" cathodes, and spurious calorimetric fluctuations due to apparatus design issues.

Dennis Letts claims that his results are highly reproducible [8]. We recommend that any future replication attempts provide for direct collaboration with Letts on a redesigned experimental apparatus.

Supplemental Information

S1. Calorimeter Temperature Control Hardware

Temperature-controlled enclosure consists of an *Edgestar 84* can beverage cooler with all but the bottom-most rack removed. Since the enclosure will only cool the system, a feedback mechanism needs to be established to provide heating to achieve a given setpoint.

The general principle of the temperature control design is to circulate mixed (hot and cold) air from the back of the enclosure up towards the top, down the front glass panel and then back towards the mixing area. The general schematic is shown in Fig. 12, an interpretation of Letts' original designs:

Two 12 V *CoolerMaster SickleFlow* 120's are used. Their activation switch is a solid state relay connected to a 12 V power supply and the NI DAQ (see below). The two fans are strapped together with twist-ties. A nichrome heating wire wrapped in a coil is connected by screws to two holes on opposite ends of the fan bank. Power for this heater is supplied by one of the two *E3632A* power supplies in the setup.

The back of the enclosure showing the cold wall built into the cooler, the two 12 V fans, and (barely visible above the fans) the heating wire is shown in Fig. 13.

The air distribution system consists of several pieces of custom-cut insulation board, with four additional 2 inch fans guiding the air up towards the enclosure roof.

Back and angled views of the air distributor are shown in Fig. 14. The bank of fans, which sits on top of the open portion of the air distributor in the right photo (Fig. 14) is shown in Fig. 15.

Each fan has a hole cut in the bottom (not pictured). These fans are powered on the same circuit that powers the two larger fans along the back wall, and the entire system is left on for the duration of the measurement.

S2. Cell

S2.1 Body

A picture of assembled cell inside the calorimeter is shown in Fig. 16.

The cell body is a *Kimble-Chase tall form Berzelius Beaker*.

S2.2 Thermistor probes

The thermistor probes are made as follows: *Flint glass tubes* are melted shut at one end, into which are placed thermistors that have had their leads soldered onto twisted pairs taken from Ethernet cables (see *this guide* for a description of the procedure). Electrical or Teflon tape is used to prevent the wires and solder blobs from contacting each other and shorting the probe. Shorts are clearly noticeable during the experiment as the apparent temperature spikes to clearly unreasonable values (hundreds of °C).

S2.3 Cell lid

Designs given by *Dennis Letts* have been used as a starting point to fabricate the cell lid. However, it was discovered that the slots into which the recombiner pellets are supposed to sit (lowest groove pictured above) are too thin at the specified width of 0.0625". When doubled, the groove allowed for a good press fit.

S3. Final Washes

The following final sample washes were applied to the cathode before the experiment began:

DLER5: (Not recorded),
DLER6: Sonicated for ∼15 min in 1:1 H_2O:IPA in cell body. Washed in copious amounts of distilled water, then dried with N_2. Left to dry completely overnight,
DLER7: None (used as received from Letts),
DLER8: Sonicated 30 min with Cole-Parmer compound remover solution, dried with N_2,
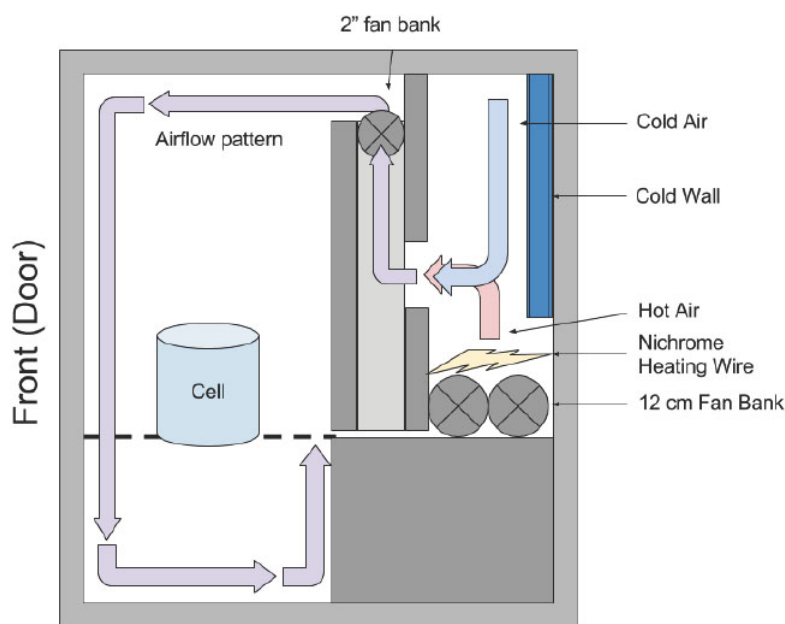
Figure 12. A schematic of the temperature-controlled enclosure.

Figure 13. The back of the enclosure showing the cold wall built into the cooler, the two 12 V fans, and (barely visible above the fans) the heating wire.

DLER10: Cathode washed with acetone before start of experiment,
DLER11: Sonicated with Cole Parmer compound remover 30 min, air-dried.

S4. Model Fitting to Calibration Data

4.1. Linear calibration

The calibration (Fig. 17) is typical of that obtained by fitting the steady-state response of the calorimeter to the input power at various steps. It is presented for comparison to the calibration obtained by the full system identification model. The inverse slope for Cell Temp1 is 0.267 W/°C which is in close agreement with the thermal resistance parameter from system identification. What is missing from a fit to only several plateau data points are all of the artifacts stemming from apparatus instabilities.

As an example of dynamic model fitting to calibration data, and some of the models that we tried, we illustrate our calibration results for Cathode DLER10. Figure 18 is the full calibration dataset for input power and measured temperatures.

Notice that the full dataset includes about 0.5 h of initial data taken before the enclosure temperature stabilized to
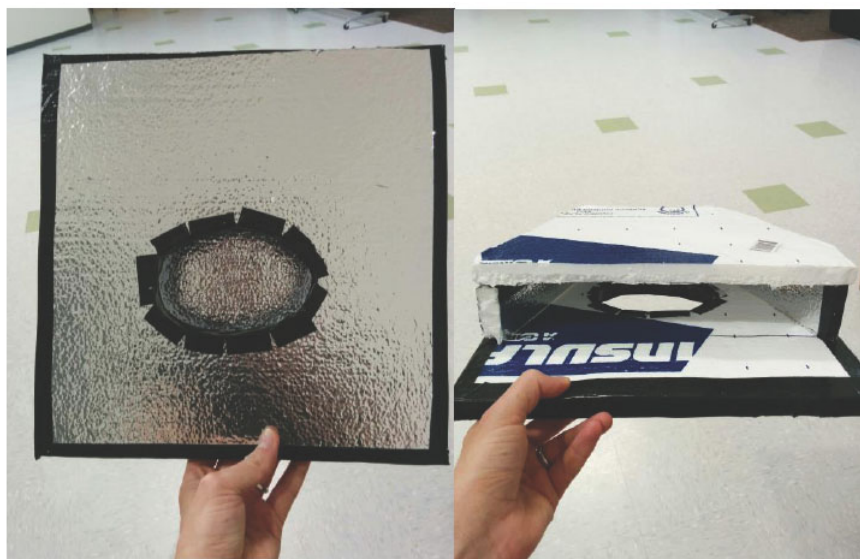
Figure 14. The custom-built air distributor, viewed from the back (left image) and top (right image) as viewed from the front of the enclosure.

about 23°C. As the calorimetry is isoperibolic, this portion of the data are excluded from the calibration. Notice also that Cell Temperature 2 is not stable. As discussed in the manuscript, Cell Temperature 1 was used. First, we show the result of applying the linear heat transport model

$$\mathrm{d}\Delta T/\mathrm{d}t = -k\Delta T/c + i_{\mathrm{cell}}v_{\mathrm{cell}}/c.$$

where ΔT is the difference between Cell Temperature 1 and the Enclosure Temperature, $i_{\mathrm{cell}}v_{\mathrm{cell}}$ is the electrical power fed into the cell, and k and c are fits to the calorimeter's thermal conductance and heat capacity respectively. This first model makes the assumption that power that gets converted into chemical energy by splitting water and is then released at heat in the recombiner exits through the calorimeter through largely the same path as the rest of the power that simply appears as direct heating of the electrodes and electrolyte. This first model also makes the

Figure 15. The bank of fans, which sit on top of the open portion of the air distributor as shown in the right image in Fig. 14.
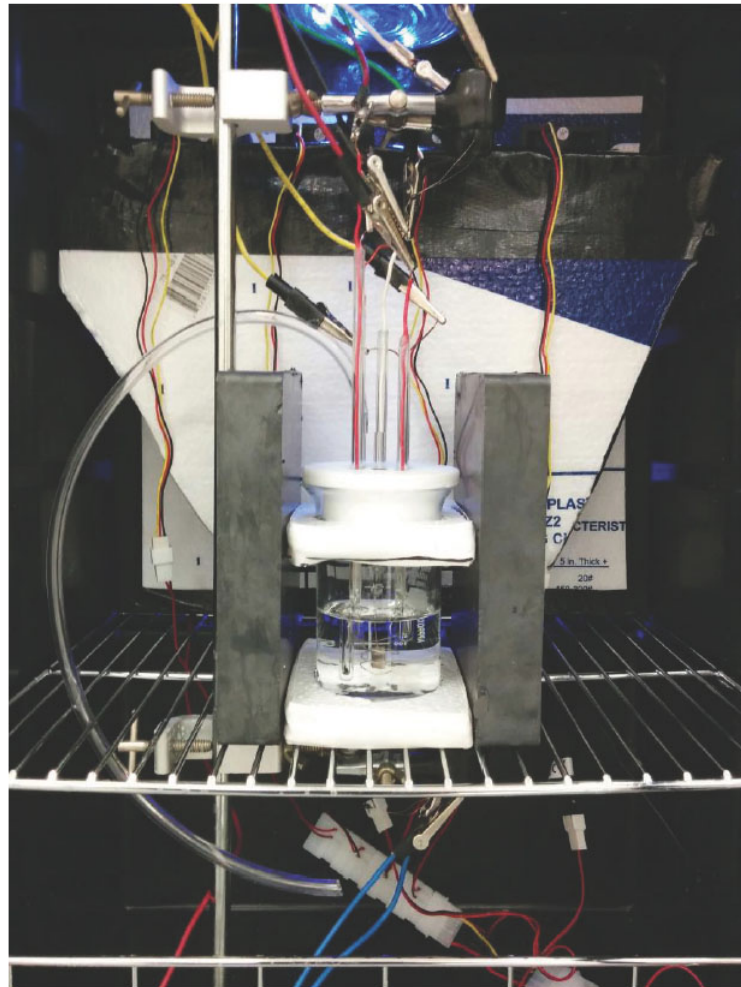
Figure 16. A picture of assembled cell inside the calorimeter, as would be present during a typical experimental run.

assumption, consistent with the assumption of Letts, that heat was removed by first order processes (conduction and convection). Figure 19 shows the measured and modeled cell temperature difference time series. The model was fit using the Matlab System Identification Toolbox's grey box model routine greyest.

Notice from Fig. 19 that this first model underestimates the cell temperature rise for small power inputs and overestimates the cell temperature rise for high power inputs. In spite of the model's simplicity, it explains the data fairly well, with a normalized root mean square error of only 4%.

S4.2 Linear calibration with subtracted electrolysis power

Next, we apply the assumption that power that goes into electrolyzing water gets carried away by the rising bubbles in the electrolyte, and thereafter, because the recombiner is somewhat removed from the electrolyte, that power does not
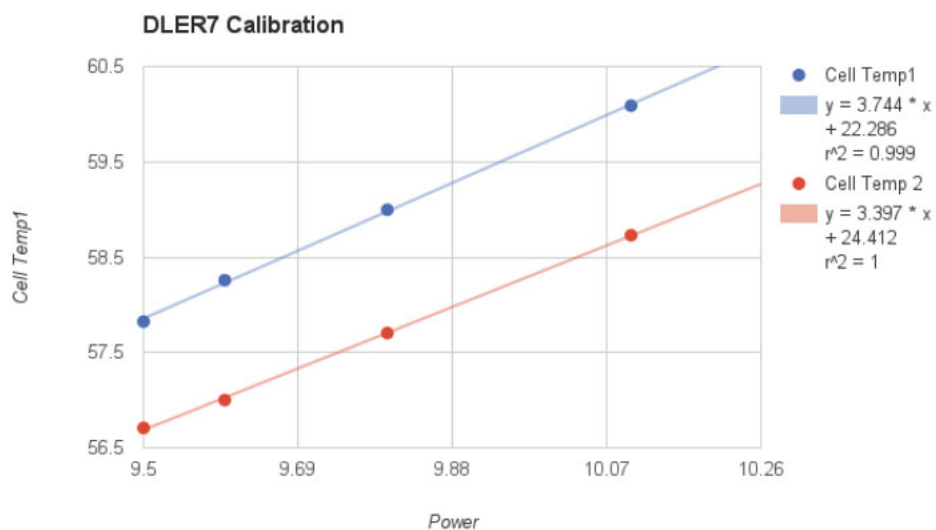
Figure 17. A typical calibration obtained by fitting the steady-state response of the calorimeter to the input power at various steps.
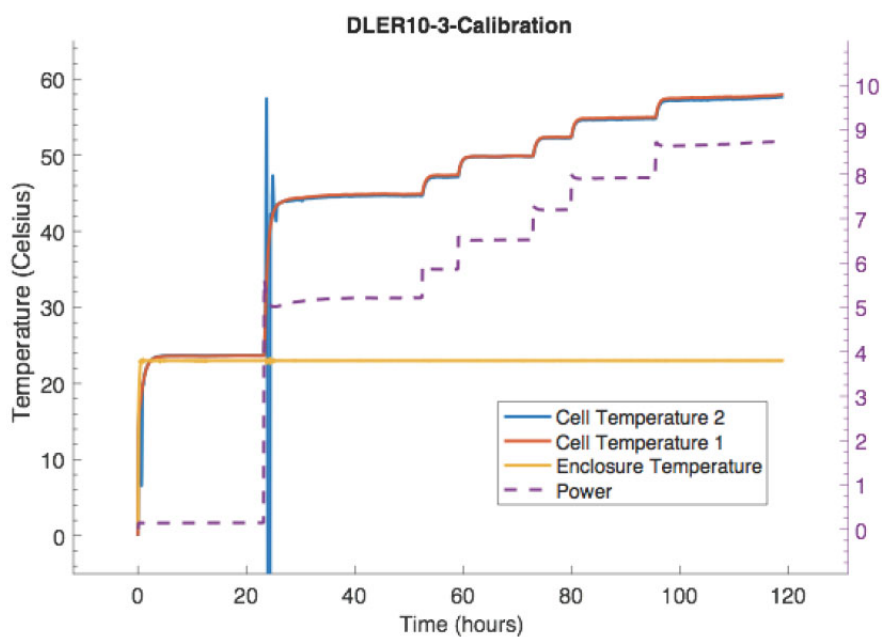
Figure 18. Full calibration data set for input power and measured temperatures.
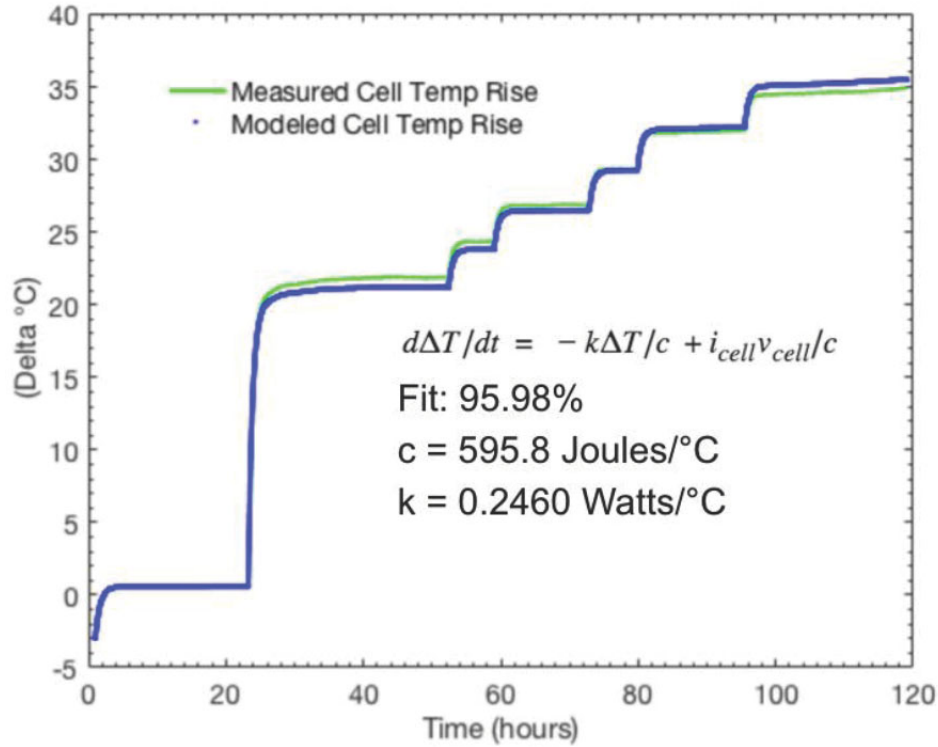
Figure 19. Measured and modeled cell temperature difference time series using linear calibration.

affect the cell temperature. This is the assumption adopted in the calibration used by Letts. This assumption entails a minor modification to the first model, namely,

$$\mathrm{d}\Delta T/\mathrm{d}t = -k\Delta T/c + i_{\text{cell}}(v_{\text{cell}} - v_0)/c,$$

where $v_0 = 1.53$ V is the thermoneutral voltage for D_2O. Figure 20 shows the measured and modeled cell temperature difference time series. As before, the model was fit using the Matlab System Identification Toolbox's grey box model routine greyest.

We see that this model does not fit the data as well as the simpler model; the fit using the model that assumes that recombiner heat escapes through the top of the cell has a normalized root mean square error of >7%, which is over 3% worse than the simple model.

S4.3 Radiation fit to calibration data

One feature common to both of the linear models is that temperature rise is overestimated at high input power. This suggests that heat is leaving the calorimeter via a superlinear process. Given that the calorimeter is constructed from a transparent glass beaker it is a natural choice to add radiative heat transfer to the model to test the hypothesis that radiation is responsible for a portion of the heat exiting the calorimeter. Next we considered the possibility that the

The figure shows two curves labeled "Measured Cell Temp Rise" and "Modeled Cell Temp Rise" plotted against Time (hours) on the x-axis (0 to 120) and (Delta °C) on the y-axis (-5 to 40). The equation and fit information displayed on the plot:

$$d\Delta T/dt = -k\Delta T/c + i_{cell}(v_{cell} - v_0)/c$$

Fit: 92.66%

c = 397.7 Joules/°C

k = 0.1785 Watts/°C
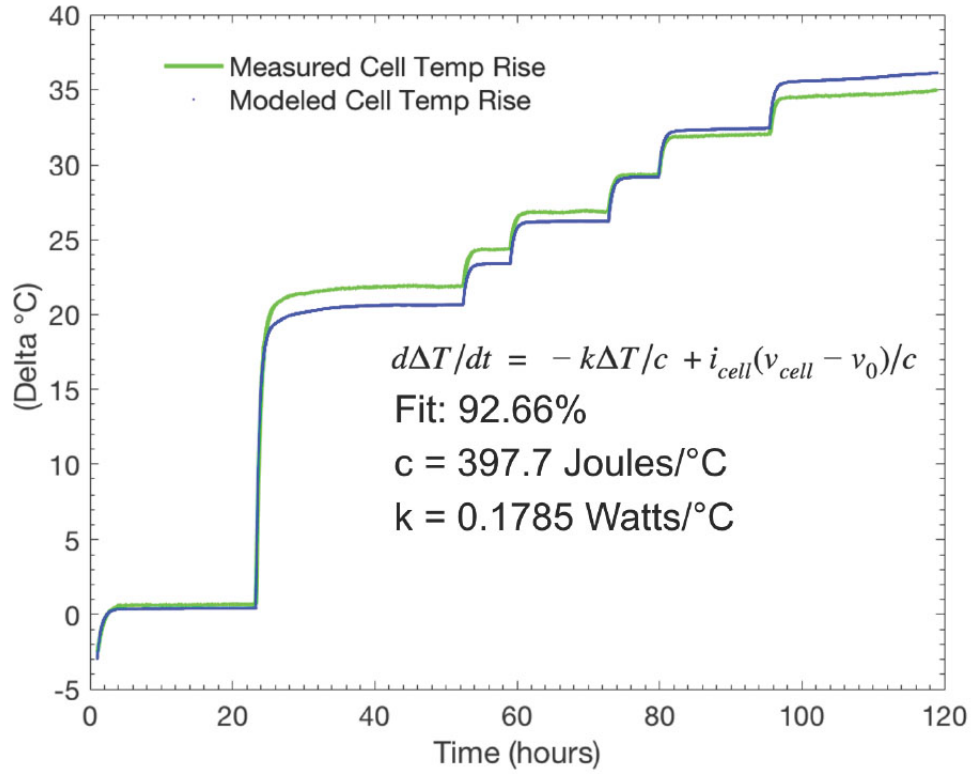
Figure 20. Measured and modeled cell temperature difference time series using linear calibration with subtracted electrolysis power.

calorimeter dynamics are governed by the equation

$$\mathrm{d}\Delta T/\mathrm{d}t = -k_{\mathrm{conc}}\Delta T/c - k_{\mathrm{rad}}(T_{\mathrm{cell}}^4 - T_{\mathrm{surroundings}}^4) + i_{\mathrm{cell}}v_{\mathrm{cell}}/c.$$

Note that the terms T_{cell} and $T_{\mathrm{surroundings}}$ are in Kelvin. A more convenient way to write this expression for parameter fitting is

$$\mathrm{d}\Delta T/\mathrm{d}t = -k_{\mathrm{conc}}\Delta T/c - k_{\mathrm{rad}}[(\Delta T + T_{\mathrm{surroundings}})^4 - T_{\mathrm{surroundings}}^4] + i_{\mathrm{cell}}v_{\mathrm{cell}}/c,$$

because this form expresses the system as a differential equation with a single state (ΔT) with two inputs ($i_{\mathrm{cell}}v_{\mathrm{cell}}$ and $T_{\mathrm{surroundings}}$) and three parameters ($c$, k_{con} and k_{rad}).

Figure 21 shows the measured and modeled ΔT using the nonlinear model. The fitting was done using the Matlab function nlgreyest.

The normalized root mean square error metric for this model is 0.67% which compares favorably to both of the linear models. The table below summarizes the results of the three models used on the DLER10 calibration dataset.
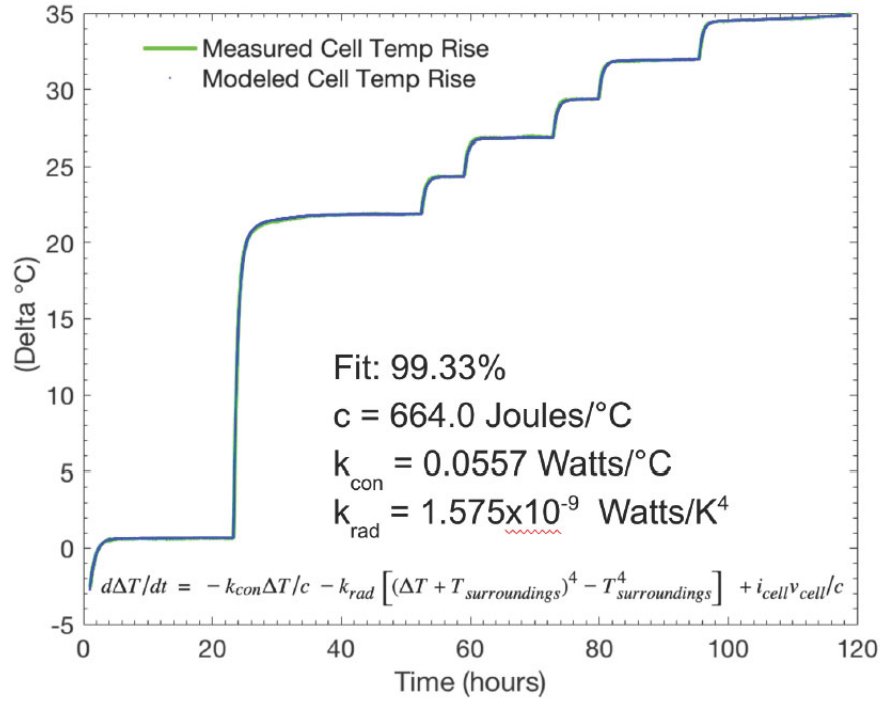
Figure 21. Measured and modeled cell temperature difference time series using the nonlinear model with thermal radiation correction.

Model	Input power (W)	Fit (%)	c (J/°C)	k_{con} (W/°C)	k_{rad}(W/K^4)
Linear	$i_{\mathrm{cell}}(v_{\mathrm{cell}} - v_0)$	92.66	397.7	0.1785	–
Linear	$i_{\mathrm{cell}}v_{\mathrm{cell}}$	95.98	595.8	0.2460	–
Non-linear	$i_{\mathrm{cell}}v_{\mathrm{cell}}$	99.33	664.0	0.0557	1.575×10^{-9}

S4.4 Summary of model fitting

By comparing the two linear fits, we see that not only is the assumption that electrolysis energy escapes without detection not well supported; but, that in addition the assumption may underestimate the heat capacity and thermal conductance.

By comparing the k_{con} term of the linear and non-linear models with $i_{\mathrm{cell}}v_{\mathrm{cell}}$ input power we see an indication that a significant portion of the power leaving the calorimeter does so by radiation.

We chose the DLER10 dataset to illustrate comparative calorimeter models because this dataset was uncharacteristically free of thermometry artifacts, at least for Cell Temperature Sensor 1. One consequence of non-physical thermometry artifacts is that nonlinear parameter estimation methods fail to converge rapidly on a global optimum. For this reason, the calibration model used throughout this report is the linear model with $i_{\mathrm{cell}}v_{\mathrm{cell}}$ input power.

Acknowledgement

References

[1] M. Fleischmann, S. Pons and M. Hawkins, Electrochemically induced nuclear fusion of deuterium, *J. Electroanal. Chem.* **201**(1989) 301. Errata, **263** (1990) 187.

[2] M. Fleischmann, S. Pons, M.W. Anderson, L.J. Li and M. Hawkins, Calorimetry of the palladium—deuterium–heavy water system, *J. Electroanal. Chem.* **287** (1990) 293.

[3] S.E. Jones, E.P. Palmer, J.B. Czirr, D.L. Decker, G.L. Jensen, J.M. Thorne, S.F. Taylor and J. Rafelski, Observation of cold nuclear fusion in condensed matter, *Nature* **338** (1989) 737.

[4] M.C.H. McKubre, S. Crouch-Baker, F.L. Tanzella, S.I. Smedley, M. Williams, S. Wing, M. Maly-Schreiber, R.C. Rocha-Fiho, P.C. Searson, J.G. Pronko and D.A. Kohler., Development of advanced concepts for nuclear processes in deuterated metals, TR-104195 Electric Power Research Institute: Palo Alto, 1994.

[5] M.H. Miles, R.A. Hollins, B.F. Bush, J.J. Lagowsi and R.E. Miles, Correlation of excess power and helium production during D_2O and H_2O electrolysis using palladium cathodes, *J. Electroanal. Chem.* **346** (1993) 99.

[6] E. Castagna, M. Sansovini, S. Lecci, A. Rufoloni, F. Sarto, V. Violante, D.L. Knies, K.S. Grabowski, G.K. Hubler, M. McKubre and F. Tanzella, Metallurgical characterization of Pd electrodes employed in calorimetric experiments under electrochemical deuterium loading, In *Proc 14th Int Conf on Condensed Matter Nuclear Science*, Washington, DC, August 10-15, 2008.

[7] P.L. Hagelstein, D. Letts and D. Cravens, Terahertz difference frequency response of PdD in two-laser experiments, *J. Condensed Matter Nucl. Sci.* **3** (2010) 59–76.

[8] D Letts, Highly reproducible LENR experiments using dual laser stimulation, *Current Science* **108** (2015) 559–561 and Supplementary Information.

[9] D.J. Nagel, Scientific and commercial overview of ICCF-19, *Infinite Energy*, July/August 2015.

[10] P.L. Hagelstein, Current status of the theory and modelling effort based on fractionation, presented at *ICCF-19*, Padua, Italy, April 13–17, 2015.

[11] D. Letts, personal communication, 2015.

[12] D. Letts and D. Cravens, Cathode fabrication methods to reproduce the Letts–Cravens effect, presented at *5th Asti Workshop on Anomalies in Hydrogen/Deuterium loaded Metals*, Asti, Italy, March 19–21 2004.

[13] http://www.ni.com/pdf/manuals/371304g.pdf

[14] ibid P.L. Hagelstein, D. Letts and D. Cravens, Terahertz difference frequency response of PdD in two-laser experiments, *J. Condensed Matter Nucl. Sci.* **3** (2010) 59–76.

[15] An example linear fit to steady state data is included in the Supplemental Information.

[16] P.L. Hagelstein and D.G. Letts, Analysis of some experimental data from the two-laser experiment, *J. Condensed Matter Nucl. Sci.* **3** (2010) 77–92.

[17] P.L. Hagelstein and D. Letts, *JCMNS* 2010, Appendix A.2.1.

[18] M.C.H. McKubre, personal communication.
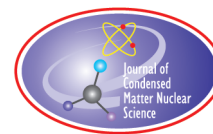
Research Article

Optical Detection of Phonon Gain Distinguishes an Active Cold Fusion/LANR component

Mitchell R. Swartz*

JET Energy Inc., Wellesley Hills, MA 02148, USA

Abstract

Successful cold fusion is heralded by a large, if not quite abnormal, increase in the anti-Stokes to Stokes (aS/S) ratio in coherent multi-wavelength optical reflection volume-enhanced electric-driven spectroscopy (CMORE-spectroscopy). This distinguishing phonon gain is not seen in the "off" state or the avalanche (undesirable) mode. It heralds seven acoustic phonons assisting nuclear reactions and a core peak calculated Stokes temperature of circa 1645 K.

© 2016 ISCMNS. All rights reserved. ISSN 2227-3123

Keywords: Avalanche mode, CMORE spectroscopy, Excess heat mode, NANOR, Phonon gain

1. Introduction

We previously used dry preloaded NANOR®-type CF/LANR (lattice assisted nuclear reaction) components [1] to investigate material science [2–8] and radiation physics [5,6] of active cold fusion systems. Several of these reports have demonstrated that several electrical transconduction states exist, but that only one is active, desired, and capable of producing "excess heat" [7]. This report extends those results and describes a spectroscopic measurement of anti-Stokes to Stokes (aS/S) peak ratios. These measurements demonstrate that the best "excess heat" results occur (with the CF/LANR nanomaterial in the active, desirable mode) with an aS/S peak ratio greater than 1 (Fig. 1).

Using several ohmic (thermal) and other controls, the aS/S ratio was (and thus acoustic phonons were) found to follow normal Boltzmann statistics when the materials were examined. This included an identical NANOR®-type component which was not loaded, and a similar loaded component in both the "off" condition and electrical avalanche region where the desired cold fusion reactions do not occur. However, that was not true when the cold fusion components are activated in the desired mode which elicits excess heat (Fig. 1). By contrast, the monitored Series 7 NANOR®-type component in "excess heat" (XSH)-mode elicited a completely unique pattern, immediately prior to the appearance of excess heat accumulation. This heralds an aS/S ratio level far above normal, suggesting increased phonon density, consistent with phonon gain. These changes were only seen in the presence of the desired

---

*Corresponding author. Dr. Mitchell R. Swartz ScD, MD, EE, E-mail: phonongaingroup@nanortech.com.
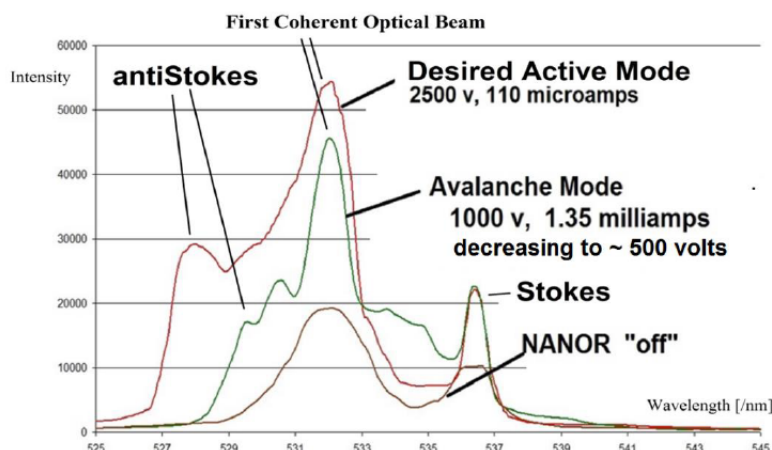
Figure 1. Three different electronic states optical signatures for the same preloaded ZrO_2PdD NANOR[R]-type CF/LANR component in three different electrical drive modes. Shown are spectra of the same NANOR[R]-type CF/LANR component in three different electronic states, resolved by dual wavelength coherent electric-driven volume-enhanced reflection spectroscopy. The three modes (responses) are the undriven "off"-state, the unwanted electrical avalanche mode [7], and the optimal operational state, the "Desired Active Mode", where "excess" energy is being released.

electronic state of cold fusion (lattice assisted nuclear reaction; CF/LANR) electrical conduction and activity in the NANOR[R]-type CF/LANR component.

In Fig. 1, the curves are from dual wavelength coherent electric-driven volume-enhanced reflection spectroscopy of the core CF/LANR nanomaterial inside NANOR[R] 7-6. The plots show reflected optical intensity as a function of wavelength, initially from two incident coherent optical beams but then reflected by backscatter along with the initial optical beams from the core. They reveal three different types of reflection spectra from the same sample, observed by the same diagnostic.

This paper also briefly discusses the response of the NANOR[R]-type CF component, loaded but not electrically driven, to a magnetic field intensity. The activity is quite complicated in the presence of it being electrically driven, and is discussed elsewhere [4,8].

There are important implications to these new findings. First, other successful cold fusion systems may also indicate their activity by a large, abnormal increase in the anti-Stokes to Stokes (aS/S) ratio. Second, these findings confirm the role of phonons in CF/LANR (previously observed indirectly [9]), and thought to be mainly optical phonons [10]. Third, acoustic phonons result from, or are required for, a cold fusion process producing energy gain in its "excess heat" (XSH) mode in this system.

2. Background – No Additional Applied Magnetic Fields

2.1. Cold fusion requires considerable engineering

The LANR method which Fleischmann and Pons first taught in March 1989 had problems, including inefficiency and non-reproducibility. This created havoc for those inexperienced in metallurgy, electrochemistry, and physics [11–14]. LANR success is rewarded by "excess heat", which means that the energy producing reactions have generated *de novo* helium into the lattice ($\sim 10^{12}$ for every watt-second [15]) and there were adequate conditions to enable energy transfer to the lattice and then to appear as excess heat [10,16]. There may also be other reactions.

One major problem to achieve successful cold fusion has been the difficulty in achieving high D/Pd loadings above ∼0.70 near room temperature, and then maintaining that, sometimes for weeks.

Simply put, the rapid increase in deuterium chemical potential acts to limit further loading, but success requires high loading of >85% for PdD$_x$ hydrides. In most initial efforts, loading was not even considered. Other problems have included the control of vacancies, adequate incubation time, concomitant flux, inadvertent quenching conditions, and lack of critical control of input power.

Many "negative" results are due to a failure to operate the system at the optimal operating point, which is an optimum peak in the excess heat and power gain curves as a function of input electrical power [12,14]. The optimal operating point reflects the relatively narrow peak (maximum) of the biphasic production rate curve for the products obtained by the desired reactions (heat, helium-4) as a function of input electrical power. The problems with loading, and later with optimal operating point manifolds (OOPs) are why initial efforts to replicate successful LANR were so difficult and failed to show excess heat.

2.2. Dry NANOR®-type CF/LANR preloaded components

NANOR®-type devices have been described in the literature [1–7]. The central core generating the excess heat in the desired state involves ZrO$_2$PdNiD, ZrO$_2$PdD, and ZrO$_2$NiD and similar materials [3,18]. A NANOR®-type component is a hermetically sealed cold fusion/lattice assisted nuclear reactions (CF/LANR) nanomaterial, preloaded with D and arranged as a two-terminal electrical component. They are designed to avoid leakage, enabling stabilization and activation of these materials.

2.3. Determination of activity

The LANR preloaded, stabilized NANOR®-type components are driven by a high voltage circuit up to 3000 V rail voltage. This is the high voltage that can be delivered in any run to either the NANOR or the ohmic control used to thermally calibrate the calorimeter.

Input power is defined as $V \times I$. There is no thermoneutral correction in denominator. Therefore, the observed power is a lower limit. The instantaneous power gain (power amplification factor (non-dimensional)) is defined as $P_{\text{output}}/P_{\text{input}}$.

The energy is calibrated by at least one electrical joule control (ohmic resistor) used frequently, and with time integration for additional validation. The excess energy, when present, is defined as $(P_{\text{output}} - P_{\text{input}}) \times$ time.

Data acquisition is taken from voltage, current, and temperature sensors at multiple sites of the solution, and outside of the cell, and even as a 4-terminal measurement of the NANOR®'s internal electrical conductivity. Data acquisition sampling is at data rates of 0.20–1 Hz, with 16–24$^+$ bit resolution; voltage accuracy 0.015$^{\pm 0.005}$ V, temperature accuracy <0.6°C). The noise power of the calorimeters have been in the range of a milliwatts (for demonstration systems) to tens of microwatts (for present R&D). The noise power of the Keithley current sources driving the reactions is generally ∼10 nW or less.

After driving the component and the control in each run, the power and energy gain for both the component and the ohmic control were separately determined both by approximations such as input-power-normalized delta-T incremental (dT/P_{in}), and input-power-normalized heat flow (delta-HF/P_{in}), and also directly by semiquantitative calorimetry. In the latter, the amount of output energy is determined from the released heat produced during the temperature rise, and then comparing that to the input energy.
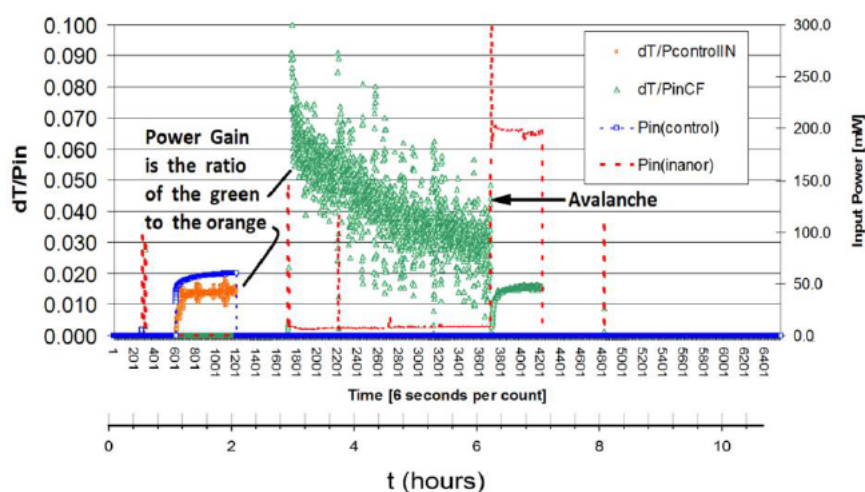
Figure 2. Demonstration of excess power gain and then sudden loss of activity after electrical avalanche for a NANOR®-type LANR component – The electrical input power and delta-T/P in (representative of the measured instantaneous power gain) from the ohmic control and then the nanostructured two-terminal NANOR®-type LANR component. Shown for the component are both sides of the electrical breakdown (avalanche) state; before where there is clear excess power gain (excess heat over time) and a return to ohmic-like behavior at, and after, the electrical avalanche.

2.4. CF/LANR activity quenched by electrical avalanche breakdown

There are two electrically driven states for a driven NANOR®-type LANR component. As described in a series of peer-reviewed publications [7], certain materials of this nature when examined electrically have distinct electrical behavior, with distinct outputs in each of the electrical driven states. To simplify, in addition to the undriven "off" state, there is the undesirable "avalanche" state, which associated with increasing electrical currents for decreasing applied electrical potentials over time. By contrast, the "desired" state produces very large amounts of heat beyond the normal electrical dissipation expected - excess heat. In that case, the electrical impedance is maintained.

Figure 2 presents the graphical output of a reproducible nanostructured NANOR®-type two-terminal CF electrical component, driven in both of its two different electrically driven states; and in its "off" state and also while "off" with an electrical ohmic control being driven. Vertical axes plot the electrical input power and the heat generated, as a function of time.

Figure 2 demonstrates that inactive states exist for "working" CF/LANR components. It shows the measured heat production from the nanostructured two-terminal NANOR®-type LANR component on both sides of the electrical breakdown (avalanche) state; active and quenched. This transformation of active CF/LANR components from active to quenched (inactive states; and there are more than one) is critical to successfully control the desired reactions, and to maximize output, and to avoid damage to some nanomaterials. In the figure, the first curve, extending from count circa 601 to 1201 (where each count is 6 s) is for the ohmic control. The second curve, extending from count circa 1701 to 3701 (where each count is 6 s) is for two-terminal nanostructure component. The electrical input is slowly increased to both the ohmic control and to the component, while each is activated, respectively.

However, only the two-terminal nanostructure component at about count 3701 suddenly undergoes paroxysmal electrical avalanche so that there is simply much more electrical input power as shown in the third curve. It lasts until about count 4201 when the input electrical power is turned off. The first vertical axis, on the left-hand side, represents the heat generated through the parameter dT/P_{in} which is the change in temperature elicited, divided by the electrical

input power. Figure 2 plots the temperature rise (delta-T in degrees C) of the ohmic control and the NANOR®-type LANR component, both normalized to input electrical power as a function of time so that the ratios can be used to estimate incremental power gain. By comparing the ratio, a qualitative to semiquantitative estimate of the incremental power gain can be derived, both before electrical avalanche (from the first pair) and after electrical avalanche (from the second pair). Thus, there is obvious incremental power gain for the CF/LANR component until the avalanche, at which time (count ~3700) the component has no energy gain, but has a response similar to an ohmic resistor.

This saliently demonstrates that outside of the desired heat-producing CF/LANR active state, the nanostructured component acts as any other ohmic resistor. Thus, it confirms that the calorimetry was calibrated, and verifies the accurate presence of excess heat yet an additional way. This result also demonstrates significant excess heat obtained from a Ni–D nanomaterial system, as reported previously in a high impedance aqueous CF/LANR system [7,17].

3. Experimental Methods

3.1. CMORE-spectroscopy

Previously, we reported the calibrated near-IR emissions from active aqueous CF/LANR systems [18]. This paper extends that range in nanomaterials to the optic spectrum. The diagnostic, coherent multi-wavelength optical reflection volume-enhanced electric-driven-sample spectroscopy (CMORE-spectroscopy), used for this report required at least two peak wavelengths, usually from two lasers. This was to co-illuminate the real target, located below the irradiated surface, and into the volume, of a sample of interest.

The high intensity coherent illumination was used to elicit Rayleigh, Brillouin, and Raman bands, and then to identify the possible roles of acoustic and optical phonons during CF/LANR, and possibly distinguish the desired active, excess heat-producing, state from the "off"-state, and the undesired inactive avalanche state. Multiple wavelength stimulation was first employed to enable wavelength calibration and thus semiquantitative measurements of the aS/S ratio.

The green laser (532 nm peak) had a power output level of about 150 mW. The orange laser (635 nm peak) had a power output level of about ∼2 mW for energy calibration. Other wavelengths used to calibrate included 436.6 and 546.5 nm peaks of mercury, and the 611.6 nm peak of europium. None was as useful as the second coherent red orange laser.

Laser polarization is usually important to the degree that the nanomaterial is electrically conductive. However, here, the nanomaterial is electrically insulating (∼ megohms to gigohms or more), and is porous, black like bituminous coal. There the light enters and has a volume interaction.

The sample illuminated was the core of a NANOR®-type LANR component capable of being electrically driven. Optics for collimation, control of beam direction, band pass filters, beam splitters, were used to obtain optical beam overlap on the sample's surface, facilitating interaction with the sample while being electrically driven. The important result is that illumination yields many photons which enter the black material which has the appearance of bituminous ground coal (and is ZrO_2–PdD) and react with it. The multifaceted craterous surface leads to a very significant volumetric photon–sample interaction. As a result of the interaction, what was initially just two initial frequencies coming from the two lasers, finally becomes a more complicated spectrum, decorated with the addition of photons of energy both above and below the two frequencies of said lasers.

The Boltzmann aS/S ratio was measured by a method enabling the simultaneous electrical driving of a ZrO_2PdD CF/LANR system in several states while simultaneously visualizing both acoustic and optical phonons using dual wavelength coherent stimulated volume-enhanced Rayleigh–Brillouin–Raman spectroscopy. When the emitted photons have less energy than the initial absorbed photon, then this energy difference is the Stokes shift. The energy goes into the lattice, and the difference is in the "red-shift" direction. On the other hand, if the emitted photon has more energy, the energy gain is called an anti-Stokes shift, and that extra energy is derived from energetic phonons in a

crystal lattice that give up their energy to create the "blue-shift" from the initial two frequencies.

To resolve the spectra (Figs. 3–10), the reflected (exit) beam leaves the illuminated sample through an optical slit and then passes through a diffraction grating where it is resolved into different energies (or in equivalent systems into wavelengths or frequencies). The intensity is measured by a detector such as a CCD or other sensitive photodetector. Analysis is made by integrating the incoming detected optical information which has been sorted by the grating. The
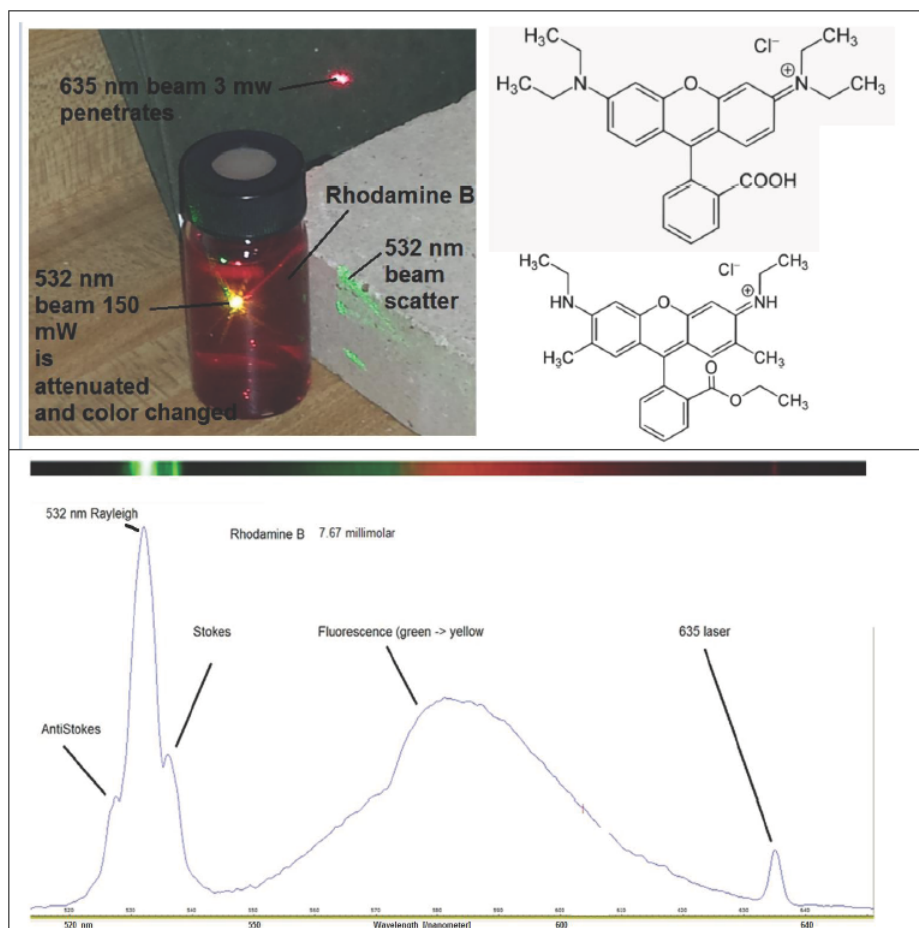
Figure 3. Dual wavelength reflection spectroscopy of a rhodamine B control. (*top-right*) Chemical structure of rhodamine B. Dyes tend to be a range of materials, here varying from (9-(2-carboxyphenyl)-6-diethylamino-3-xanthenylidene)-diethylammonium chloride (above) to the ethyl ester carboxyphenyl methylamino methyl xanthenylidene-ethylammonium chloride (below). (*top-left*) Optical scatter and passage through a small glass container of 7.6 mmol rhodamine B solution. The glass, irradiated by two co-linear lasers (532 and 635 nm) from the lower left (not seen), reveals the green laser only by fluorescence as yellow, although the scatter remains green on the right. Passing through the glass, the orange laser beam continues, exiting on the top right. (*bottom*) This CMORE-spectroscopic spectrum is a control experiment of rhodamine B (7.6 mmol aqueous solution). The vertical axis is non-linear and represents the intensity of the returned backscatter along with the reflected optical information, plotted as intensity as a function of wavelength. The horizontal axis plots the decreasing frequency to the right. The Stokes, anti-Stokes and fluorescence bands are seen in their well-known locations, and the two laser initiation wavelengths (532 and 635 nm) are seen and labeled. The actual image is located above the graph.

final plots show the total energy of the reflected beams in a distribution of amplitude (intensity) as a function of wavelength.

3.2. Electrical driving components

The sample or component was electrical driven, or not, while it was irradiated by the two lasers while physically maintained in position. The NANOR®-type component was electrically activated and controlled, and was designed to include and use several controls: several metals and material controls such as ZrO_2Pd and ZrO_2Ni, pn-junctions (as an energy conversion control), a thermal ohmic control, a non-functional unloaded NANOR®-type component control, an inactive undriven component as a control, an inactive driven avalanche-mode component as a control, and a component driven in the desired active mod*e*.

The electrical power supply is capable of delivering an electric current (Norton equivalent) or electric voltage (Thevenin equivalent) through the two wires which connect to the sample. The system has several electrical states, the simplest of which are "off", meaning that the sample is not electrically driven by the electrical power supply, and "on" where there may be a range of electrical driving levels of electrical power (W). Within the holding container there are temperature detectors, and a heat flow detector, linked to a temperature measurement and analytic unit. This enables thermometry to measure any possible incremental temperature change, and therefore analysis of possible heat output from the sample, itself.

3.3. Rhodamine B control

In order to test the system, and here to show the optical purity of the two lasers as well, dual wavelength reflection spectroscopy was performed on a solution of rhodamine B, as a control. The generated spectrum acts as a control to demonstrate the impact of the system on a rhodamine B aqueous solution of which the Stokes, anti-Stokes, and fluorescence bands are well known.

Figure 3 presents the chemical structure, what a solution of the rhodamine B does to two incoming laser beams, and the resultant spectrum by this system. This control experiment used a 7.6 mmol rhodamine B solution irradiated by the two laser wavelengths (532 and 635 nm). They are labeled in the figure, and the Stokes, anti-Stokes and fluorescence bands are clearly seen, demonstrating the effectiveness of the CMORE-spectroscopic system. The second laser peak permits semiquantitative wavelength (and thus energy) calibration.

4. Results – No Applied Magnetic Field

4.1. ZrO_2Pd – control – unloaded, undriven

As a control, the dual wavelength r**e**flection spectroscopy was used to examine an unloaded, undriven NANOR®-type component (ZrO_2Pd). The results are shown in Fig. 4.

4.2. ZrO_2PdD – control – undriven (null, "off state")

Figure 5 shows the response of the loaded, deuterated material, ZrO_2PdD, in a NANOR-type component to the dual wavelength reflection spectroscopy. This is a loaded, electrically undriven NANOR-type component (ZrO_2PdD). There was no additional electrical activation (as will be seen in some of the following figures).

This figure (like the next two) is also in Fig. 1, where the curves are superimposed as much as possible to summarize the discovery.
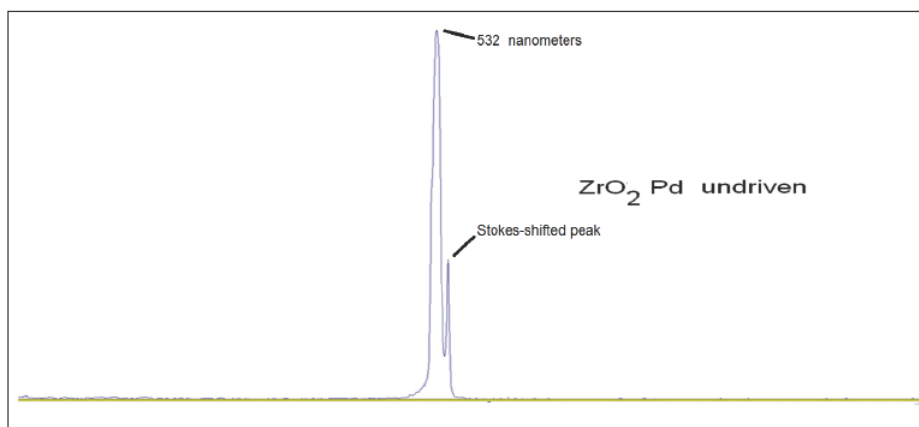
Figure 4. Dual wavelength volume-enhanced reflection spectroscopy of an unloaded, undriven NANOR-type component (ZrO_2Pd). This material is discussed elsewhere [3,17] and does not give excess heat [7]. Here the CMORE-spectroscopy reveals a clear Stokes peak with small, negligible, anti-Stokes component. This is discussed further below.

4.3. ZrO_2PdD-loaded, driven (electrical avalanche state)

Figure 6 shows the avalanche behavior by presenting the dual wavelength electric-driven volume-enhanced reflection spectroscopic signature of a loaded (over)-driven NANOR®-type component (ZrO_2PdD) in its avalanche mode.
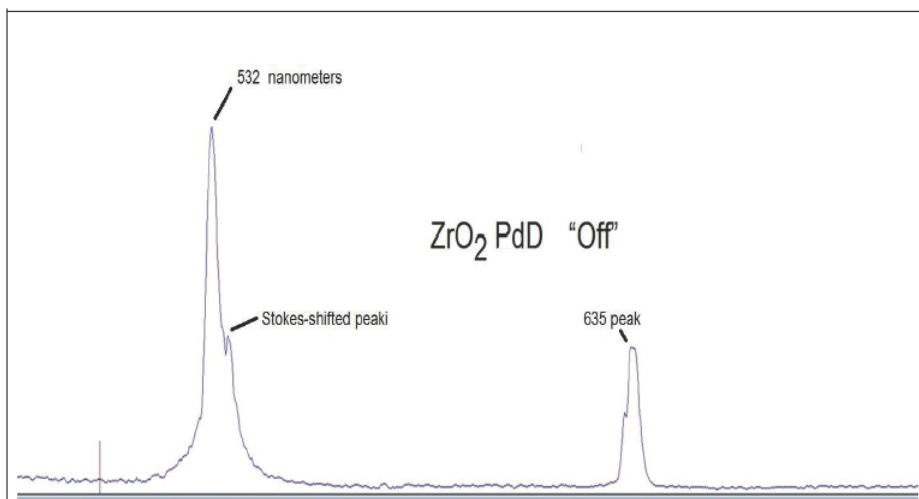
Figure 5. Dual wavelength volume-enhanced reflection spectroscopy of a loaded, undriven NANOR®-type component (ZrO_2PdD). This spectrum is obtained from the NANOR®-type component electrically "Off". Functionally, that makes the observed optical output to be that of the raw material, ZrO_2PdD with no additional electrical drive or activation. The vertical axis represents the intensity of the returned backscatter plotted as intensity as a function of wavelength. The horizontal axis plots the decreasing frequency to the right. The output of the first laser is shown as the peak on the left side, located at 532 nm. The output of the second laser is also shown on the right side, located at 635 nm
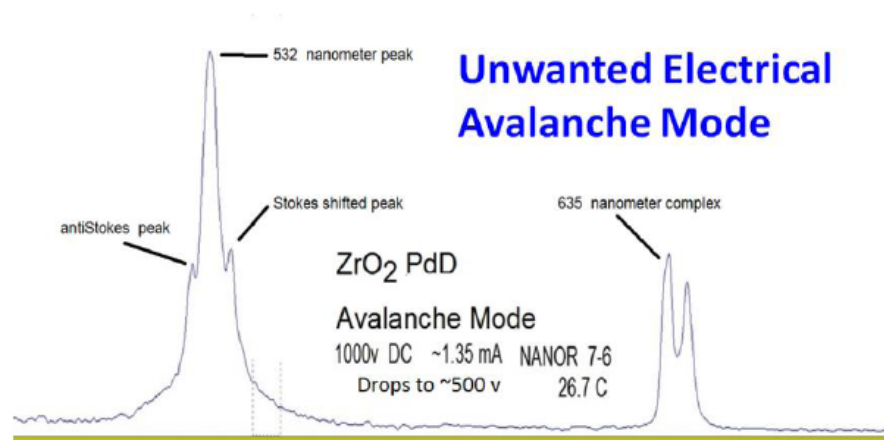
Figure 6. Dual wavelength electric-overdriven volume-enhanced reflection spectroscopy of ZrO$_2$PdD, a loaded, electrically over-driven NANOR®-type component in avalanche mode – This is the observed optical output in the undesired over-driven avalanche "state" as observed by the diagnostic. The graph, as the others, shows intensity as a function of wavelength of what was returned by backscatter along with the reflected optical beams. There are two groups of peaks. On the left, the peak of the first laser is at 532 nm. In this volume enhanced dual laser backscatter diagnostic, the largest peak is a Rayleigh scattering peak. It can be seen that just to the right of the largest peak is a smaller peak. This peak is almost balanced by a second, slightly smaller peak on the opposite side of the largest peak. These peaks are called Stokes-shifted and anti-Stokes-shifted peaks. What is seen to the left of the tallest peak is termed an anti-Stokes peak. On the right, the second laser interacted with the material and shows its own interactions, making calibration more difficult, so it is usually avoided, but is shown here to demonstrate this effect.

This is the third control "null", in that it is a non-functional (with respect to the desired excess heat) state. However, it is a very high intensity state known as the "Electrical Avalanche" mode, as described elsewhere [7].

This mode, associated with loss of excess heat, was previously presented as a function of time in Fig. 2. For Fig. 6, this loaded nanomaterial, ZrO$_2$PdD, in a modified two terminal, dry, NANOR®-type LANR electrical component was electrically driven at 1000 V initially (direct current) which enabled a current of about 1.35 mA. Thereafter, the voltage decreased with time to about 500 V. This behavior is what is termed "avalanche mode" and usually results

from excessive applied voltage. The ambient temperature was 26.7°C. Figure 6 shows the observed optical signature during its avalanche "state".

In Fig. 6, the peak of the first laser is at 532 nm; this is the Rayleigh scattering peak. To its right side is a smaller, Stokes-shifted, peak. This is almost balanced by a second, slightly smaller, anti-Stokes peak on the opposite, left side of the largest peak.

Intensity is shown as a function of wavelength, as returned by backscatter along with the reflected optical beams. There is a second peak far to the right, near 635 nm, from the orange laser. In this figure, the second beam was aligned to interact with the reaction volume. Thus, there is more than one single peak. There is a second group of two peaks, located far to the right, near 635 nm, which arise from the orange laser overlap interactions. Usually, the second laser is kept from interacting, and is used as a calibration signal. Here, a rich material science field of energy hopping and conversion are seen, which will be resolved in future efforts.

4.4. ZrO_2PdD-loaded, driven (desired, excess heat state)

The NANOR®-type LANR component is representative of driven CF/LANR systems, in that they are associated with two distinct outputs; one is rather conventional like an ohmic resistor, however, the other state is the electrical "desired" state. That desired mode is characterized by excess heat generation here, and in some experiments involving aqueous D_2O/Pd systems has shown to be linked, in a commensurate way, with the formation of *de novo* ^4He [15].

The functional, desired excess heat state of a correctly driven NANOR®-type component (ZrO_2PdD) in its "XSH" mode is non-thermally optically revealed in Fig. 7. The figure shows that the desired CF/LANR activity is indicated by a unique signature using dual wavelength electric-driven volume-enhanced reflection spectroscopy.

This signature advertises behavior which is called "desired mode" or "excess heat production mode" and only results from proper drive voltage, maintaining high impedance, and avoiding quenching materials and quenching states, as discussed elsewhere [1,3,7] and demonstrated conclusively in this report.

For Fig. 7, the nanomaterial NANOR®-type CF/LANR component was properly, correctly electrically driven at 2500 V which produced an electrical current of about 0.11 mA. The sample maintained its high impedance (compared to that seen during avalanche mode) during the very short run and there was no electrical avalanche quenching the desired reactions.

In Fig. 7, the peak of the first laser is at 532 nm; this is the Rayleigh scattering peak. To its right side is a smaller, Stokes-shifted, peak. This is over-balanced by a second, much larger, anti-Stokes peak on the opposite, left side of the largest peak. Note closely that in the best, most preferred, heat producing mode, the so-called "desired state", there is a much larger-than-expected anti-Stokes peak. This is the unique reflected optical output from the desired "excess heat" state where large amounts of energy are being released. Intensity is shown as a function of wavelength, as returned by backscatter along with the reflected optical beams. There is a second peak far to the right, near 635 nm, from the orange laser. The second beam was aligned to not interact with the reaction volume and was only used for calibration. Thus, there is a single peak.

In Fig. 7, the XSH mode can be seen by a unique reflected optical backscatter along with the reflected optical beams from the component in its desired "excess heat" state. Intensity is shown as a function of wavelength, as returned by backscatter along with the reflected optical beams. This is the observed optical output in the desired correctly driven active "state" as observed by the diagnostic. Shown is the output as intensity as a function of wavelength, as returned by backscatter along with the reflected optical beams from the volume-enhanced interactions (*vide infra*). In this run, the second beam did not interact with the reaction volume and was used for calibration. The nanomaterial NANOR®-type CF/LANR component was properly, correctly electrically driven at 2500 V which produced 0.11 mA, and it maintained its high impedance, without electrical avalanche, during the relatively short run.
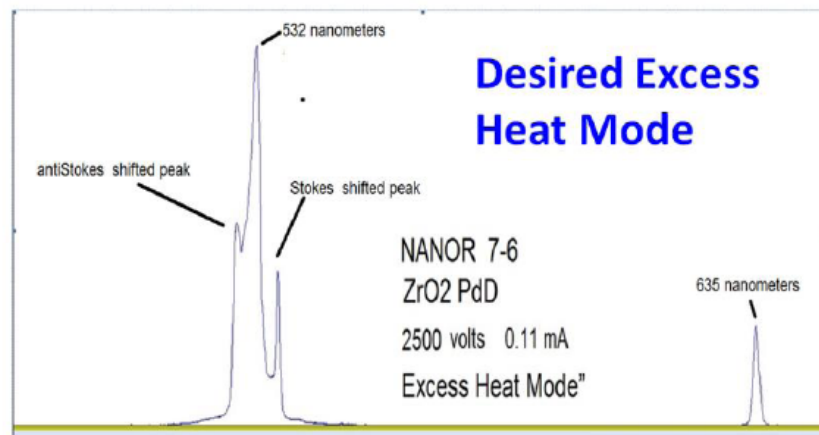
Figure 7. Dual wavelength electric-driven volume-enhanced reflection spectroscopy of a preloaded ZrO_2PdD NANOR®-type component in its correctly driven mode.

4.5. ZrO_2PdD – Optical phonons

In a solid lattice, alloyed with deuterons, there are multiple modes of vibration. The acoustical phonons are those where the palladium and deuterons move in phase in the long wavelength limit, located in reciprocal space at the center of the Brillouin zone. By contrast, optical phonons have from out-of-phase vibrations between neighboring atoms. They are called "optical" because in ionic crystals they can be excited by EM radiation, with the positive ions moving one way while their negatively charged neighbors move the other way. In k (momentum)-space, the phonons appear and manifolds in two branches. The lower manifold contains the acoustical branch, and the higher manifold contains the optical branch. There is an energy gap between them when a single metal is alloyed with hydrogen or deuterium.

To better observe the optical phonons, Fig. 8 is Fig. 7 redrawn, but with a logarithmic vertical axis to enable other peaks, of less intensity, the optical phonons, to stand out. CMORE-spectroscopy resolves and measures all phonon bands, which can be seen at optical frequencies (generally 5–30 THz) and acoustic frequencies (generally 5–15 GHz). The optical phonon bands are not yet well resolved in these first CMORE systems, but the need to do so clearly remains, and explorations should be fruitful.

In Fig. 8, the electrical driving mode of the two-terminal NANOR®-type CF/LANR component is the desired "XSH mode" and only results from proper drive voltage, maintaining high impedance, avoiding quenching materials and quenching states. Importantly, the phonon peaks visualized and measured in the present diagnostic, are both direct evidence of possible optical phonons being involved, and also corroborating the indirect evidence of Cravens et al. [9].

The XSH mode can be visualized by a unique reflected optical backscatter signature. The observed logarithmic optical output in the desired "excess heat" state is returned by backscatter along with the reflected optical beams. Intensity is shown as a function of frequency here to make comparison to the important work of Cravens et al. [9] easier.
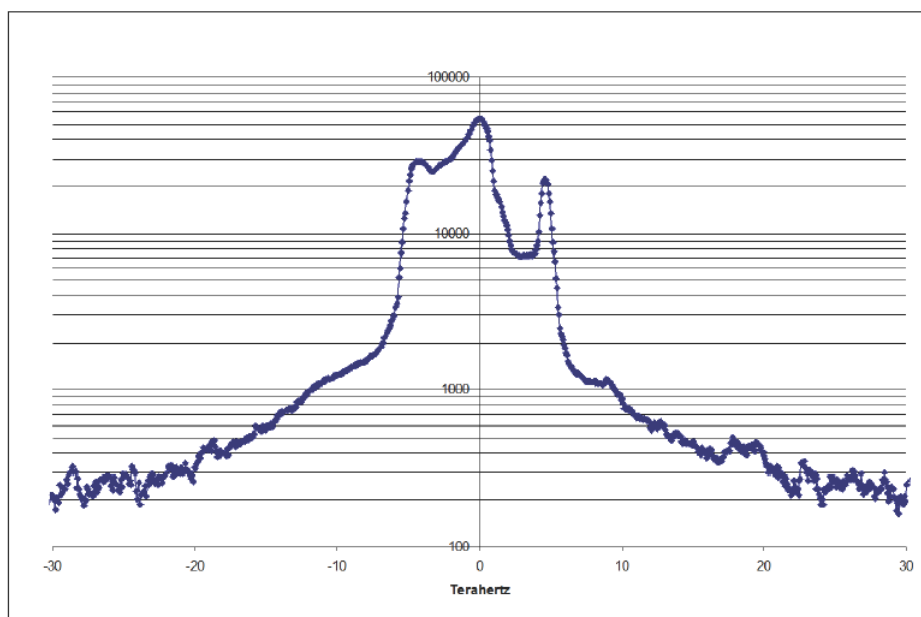
Figure 8. Logarithmic presentation of dual wavelength electric-driven volume-enhanced reflection spectroscopy of a preloaded, correctly driven, ZrO$_2$PdD NANOR®-type component. The x-axis here presents the frequency difference from the main laser frequency.

5. Results – Magnetic Fields Applied; No Electrical Drive

5.1. Impact of magnetic fields on aqueous CF systems

Previously, magnetic [20–22], and radiofrequency electromagnetic [23] effects have been reported in aqueous cold fusion (a.k.a. lattice assisted nuclear reactions, CF/LANR) systems. In aqueous CF/LANR systems, steady magnetic fields have a small effect which may be inhibitory, especially if perpendicular [22]. In nanomaterial CF/LANR systems, constant magnetic fields produce small effects which may be inhibitory, especially if applied perpendicular to the direction of the applied electric field intensity.

5.2. Impact of magnetic fields on NANOR®-type LANR components

It was discovered that for time varying alternating magnetic interactions with nanostructured CF/LANR systems [4], the post-magnetization effects are significant and time-variant. There is also enhanced improvement of LANR (which occurs at the same time as the magnetization and therefore is called "synchronous").

There are also metachronous effects (occurring later) including power gain and on the observed "heat after death" (HAD); another name for which is the time-integral of the tardive thermal power [12,13], and strong evidence of the first-ever observed two (2) optimal operating point (OOP) manifolds [4].

The application of dH/dt created an increase of 4–10 times the peak power gain over conventional LANR with the same system. The peak power gain of such treated NANOR®s (M-NANOR®s) ranged from 22 to up to ∼80 times input electrical power or more beyond the control, as determined by calorimetry [4]. Furthermore, in contrast to previously observed exponential falloffs of sample activity (peak incremental excess power gain), post-magnetization

activity demonstrates oscillatory activity circa 1.3×10^{-4} Hz (range 0.2-5 $\times 10^{-4}$ Hz). Because of the very complicated issues, magnetically treated NANOR®-type components are called M-NANOR®-type components to distinguish them and anticipate their unique and unusual behavior, and the report here is only of the component in the undriven state with an applied H-field.

There are other impacts of applied magnetic fields intensities on these CF/LANR components. Previously, all CF systems and the NANOR®s have shown a single optimal operating point manifold for excess heat operation, ^{4}He production, and other products. Today, that is no longer accurate. Even after a single treatment to a high intensity Fractionated Magnetic field, there arise two OOP manifolds. The new one is at higher input electrical currents to the NANOR®, and is located to the "right" of the conventional CF/LANR OOP. Thus, magnetically activating preloaded nanostructured CF/LANR devices is very useful [4,18]. Although cold fusion (LANR) has a first stage mediated by phonons within the loaded lattice, there is a magnetically coerced second stage, which we believe may be mediated by magnons, or interactions of phonons in H-field and included magnetization field.

For these very complicated reasons, therefore only the applied H field without activation will be discussed in this initial manuscript.

5.3. ZrO$_2$PdD "Off" mode, undriven with applied magnetic field

Figure 9 shows the CMORE-spectroscopic signature of the undriven NANOR®-type LANR component (containing ZrO$_2$PdD) with the simultaneous application of an applied magnetic field of estimated intensity $\sim$2 T. For simplicity, as discussed above, this component was not electrically driven. The electronic vibrations themselves do not produce the desired reactions of excess heat, but with the desired mode they have been demonstrated to produce even more heat [1,3].

Yet, even in the undriven state, it can be observed in Fig. 9, that for this ZrO$_2$PdD nanomaterial component, the applied high intensity H-field produces an unusual distribution of anti-Stokes electronic vibrations. There is not a single peak like the others, but instead a complex set of H-field induced anti-Stokes peaks. This may be consistent with a distribution of energies or energy level splits as magnetic fields wrought, such as with the Zeeman effect, or as discussed below consistent with inhibiting the effect of the ZrO$_2$ alone.

5.4. ZrO$_2$PdD "Off" – width of anti-Stoke peaks and magnetic field

Figure 10 shows the half width of these H-induced distributions of anti-Stokes peaks which appear during the presence of the applied magnetic field. Figure 10 was obtained by three consecutive runs in which the magnet was brought next to, and half way to, the optically irradiated component. It can be seen that the H-induced width of the anti-Stokes peaks increases, but that the increase appears to plateau in this most qualitative of experiments.

In Fig. 9, at 105.6/cm, the calculated Boltzmann statistics ratio is 0.60. The Boltzmann intensity ratio was actually 0.32. At 56/cm, the calculated Boltzmann statistics ratio is 0.76. The Boltzmann intensity ratio was actually 0.51. Both are qualitatively close.

This curve, shown as intensity as a function of wavelength, was returned by backscatter along with the reflected two optical laser beams. Only one laser peak is shown here, with the upper level well beyond the range of the graph; the other peak is far to the right. The units are 1/cm from Raman spectroscopy.

6. Interpretation

6.1. Excellent signal picked up by CMORE spectroscopy

There are many important questions, issues, and ideas that accrue from these studies and observations. They begin with the response itself. The black granular nanomaterials fortunately give very large signals. Why are there such
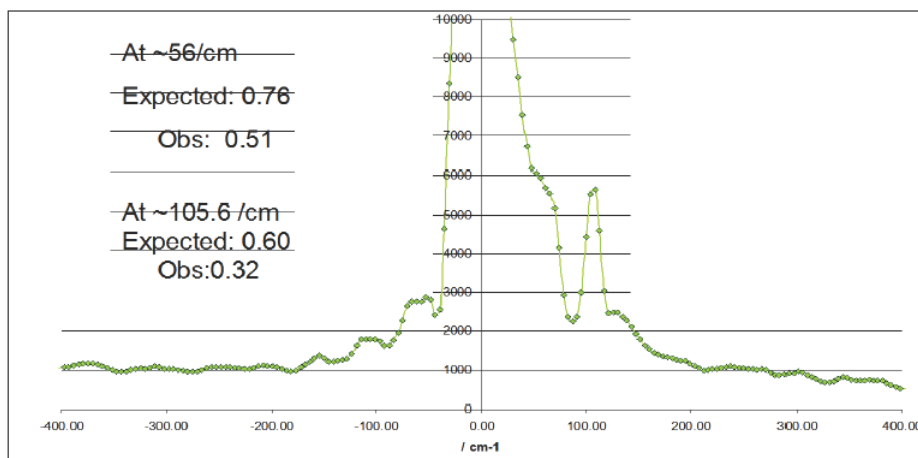
Figure 9. Dual wavelength volume enhanced spectroscopy. The observed optical output of the NANOR®-type LANR component (containing ZrO$_2$PdD) with no additional electrical drive/activation, the "off" state, but with an additional static applied magnetic field intensity of approximately 2 T at its peak, abutting the core. The x-axis here is plotted as normally done in Raman spectroscopy with the units of (1/cm), to which it is normalized.

large peaks? And, a corollary is: why is there such volume enhancement. The volume enhancement is probably from the black nanostructured CF/LANR materials which are black, electrically insulating, and therefore will accept light deeply into the material, very unlike a conductive metal electrode.
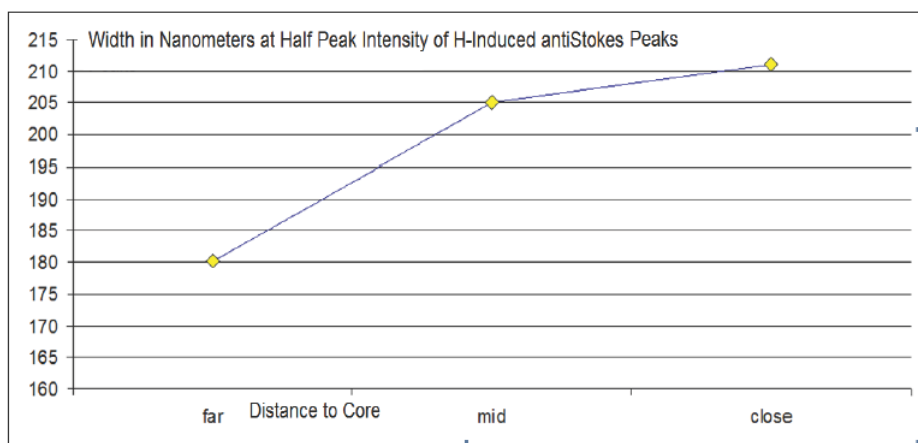
Figure 10. Half width of the newly appearing distribution of anti-Stokes peaks which appeared only with a magnetic field intensity, imaged using dual wavelength electric-driven volume enhanced (CMORE) spectroscopy. Shown is the half intensity width in nanometers in the presence of an applied magnetic field. This figure qualitatively represents three runs in which the magnet was brought successively closer to the surface of the irradiated, undriven, loaded component.
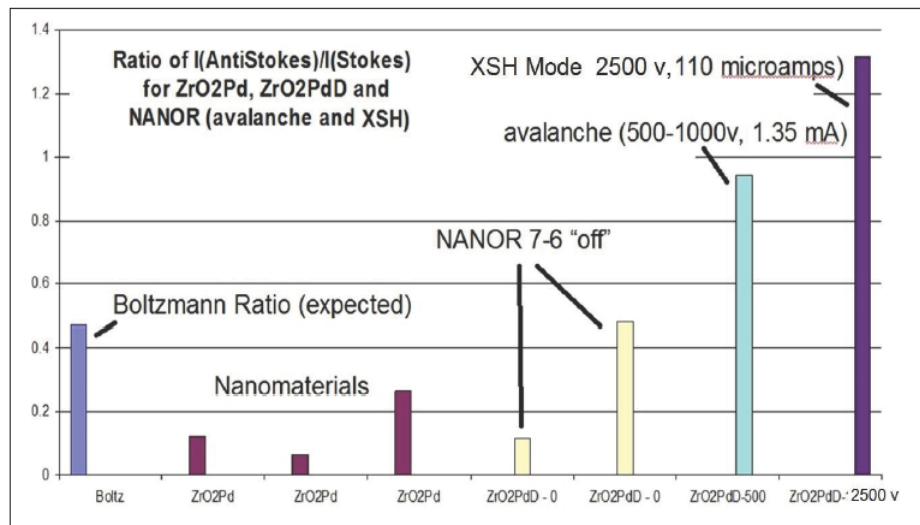
Figure 11.   Histogram of measured Boltzmann ratios and what is expected. Shown are the experimental Boltzmann ratios measured for a series of materials, and a NANOR®-type LANR component in its three modes.

6.2. Boltzmann statistic and intensity ratio analysis

Figure 11 is a histogram that presents both the Boltzmann statistic ratio and the Boltzmann aS/S intensity ratios which were experimentally measured by the CMORE-spectroscopy for a series of materials, and a NANOR®-type LANR component in its three electrical modes (states). In Fig 11, the horizontal axis shows and identifies eight different categories of said ZrO_2Pd, ZrO_2PdD nanomaterial, and three electrical drive states, and what is expected normally. The vertical axis shows the amplitude of the theoretical Boltzmann statistic ratio and the experimental Boltzmann aS/S Intensity ratios.

In physics, the calculated Boltzmann statistic ratio (also known as the Boltzmann factor) is derived from the frequency and the temperature. Numerically, it is calculated from the exponential of the ratio of two energies. Those energies are the energy of the difference in energies and the thermal energy (which is the Boltzmann constant times the thermodynamic temperature in Kelvin). This is done because the ratio thus reflects the magnitude of the expected populations of the two states.

When those values are inserted into the conventional formulae, the expected Boltzmann statistic ratio is a number between 0.4 and 0.6, as can be seen in the first column of Fig. 11. The other columns were derived experimentally for this report. The Boltzmann aS/S intensity ratio is derived from the actual measured relative intensities of the anti-Stokes peak divided by the intensity of the Stokes peak. Here, those values were determined by CMORE-spectroscopy. Then, the ratio is derived from the intensity of the anti-Stokes peak divided by the intensity of the Stokes peak. The histogram shows the collected information. It was obtained from the data obtained using measured Boltzmann ratios for a variety of related samples; including the relevant ZrO_2Pd nanomaterial, before heavy hydrogen is added, and after the loading deuterons to a very high level [3], and then with the two-terminal component in several electrical drive states.

6.3. Results for unloaded ZrO_2Pd

The second through fourth columns are different preparations of nanomaterial ZrO_2Pd, itself, without the addition of deuterons (heavy hydrogen). The results shown for these three samples demonstrate that they have Boltzmann ratios which are less than expected. This was surprising because for metals and most materials examined, the aS/S ratio was at the level expected, whereas for these nanomaterials examined, the aS/S ratio was at, or below, the level expected.

Why do they act this way? One hypothesis is the presence of volume polaritons removing the anti-Stokes population by dissipating the energy. A polariton is light bound to an exciton. They are bosonic quasiparticles, different from polarons (which is an electron bound to a group of coherent phonons) which are fermionic. Polaritons are usually considered as surface plasmon polaritons (SPP) which involve infrared through blue electromagnetic waves which travel along a metal–dielectric or metal–air interface. However, here, we propose that the nanomaterial is an electrically insulating (megohms to gigohms or more), volume porous, black (like bituminous coal) absorber. The light enters the volume and has a volume interaction, and some gets reflected back to the surface to be picked up by CMORE spectroscopy.

This volume interaction, through volume plasmon polaritons (VPP) which travel inside the core material, relies on the high impedance dielectric mixed with the island-like widely sequestered highly loaded alloy. VPP would explain the missing anti-Stokes peaks nanomaterials because just as an SPP will evanescently propagate along the surface interface, the VPP will travel further through the volume until its energy is lost.

6.4. Results for loaded undriven ZrO_2Pd

The next two columns were obtained from two samples which were originally from two of the three same nanomaterial samples, except that these two had been very highly loaded with heavy hydrogen. The dry loaded materials were each inserted into a two terminal NANOR®-type CF/LANR component and optically examined. Those samples, not electrically driven, had Boltzmann intensity ratios which ranged from the lowest values up to the normal expected Boltzmann ratio. The upper value for a two-terminal ZrO_2PdD component which was loaded, and "off" with no electric drive, was in the normal range.

The present diagnostic CMORE spectroscopy has revealed the relative absence of anti-Stokes-type peaks in nanostructured materials which are not electrically driven, with the result that the expected Boltzmann ratio is far below what is expected. Why are anti-Stokes-shifted peaks substantively absent for nanomaterials not electrically driven? What is there about nanostructured CF/LANR materials at rest that makes them only dissipate acoustic phonon energy? Probably the multiplicity of available stereoconstellations of the material that allow their dissipation making phonons ephemeral.

6.5. Loaded, avalanche driven ZrO_2PdD

Then, the next columns involve electrical activation: first electrical avalanche, and then the excess heat producing ("desired") mode. When nanostructured NANOR®-type components are driven in Avalanche Mode, the anti-Stokes-type components which appear are different in type, location, and amount, from those which appear during the excess heat producing "desired mode". It has been discovered that there exist increased levels of anti-Stokes-type peaks for all nanostructured materials undergoing electrical drive. Specifically, there is for the avalanche mode for the two-terminal NANOR®-type CF/LANR component close to the near-expected amount of anti-Stokes peaks.

Why the difference? It might be higher in amplitude than the undriven samples in part because the temperature is increased in the sample, and to a lesser degree due in part to second-order curve shift, but the most likely cause is an increase in the acoustic phonon population.

6.6. Loaded, XSH-producing driven ZrO_2PdD

For the activated NANOR$^{\circledR}$-type CF/LANR component, there was a major, dramatic increase of the anti-Stokes component and the aS/S ratio both greater than expected. It has been discovered that there exist increased levels of anti-Stokes-type peaks for all nanostructured materials undergoing electrical drive, however, the aS/S ratio goes above one only in active, desired mode.

In fact, not only is the anti-Stokes peak of the "desired state" much higher in amplitude than expected for an initial Boltzmann Statistic calculation, it is beyond any known calculated temperature, and beyond what could accrue due to curve shift to a very slight amount.

Figure 11 shows the dramatic increase of the anti-Stokes component for an activated NANOR$^{\circledR}$-type CF/LANR component. This unusual aS/S ratio exists ONLY with active NANOR$^{\circledR}$-type LANR component in excess heat producing mode, characterized by a larger electrical impedance which precedes electrical breakdown.

6.7. Magnetic fields in undriven ZrO_2PdD

These magnetic field observations may be quite important. The present diagnostic has discovered that an applied magnetic field of high intensity creates new, multiple low level, distributed anti-Stokes-type peaks which appear for unelectrically driven nanostructured materials.

The increased levels of anti-Stokes-type peaks in correctly driven CF/LANR nanostructured components and materials, and the new lower intensity, but distributed anti-Stokes-type peaks which appear only when a magnetic field intensity is applied, both teach about their role in the coupling of energy production and energy conversion. These new magnetic-induced anti-Stokes-type peaks which appear and indicate a range of energies suddenly having become available (Fig. 9). This may help explain, in part, what applied magnetic fields are doing [4,8], here perhaps working by splitting energy levels like the Zeeman effect [24], thus making them more available.

Another possibility is that the applied magnetic field intensity separates molecular hydrogen into spin isomers. Normally only molecular hydrogen is considered, but another possibility is that it may also separate deuterons within the ZrO_2PdD lattice structure, specifically the local regions interacting where deuterons are held together in a solid solution [25] stereoconstellation with the electrically insulating ZrO_2. This may enable ortho-para states which could influence resonance scattering of phonons by any group of paired or organized clusters of ortho-para deuterons.

7. Conclusions

7.1. Summary of results

The results of measuring $R_{aS/S}$ in several types of CF/LANR nanomaterials and during different types of electrical activation can be simply summarized in Fig. 11, and in the following Table 1. Figure 11 shows by, histogram of the experimentally measured Boltzmann ratios, and the first column in the histogram shows exactly what is expected by calculation. To the right of that "' expectation" column ("expected"), are shown the experimental Boltzmann ratios actually measured for a series of nanomaterials, and then a NANOR$^{\circledR}$-type LANR component in its three electrically driven modes.

From Fig. 11, Table 1 compares the information experimentally derived to what was expected by calculation (shown as first column of Fig. 11). The table indicates what was actually experimentally measured compared to those calculated Boltzmann aS/S ratios. In the first two rows, the presence of the lower-energy Stokes-type peaks, and the presence of higher energy anti-Stokes-type peaks are denoted. The final row summarizes how the measured Boltzmann ratios compare to the expected and calculated.

For the first column, the results are for nanostructured material not electrically driven, and therefore is in the "off" state. The second column denotes the result of the application of a very large magnetic fields intensity in the "off"

Table 1. Summary results Boltzmann Stokes ratios: measured versus calculated. The ratio of the actual measured Boltzmann Stokes ratio (Intensity of anti-Stoke-type peak to the Stoke-type peak) as compared to the expected calculated Boltzmann statistic ratios for ZrO_2PdD in a NANOR-type component. The columns represent variants of electric field (E-) drive and H-applied state (not all categories are present).

	Undriven	H-field no E-field	Avalanche E-field	XSH E-field
Stokes	+	+	+	+/-
Anti-Stokes	0/–	–/+	+	+++
I(aS)/(S)	$\ll$ BRatio(calc)	< BRatio(calc)	$\sim$ BRatio(calc)	$\gg$ BRatio(calc)

state. The last two columns denote the results of the loaded ZrO_2PdD NANOR®-type component in both its avalanche (non-excess heat-producing) mode and the desired (excess heat-producing) mode.

7.2. Phonons have been visualized

Previously, cold fusion investigators have not been able to directly see phonons in their hydrogen loaded systems, although they have been inferred indirectly through beat frequency two wavelength systems [9]. By contrast, this new diagnostic enables direct visualization of the actual phonon states of the hydrogen loaded material, even while it is being electrically driven. Specifically, volume-enhanced electrically driven multiwavelength optical (CMORE) spectroscopy decodes cold fusion as it images acoustic and optical phonon prevalence and their diversity.

This preliminary effort has resolved the phonon bands directly in several metals and other materials, and has shown the impact of magnetic fields, of the zirconia itself, of the loading, and of the impact of electrical activation – including the obvious existence of two (2) states (desired XSH and electrical avalanche).

Several questions arise, such as: what are the implications of the separate characterizations of these similar materials? These are important for at least three reasons. First, the phonon gain represent CF/LANR activity, precedes the excess heat, and as has been stated, "LANR and cold fusion have been treated as a "ghost", as there was no way to see the desired state (short of measuring the accrued excess heat later), but this method enables the "ghost" to be seen [26]. This can impact CF/LANR R&D in general, and education and acceptance, as well.

Second, the present CMORE-spectroscopic system reveals that not all CF/LANR nanomaterial states are the same. Note that the active, driven CF/LANR state is not similar to other states or other materials – and it is now distinguishable.

Third, it also reveals that not all electric drive regimes of such CF/LANR systems are the same optically, consistent with thermal and electrical reports [7].

7.3. Acoustic phonon gain during XSH mode

The present diagnostic has revealed new direct evidence of the crucial role of acoustic phonons when a NANOR®-type CF/LANR component is driven in its XSH mode. Specifically, CMORE spectroscopy has revealed a greater-than-normal intensity of anti-Stokes peaks (Figs. 6–11), and therefore acoustic phonon density, only during XSH heat mode compared to both the "off" state and compared to the avalanche mode.

CF/LANR activity is now absolutely linked with acoustic phonons - and only the lattice enables them. Therefore, there are some implications. First, acoustic phonon gain either results from, or is required for, a cold fusion process which produces energy gain in XSH mode. Successful cold fusion creates an aS/S ratio greater than 1 during excess heat. Attention is directed to the fact that in the desired electric-driven excess heat-producing mode, characterized by very high electrical impedance, the two-terminal deuterided NANOR®-type CF/LANR component has a measured Boltzmann Stokes ratio $\sim$1.3.

Second, this discovery is consistent with the role of phonons previously observed indirectly [9], thought to be mainly optical phonons [10]. However, although optical phonons had previously been considered key to the energy transfer of ^{4}He* formed *de novo*, the present diagnostic system has determined a role for acoustic phonons in active CF/LANR systems.

Third, in retrospect, this discovery may also be consistent with the fact that only acoustic phonons are used to calculate the thermal conductivity of a material.

Fourth, how do the XSH-generated acoustic phonons enable the creation of, or de-excitation loss of, ^{4}He* (which is the precursor to de novo ^{4}He seen with the excess heat in aqueous systems [15]?) This diagnostic has detected the existence and visualized a large single anti-Stokes peak, heralding phonon gain, which is ONLY associated with active CF/LANR XSH-production.

7.4. Absent anti-Stokes peaks of undriven ZrO$_2$PdD and ZrO$_2$Pd

7.4.1. *Anti-Stokes peaks of undriven ZrO$_2$PdD and ZrO$_2$Pd are missing*

Why are the anti-Stokes peaks missing in CF/LANR nanomaterials in ZrO$_2$?

As discussed above, and seen in Fig. 12, there is significant loss of anti-Stokes peaks in the CF/LANR nano-materials by this spectroscopy. Where did the anti-Stokes peaks go in the depth of the nanomaterials? The key to understanding that arises from the use of another control, which is ZrO$_2$, alone. Pure zirconia's CMORE signature is shown in Fig. 12 where the two laser initiation wavelengths of 532 and 635 nm are obvious. However, note that the first peak has a very extended array of Stokes peaks observed falling to its right, in an intensity-decreasing sequence. This optical signature of pure zirconia is unique of all the materials so far examined. ZrO$_2$ has a thick richness of Stokes peaks. As a control, a white ceramic crucible shows the purity of the laser beam and the absence of the intensity-decreasing pattern of ZrO$_2$.

This very unusual pattern for ZrO$_2$ might explain exactly where the anti-Stokes peaks of nanomaterial ZrO$_2$Pd and
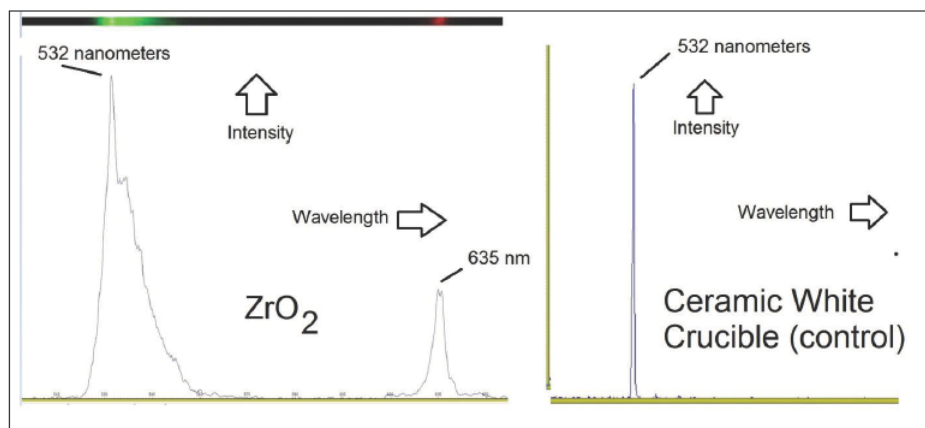
Figure 12. Dual wavelength reflection CMORE Spectroscopy of ceramic control and ZrO$_2$. (*left*) This CMORE-spectroscopic spectrum is a control experiment of a polished spherical surface of zirconia (ZrO$_2$) without any other added material. The horizontal axis plots the increasing wavelength to the right. The extended multi-peak Stokes sequence of zirconia is unique for all materials so far examined by this system. The two laser initiation wavelengths (532 and 635 nm) are seen. The actual reflected image is located above the graph. (*right*) As a control, a ceramic white crucible demonstrates the relative purity of the beam, and the absence of the decreasing Stokes peaks that occur with ZrO$_2$.

ZrO_2PdD disappear prior to electrical activation. Given that Stokes peaks herald loss of energy of incident surface irradiation, it certainly seems possible that ZrO_2 is a molecular system able to dissipate energy through phonons (Fig. 12).

The molecular engineering of ZrO_2PdD thus implies an energy-dissipating cohort of intra-lattice phonons in ZrO_2 under normal conditions prior to electrical activation. What material science stereoconstellation might possibly be the origin of this?

7.4.2. *ZrO_2 unit cell features seven Zr atoms and a vacancy*

The material science must explain why ZrO_2 has the unique feature of an extended array of multiple Stokes peaks in an intensity-decreasing sequence, as shown in Fig. 12. It's unit cell may explain the unique spectrum. Zirconium dioxide (ZrO_2, or "zirconia" from the Persian word "zargun" meaning "gold-colored") is a monoclinic crystal characterized by low thermal conductivity, low electronic conductivity, high tensile strength and a band gap of 5–7 eV. The color may result from the array of optical phonons available (Fig. 12), and be consistent with the observation shown in that figure that ZrO_2 has successive Stokes peaks. However, the acoustic phonon peaks, which are features of Fig. 12, may result because the unit cell of the lattice of ZrO_2 is unlike all the others, such as TiO_2. TiO_2 has a body-centered tetragonal unit cell, with eight titanium atoms in the eight corners. But unlike TiO_2, in ZrO_2 (zirconia), the zirconium eight atoms cannot all fit in the unit cell's corner positions. Instead of eight, because of size and electrostatic considerations, only seven Zr nuclei can fit. As a result, there is a vacancy; and that empty site may be very important for cold fusion (perhaps the very location where cold fusion occurs, driven by the in-phase acoustic phonons). Functionally, the vacancy must be unstable enabling large numbers of vibrations, as revealed in Fig. 12.

7.5. Avalanche anti-Stokes peaks differ from excess heat peaks

The avalanche mode-induced anti-Stokes peaks differ considerably from those observed in the XSH mode, and anti-Stokes peaks are relatively missing in the undriven mode. The avalanche anti-Stokes peaks are greater in number, energy variation, and in lower amounts than the XSH mode-produced anti-Stokes peak.

So one must consider in what way(s) are the XSH-generated acoustic phonons an alternative to the avalanche-generated acoustic phonons for electrical energy dissipation and transfer through the ZrO_2, which acts as an electrical insulator? There appear to be two electrical heat-generating mechanisms which both dissipate energy (both applied and possibly generated internally), and they are distinguished by two entirely different end products, amounts of output heat production, and CMORE signatures. In the unwanted mode, the anti-Stokes peaks of the electrical avalanche indicate conventional dissipation including undesirable electronic and lattice vibrations. In contrast, in the desired excess heat-producing mode, the phonon gain heralded by the large anti-Stokes peaks must somehow tie to unlocking the excited ^{4}He* and coupling the energy released to the lattice as whole.

7.6. Magnetic field increases anti-Stokes peaks

The applied magnetic field intensity-induced anti-Stokes peaks are greater in number, energy variation, and in lower amounts than both the avalanche and the XSH mode-produced anti-Stokes peaks. The complex set of applied H-field-induced anti-Stokes peaks has levels which are qualitatively closer to those expected by calculation. One possibility is that the H-field inhibits movement of charged particles in CF/LANR systems [22], and so here the normal effect of ZrO_2 removing the anti-Stokes peaks of nanomaterials is itself inhibited; and so they reappear. Furthermore, note that the applied magnetic field intensity creates a distribution of energy levels, similar to the Zeeman effect [24,28,29].

7.7. Direct new information about CF/LANR excess heat

7.7.1. *Implications of the aS/S ratio >1 during excess heat*

Why is the aS/S ratio so high with XSH mode in ZrO_2PdD?

There are important implications of an XSH-related aS/S ratio greater than one, from/during the desired cold fusion/LANR state. First, it can indicate, and so far is ONLY associated with, the desired electronic state of cold fusion (lattice assisted nuclear reaction; CF/LANR) activity in a NANOR-type CF/LANR component.

Second, that ratio is significant evidence of acoustic phonon gain, which itself is present only while the preloaded NANOR-type component is driven electrically. The highest levels indicate that the active CF/LANR system, confirmed by the CMORE-spectroscopy, is driven properly.

Third, that ratio is far outside of the range expected normally by temperature alone. It passes through a region which is beyond any known calculated temperature [27]. It is a level greater than could be accounted for by a prosaic curve shift secondary to temperature.

7.7.2. *Calculation of effective temperature during excess heat*

The fact that the Boltzmann Stokes ratio is $\sim$1.3 reveals more about successful cold fusion. Because the Stokes and anti-Stokes energies are derivable, the effective Stokes temperature can be computed from the experimental data to reveal the core temperature during the XSH mode. The next equation derives the calculated Boltzmann Stokes ratio (BRatio(calc) in Table 1, and sometimes called the calculated Boltzmann Statistic ratio). The equation involves temperature, and is

$$R_{\text{aS/S(calculated)}} = Intensity(\text{anti-Stokes})/Intensity(\text{Stokes}) = \exp(-E_{\text{diff}}/(k_{\text{B}} \times T)), \tag{1}$$

where E_{diff} is the energy difference between the two states is 5.96×10^{-21} J and k_{B} is the Boltzmann's constant. The calculated temperature at core is, therefore, $\sim$1645 K ($\sim$1372°C).

7.7.3. *Implication of cross-over to phonon gain*

Temperature results from the number of states available to a system [24,28,29]. As the Stokes ratio first rises from the unusually low levels of the CF/LANR nanomaterials, the Stokes ratio is less than 1, the energy difference is positive and temperature has a real, physical value which increases. As the Stokes ratio approaches 1, the energy difference approaches zero, and the temperature is determined by l'Hospital's rule. The limit at a Boltzmann Stokes ratio of 1 is infinity; so technically, this suggests a sudden, tunneling, crossing between the two states. Once the system is on the other side, with a Bolzmann ratios >1, which is the heat producing state, the energy difference is negative and temperature again has a real, physical value.

7.7.4. *Calculation of phonon number during excess heat*

How does the desired XSH mode actually create the anti-Stokes components at levels higher than observed for all other material precursor and avalanche mode? The Stokes and anti-Stokes energies are derivable, and therefore the number

Table 2. Variables used in calculation.

R_{s}	the Stokes ratio $=$ Intensity(anti-Stokes)/Intensity(Stokes)
k_{B}	the Boltzmann's constant $= 1.38066 \times 10^{-23}$ J/K
T	Temperature (K)
$E_{\text{diff}} = \Delta E$	Energy difference

of phonons involved during excess heat can be computed. As discussed in solid state texts [28,29], with an acoustic frequency of 4.9 $^{\pm 0.1}$ THz, there are ~ 7 $^{\pm 0.15}$ phonons involved. The important point is that this is much lower than has ever been expected before in most theoretic analyses of energy transfer, although it was considered from the point of view of a palladium lattice Pd vacancy surround by 6 deuterons [31].

7.8. The XSH-anti-Stokes peaks and CF/LANR material science

Many questions arise.

- Now, given that acoustic phonons are so important to active CF/LANR systems, then how are they actually linked to the material science?
- What are the material science implications of deriving seven (7) acoustic phonons?
- What might be the physical basis and origin of this?

In this case, perhaps the role results from the inability of hydrogen (deuteron or protium) to normally penetrate the ZrO_2 easily (unlike ionic oxygen), because ZrO_2 is a known electrical insulator. Thus, in zirconium oxide nanostructured CF/LANR materials, one would not expect the lightweight hydrogen nuclei to move across it, but instead rather to remain sequestered as an alloy in the group VIII metallic palladium (or nickel, as it is also used) portions of the separated mixture. The hydrogen remains sequestered, yet crushed by the applied electric field intensity, at the boundary between the alloy and the zirconia.

7.9. Phuson theory corroborated

The proof that phonons are involved as a cohort for the excess heat in active cold fusion (LANR) systems supports the PHUSON Theory. The PHUSON theory [16] of coherent energy transfer to the lattice using phonons appears to be corroborated. It explains the massive energy cooperative transfer from the megavoltage energy of the ^{4}He* to the lattice in a coherent de-excitation process which proceeds by way of lossy spin bosons involving phonons [10] and magnons [4,8]. Hagelstein incorporates the optical phonons in his theory. We have shown here that acoustic phonons have an indelible role.

The PHUSON is the quantum of that energy transfer, in a process which is consistent with conventional physics, and where the energy then appears as "excess heat" [1,11]. The PHUSON theory explains why there is a relative absence of strong neutron and gamma ray emissions in CF (LANR). The gamma emission branch from the excited state of ^{4}He* is actually spin-forbidden for both hot and cold fusion [16]. However, at higher hot fusion temperatures the restriction is lifted slightly. This is consistent to what is seen for both hot and cold fusion. Thus, the PHUSON theory correctly describes the relative absence of neutron emissions in CF (LANR). The only nuclear branches available are those whose band gaps are surmountable by the available activation energy (limited by the ambient temperature and incident radiation).

The neutron emission branch is more than 1 MeV above the first excited state (^{4}He*). Hot fusion has large activation energies available (it is 'hot'). LANR/CF is not. In LANR, given the actual much smaller amount of thermal energy, $k_B \times T$, available for cold fusion ($\sim 1/25$ eV), absence of adequate activation energy decisively means that that branch is NOT available, as it is for hot fusion. Neutrons are not observed, ^{4}He production is in its stead. The normally important neutron branch is unavailable at "cold" temperatures. Thus, the PHUSON theory incorporates the observed products, and the energy levels, which explains the branching ratios based on, and explained by, thermal issues. It also explains the origin of the excess heat in active cold fusion systems.

7.10. CAM theory corroborated

The rise in Stokes temperature to circa 1645 K supports that catastrophic solubility effects do occur in PdD driven by local temperatures, and is consistent with, and supports, the Catastrophic Active Medium (CAM) theory [30]. The CAM model of CF considers the deuteron solubility in, and the solubility–temperature relationship of, palladium. The CAM hypothesis treats the metal as an active medium capable of rapid desorption of deuterons with recruitment potential of even more deuterons. The CAM theory describes a quasiparticle related to the sudden catastrophic desaturation of highly loaded Pd involving phonons and moving deuterons into vacancies. The model includes two possible positive feedback loops to account for both the bursts and a plethora of termination sequelae, which declare themselves in several material changes. The results of this model was confirmed by Martin Fleischman just after ICCF-4.

7.11. Implications for development and improvement of LANR systems

The present diagnostic generates spectra in real time which are able to illuminate, visualize, and help identify at least three states for a CF/LANR material or component which is potentially active. The system can determine which state the material or component is in, in real time, even as it is electrically driven, and may be able to determine time constants for changes between levels. Most importantly, it can saliently detect the desired reactions just as products begin to appear and accumulate (e.g. heat). Therefore, it has great use because it reveals both the desired, and undesired, reactions and states and may enable better control, and possible detection of other states of operation – and therefore reactions and products.

7.12. Implications for education

The system enables education of CF/LANR systems. Previous CF/LANR systems have not fully convinced educators and scientists of the importance of hydrogen loaded systems. However, this new diagnostic has additional use as an scientific and educational tool for visualizating different states. The advantage may be the immediate telegraphing of the state, rather than having impatient skeptics await the appearance of excess heat.

7.13. Implications for CF/LANR systems

The use of CMORE-spectroscopy has implications for examining substates in material science and metallurgy, cold fusion physics, and in the electrical engineering of CF/LANR systems. This novel electric-driven coherent high intensity volume-enhanced spectroscopy involves the backscatter of two+ wavelengths from a hydrogen loaded nanomaterial. It is capable of semiquantitative calorimetry (discussed elsewhere [1–3]) and is now demonstrated capable of spectroscopically opening new types of controllable-in-real-time materials science, metallurgy, material engineering, electrical engineering, and electrophysics. Other spectroscopies only identify materials, while the present diagnostic reveals the electrical state of the component while continuing the means to electrically drive, control, and monitor that component and state as desired.

PHUSOR®-technology, and the technology described here are protected by U.S. Patents D596724, D413659 and several other patents pending.

References

[1] M.R. Swartz, G. Verner, J. Tolleson and P.L. Hagelstein, Dry, preloaded NANOR®-type CF/LANR components, *Current Science* **108**(4) (2015) 595.

[2] M.R. Swartz and P.I. Hagelstein, Demonstration of energy gain from a preloaded ZrO_2–PdD nanostructured CF/LANR quantum electronic device at MIT, *J. Condensed Matter Nucl. Sci.* **13** (2014) 516. www.iscmns.org/CMNS/JCMNS-Vol13.pdf.

[3] M.R. Swartz, G. Verner, J. Tolleson and P.L. Hagelstein, Energy gain from preloaded ZrO_2–PdNi–D Nanostructured CF/LANR quantum electronic components, *J. Condensed Matter Nucl. Sci.* **13** (2014) 528. www.iscmns.org/CMNS/JCMNS-Vol13.pdf.

[4] M.R. Swartz, G. Verner, J. Tolleson, L. Wright, R. Goldbaum, P.L. Hagelstein, Amplification and restoration of energy gain using fractionated magnetic fields on ZrO_2–PdD nanostructured components, *J. Condensed Matter Nucl. Sci.* **15** (2015) 66. www.iscmns.org/CMNS/JCMNS-Vol15.pdf.

[5] M.R. Swartz, Incremental high energy emission from a ZrO_2–PdD nanostructured quantum electronic component CF/LANR, *J. Condensed Matter Nucl. Sci.* **15** (2015) 92. www.iscmns.org/CMNS/JCMNS-Vol15.pdf.

[6] M.R. Swartz, G. Verner et al., Imaging of an active NANOR®-type LANR component using CR-39, *J. Condensed Matter Nucl. Sci.* **15** (2015) 81. www.iscmns.org/CMNS/JCMNS-Vol15.pdf.

[7] M.R. Swartz, P.I. Hagelstein and G. Verner, Impact of electrical avalanche through a ZrO_2–NiD nanostructured CF/LANR component on its incremental excess power gain, *ICCF-19*, Padua, Italy, April 16, 2015.

[8] M.R. Swartz, Oscillating excess power gain and magnetic domains in NANOR®-type CF/LANR component, in preparation.

[9] D. Cravens, D. Letts and P.I. Hagelstein, Progress on two-laser experiments, *Proc. ICCF15*, 2009. http://lenr-canr.org/acrobat/Hagelsteinprogresson.pdf.

[10] P.L. Hagelstein, Current status of the theory and modeling effort on fractionation, *J. Condensed Matter Nucl. Sci.* **19** (2016)1–9.

[11] M.R. Swartz, Survey of the observed excess energy and emissions in lattice assisted nuclear reactions, *J. Scientific Exploration* **23**(4) (2009) 419–436.

[12] M.R. Swartz, Excess power gain using high impedance and codepositional LANR devices monitored by calorimetry, heat flow, and paired stirling engines, *Proc. ICCF14* **1** (2008) 123. ISBN: 978-0-578-06694-3, 123, (2010); www.iscmns.org/iccf14/ProcICCF14a.pdf.

[13] M.R. Swartz and G. Verner, Excess heat from low electrical conductivity heavy water spiral-wound $Pd/D_2O/Pt$ and Pd/D_2O–$PdCl_2/Pt$ devices, *Condensed Matter Nuclear Science, Proc.ICCF-10*, World Scientific, New Jersey, ISBN 981-256-564-6, 29-44; 45-54 (2006).

[14] M.R. Swartz, Consistency of the biphasic nature of excess enthalpy in solid state anomalous phenomena with the quasi-1-dimensional model of isotope loading into a material, *Fusion Technol.* **31** (1997) 63–74.

[15] M. Miles, R.A. Hollins, B.F. Bush, J.J. Logowski and R.E. Miles, Correlation of excess power and helium production during D_2O and H_2O electrolysis using palladium cathodes, *J. Electroanal. Chem.* **346** (1993) 99–117.

[16] M.R. Swartz, Phusons in nuclear reactions in solids, *Fusion Technol.* **31** (1997) 228–236.

[17] Y. Arata and Y.C. Zhang, Observation of anomalous heat release and helium-4 production from highly deuterated palladium fine particles, *Jpn. J. Appl. Phys.* **38** (Part 2, No. 7A) (1999) L774–L776.

[18] M.R. Swartz, Deuterium production and light water excess enthalpy experiments using nickel cathodes, *J. New Energy* **1**(3) (1996) 219. www.iscmns.org/FIC/J/JNE1N3.pdf.

[19] M.R. Swartz, G. Verner and A. Weinberg, Non-thermal near-IR emission from high impedance and codeposition LANR devices, *Proc. ICCF14* **1** (2008) 343, D.J. Nagel and M.E. Melich (Eds.), ISBN: 978-0-578-06694-3, 343, (2010). www.iscmns.org/iccf14/ProcICCF14a.pdf.

[20] D. Cravens, Factors affecting success rate of heat generation in CF cells, *Proc. ICCF-4,* Maui, Hawaii, 1993.

[21] S. Szpak, P.A. Mosier-Boss, F.E. Gordon, Further evidence of nuclear reactions in the Pd/D lattice: emission of charged particles, *Naturwissenschaften* **94** (2007) 511–514.

[22] M.R. Swartz, Impact of an applied magnetic field on the electrical impedance of a LANR device, Vol. 4, *JCMNS Proc.*, March 2010, New Energy Technology Symposium held at the 239th American Chemical Society in San Francisco, 2011.

[23] J. O'M. Bockris, R. Sundaresan, D. Letts and Z.S. Minevski, Triggering and structural changes in cold fusion electrodes, *Proc. ICCF4*, Maui, Hawaii, 1993.

[24] A.R. von Hippel, *Molecular Science and Molecular Engineering*, MIT Press, Cambridge, 1959.

[25] B.Ya. Gorodilov, Phonon scattering in ortho-para hydrogen solid solutions (role of configurational relaxation), DOI: 10.1063/1.1542498.

[26] G. Verner, Personal communication.

[27] Anonymous referee, Personal communication.

[28] C. Kittel, *Introduction to Solid State Physics*, Wiley, New York, 1976.

[29] N.W. Ashcroft and N.D. Mermin, *Solid State Physics*, Holt, Rinehart and Winston, New York, 1976.

[30] M.R. Swartz, Catastrophic active medium (CAM) theory of cold fusion, *Proc. ICCF4,* Vol. 4, Maui, Hawaii, 1993, p. 255; sponsored by EPRI and the Office of Naval Research. www.lenr-canr.org/acrobat/EPRIproceedingc.pdf.

[31] D. Letts, A method to calculated excess power, *Infinite Energy* **112** (2013) 63.
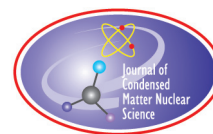
Models for the Phase Diagram of Palladium Hydride Including O-site and T-site Occupation

Peter L. Hagelstein*

Massachusetts Institute of Technology, Cambridge, MA, USA

Abstract

Early statistical mechanics models for palladium hydride allowed for a good description of the phase diagram based on a simple parameterization of the O-site energy. In this work we study generalizations of these models to include higher-order dependence on loading, temperature-dependent O-site energies, and also to include T-site occupation. Experimental data sets for 10 isotherms were assembled, and augmented with additional extrapolated points for the low-pressure α-phase region as well as the high pressure β-phase region. Loading-dependent O-site energies are optimized by minimizing the mean square error in the chemical potential between the model and data set. The resulting models give a good match to the phase diagram. If the O-site energy is allowed to be temperature dependent then the fit is better, but the resulting optimum is a mathematical optimum not so closely connected with the physical system. Models were studied in which O-site and T-site occupation occurs. When optimized these models are able to provide a good match to the phase diagram. When the O-site to T-site excitation energy is fixed according to estimates developed in earlier studies, the resulting temperature-dependent O-site energies are physically plausible. When the excitation energy are optimized together with the O-site energy, the resulting optimum is a mathematical one much less connected to the physical system. An earlier analysis of solubility in the α-phase led to a strong argument that T-site occupation occurs in palladium hydride and in palladium deuteriude; the present study supports this conclusion based on an independent data set.

© 2016 ISCMNS. All rights reserved. ISSN 2227-3123

Keywords: Mean field model, Palladium hydride, Phase diagram, Statistical mechanics, T-site occupation

1. Introduction

Palladium hydride [1–5] is perhaps the most studied of the metal hydrides [6–14], in both experiment and theory. Our interest in the problem is motivated by issues associated with the development of models for excess heat in the Fleischmann-Pons experiment [15–17]. In a realistic simulation models are needed for the loading and electrochemical reactions; for hydrogen and deuterium occupation of bulk sites; for vacancy creation and the occupation of vacancy sites. Fundamental to all of these problems are basic statistical mechanics models for hydrogen and deuterium in palladium, which is the focus of the study described in this work. Similar issues arise in the case of modeling nickel systems, which we hope to address in subsequent research.

---

*E-mail: plh@mit.edu

The first basic statistical mechanics models of this type were described long ago in papers now considered to be classics; by Fowler and Smithells [18]; and by Lacher [19]. Since the chemical potential of hydrogen in gas was known theoretically, it was possible to construct relevant models for hydrogen in palladium since the chemical potentials are equal in equilibrium (the formulations used in the early papers seem more complicated, but are equivalent to matching the solid and gas phase chemical potentials). From a comparison of the model isotherms with data, it was possible to estimate the O-site energy of interstitial hydrogen in Pd, resulting in a statistical mechanics model for part of the phase diagram. In what follows we study generalizations of these models to include higher-order polynomial dependence on loading, temperature-dependent O-site energies, and T-site occupation, to develop models that can describe more of the phase diagram.

To proceed, a set of isotherms are first assembled, and then a set of Lacher models with polynomial dependence of the O-site energy on the loading are optimized. This classic model is found to provide a good match to the data set at elevated temperature, but noticeable deviations occur near room temperature.

In the literature one can find more sophisticated models for interstitial hydrogen in metals termed "lattice gas" models [20–26]. In this case a model Hamiltonian is used with the O-site energy and interactions between the hydrogen atoms specified; statistical mechanics allows for the calculation of the phase diagram or other observables. Model parameters are selected which give the best fit with experiment. The interaction between interstitial hydrogen atoms in the lattice gas model gives rise to a splitting of the energies of the different configurations which cannot be described in terms of a simple loading-dependent O-site energy (independent of temperature). The average O-site energy in this case increases with temperature as more energetic configurations contribute in a statistical mechanics calculation.

Lattice gas models are both interesting and desirable; however, the development and optimization of such models involves significant computation, and research is ongoing to develop models which are better able to match experiment. The focus here is focused on simpler mean field models (alternatively. empirical models) that can be used for applications; our interest in this study is not to determine a better lattice gas Hamiltonian. Nevertheless, we know from these studies, and also from density functional calculations, a substantial splitting of the configuration energies occurs [27,28], and this impacts the empirical models under discussion. In what follows models are considered in which the O-site energy is allowed to depend on temperature, to account approximately for this configurational splitting. The mean-field models when optimized are able to provide better matches to the data set than more basic Lacher models. Unfortunately, the optimized solutions have O-site energies which do not increase with temperature for all loading, and hence are not consistent with a physical model for configurational splitting.

Interstitial hydrogen is known to occupy octahedral sites [29,30], which is consistent with the models discussed so far. In high pressure experiments it is thought that the H/Pd loading has exceeded unity [31,32], conditions under which the occupation of additional sites beyond the O-sites is required. Similar claims have been made for the deuterium loading in electrochemical Fleischmann–Pons experiments [33]. At present the development of over-unity loading of H or D in bulk Pd in any experiment is not universally accepted. There is also not general agreement as to where excess interstitial H or D might go once the O-sites are fully occupied. We have recently studied new models in which both O-site and T-site occupation occurs [34,35], and compared them with experiment in different regimes. Models that include T-site occupation can account for the observed experimental solubility data in the α-phase over a wide range of temperatures [34], conditions where models with only O-site occupation have trouble. Estimates for the O-site to T-site excitation energy for α-phase PdH$_x$ and PdD$_x$ near 100 meV resulted from this study. The new models were used to compare with experiment in the β-phase [35] and higher, which resulted in a parameterization of the loading-dependent O-site to T-site excitation energy near room temperature.

As indicated above the primary motivation for this work is to develop simple mean-field models that can be used for applications. However, another motivation was to see whether models developed for O-site to T-site occupation were compatible with the isotherms of the phase diagram. A related issue is whether T-site occupation is necessary to understand the phase diagram. We know from previous work that T-site occupation is required to model loading

in the α-phase; however, whether T-site occupation is needed for the rest of the phase diagram has not previously been addressed. In the end, our results suggest that it may not be possible to develop an accurate model that is also acceptable on physical grounds without T-site occupation.

2. Isotherms and Phase Diagram

The first task is to assemble isotherms for a reference phase diagram. Since palladium hydride is perhaps the best studied of the metal hydrides, there are many data sets with which to work. We made use of a subset of isotherms presented by Manchester et al. [4], which recommended itself since a sizeable collection of individual pressure-composition-temperature (PCT) data points were plotted. The online web digitization program of Ankit Rohagti allowed for the conversion of the published data points into digital form.

It was found necessary to extend the isotherms to lower loading in the α-phase, and also to higher loading in the β-phase. Reliable isotherms for the α-phase could be constructed based on an empirical fit to literature data as described in the following subsection. For high concentration a (less reliable) generalization of an empirical fit due to Baranowski et al. [31] was used. This allowed for a "complete" set of isotherms at ten different temperatures between $20°C$ and $433°C$ which could be used for fitting statistical mechanics model parameters.

Extrapolated α-phase data points at low pressure are needed to provide an "anchor" for the model at low loading. There is a differential relation between the O-site and T-site energies, and the chemical potential; consequently, a boundary condition is required in order to determine a unique solution for the chemical potential as a function of loading. The extrapolated low pressure points serve to fix the boundary condition in the optimizations. Good agreement using this approach is found with the results obtained previously based on a different data set (the data set of Clewley et al. [36]).

The biggest issue with the extrapolated points at high loading is that far fewer experimental studies have been published, so that the development of an accurate extrapolation is problematic. Another concern is that if T-site occupation is significant, then there is reason to be concerned whether the extrapolation used includes it (and there is no reason to believe it does). Consequently, it would not be expected that a reliable O-site to T-site excitation energy can be determined at high loading from the isotherms, since the impact of T-site occupation is greatest at high temperature where there is no data at high loading.

2.1. Empirical fit for the α-phase

Empirical fits for the α-phase have been studied previously [18,37–43]; for example Simons and Flanagan [39] give the empirical formula (in our notation)

$$\ln P(\text{atm}) = 13.04 - \frac{2327}{T} - \frac{11110}{T}\theta + 2\ln\frac{\theta}{1-\theta}. \tag{1}$$

It was found that this formula is useful over a restricted temperature range. A new empirical formula was developed based on

$$\ln P(\text{atm}) = \left(\frac{a_{-1}}{T} + a_0 + a_1 T\right) + \left(\frac{b_{-1}}{T} + b_0 + b_1 T\right)\theta + 2\ln\frac{\theta}{1-\theta}. \tag{2}$$

The fitting parameters were optimized to give

$$a_{-1} = -2478.35\,\text{K}, \quad a_0 = 14.1429, \quad a_1 = -0.00204315\,\text{K}^{-1},$$
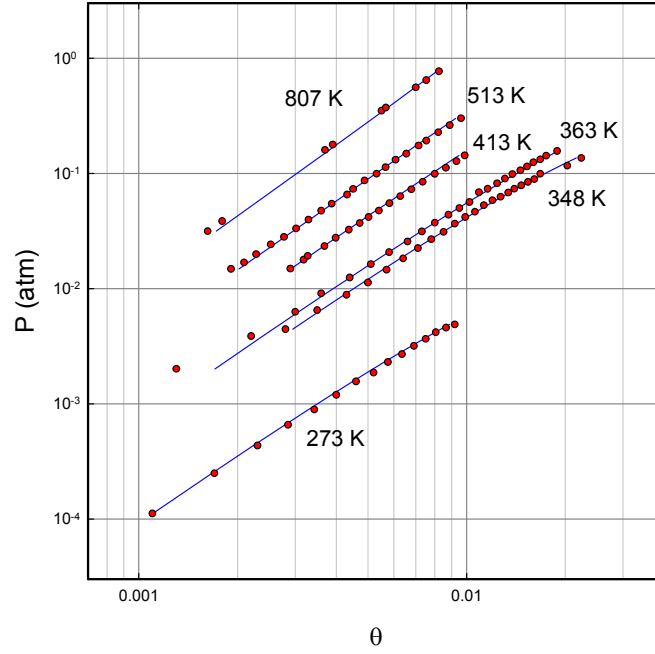
Figure 1. Solubility data in the α-phase region of PdH$_x$ (*red triangles*); empirical fit (*blue lines*).

$$b_{-1} = -24147.1\,\text{K}, \quad b_0 = 57.5628, \quad b_1 = -0.0534775\,\text{K}^{-1}. \tag{3}$$

The resulting empirical fit is compared with data used for parameter optimization in Fig. 1. For the data sets at 273, 348 and 363 K we used the tabulated data of Simons and Flanagan [39]; the isotherms at 413 and at 513 K are from Oates et al. [44]; and the solubility data at 807 K is from Kleppa and Phutella [42].

2.2. Empirical fit at high loading

At high loading there are empirical formulas in the literature, such as the empirical fit of Baranowski et al. [31] given by

$$\ln f_{\text{H}_2} = \frac{-(100.4 - 90.1\theta)(\text{kJ/mol})}{RT} + \frac{106.4\text{J/(mol K)}}{R} + 2\ln\frac{\theta}{1-\theta}. \tag{4}$$

Motivated by this, we decided to construct an empirical fit of the form

$$\ln f_{\text{H}_2} = \frac{(a_0 + b_0\theta)}{T} + \left(a_1 + b_1\theta\right) + T\left(a_2 + b_2\theta\right) + 2\ln\frac{\theta}{1-\theta} + 2\frac{PV_{\text{H}}}{k_{\text{B}}T}. \tag{5}$$

This fit includes the next order in temperature, and adds a $P\,dV$ term. The fitting parameters are:
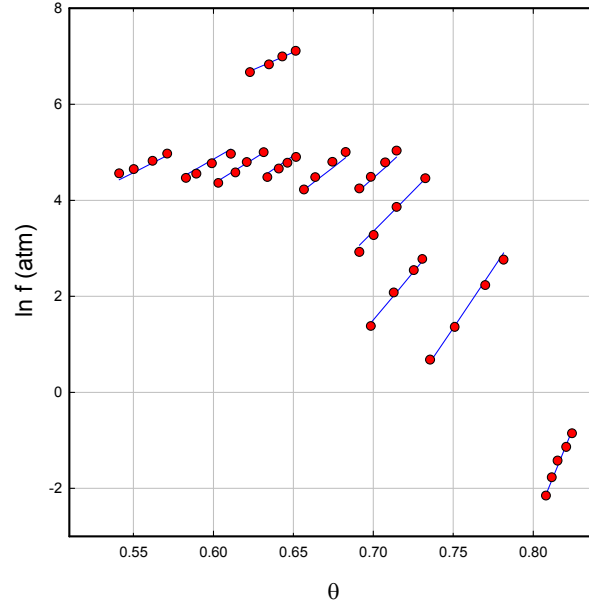
Figure 2.   Data points and fit for the empirical model at high pressure.

$$a_0 = -18215.5\,\mathrm{K}, \quad b_0 = 17469.8\,\mathrm{K}, \quad a_1 = 35.3611, \quad b_1 = -22.1764,$$

$$a_2 = -0.0102061\,\mathrm{K}^{-1}, \quad b_2 = 0.0038497\,\mathrm{K}^{-1} \tag{6}$$

with fugacity in atmospheres. This empirical fit is compared against the high loading data points from our data set in Fig. 2.

2.3. Isotherms

The resulting isotherms are shown in Fig. 3. We selected data sets from Manchester et al. [4] for 20, 70, 120, 160, 200, 243, 270, 300, 340, and 433°C; and we extended the data set to both lower and higher H/Pd loadings using the extrapolations described in this section.

3. Model with Loading-dependent O-site Energy

The first realistic model for the phase diagram of PdH was put forth in Lacher's classic paper [19], which assumed that the O-site energy is quadratic in the loading and independent of temperature. Models of this kind have been used to predict phase diagrams previously [19,45,46]. In this section O-site energy models that are polynomial in loading are optimized against the reference isotherm data set to determine fitting parameters.
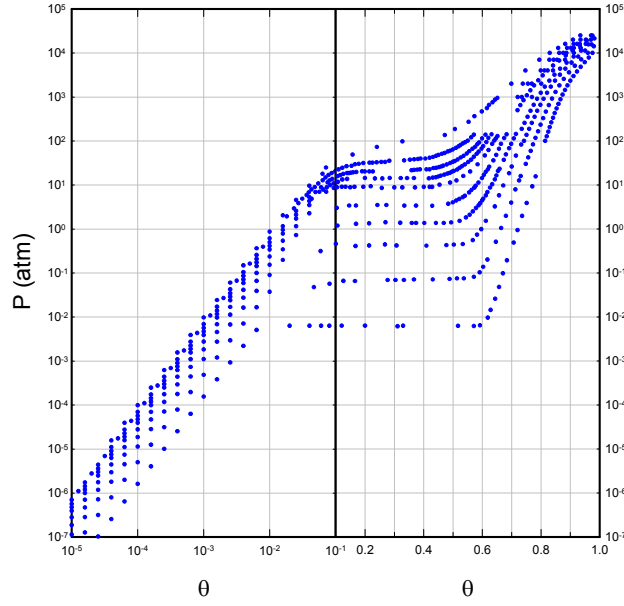
Figure 3. Data points used in this study for the isotherms of the phase diagram.

3.1. Model

A model for O-site occupation can be derived by assuming that hydrogen is in equilibrium in the gas phase and solid phase, so that the chemical potential in the two phases match

$$\mu_H^s = \mu_H^g = \frac{1}{2}\mu_{H_2}^g. \tag{7}$$

The chemical potential in the gas phase is accurately known. For the solid phase and only O-site occupation we may write [34]

$$\mu_H = E_O + \theta\frac{\partial E_O}{\partial \theta} - k_B T \ln\frac{1-\theta}{\theta} - k_B T \ln z_O + PV_H, \tag{8}$$

where E_O is the O-site energy which depends on the loading θ, and may also depend on temperature in some of the models under consideration.

3.2. O-site partition function

For the modeling in this work a non-SHO O-site partition function is used as discussed in [34]. For O-site occupation the partition function is taken to be

$$z_O = 4 \left(\sum_n \exp\left\{ -\frac{E_n}{k_B T} \right\} \right)^3 \tag{9}$$

with

$$E_n = \hbar \omega_O n^s. \tag{10}$$

The excitation energy and scaling parameter for O-site occupation are

$$\hbar \omega_O = 69.0 \text{ meV}, \quad s_O = 1.2. \tag{11}$$

3.3. Optimization

For the optimization in this work, a measure of the error I is defined according to

$$I = \frac{1}{N} \sum_j \left[\mu_H(\text{data}) - \mu_H(\text{model}) \right]_j^2, \tag{12}$$

where the summation is over all of the data points of the isotherms in the phase diagram. The hydrogen in gas chemical potential [34,35] is determined at the loading of a given data point, and then compared with the chemical potential for the hydrogen in solid determined from the model under consideration. The model parameters are optimized from a minimization of the resulting mean square error I.

3.4. O-site energy results

We optimized models with polynomial O-site energy of the form

$$E_O(\theta) = a_0 + a_1\theta + a_2\theta^2 + a_3\theta^3 + a_4\theta^4 + a_5\theta^5 + a_6\theta^6 \tag{13}$$

for polynomial O-site energy models models with third- to sixth-order dependence on the loading θ. The errors associated with the different optimizations are given in Table 1. One sees that the errors are smaller for higher-order models.

Table 1. Error associated with the optimization of the different models assuming θ-dependent O-site energies considered in this section.

Order	I
3	4.22×10^{-4}
4	1.63×10^{-4}
5	1.37×10^{-4}
6	1.34×10^{-4}
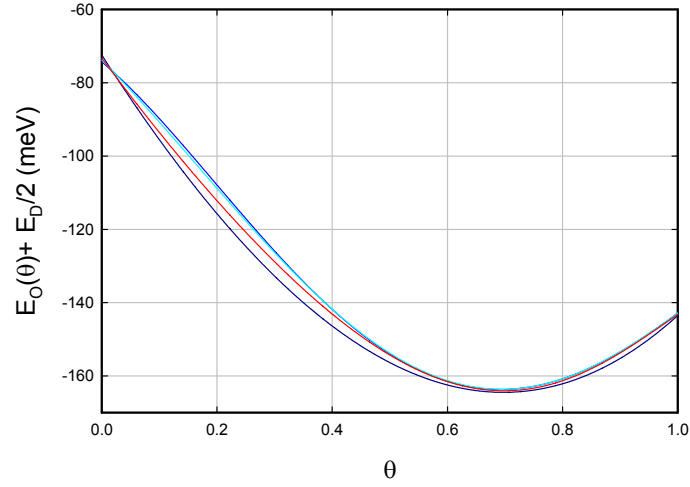
Figure 4. O-site energy as a function of θ with only O-site occupation; third-order polynomial (*dark blue line*); fourth-order polynomial (*blue line*); fifth-order polynomial (*cyan line*); and sixth-order polynomial (*red line*).

Results for the O-site energy are shown in Fig. 4. There are minor differences in the different models, with a general convergence toward a curve close to the sixth-order polynomial model result. Fitting parameters for the sixth-order optimized O-site energy are given by

$$a_0 = -73.244, \quad a_1 = -211.382, \quad a_2 = 67.137, \quad a_3 = 93.793$$

$$a_4 = -212.541, \quad a_5 = 404.335, \quad a_6 = -211.373 \tag{14}$$

with individual a_j coefficients in meV.

3.5. Comparison of predicted phase diagram with experiment

The phase diagram for the sixt-order polynomial fit for E_O is shown in Fig. 5. In general this model does pretty well; however, the predicted isotherms lie noticeably above the experimental data points at the lower temperatures.

4. O-site Energy Dependent on Loading and Temperature

In a more sophisticated lattice gas treatment the different configurations (corresponding to different arrangements of hydrogen atoms in different lattice sites) have different energies. Consequently, the use of a loading-dependent O-site energy itself constitutes a significant approximation (in the literature this is referred to as a mean-field approximation). Here we make use of a mean field approximation where the (mean) O-site energy is allowed to depend both on loading and on temperature. As before the fitting parameters of the O-site energy are determined by optimization against the reference phase diagram.
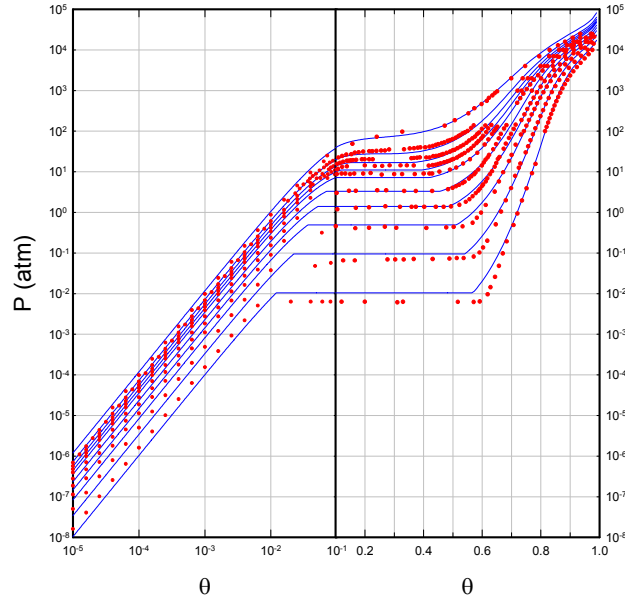
Figure 5. Isotherms and data points for the temperature-independent sixth-order polynomial fit of E_O.

Some intuition about how this model might work seems useful here. If there is a substantial splitting in the different configuration energies, we would expect this to be captured in the empirical model with model O-site energies lower at low temperature, and model O-site energies higher at high temperature. This will provide a check on the results, to make sure that the intended physics is captured in the optimization results.

4.1. Model and optimization

We have optimized models with a polynomial dependence on loading as before, but now the model is expanded to assume in addition a linear dependence on the temperature according to

$$
E_O(\theta, T) = \left[a_0 + a_1\theta + a_2\theta^2 + a_3\theta^3 + a_4\theta^4 + a_5\theta^5 + a_6\theta^6 \right] \\
+ T\left[b_0 + b_1\theta + b_2\theta^2 + b_3\theta^3 + b_4\theta^4 + b_5\theta^5 + b_6\theta^6 \right]. \tag{15}
$$

We have optimized the model parameters by minimizing the associated error I as described in the previous section. The additional degrees of freedom have allowed for the error I to be significantly reduced, as can be seen by comparing the results of Table 1 with those of Table 2.

a,b order	I
3,3	1.67×10^{-4}
4,4	4.40×10^{-5}
5,5	2.06×10^{-5}
6,6	2.01×10^{-5}

4.2. O-site energies

The optimized O-site energies that result for the model with sixth-order polynomial dependence on the loading is shown in Fig. 6. The associated expansion coefficients are

$$a_0 = -57.269, \quad a_1 = -269.674, \quad a_2 = 42.263, \quad a_3 = -10.436,$$

$$a_4 = 376.561, \quad a_5 = -222.779, \quad a_6 = -7.575,$$

$$b_0 = -0.0282103, \quad b_1 = 0.1068191, \quad b_2 = 0.3125901, \quad b_3 = -1.0341667,$$

$$b_4 = 1.0675563, \quad b_5 = -0.4938008, \quad b_6 = 0.0728168. \tag{16}$$

The a_j coefficients are in meV, and the b_j coefficients are in meV/K.

We see a modest spread in the O-site energies, with the O-site energy increasing with temperature at high loading (as would be expected for a physical system). At low loading, the O-site energy appears to decrease with temperature,

Figure 6. O-site energies as a function of loading for the different temperatures of the isotherms (*blue lines*); extrapolation to $T = 0$ (*black line*).
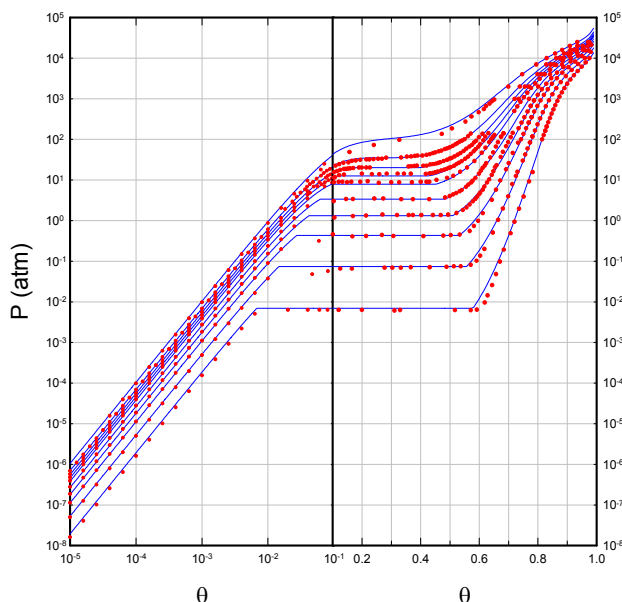
Figure 7. Isotherms and data points for the temperature-dependent sixth-order polynomial fit of E_O.

an effect not consistent with our picture above involving a spread in O-site energies. Consequently, we recognize that this optimized model corresponds to a mathematical optimum, but one that is not particularly closely connected to a physical picture at low loading.

4.3. Model phase diagram

Given the reduced error associated with the optimization of the models, the fit to the isotherms is expected to be improved. This can be seen in the associated phase diagram for the lowest error sixth-order polynomial model in Fig. 7. The agreement is now better for the lower temperature isotherms.

5. Inclusion of T-site Occupation with a Model Excitation Energy

As discussed briefly in the Introduction the issue of T-site occupation in palladium hydride is controversial; based on the results of modern density functional calculations T-site occupation should be expected, but there is not at present an unambiguous experimental demonstration of T-site occupation. In previous work we made estimates for the O-site to T-site excitation in the α-phase [34] and in the β-phase [35]. In this section we make use of these earlier estimates for the excitation energy to construct a statistical mechanics model that can be fit to experimental data. The O-site to T-site excitation energy in this case is assumed to depend on loading, but not on temperature.

5.1. Model for O-site and T-site occupation

A model for the chemical potential in terms of the O-site and T-site loading θ_O and θ_T, in terms of the O-site and T-site energies E_O and E_T, was developed previously [35]. The chemical potential for interstitial hydrogen in O-sites and in T-sites is given by

$$\mu_H = E_O + \theta_O \frac{\partial E_O}{\partial \theta} + \theta_T \frac{\partial E_T}{\partial \theta} - k_B T \ln \frac{1 - \theta_O}{\theta_O} - k_B T \ln z_O, \tag{17}$$

$$\mu_H = E_T + \theta_T \frac{\partial E_T}{\partial \theta} + \theta_O \frac{\partial E_O}{\partial \theta} - k_B T \ln \frac{2 - \theta_T}{\theta_T} - k_B T \ln z_T. \tag{18}$$

Subtracting these two relations leads to

$$E_T - E_O = k_B T \left\{ \ln \left(\frac{2 - \theta_T}{\theta_T} \frac{\theta_O}{1 - \theta_O} \right) + \ln \frac{z_T}{z_O} \right\}. \tag{19}$$

This we solve to determine θ_T given θ_O, and then make use of Eq. (17) for the chemical potential of H in the solid phase.

5.2. T-site partition function

In this analysis we have made use of a non-SHO T-site partition function of the form

$$z_T = 4 \left(\sum_n \exp \left\{ -\frac{E_n}{k_B T} \right\} \right)^3 \tag{20}$$

with

$$E_n = \hbar \omega_T n^s. \tag{21}$$

The excitation energy and scaling parameter for O-site occupation are

$$\hbar \omega_T = 53.8 \text{ meV}, \quad s_T = 1.2. \tag{22}$$

5.3. O-site to T-site excitation energy

For T-site occupation we make use of a model for the O-site to T-site energy parameterized by

$$\Delta E(\theta) = \frac{\alpha_0 + \alpha_1 \theta}{1 + \beta_1 \theta} + 1 \text{ meV} \tag{23}$$

with fitting parameters

$$\alpha_0 = 100.676 \text{ meV}, \quad \alpha_1 = 824.259 \text{ meV K}^{-1}, \quad \beta_1 = 3.1108 \text{ K}^{-1}. \tag{24}$$
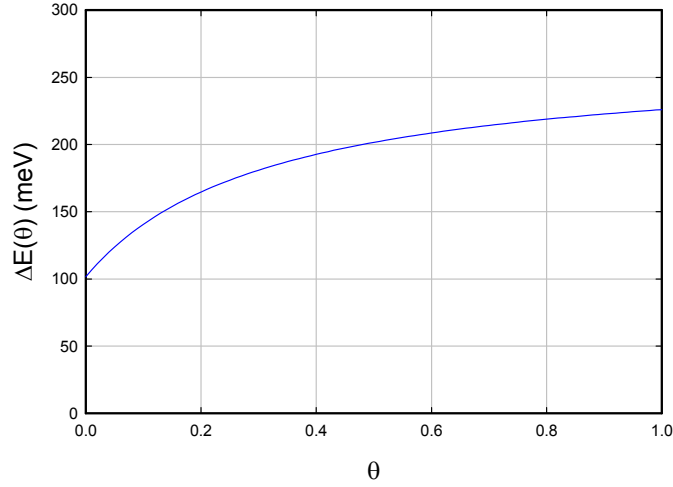
Figure 8. Empirical model for the O-site to T-site excitation energy as a function of loading θ.

This empirical model is shown in Fig. 8. Estimates for the excitation energy in the α-phase near $\theta = 0$ and in the β-phase near $\theta = 1$ were developed previously from the analyses reported in [34,35]. For the intermediate loading regime the neutron diffraction measurements of Pitt and Gray [47] can be interpreted in terms of an excitation energy for palladium deuteride. Based on our earlier analysis we would expect that the O-site excitation energy is probably similar for palladium hydride near room temperature and above.

5.4. Models based on a temperature-independent O-site energies

We have optimized a set of models with O-site and T-site occupation assuming a temperature-independent O-site energy model. The errors are given in Table 3.

The fitting coefficients (in meV) for the sixth-order polynomial solutions are

$$a_0 = -62.763, \quad a_1 = -249.626, \quad a_2 = 173.686, \quad a_3 = -91.330,$$

$$a_4 = 32.832, \quad a_6 = -110.942. \tag{25}$$

Table 3. Errors associated with the optimization of models with O-site and T-site occupation considered in this subsection.

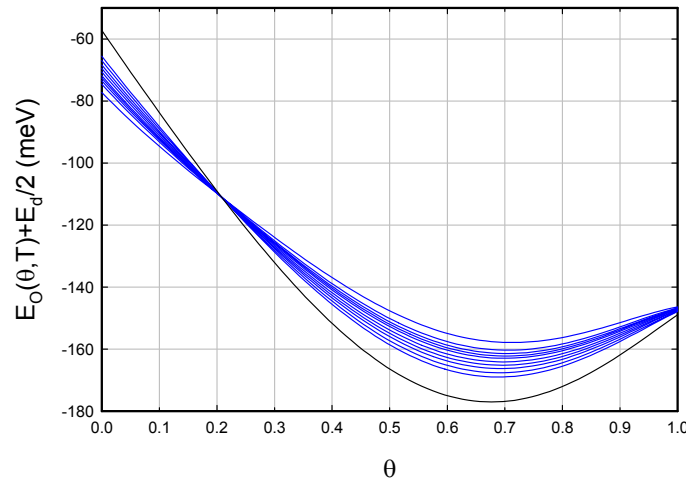| Order	I
3 | ΔE model	4.22×10^{-4}
4 | ΔE model	4.19×10^{-4}
5 | ΔE model	4.09×10^{-4}
6 | ΔE model	4.05×10^{-4}
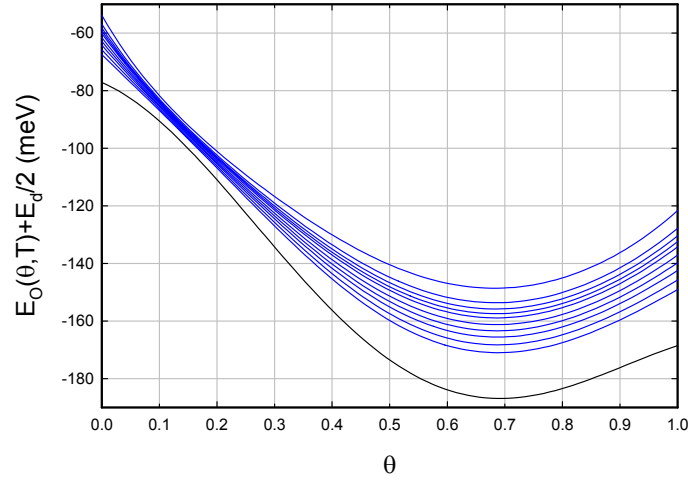
Figure 9.   O-site energies as a function of loading for the different temperatures of the isotherms (*blue lines*); extrapolation to $T = 0$ (*black line*).

In this case lower errors would have been obtained with no T-site occupation, as we can see by comparing with Table 1. According to this there is no benefit (in terms of error reduction) to augmenting a model based on O-site occupation with a temperature-independent $E_O(\theta)$ so that it includes T-site occupation based on the $\Delta E(\theta)$ model given above.

5.5. Temperature-dependent O-site energy

Next we consider models based on an O-site energy that depends on both loading and on temperature, combined with a T-site model based on the O-site to T-site excitation energy given above. The intention here is to account for the configurational splitting discussed above, and by doing so reduce the associated optimization error. Results for the errors are given in Table 4.

   Results for the different O-site energies for the sixth-order version of the model are shown in Fig. 9. In contrast to the previous unphysical results for the temperature-dependent O-site energies in the last section (Fig. 6), these O-site energies are increasing with increasing temperature. Also, the increase in the O-site energy at $\theta = 0$ is now comparable to what was found in our earlier analysis of the α-phase solubility in Ref. [34].

   The fitting coefficients for the 6th-order polynomial model are

Table 4.   Errors associated with the optimization of the different models with O-site and T-site occupation considered in this section.

a,b Order	I
3,3 | ΔE model	8.07×10^{-5}
4,4 | ΔE model	2.99×10^{-5}
5,5 | ΔE model	2.65×10^{-5}
6,6 | ΔE model	1.93×10^{-5}
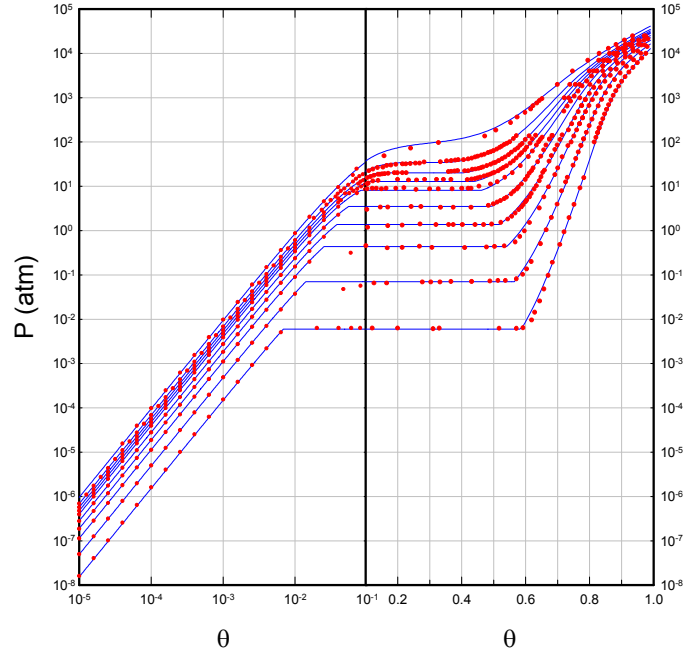
Figure 10. Isotherms and data points for the model with temperature-dependent 6th-order polynomial fit of E_{O} and an empirical ΔE model.

$$a_0 = -77.093, \quad a_1 = -92.584, \quad a_2 = -496.658, \quad a_3 = 361.628,$$

$$a_4 = 940.828, \quad a_5 = -1130.451, \quad a_6 = 325.675,$$

$$b_0 = 0.0330887, \quad b_1 = -0.3739481, \quad b_2 = 2.0569084, \quad b_3 = -3.9515725,$$

$$b_4 = 3.7471947, \quad b_5 = -1.9623168, \quad b_6 = 0.5147468, \tag{26}$$

where the a_j coefficients are in meV, and the b_j coefficients are in meV/K.

5.6. Phase diagram

The phase diagram that results is shown in Fig. 10. Although there are minor issues, in general this appears to be a pretty solid match between model and data. We have in this model succeeded in obtaining a good match with the phase diagram with a model that is physically plausible.

6. Unconstrained Models with Both O-site and T-site Occupation

In the previous section we made use of a fixed model for O-site to T-site excitation energy based on earlier analyses with different data sets. In this section we allow for the loading-dependent excitation energy itself to be determined directly as a result of the optimization. The motivation for this is to see whether the phase diagram data set itself can be used to provide an independent estimate for the O-site to T-site excitation energy.

6.1. Models with temperature-dependent O-site energy

We discussed above that there is a spread in the energies of the different configurations for partially loaded palladium hydride, and that a crude way to account for this might be to work with a temperature-dependent O-site energy. The O-site energy in this case is parameterized using fifth-order polynomials in loading according to

$$E_{\mathrm{O}}(\theta, T) = \left[a_0 + a_1\theta + a_2\theta^2 + a_3\theta^3 + a_4\theta^4 + a_5\theta^5 \right] \\ + T\left[b_0 + b_1\theta + b_2\theta^2 + b_3\theta^3 + b_4\theta^4 + b_5\theta^5 \right]. \tag{27}$$

The O-site to T-site excitation energy is similarly parameterized according to

$$\Delta E(\theta) = d_0 + d_1\theta + d_2\theta^2 + d_3\theta^3 + d_4\theta^4 + d_5\theta^5. \tag{28}$$

We have optimized a set of models of this kind, with the results of optimization listed in Table 5. We see that the associated errors are lower than what we found for all other models considered in this work.

Figure 11. O-site to T-site excitation energy as a function of θ, for models with temperature-dependent O-site energy E_{O} and unconstrained temperature-independent O-site to T-site excitation energy; ΔE linear in θ (*dark blue line*); second-order model (*dark green line*); third-order model (*blue line*); fourth-order model (*red line*); fifth-order model (*pink line*).

The fitting coefficients for the lowest error fifth-order polynomial solution are:

$$a_0 = -65.426, \quad a_1 = -5.627, \quad a_2 = -1099.972,$$

$$a_3 = 1503.386, \quad a_4 = -266.445, \quad a_5 = -226.248,$$

$$b_0 = -0.007048, \quad b_1 = -0.364993, \quad b_2 = 2.052026,$$

$$b_3 = -2.207565, \quad b_4 = -0.033973, \quad b_5 = 0.596698,$$

$$d_0 = 178.523, \quad d_1 = 615.281, \quad d_2 = -2641.792,$$

$$d_3 = 3242.712, \quad d_4 = -1066.321, \quad d_5 = -17.063, \tag{29}$$

where the a_j and d_j coefficients are in meV, and the b_j coefficients are in meV/K.

6.2. O-site to T-site excitation energy

These results support the notion that T-site occupation occurs in palladium hydride, since we obtain better agreement with the phase diagram when T-site occupation is included. The optimized O-site to T-site excitation energies (shown in Fig. 11) are between about 100 and 300 meV, which are in the general range of what we estimated in earlier studies [34,35]. We note that the fifth-order polynomial curve with the lowest associated error lies well above the empirical model of Fig. 8 at $\theta = 0$, where we have some confidence in the excitation energy based on our analysis of the α-phase experimental data. It also lies well above the empirical model of Fig. 8 where we have some confidence in the analysis of experimental results at high loading.

6.3. O-site energy

Next consider the spread of O-site energies for the lowest error model, shown in Fig. 12. We recall that in the physical system there is a spread in the energies of the different configuration, which we seek to model with a temperature-dependent O-site energy. At high loading the O-site energies are seen to increase with temperature, consistent with the splitting effect under consideration. However, at low loading the situation is reversed. We recognize this solution as a mathematical optimum, and not as an acceptable physical solution.

Table 5. Errors associated with the unconstrained optimization of different models with O-site and T-site occupation.

$a,b \mid d$ order	I
5,5 | 0	2.17×10^{-5}
5,5 | 1	2.03×10^{-5}
5,5 | 2	1.34×10^{-5}
5,5 | 3	9.28×10^{-6}
5,5 | 4	8.22×10^{-6}
5,5 | 5	8.08×10^{-6}
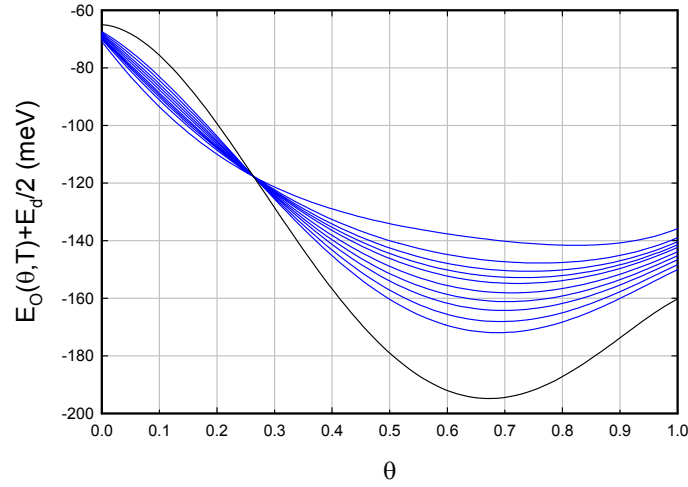
Figure 12. O-site energies as a function of loading for the different temperatures of the isotherms (*blue lines*); extrapolation to $T = 0$ (*black line*). Above an H/Pd loading of 0.26 the curves are ordered with increasing excitation energy corresponding to increasing temperature.

6.4. Phase diagram

The phase diagram for the model with the lowest error is shown in Fig. 13. The fit is very good, as expected.

7. Constrained Models with Both O-site and T-site Occupation

The low errors found in the optimization of the previous section provide motivation to consider a constrained optimization, where the O-site to T-site excitation energy is again determined based on optimization, but now we constrain the excitation energy to values estimated in previous work at $\theta = 0$ and at $\theta = 1$. It is possible that an independent estimate for the excitation energy at intermediate loading can be determined from this kind of optimization.

7.1. Model

In this case we use an excitation energy of the form

$$\Delta E(\theta) = d_0 + d_1\theta + d_2\theta^2 + d_3\theta^3 + d_4\theta^4 + d_5\theta^5$$

with [34]

$$d_0 = 101.676 \,\text{meV}. \tag{30}$$

For the O-site energy, we made use of fifth-order polynomials in θ and assumed a linear temperature dependence as before.

The optimization is carried out on the modified error J given by

Figure 13. Isotherms and data points for the model with temperature-dependent fifth-order polynomial fit of E_O and optimized fifth-order model for $\Delta E(\theta)$.

$$J = \frac{1}{N} \sum_j \left[\mu_H(\text{data}) - \mu_H(\text{model}) \right]_j^2 + \gamma \left(226\,\text{meV} - \sum_{i=0}^{5} d_i \right)^2. \tag{31}$$

We choose low values for γ in the vicinity of unity for the initial optimizations, and then later on increase γ to 100. This leads to values of ΔE at $\theta = 1$ close to 226 meV.

7.2. Results

Constrained optimizations have been carried out on a set of models with the results given in Table 6. The errors I (see Eq. (12)) that result are larger than what we obtained in the unconstrained optimizations of the previous section (see Table 5). There is a minor penalty associated with imposing constraints on the model parameters.

The fitting coefficients for the lowest error model with fifth-order polynomial fits are

$$a_0 = -77.889, \quad a_1 = -6.933, \quad a_2 = -1102.321,$$

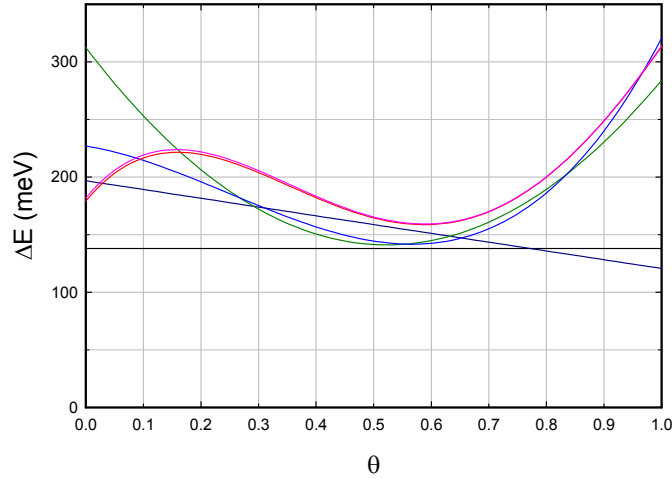$$a_3 = 1616.798, \quad a_4 = -453.666, \quad a_5 = -149.614,$$
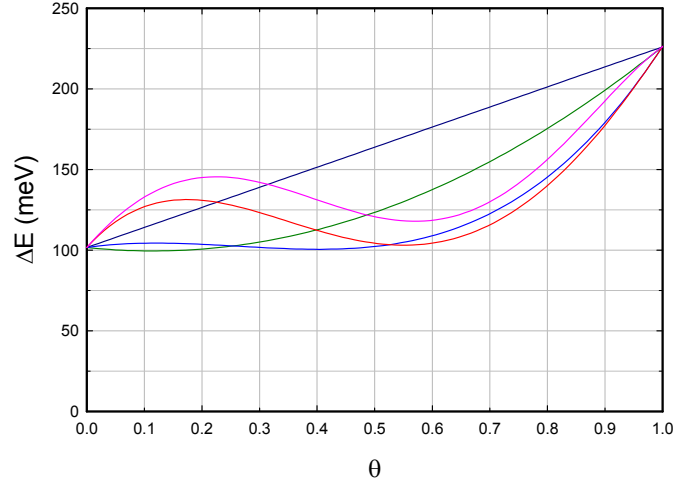
Figure 14. O-site to T-site excitation energy as a function of θ, for models with temperature-dependent O-site energy E_O and temperature-independent O-site to T-site excitation energy; ΔE linear in θ (*dark blue* line); second-order model (*dark green* line); third-order model (*blue line*); fourth-order model (*red line*); fifth-order model (*pink line*).

$$b_0 = 0.034584, \quad b_1 = -0.454285, \quad b_2 = 2.306099,$$

$$b_3 = -2.428471, \quad b_4 = -0.179903, \quad b_5 = 0.805586,$$

$$d_1 = 413.703, \quad d_2 = -951.745, \quad d_3 = -612.564,$$

$$d_4 = 2793.066, \quad d_5 = -1517.832, \tag{32}$$

where the a_j and d_j are in meV, and the b_j are in meV/K.

7.3. Excitation energy

The excitation energy for the different versions of the model are shown in Fig. 14. The models converge slowly with order (and have not finished converging as a function of the polynomial order), with the O-site to T-site excitation

Table 6. Errors associated with the constrained optimization of the different models with O-site and T-site occupation considered in this section.

| $a,b \mid d$ Order	I
5,5 | 1	2.71×10^{-5}
5,5 | 2	2.47×10^{-5}
5,5 | 3	2.16×10^{-5}
5,5 | 4	1.70×10^{-5}
5,5 | 5	1.50×10^{-5}
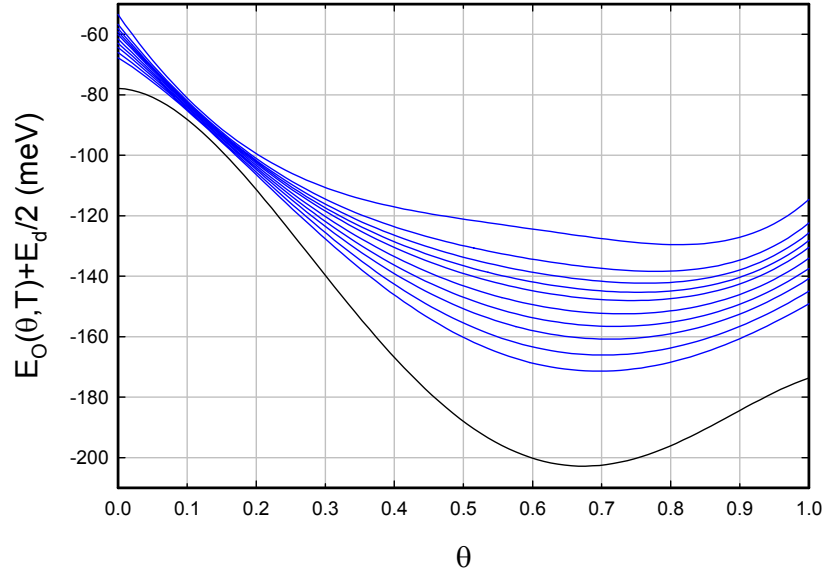
Figure 15. O-site energies as a function of loading for the different temperatures of the isotherms (*blue lines*); extrapolation to $T = 0$ (*black line*).

energy for the fifth-order model (*in pink*) first increasing with loading, then decreasing, and then increasing again. This reversal leads to low values for the excitation energy going down to about 117 meV at $\theta = 0.56$. This reversal moves the excitation energy sufficiently low to be in disagreement with the neutron diffraction data for palladium deuteride.

7.4. O-site energy

The O-site energies for the lowest error version of the model are shown in Fig. 15. Constraining the excitation energy at $\theta = 0$ results in O-site energies which seem generally reasonable. We might also expect the largest change with temperature to occur generally in the vicinity of $\theta = 1/2$, since this is where the splitting is probably largest. We see in Fig. 15 that the largest increase in temperature occurs at a loading closer to $\theta = 0.66$, and that there is a decrease for larger θ. Such a behavior might be explained if there is an additional thermal effect, such as an increase in lattice expansion with temperature at high loading.

The spread in O-site energy for these models has gotten sufficiently large in this case that we would be concerned about the resulting model being acceptable on physical grounds. If the excitation energy were larger in the general vicinity of $\theta = 1/2$, then the spread would be reduced. This suggests that an excitation energy more consistent with the neutron diffraction experiments in this regime would result in a more physical and better model.

There is a spread near $\theta = 0$ which is worth some discussion. We note that we found a similar increase in the O-site energy with temperature in our previous analysis of solubility for α-phase PdH_x and PdD_x [34]. There is agreement in the magnitude of this effect in the different models (of this work, and of the previous one), which are derived from different data sets; this is encouraging, and suggests consistency both in the experimental data and in the analysis. The origin of the effect lies in the anomalously large shift of the Fermi level which at $T = 0$ is part way down a sudden
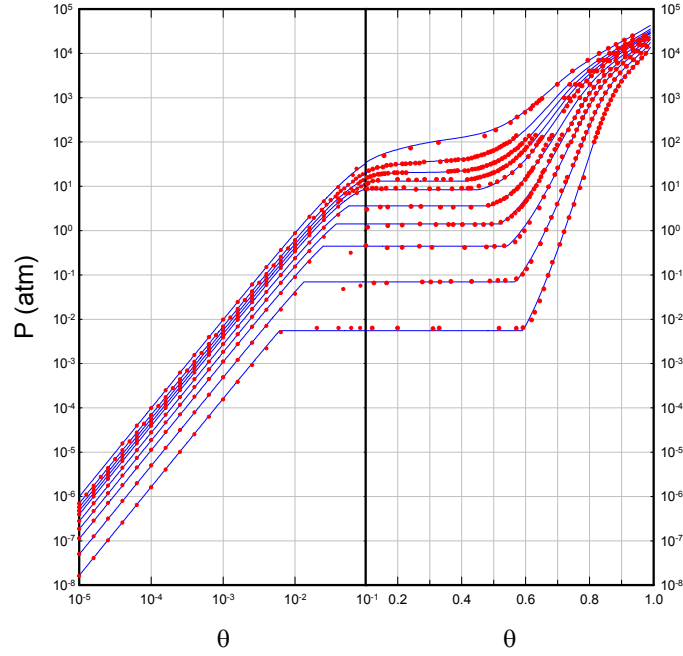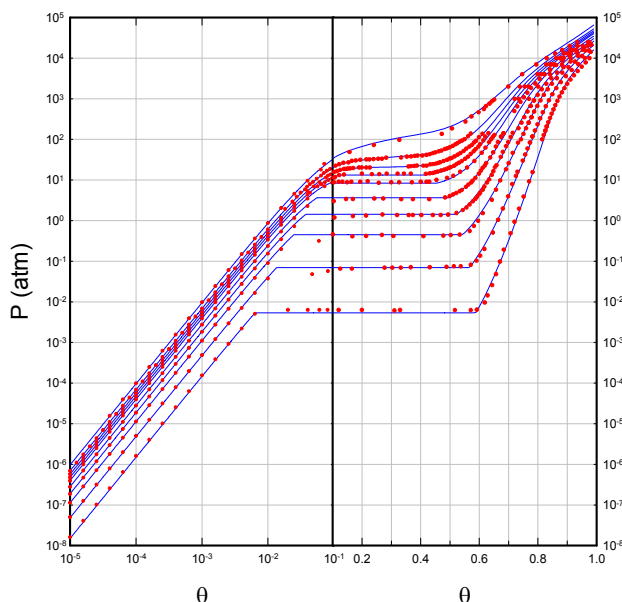
Figure 16. Isotherms and data points for the model with temperature-dependent fifth-order polynomial fit of E_O and optimized constrained fifth-order model for $\Delta E(\theta)$.

drop in the density of states (see Fig. 2 of Ref. [34]). We would not expect to see such a large shift due to the Fermi level at higher loading. This expectation is consistent with the rapid fall off of the spread with θ that can be seen in Fig. 15.

7.5. Phase diagram

The phase diagram that results from the lowest error constrained optimization is shown in Fig. 16. This phase diagram is very similar to the one we obtained with the unconstrained optimization. It looks very good in general.

8. Discussion and Conclusions

In this study we optimized a set of empirical models for the O-site energy, and in many cases also the O-site to T-site excitation energy, by minimizing the error between the model chemical potential and the isotherm data set. The general approach seems to be quite successful in giving models that match the isotherms of the data set, and also sheds light on the physical system. These are some of the simplest empirical models that can produce relatively high quality phase diagrams.

The optimization of a Lacher type of model with a temperature-independent O-site energy that is higher-order in θ is conceptually straightforward, and it produces better results than we had expected initially. We have not found such models studied systematically previously in the literature. The generalization to temperature-dependent O-site energies results in a phase diagram that is probably good enough to work with for some applications. The only problem

with it is that it does not correspond to a plausible physical model since the O-site energies decrease with temperature at low loading.

The issue of T-site occupation remains somewhat controversial at this time, primarily due to the lack of completely unambiguous experimental evidence showing explicitly significant T-site occupation. There is substantial theoretical support in density functional calculations and in quantum chemistry calculations for sufficiently low T-site energies such that one would expect them to have noticeable occupation and impact the phase diagram. The results from neutron diffraction experiments in palladium deuteride (showing T-site occupation) seem clear enough; however, the significance of these experimental results do not appear at this time to be widely appreciated. Consequently, our use of models with both O-site and T-site occupation in this work is likely to be acceptable to the theorists, and objectionable to the experimentalists.

Unconstrained optimization assuming both O-site and T-site occupation leads to models with very low mean square errors, but which are not physically acceptable at low loading since the O-site energy decreases with temperature. Constrained optimization with the excitation energy fixed at $\theta = 0$ fixes this problem, and results in a good match with low error. The biggest headaches in this case are that the excitation energy seems a bit low relative to the PdD neutron diffraction experiments, and the spread in the O-site energies in the mid-range of loading is larger than what we would hope for.

When we make use of a model with fixed $\Delta E(\theta)$ in Section 5, these problems are improved; the resulting phase diagram looks very good. In this case the only headache is that the error I is a bit larger, due mostly to the imposed boundary condition at $\theta = 1$. This draws attention to the extrapolation that we used for high loading, based on a generalization of the approach of Baranowski et al. [31]. The issue here is that in neither case does the extrapolation take into account possible T-site occupation. Additional experimental PCT data at high loading and at high temperature will be needed to resolve this issue.

In general these results strongly support the hypothesis that T-site occupation occurs and impacts the phase diagram. One could argue that the results are not site specific, as any other site with a similar excitation energy would work equally well. However, at this point for us there are no other obvious competitive candidates.

It seems useful to consider the arguments in support of T-site occupation briefly here. We have made use of a temperature-dependent O-site energy to account for configurational splitting that would be associated with a more general lattice gas model. The optimization of the associated parameters leads to models in the absence of T-site occupation with the wrong temperature dependence at low loading (as discussed in Section 4). Including T-site occupation corrects this, in the case that the O-site to T-site excitation energy is close to the empirical model discussed in Section 5. One interpretation is that this means that we would not expect a lattice gas model based on O-site occupation to give as good of a match to the data set as an equivalent lattice gas model which includes T-site occupation. In our earlier analysis of α-phase solubility, where the O-site to T-site excitation energy is lowest, and where we have access to a larger spread in temperature, the analysis is unambiguous [34]. With T-site occupation a good fit to the data can be obtained; without T-site occupation there is no hope for a physically acceptable model. Consequently, this earlier analysis weighs more heavily in support of T-site occupation, and the present study is supportive based on an analysis of different data over a larger range of loading. Our earlier analysis of PdH and PdD at high loading near room temperature also requires T-site occupation in order to make sense of published data. Here our basic conclusion is that the available PCT data for palladium hydride over the entire range of available temperature and loading independently provides support for T-site occupation.

The error I from the optimizations is the variance of the chemical potential. We can relate the associated standard deviation to the standard deviation of the fugacity approximately according to

$$\frac{\Delta \mu_{\mathrm{H}}}{k_{\mathrm{B}} T} = \frac{1}{2} \frac{\Delta f}{f}. \tag{33}$$

The lowest errors from the different models correspond to values of $\Delta\mu_H$ near 3–4 meV. At low pressure the fugacity is very nearly equal to the pressure; at high pressure the fugacity can be much larger. In this case it may be that optimizations based on $\ln P$ instead of μ_H would be preferred, as this would tend to reduce the weight associated with the (poorly known) high pressure points. This might be of interest in a future study.

Yet another issue that might be addressed in future work involves the issue of the statistical weight of the O-site states in the presence of splitting. Including temperature dependence of the O-site states as in the empirical models studied in this paper implies a splitting in the O-site states, where lower energy states have more occupation at low temperature, and with where higher energy states have more occupation at elevated temperature. In this kind of picture, we would expect a reduction in the associated entropy of the O-site states which would occur if the splitting were modeled explicitly. This has not been addressed in the models considered above. It may be possible to develop even better empirical models by including this effect.

We note that there are other approaches to modeling the phase diagram; for example, as in the recent analysis of Joubert and Thiébaut [5]. In this work the parameterization is a physical chemistry model in terms of the Gibbs energy rather than a physics type of parameterization in terms of site energies as we have used.

The optimizations reported here lead to estimates for the O-site and T-site energies, which are not so readily available otherwise from experiment. These energies are of interest as many groups at present work with density functional codes and quantum chemistry codes which predict them.

Appendix: No Abrupt Change Near a Loading of Unity

In the course of the review process the reviewer raised issues pointing out the absence of an abrupt change in the experimental data near a loading of unity, which underscores the absence of experimental support for T-site occupation at high loading.

In one communication the reviewer wrote:
The upper phase limit for the beta phase cannot be obtained simply by measuring the H/Pd (D/Pd) ratio because a second hydrogen-rich phase can form, thereby creating a two phase mixture beyond the limit of the beta phase that would have an overall composition above the fcc limit of the beta phase. This behavior is seen in the other hydride systems as well as in the behavior of fcc compounds containing C and N. Instead, the upper limit has to be based on seeing an abrupt change in slope of some measured value. In fact, this change in slope is detected in the data near D/Pd=0.98 using the resistivity and the temperature effect on the resistivity combined with the overall composition.

In another communication the reviewer wrote:
A phase boundary occurs at the composition at which another crystal structure forms with a greater concentration of the second atom. For example, the phase limit of beta-VH occurs at H/V=0.8 where another phase having the crystal composition of VH$_2$ forms (page 15, Fukai). If only the overall composition were measured, the composition would be seen to increase beyond 0.8. This increase alone would not reveal that the increase resulted from formation of the VH$_2$ phase rather than H being added to the beta phase. This limitation applies to PdH when the composition is noted to increase above H/Pd=1. In the absence of being able to detect the additional crystal structure, the boundary has to be identified by a change in behavior, such as a change in slope seen in the resistivity or chemical activity. Changes in slope of both are seen near D/Pd=1. Graphs showing the result of pressure reported by Baranowski et al. and the effect of temperature on the resistivity by Tripodi et al. are attached.

In other words, no evidence supports the ability of the beta phase to accommodate D or H above the normal filling of the O-sites. Extra D or H in the T-sites or in metal atom vacancies is not supported by the location of the upper phase boundary, at least to an amount of occupancy that the accuracy of the measurements permit.

A person might argue that even though no extra H were present, the H in the lattice might be distributed between the O and T sites while retaining a H/Pd ratio below unity at the upper boundary. Why this novel distribution might form would provide a challenge for the paper to explain.

These comments of the reviewer are interesting, and worth some additional discussion. The issues under discussion are relevant to the analysis presented in an earlier work [35], and somewhat less so to the analysis of this paper since we included phase diagram data only below $\theta = 1$.

When we began the earlier analysis we were expecting to see a sudden change in the chemical potential at the $\theta = 1$ boundary, consistent with intuition that suggested the O-site to T-site excitation energy is large near $\theta = 1$. A very large number of models were analyzed with an excitation energy between 350 meV and 600 meV, and the results showed an abrupt change where below $\theta = 1$ only O-site occupation occurred, and above $\theta = 1$ the O-sites were completely filled and only incremental T-site occupation occurred with increased loading. Predictions from these early models would correspond will to the expectation that one would expect a sharp boundary between the β-phase for $\theta < 1$ and a T-site phase for $\theta > 1$.

It took a long time to move past this initial perspective and investigate models with lower O-site to T-site excitation energies. Such models behave qualitatively differently in that there is no sharp boundary in the chemical potential, or in any readily observable model parameter, at $\theta = 1$. The 226 meV excitation energy estimated in [35] is sufficiently low that a smooth transition occurs with partial occupation of O-sites and T-sites below and above $\theta = 1$.

References

[1] F. Lewis, *The Palladium/Hydrogen System*, Academic Press, New York, 1967.
[2] E. Wicke, H. Brodowsky and H. Züchner, Hydrogen in palladium and palladium alloys, in *Hydrogen in Metals*, Vol. 2, Springer, Berlin, 1978, pp. 73–155.
[3] T.B. Flanagan and W.A. Oates, The palladium–hydrogen system, *Ann. Rev. Materials Sci.* **21** (1991) 269–304.
[4] F.D. Manchester, A. San-Martin and J.M. Pitre, The H–Pd (hydrogen–palladium) system, *J. Phase Equilibria* **15** (1994) 62–83.
[5] J.M. Joubert and S. Thiébaut, Thermodynamic assessment of the Pd–H–D–T system, *J. Nucl. Materials* **395** (2009) 79–88.
[6] Y. Ebisuzaki and M. O'Keeffe, The solubility of hydrogen in transition metals and alloys, *Prog. Solid State Chem.* **4** (1967) 187–211.
[7] W.M. Mueller, J.P. Blackledge and G.G. Libowitz, *Metal Hydrides*, Academic Press, New York, 1968.
[8] W. A. Oates and T.B. Flanagan, The solubility of hydrogen in transition metals and their alloys, *Prog. Solid State Chem.* **13** (1981) 193–272.
[9] T.B. Flanagan, Thermodynamics of Metal–Hydrogen Systems, in *Metal Hydrides*, Springer, New York, 1981, pp. 361–377.
[10] E. Wicke, Some Present and Future Aspects of Metal–Hydrogen Systems, *Zeitschrift für Physikalische Chemie* **143** (1985) 1–21.
[11] N.A. Gokcen, Interstitial Solutions, in *Statistical Thermodynamics of Alloys*, Springer, New York, 1986, pp. 149–193.
[12] L. Schlapbach, *Hydrogen in Intermetallic Compounds I,* Springer, New York, 1988.
[13] R. Lässer, Properties of Protium, Deuterium and Tritium in Selected Metals, in *Tritium and Helium-3 in Metals*, Springer, Berlin, 1989, pp. 48–107.
[14] Y. Fukai, *The Metal–Hydrogen System*, Springer, New York, 1991.
[15] M. Fleischmann, S. Pons and M. Hawkins, Electrochemically induced nuclear fusion of deuterium, *J. Electroanal. Chem. and Interfacial Electrochem.* **261**(1990) 301–308; Errata, **263** (1990) 187.
[16] M. Fleischmann, S. Pons, M.W. Anderson, L.J. Li and M. Hawkins, Calorimetry of the palladium–deuterium-heavy water system, *J. Electroanal. Chem. Interfacial Electrochem.* **287** (1990) 293–348.
[17] E. Storms, *The Science of Low Energy Nuclear Reactions: A Comprehensive Compilation of Evidence and Explanations about Cold Fusion*, World Scientific, Singapore, 2007.
[18] R.H. Fowler and C.J. Smithells, A theoretical formula for the solubility of hydrogen in metals, *Proc. Roy. Soc. London, Series A, Mathematical and Physical Sciences* **160** (1937) 37–47.

[19] J.R. Lacher, A theoretical formula for the solubility of hydrogen in palladium, *Proc. Roy. Soc. London, Series A, Mathematical and Physical Sciences* **161** (1937) 525–545.

[20] F.D. Manchester, Lattice gas aspects of metal–hydrogen system, *J. Less Common Metals* **49** (1976) 1–12.

[21] S. Dietrich and H. Wagner, Model calculation for the incoherent phase-transition in the palladium–hydrogen system, *Zeitschrift für Physik B Condensed Matter* **36** (1979) 121–126.

[22] C.K. Hall and M. Futran, Statistical theory of the phase change behavior of metal–hydrogen systems, *J. Less Common Metals* **74** (1980) 237–242.

[23] R.A. Bond and D.K. Ross, The use of Monte Carlo simulations in the study of a real lattice gas and its application to the alpha Pd–D system, *J. Phys. F: Metal Physics* **12** (1982) 597.

[24] C.K. Hall, A review of the statistical theory of the phase-change behavior of hydrogen in metals, *Electronic Structure and Properties of Hydrogen in Metals*, Springer, New York, 1983, pp. 11–24.

[25] E. Salomons, On the lattice gas description of hydrogen in palladium: a molecular dynamics study, *J. Physics: Condensed Matter* **2** (1990) 845.

[26] I.K. Robinson, Computational Studies of Hydrogen in Palladium, Doctoral dissertation, University of Salford, 2015.

[27] Y. Wang, S.M. Sun and M.Y. Chou, Total-energy study of hydrogen ordering in PdH_x $(0 \leq x \leq 1)$, *Phy. Rev. B* **53** (1996) 1.

[28] P.O. Orondo, A Theoretical Model of Interstitial Hydrogen: Pressure–Composition–Temperature, Chemical Potential, Enthalpy and Entropy, MIT PhD Thesis, 2012.

[29] J.E. Worsham, M.K. Wilkinson and C.G. Shull, Neutron-diffraction observations on the palladium–hydrogen and palladium–deuterium systems, *J. Phys. Chem. Solids* **3** (1957) 303–310.

[30] G. Nelin, A neutron diffraction study of palladium hydride, *Phys. Status Solidi (b)* **45** (1971) 527–536.

[31] B. Baranowski, S.M. Filipek, M. Szustakowski, J. Farny and W. Woryna, Search for "cold-fusion" in some Me–D systems at high pressures of gaseous deuterium, *J. Less Common Metals* **158** (1990) 347–357.

[32] I.F. Silvera and F. Moshary, Deuterated palladium at temperatures from 4.3 to 400 K and pressures to 105 kbar: search for cold fusion, *Phy. Rev. B* **42** (1990) 9143.

[33] M.C.H. McKubre, F.L. Tanzella and V. Violante, What is needed in LENR/FPE studies? *J. Cond. Mat. Nucl. Sci.* **8** (2012) 187.

[34] P.L. Hagelstein, O-site and T-site occupation of α-phase PdH_x and PdD_x, *J. Cond. Mat. Nucl. Sci.* **17** (2015) 67–90.

[35] P.L. Hagelstein, An empirical model for octahedral and tetrahedral occupation in PdH and in PdD at high loading, *J. Cond. Mat. Nucl. Sci.* **17** (2015) 35–66.

[36] J.D. Clewley, T. Curran, T.B. Flanagan and W.A. Oates, Thermodynamic properties of hydrogen and deuterium dissolved in palladium at low concentrations over a wide temperature range, *J. Chem. Soc., Faraday Trans. 1: Phy. Chem. in Condensed Phases* **69** (1973) 449–458.

[37] K.A. Moon, Pressure–composition–temperature relations in the palladium–hydrogen system, *J. Phy. Chem.* **60** (1956) 502–504.

[38] D.H. Everett and P. Nordon, Hysteresis in the palladium+hydrogen system, *Proc. Roy. Soc. London A: Mathematical, Physical and Engineering Sciences* **259** (1960) 341–360.

[39] J.W. Simons and T.B. Flanagan, Absorption isotherms of hydrogen in the α-phase of the hydrogen–palladium system, *J. Phy. Chem.* **69** (1965) 3773–3781.

[40] R. Burch, Theoretical aspects of the absorption of hydrogen by palladium and its alloys. Part 1. A reassessment and comparison of the various proton models, *Trans. Faraday Soc.* **66** (1970) 736–748.

[41] M.J.B. Evans and D.H. Everett, Thermodynamics of the solution of hydrogen and deuterium in palladium, *J. Less Common Metals* **49** (1976) 123–145.

[42] O.J. Kleppa and R.C. Phutela, A calorimetric-equilibrium study of dilute solutions of hydrogen and deuterium in palladium at 555 to 909 K, *J. Chem. Phys.* **76** (1982) 1106–1110.

[43] R. Lässer and G.L. Powell, Solubility of protium, deuterium and tritium in palladium–silver alloys at low hydrogen concentrations, *J. Less Common Metals* **130** (1986) 387–394.

[44] W.A. Oates, R. Lässer, T. Kuji and T.B. Flanagan, The effect of isotopic substitution on the thermodynamic properties of palladium–hydrogen alloys, *J. Phys. Chem. Solids* **47** (1986) 429–434.

[45] A. Harasima, T. Tanaka and K. Sakaoku, Cooperative Phenomena in Pd–H System I, *J. Phy. Soc. Japan* **3** (1948) 208–213.

[46] T. Tanaka, K. Sakaoku and A. Harasima, Cooperative Phenomena in Pd–H System II, *J. Phy. Soc. Japan* **3** (1948) 213–218.
[47] M.P. Pitt and E.M. Gray, Tetrahedral occupancy in the Pd–D system observed by in situ neutron powder diffraction, *Europhys. Lett.* **64** (2003) 344.

Research Article

Anomalous Energy Produced by PdD

Edmund Storms*

LENRGY LLC, Santa Fe, NM 87501, USA

Abstract

Two samples of commercial Pd from the same batch were reacted with D using the electrolytic method and found to produce sustained excess power and energy. The effects of temperature, applied current, and D/Pd ratio on the amount of excess power were studied.

© 2016 ISCMNS. All rights reserved. ISSN 2227-3123

Keywords: Cold fusion, Enthalpy of reaction, Excess energy, PdD, Volume expansion

1. Introduction

When a material is involved in a chemical reaction, energy is frequently released. The amount of energy has been measured for most chemical reactions and the values are, in general, very accurate. After all, the entire field of chemistry is based on such measurements. When careful measurements reveal release of extra energy over that expected, either the claim is rejected as error or something very strange must be taking place. Once the possibility of error is eliminated, finding the source becomes a worthy effort.

In 1989, Profs. Fleischmann and Pons [1] observed extra energy being produced when they reacted deuterium with palladium using electrolysis. This reaction is very simple and well known, involving splitting D_2O into D_2 and O_2, with the D_2 reacting with the palladium to form the compound PdD. On occasion, more energy was made than could be explained by any chemical reaction. Over the years, this effect was replicated many times [2] and considerable evidence shows the extra energy results from formation of helium [3,4] and sometimes a little tritium, both of which can only be produced by nuclear reactions. A variety of other nuclear products have been observed on rare occasions [5]. Consequently, the process has been called Low Energy Nuclear Reaction (LENR) because it takes place at a much lower energy than is required to initiate hot fusion, the conventional version of the fusion process [6].

Explaining how LENR can occur in a common material has confounded science [7] while the supporting evidence just keeps growing. This and other nuclear reactions caused by LENR in several kinds of materials have been described in scientific journals, many peer reviewed. Nevertheless, the general rejection by the scientific community has forced publication of most information in unconventional places that, fortunately, are available on the web.[a]
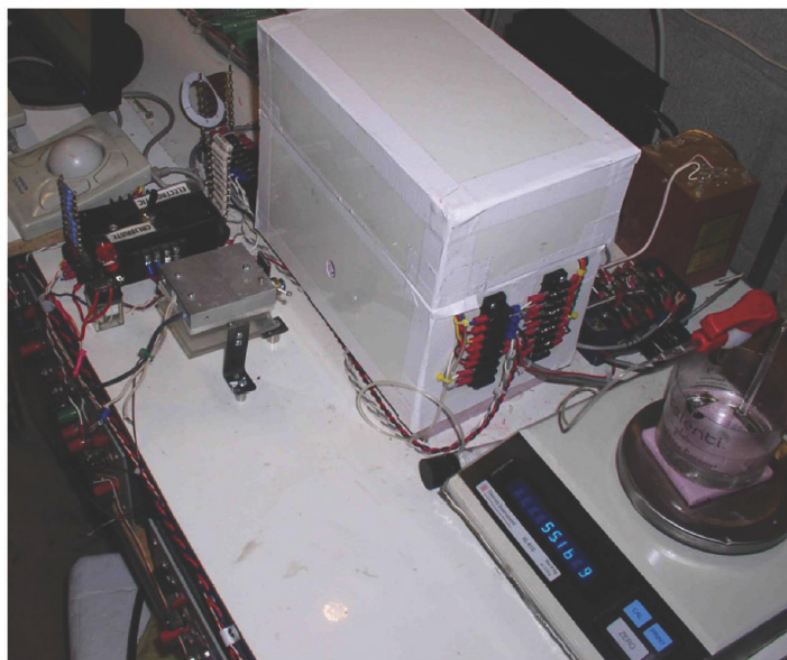
Figure 1. Picture of the closed Seebeck calorimeter. The balance used to measure the deuterium content of the cathode using the orphaned oxygen method is seen in the foreground. A laser is positioned to expose the cathode to laser light though a hole in the side of the calorimeter. This feature is not discussed in this paper.

This study demonstrates production of anomalous energy using two different samples and the behavior of this energy when temperature, deuterium content of the material, and applied current are changed. The observed response gives additional insight into the possible mechanism and corrects some previously incorrect conclusions about this behavior.

The problem is compounded by the difficulty in finding palladium able to cause the effect, i.e. be activated. Most palladium shows no ability to host such a reaction. This difficulty has frustrated replication, hampered research, and fueled rejection. Persistent effort has improved reproducibility by finding treatments that make the palladium more susceptible to activation [8,9]. Various alloys containing palladium and other metals have also been found to improve success [10]. In other words, the effect is not unique to palladium and can now be initiated when suitable skill is used. The common mantra that the effect has not been nor can be reproduced is simply not true, as this and hundreds of published studies have demonstrated [11].

Palladium found to produce extra energy has a few properties different from ordinary palladium. The palladium can achieve a very high D/Pd ratio without forming large cracks in the surface or voids [12–14] in the interior when it reacts with the isotopes of hydrogen. This feature provides a possible test of potentially active material. In addition, the surface frequently shows an array of crystals having a size of less than 100 μm with a preferred orientation [8]. However, these conditions alone do not result in extra energy although they are consistent with the requirements to achieve success identified by the author in previous papers [7,15,16].

This paper describes a successful effort to activate samples of palladium obtained from a commercial source. The conditions required to initiate energy production and the effect of various variables on its behavior are explored.
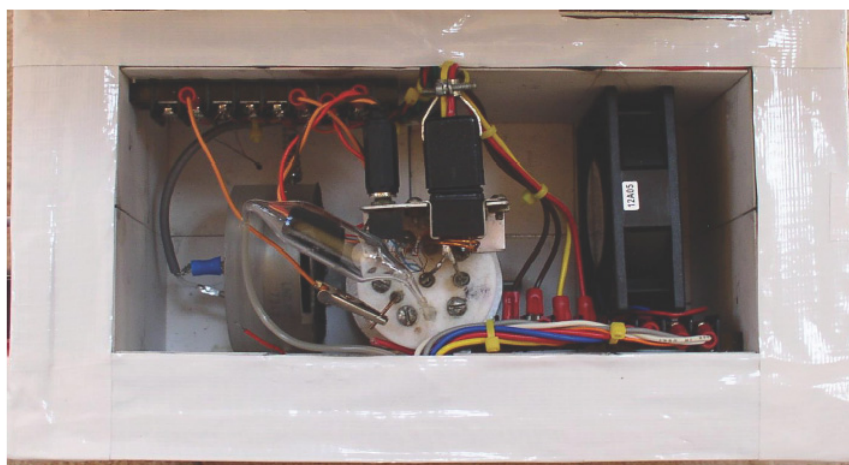
Figure 2. View inside the calorimeter enclosure. The GM detector is on the left, the top of the electrolytic cell is seen in the center, and a fan is on the right. A catalyst is contained in a tube located in the gas line to the orphaned oxygen measurement in order to eliminate any D_2 that failed to react with O_2 in the cell.

2. Results

2.1. Energy measurement

Because the effect is based on a claim for excess energy, accurate measurement of this energy becomes important. A Seebeck-type calorimeter is used, shown in Fig. 1, consisting of a water-cooled aluminum box with thermoelectric
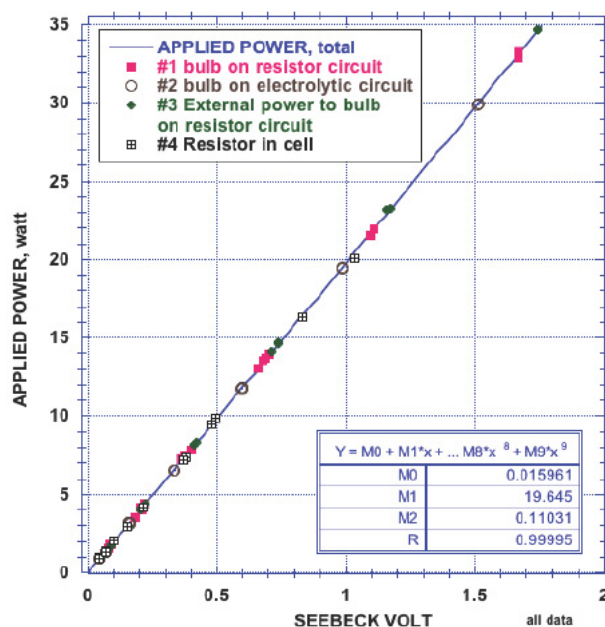
Figure 3. Typical calibration using several methods to apply heat energy to the calorimeter.
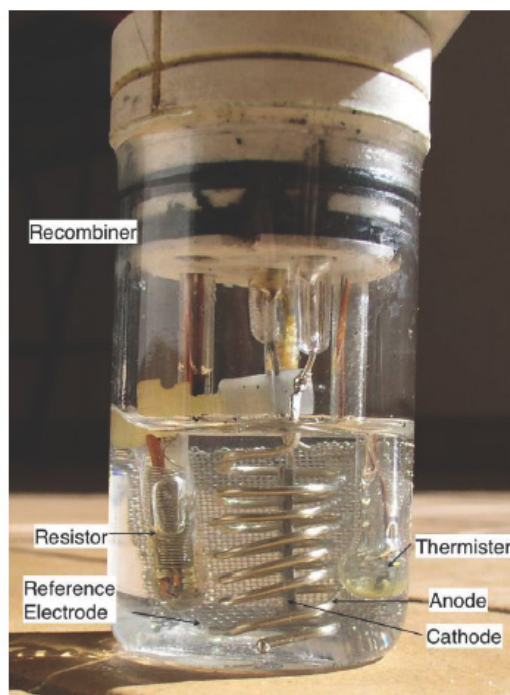
Figure 4. Pyrex electrolytic cell. The anode consists of Pt wire encircling the cathode. The cell is sealed using O-rings.

panels covering the inside surface. Excess power is defined as all power in excess of that applied to the cell as electric power based on a calibration using applied electric power.

The arrangement of the electrolytic cell, GM detector, and fan within the box can be seen in Fig. 2. Energy generated inside the box produces a voltage generated by the thermoelectric converters proportional to the magnitude of applied power. The amount of power is based on a calibration using electrical power applied to a resistor inside the electrolytic cell, as electrolytic current using an inert platinum cathode, or as current applied to a 50 W Quartz–iodine light bulb in place of the electrolytic cell. As can be seen in Fig. 3, each method for generating heat results in the same generated voltage when using the same amount of applied power.

The stability of the calibration is tested regularly by applying current using one of these methods. The uncertainty is ± 0.02 W from 0 to 30 W of total applied power based on fitting a quadratic equation to at least 10 data points measured over the range of power applied during the excess power measurement.

The electrolytic cell containing the Pd cathode is shown in Fig. 4. The cathode is attached by a Teflon clamp to a Pt wire that exits the cell through a glass-metal seal. The anode is made of platinum wire. The reference electrode is made of platinum mesh and is used to measure the open circuit voltage (OCV) relative to the cathode. A thermistor contained in a Pyrex tube is used to determine the electrolyte temperature. The electrolyte temperature can be changed independent of electrolytic power by applying electric power an internal resistor contained in a Pyrex tube. A catalyst consisting of Pt on Al_2O_3 is present in the cell to recombine any excess D_2 and O_2. Consequently, the cell is chemically closed and physically sealed to the atmosphere. A tube connects the cell to an oil reservoir used to measure the deuterium content of the cathode by the orphaned oxygen method. Pictures and a detailed description can be found at
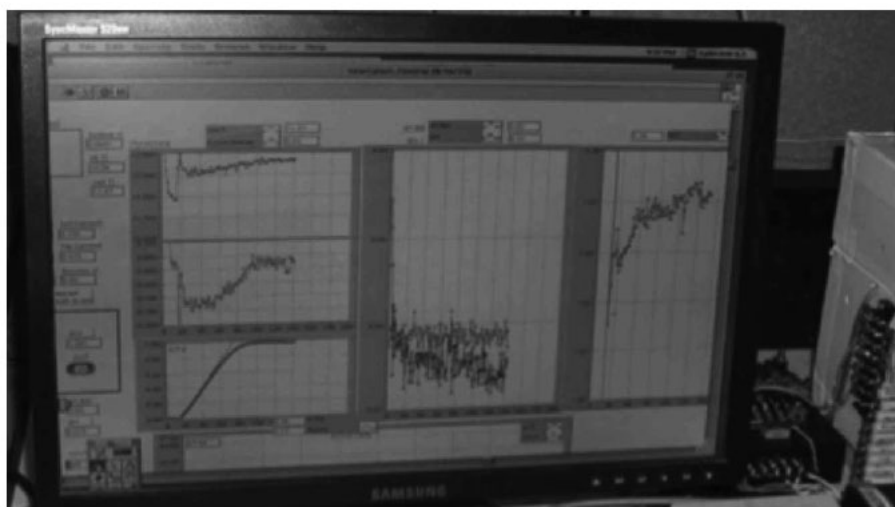
Figure 5. Computer screen showing real time display of cell temperature, excess power, D/Pd ratio, GM counting rate and OCV. The center graph compares the GM flux measured by the detector in the calorimeter to the background flux outside the calorimeter. This measurement will be discussed in a future paper.

www.LENRexplained.com.

Values are taken every 6 min and plotted on a computer screen (Fig. 5) as well as being saved to an Excel file. Measurements are made of the current and voltage applied to the cell, temperature inside the cell, temperature inside the Seebeck box, the OCV, the radiation flux measured by the detector inside the box and by another identical detector located 3 m away from the calorimeter, the current and voltage delivered to the fan, the voltage produced by the thermoelectric converters in the box, and the weight of oil delivered from the reservoir as result of orphaned oxygen formation. All voltages are measured at the calorimeter boundary.

The electrolyte is 99.8% D as D_2O containing LiOD that is formed by adding about 0.1 g of Li metal to 30 ml of D_2O. The cell is made of Pyrex, the top is Teflon, and, other than the cathode, only platinum is exposed to the electrolyte.

The average D/Pd ratio is measured using the orphaned oxygen method. This method involves measuring the amount of oxygen released when deuterium is absorbed in the Pd. Oil is displaced by the extra O_2 from a reservoir onto a balance, seen on the right in Fig. 1. The accuracy of the D/Pd ratio is ±0.01.

2.2. Loading behavior

The first step in initiating excess power production starts by creating a chemically active surface on the palladium cathode. In this study, an efficient reaction with D results when the surface has been subjected to cleaning using fuming HNO_3 and heating to 900°C in air for several hours, followed by slow cooling over several hours. The treatment at 900°C cleans the surface by either vaporizing the impurities or causing them to diffuse into the interior where they do no harm. A very thin layer of PdO forms during cooling, which is easily reduced by deuterium to produce chemically active Pd. Typically, the surface used in this study initially contains only Pd, O, and C, based on EDX analysis.

The loading process was studied extensively as part of this investigation, an example of which is shown in Fig. 6. Typically, each sample has a different upper limit to the D/Pd atom ratio while showing a similar behavior of energy
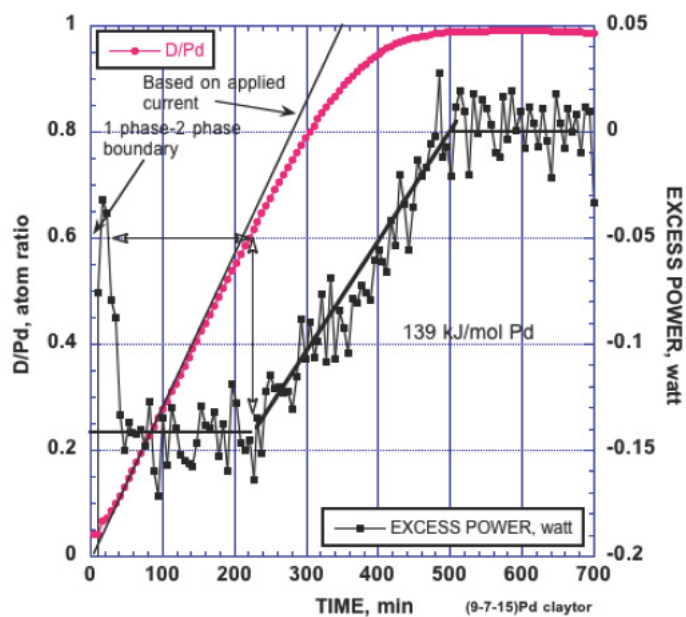
Figure 6. Typical behavior of palladium when reacted with deuterium at 11°C using Pd-#A. The average D/Pd ratio and the power associated with the reaction are shown. The initial behavior of the excess power results because sudden application of power causes the calorimeter to shift from the equilibrium condition when 0.1 A is applied. The negative numbers indicate loading is an endothermic process.
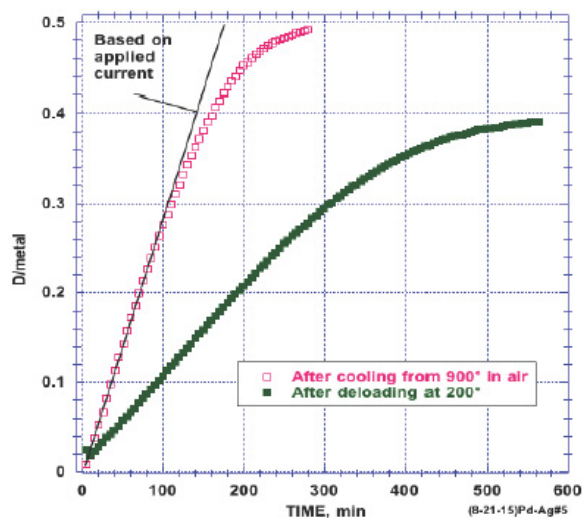
Figure 7. Reaction of Pd-#B with D after being previously loaded to D/Pd = 0.86 followed by partial removal of D without the surface being cleaned.
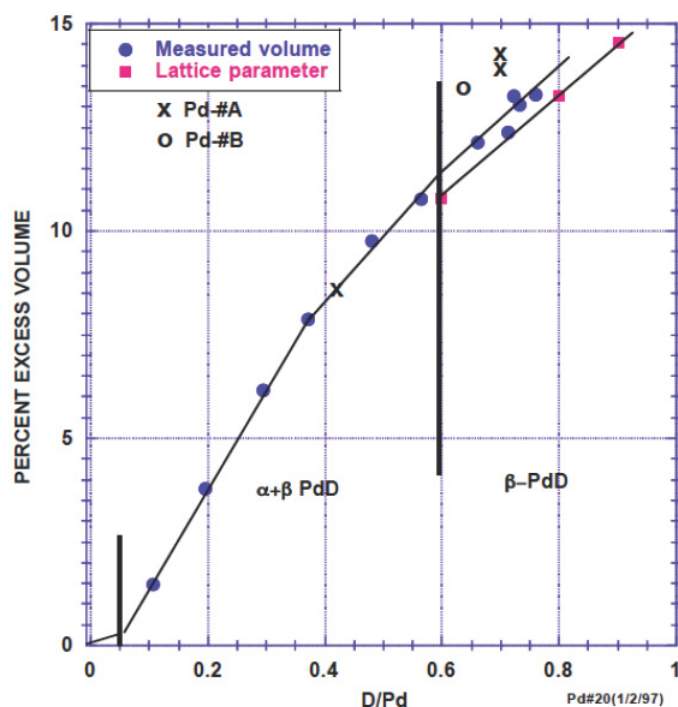
Figure 8. Physical expansion of the volume relative to the initial volume as D is added to typical Pd. The expansion based on the reported behavior of the lattice parameter is compared to the physical measurement. The behavior of Pd-#A and Pd-#B are also plotted.

consumed as deuterium is reacted. Energy is consumed because more energy is required to remove the D from D_2O than is recovered when the D reacts with Pd. This absorbed energy can be recovered when the D is reacted with O_2 to produce D_2O and pure Pd, which can take place within the calorimeter when deuterium is lost from the PdD after electrolysis is stopped or can cause self-heating when unloading occurs in air. The amount of stored energy is trivial

Table 1. Physical changes in Pd samples

Treatment	Width (mm)	Length (mm)	Thickness (mm)	Volume (mm^3)	Volume expansion (%)	D/Pd
Pd-#A						
Initial, uniform blue surface	10.91	18.43	1.008	202.7	0.00	0
Loaded-partially deloaded	11.17	18.70	1.107	231.2	14.09	0.70
Deloaded–loaded	11.22	18.79	1.100	231.9	14.42	0.70
Deloaded @ 150°C	10.93	18.57	1.084	220.0	8.56	0.42
Pd-#B						
Initial, uniform blue Surface	12.73	12.09	0.976	150.2	0.00	0
Loaded	12.93	12.26	1.077	170.7	13.65	0.64
Deloaded @ 900°C	12.60	11.97	0.998	150.5	0.21	0
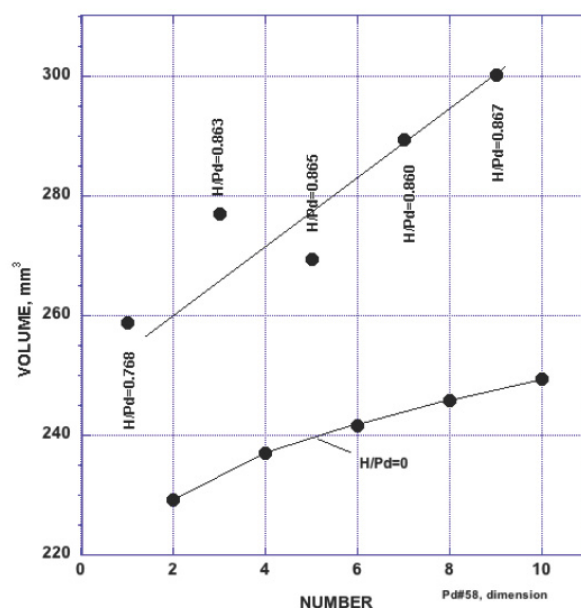
Figure 9.   Changes in volume produced when H is repeatedly reacted with Pd and then removed at 150°C.

compared to the amount of excess energy created by the LENR process.

The behavior observed when Pd reacts with D is important because it helps to identify potentially active Pd and reveals information about the nature of the reacting surface. A metal having a surface free of metallic deposits and activated by the method used here will react initially with most D presented to the surface. Gradually, the amount of D being reacted decreases until all the D created at the surface forms D_2 gas at the composition limit. The sample shown in Fig. 6 is unusual in reaching a D/Pd very near the upper limit of the beta phase composition at D/Pd = 1.

The loading process deposits impurities on the surface, which generally consists of Fe, Cr, Si, and Pt, with the first two being supplied by the stainless steel lead attached to the Pd sample. The effect of these impurities on the loading behavior can be made clear by partially unloading a sample of previously reacted Pd and reloading without removing the acquired surface impurity. Figure 7 shows the loading behavior of a sample after being first loaded to D/Pd = 0.86 and then partially deloaded by heating in air at 150°C . In this case, the impurities deposited on the surface during the first loading allowed only 1 in 10 of the D presented to the surface by the electrolytic current to react. This rejected fraction remained constant until the average bulk material reaches about D/Pd = 0.6, similar to the behavior seen in Fig. 6.

This deposited impurity is not uniform on the surface; hence it affects some regions more than others. Consequently, the local D/Pd is not uniform and non-uniform stress is produced between the different compositions. In general, the greater the electrolytic current, the faster this deposit forms on the surface and the sooner the loading behavior deviates from the ideal. Once the surface deposit is removed by concentrated HNO_3, a repeat of the loading process causes the behavior to match that shown by a clean surface. Apparently, the fraction of D reacted initially depends only on the presence of surface impurities.

In summary, a clean Pd surface reacts initially with every D presented to the surface by electrolysis. Accumulation of deposited impurities interferes with this process more in some regions of the surface than in others. The final D/Pd
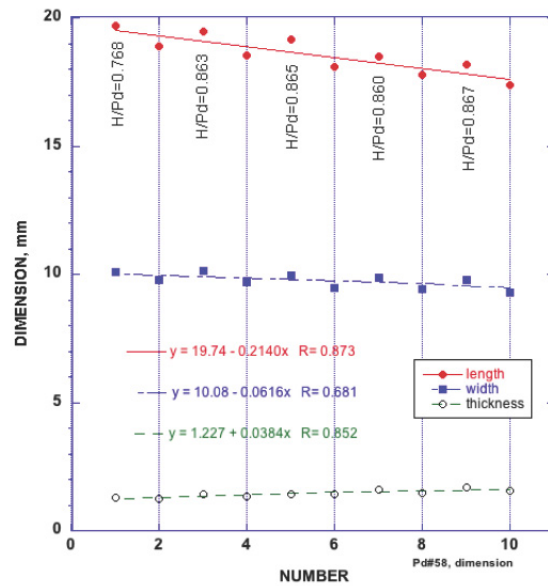
Figure 10. Changes in the physical dimensions of the sample shown in Fig. 9 after reacting with H and after the H is removed, with the values obtained after H is removed plotted on the vertical lines.
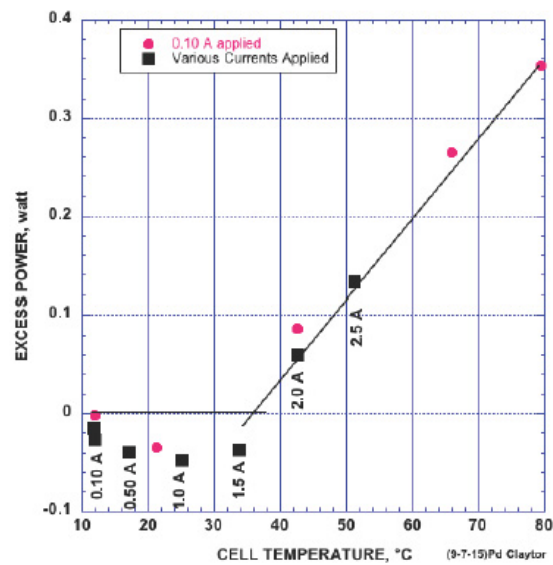
Figure 11. Comparison between excess power produced by applying electrolytic current and by changing the temperature at fixed current.
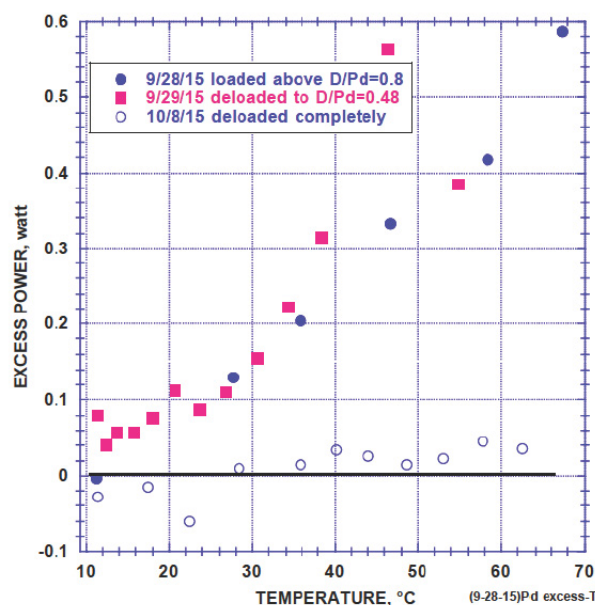
Figure 12.　Effect of temperature on excess power when the average D/Pd ratio is changed.

ratio achieved is determined largely by the initial properties of the Pd, which are different for each sample.

2.3.　Excess volume

As PdD forms in the material, the shape and volume of the sample change [13]. In general, the material expands in response to the increase of the lattice parameter, as can be seen in Fig. 8. In many cases, the expansion exceeds the amount expected based on the lattice parameter and this extra volume remains after the D is removed. This extra volume is called excess volume and the amount is different for each sample.

In addition, the length and width of the sample shrink while the thickness increases. Palladium that produces more than a few percent of excess volume tends to form large cracks and is limited to a lesser limit to the D/Pd ratio [14]. Consequently, potentially active material is sought among palladium having very little excess volume [17].

Table 1 compares the dimension and volume for the samples used in this study. This expansion is important because it produces stress in the surface region and causes cracks to form. These cracks, depending on their gap width, can cause excessive loss of D_2 or creation of the NAE, in which, according to Storms [2,18], the fusion process takes place. The rate of loading will affect the rate at which this stress is generated and, consequently, the response of the structure to crack formation. The sample used in this study showed production of only 0.21% excess volume, which identified this material as being potentially nuclear active, as later experience demonstrated.

A study was undertaken to examine the volume change in more detail using light hydrogen. A sample was loaded with H and caused to reach the H/Pd ratio, as shown in Fig. 9. The volume increased as expected when H was added, but each time the H was removed and then added again, the volume increased further. The dimensions also changed, with the length and width becoming smaller while the thickness increased, as shown in Fig. 10. Numerous people have previously studied this well-known effect [13,19–21] and reported similar behavior. Repeated loading followed by unloading causes the shape to change with the result that a flat plate tends to form a cube having greater volume
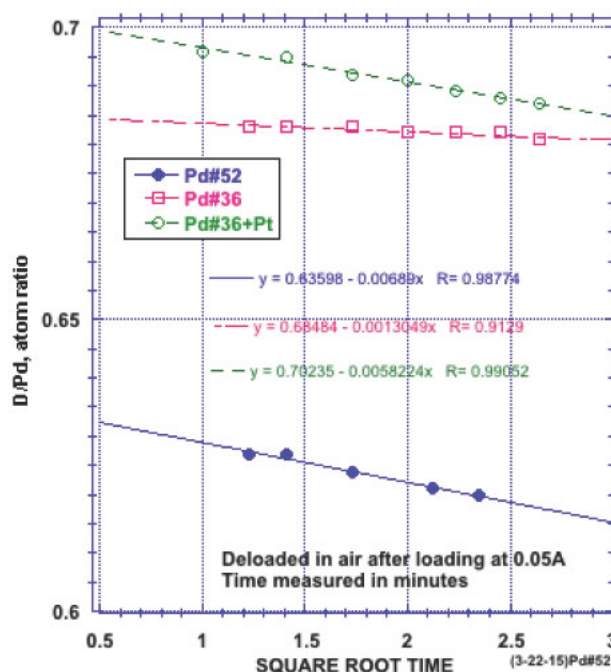
Figure 13. Examples of the change in the average D/Pd ratio as deuterium is lost from various samples of PdD in air at room temperature after electrolytic current is stopped. The least-squares line is extrapolated to zero time to determine the initial D/Pd ratio. The time is measured in minutes.

than the original palladium.

2.4. Excess power

Potentially active palladium does not produce excess power when it is initially reacted with D no matter how high the achieved D/Pd ratio. A process of partial unloading and reloading is required. Even this treatment will not always result in excess power production. Once excess power is produced, it tends to be very reproducible even after some of the D is removed by allowing the D to leak out when electrolytic current is turned off or by heating in air at 150°C. Both samples used in this study were subjected to a loading–unloading treatment before excess power was detected.

Separating the variables thought to affect energy production is the next task. The effect of temperature can be seen in Fig. 11, where the temperature is changed by applying power two different ways. In both cases, the resulting excess power shows the same relationship to temperature. This behavior strongly indicates that temperature alone is the controlling variable.

Figure 12 compares the excess power measured when the average D/Pd is fixed above 0.8 by applying electrolytic current and at a value near 0.48 after some deuterium had been lost by heating at 150°C in air. Excess power production no longer occurs when deuterium is completely removed by heating at 150°C in vacuum.

The D/Pd ratio is determined after each study by weighing the contained deuterium. This is done by measuring the weight change as a function of the square root of time, as shown in Fig. 13, and extrapolating the values to the time electrolytic current was stopped. The total deuterium content is also determined by measuring the weight change after
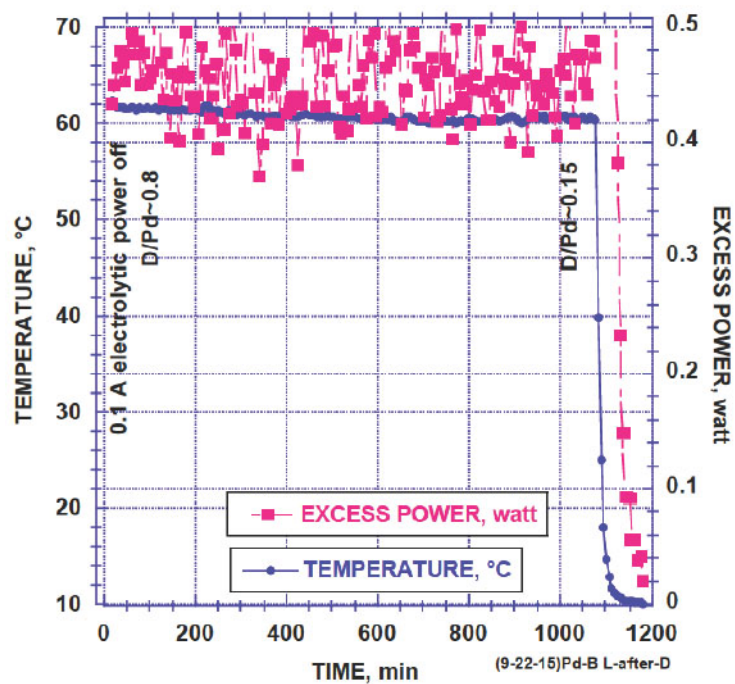
Figure 14. Excess power as a function of time while a sample lost deuterium at about 60°C after applied current was stopped. The excess power rapidly dropped to a value too small to measure when the temperature was reduced to 10°C.
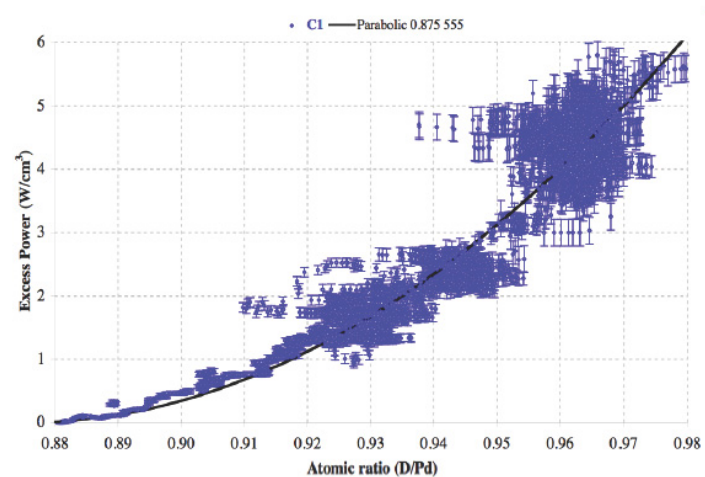
Figure 15. Example of the apparent relationship between the average D/Pd ratio and excess power production [25].

all deuterium is removed. These values represent the average deuterium content; not the deuterium content close to the NAE, which is the composition that would affect excess power production. In view of the non-uniform composition known to be present in such samples, the composition at the NAE is unknown and cannot be assumed equal to the average measured composition.

Turning off the electrolytic current while a sample is making energy produces the so-called "heat after death" behavior, as can be seen in Fig. 14. In the past, Fleischmann and Pons observed energy production to continue for extended times [22]. The various reported runaway heating events [23,24] are consistent with this behavior. In the present study, the temperature is held constant at about 60°C by an internal heater after the electrolytic power is turned off. Excess power remains constant as the average D/Pd ratio changes from above 0.8 to 0.15 as the sample deloads. The excess power continues and drops to an undetectable value only after the temperature falls to 10°C because the internal heater was turned off. A total of 30 kJ excess energy was produced, 2.5 kJ of which resulted from the unloading process.

The deuterium content after the study is determined by weighing the total amount of deuterium lost by heating at 150°C in air.

3. Discussion

Conventional belief says that excess power is increased when either the D/Pd ratio or the applied current are increased. Evidence for these conclusions is shown in Figs. 15 and 16. This study is in direct conflict with the conclusions based on the information in these figures. The conflict is proposed to result because the effect of temperature on excess power production was ignored during the previous studies. In general, applying different amounts of electrolytic current, which also changes the temperature, will change the D/Pd ratio. Consequently, these three variables are interrelated and must be separated in order to find the effect of each.

3.1. Effect of applied electrolytic current

McKubre et al. [25] were unique in attempting to keep the temperature of the electrolyte constant during their measurement of excess power production. Based on the design of the calorimeter they used, this goal would have been only partly successful. Consequently, the effect of applied electrolytic current measured by McKubre, as shown in
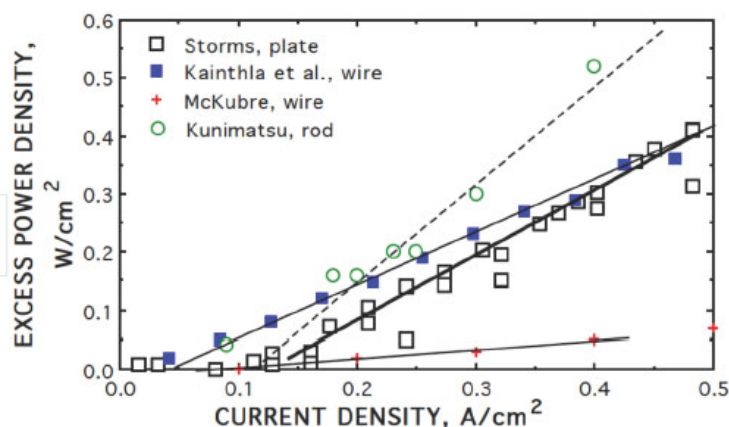
Figure 16. Comparison between several studies showing the apparent effect of applied electrolytic current on excess power production [26].
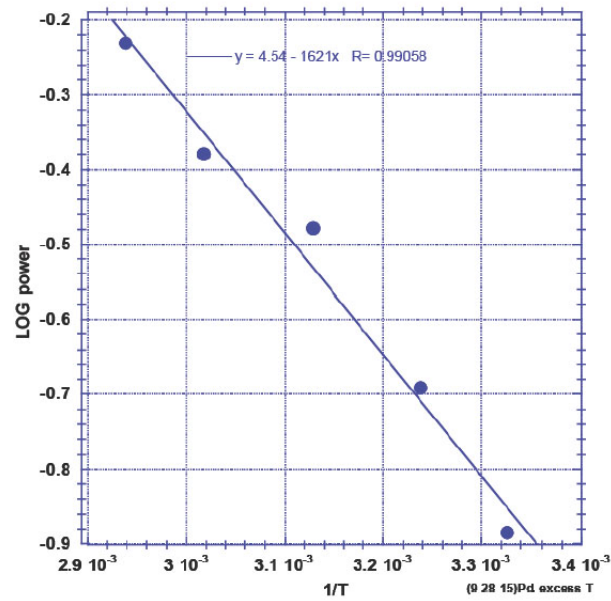
Figure 17. Effect of temperature when plotted as $1/T$ vs log watt and has a slope of 1621.

Fig. 16, is smaller compared to measurements made when the temperature is allowed to change during other studies,
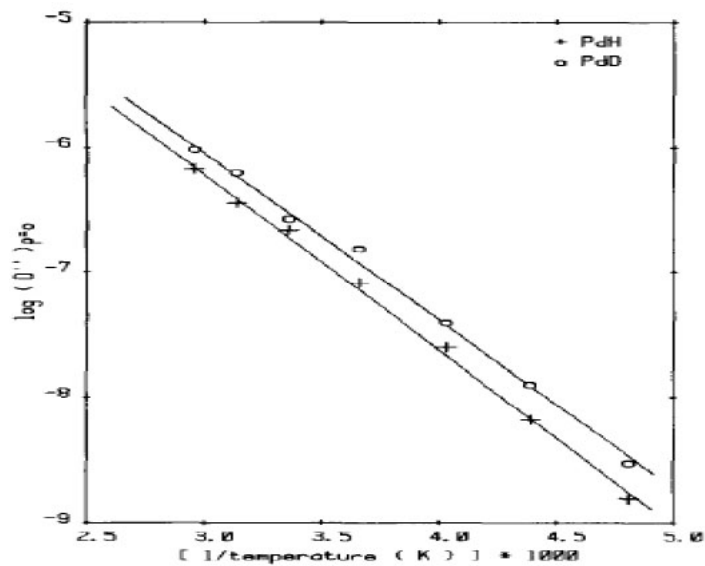
Figure 18. Effect of temperature on the Fick's diffusion constant for PdD and PdH [27]. The slope describing the diffusion of D in PdD is 1760.
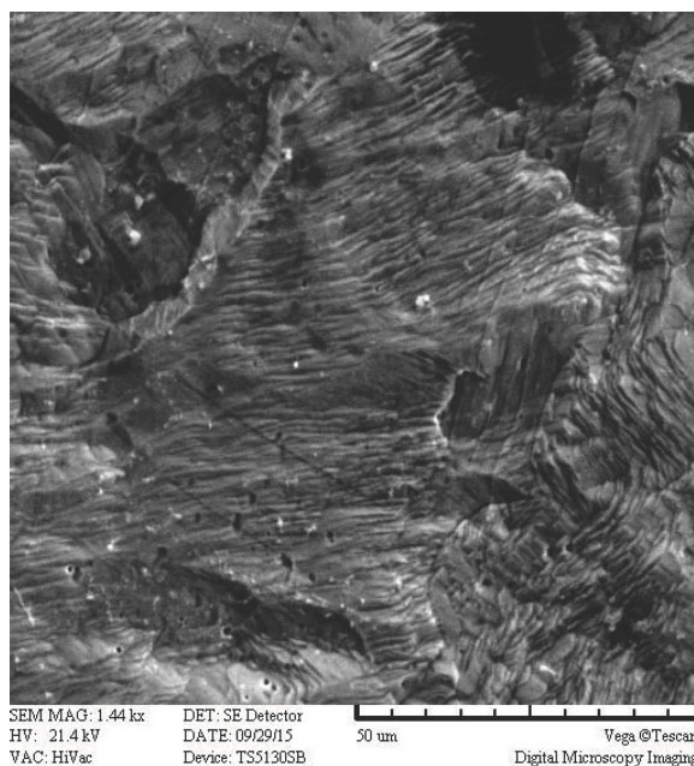
Figure 19.   Surface of the active material after excess energy was made.

as would be expected.

3.2.   Effect of temperature

The effect of temperature can be presented as an Arrhenius plot (Fig. 17) from which an activation energy of 1.8 kJ/mol can be obtained. The activation energy is very close to the activation energy of 1.9 kJ/mol based on the diffusion of D in the PdD lattice, as shown in Fig. 18. This amount of energy is much too small to directly affect a nuclear reaction. Consequently, the temperature is proposed to influence how fast D can diffuse in the PdD and reach the NAE where the nuclear fusion process takes place.

Diffusion would have a greater effect on power production than would the average composition when the concentration of energy-generating sites is relatively small and the distance over which D needs to diffuse from its source in the lattice is relatively large. These conditions are consistent with the observed non-uniform nature of the surface region where LENR apparently takes place.

3.3.   Effect of D/Pd ratio

When the temperature is isolated as a variable, excess power is independent of the D/Pd ratio and applied electrolytic current, being only sensitive to temperature. If the effect of temperature is taken into account, the threshold effect
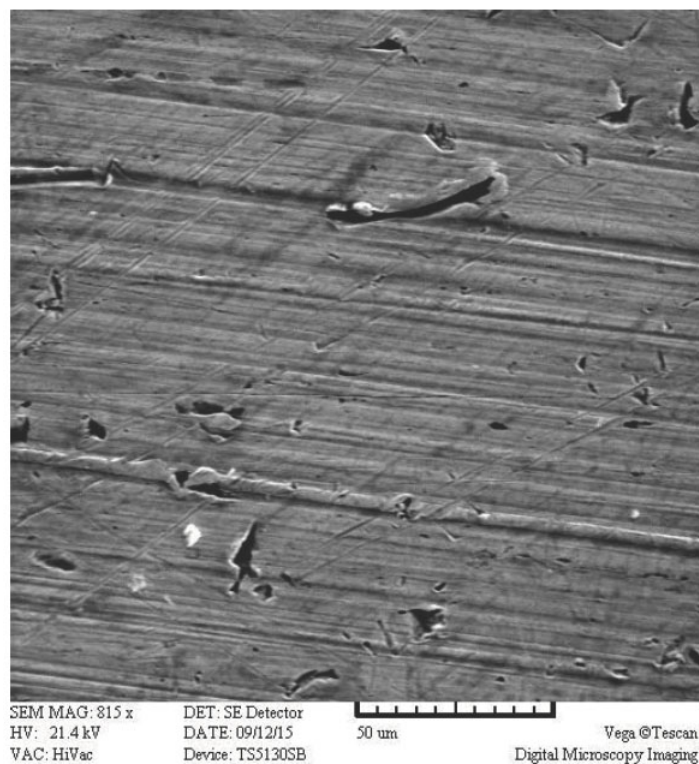
Figure 20.   Surface of sample before reacting with D_2.

proposed by McKubre et al. [28] (Fig. 15) does not appear to be present. Clearly, excess power can be produced when the D/Pd ratio is well below 0.88, in contrast to conclusions drawn from the McKubre data. The data obtained in this study show that once the unique conditions required to produce excess energy have been created, power production can be detected after the temperature is increased above a critical value (Fig. 11). This conclusion is consistent with the reports of excess power continuing after the electrolytic current was turned off and even increasing as the temperature increased enough to destroy the apparatus [1,29,30].

In view of the above conclusion, presence of vacancies formed at high deuterium content, as proposed by Haglestein and Chaughary [31], would appear not to be involved in the nuclear process. Apparently, a unique condition continues to support the nuclear process as the average D/Pd ratio changes even when the alpha phase forms in the bulk material. We can assume the deuterium concentration near the NAE is unaffected by the average concentration until nearly all the deuterium is removed. Once all deuterium is removed, excess power production stops and does not start again even after the sample has again reacted with D until an activation process is used.

3.4.   Effect of stress

Storms [16] proposes the nuclear-active sites are nano-cracks with a gap near 1 nm, which are created by stress relief. This idea is consistent with the role of volume expansion in influencing the ability to initiate the nuclear process. The potentially active material is proposed to form many very small cracks rather than a few large ones, as is common

behavior when a great deal of stress is applied to the surface by uneven expansion. Most important to the formation of a suitable gap is the morphology of the Pd before it reacts with deuterium. Without this critical morphology being present, no amount of later treatment is able to cause the LENR process. Based on the model of Storms combined with this and similar studies, the potentially active surface is one containing many weak regions having nearly identical strength. Since the initial stress was removed by annealing at 900°C without harming the ability to cause LENR, initial stress is not important. High concentrations of oxygen and carbon in the surface region are also not important.

Regardless of how the initial surface looks, the electrolytic process causes significant changes with few common features seen at the available magnification. The surface of the active sample Pd-#A is shown in Fig. 19 where layers of material have grown. The initial surface, shown in Fig. 20, shows no indication of being any different from normal inactive Pd at the available magnification. Many different variations in the surface condition have been reported to host LENR. A common feature is not obvious at the magnification used. Use of a greater magnification is suggested by this work.

3.5. Role of initial material

Two samples cut form the same piece of Pd were studied and both were found to have similar behavior with respect to excess volume and excess power. Other samples and alloys obtained from other sources produced no excess energy during this study. This experience is similar to the experience reported in the past when the entire batch of Pd containing the active sample is found to be nuclear active [32]. Apparently, the LENR effect is sensitive to conditions created in the material, which are replicated throughout the batch. These conditions then allow a special and unique structure to form in which the nuclear process can occur. The nature of this condition is not yet known although much effort has been devoted to the search by Violante et al. [33].

4. Conclusions

The applied electrolytic current and the resulting average D/Pd ratio have very little if any effect on the amount of excess power produced by a nuclear-active sample of PdD. The only variable of importance is temperature of the PdD. The temperature effect shows an activation energy similar to that involved in the diffusion of D in PdD. This behavior suggests the heat energy is generated in isolated regions, such as the proposed NAE, to which the deuterium fuel has to diffuse.

Electrolysis apparently produces significant deuterium concentration gradients in the material. In addition, reaction with D causes significant expansion, distortion in shape, and changes in surface morphology. Repeated partial loading and unloading are found necessary to initiate excess power production. This process, combined with the composition gradients and shape changes, would produce stress that is proposed to create the NAE.

A critical average D/Pd ratio does not appear to be required to initiate excess power production. Once initiated, excess power will continue at average compositions as low as D/Pd = 0.15.

In this study, as much as 27.5 kJ (1719 kJ/mol Pd) of excess energy was produced without any electrolytic power being applied and this energy production showed no sign of stopping for 1100 min. In other words, the sample produced a (power out)/(power in) ratio equal to infinity for an extended time.

If a sample is found to produce excess energy, most other samples in the batch of Pd will show the same ability, which suggests the critical features are present throughout the batch. The ability of Pd to become nuclear active is not affected by it being heated at 900°C in air for as long as 5 h or by removing about 1 μm from the surface using HNO_3. Apparently, the potentially nuclear-active region is a stable variation of the normal palladium structure located below the surface that needs to be modified in some way to become active.

Acknowledgement

References

[1] M. Fleischmann, S. Pons and M. Hawkins, Electrochemically induced nuclear fusion of deuterium, *J. Electroanal. Chem.* **261**, 301–308 and errata **263** (1989) 187–188.

[2] E. Storms, *The Science of Low Energy Nuclear Reaction,* World Scientific, Singapore, 2007, pp. 312.

[3] E. Storms, The status of cold fusion (2010), *Naturwissenschaften* **97** (2010) 861.

[4] A. Lomax, Replicable cold fusion experiment: heat/helium ratio, *Current Science* **108** (2015) 574–577.

[5] M. Srinivasan, Introduction to isotopic shifts and transmutations observed in LENR experiments, *Current Science* **108** (2015) 624–627.

[6] D. Nagel, Hot and cold fusion for energy generation, *J. Cond. Matter Nucl. Sci.* **4** (2011) 1–16.

[7] E. Storms, *The Explanation of Low Energy Nuclear Reaction,* Infinite Energy Press, Concord, NH, 2014, pp. 365 (updated e-version available at Amazon.com).

[8] V. Violante, E. Castagna, S. Lecci, F. Sarto, M. Sansovini, A. Torre, A. La Gatta, R. Duncan, G.K. Hubler, A. El Boher, O. Azizi, D. Pease, D.L. Knies and M.C.H. McKubre, Review of materials science for studying the Fleischmann and Pons effect, *Current Science* **108** (2015) 540–558.

[9] V. Violante, Material science for understanding the Fleischmann and Pons effect, Presented at the New advances on the Fleischmann–Pons Effect, European Parliment, Bruxelles, 2013.

[10] M. Miles and M.A. Imam, Palladium–boron alloys and methods making and using such alloys, United States, Patent #: 6764561, 2004.

[11] E. Storms, Introduction to the main experimental findings of the LENR field, *Current Science* **108** (2015) 535–539.

[12] E.K. Storms, My life with cold fusion as a reluctant mistress, *Infinite Energy* **4** (1999) 42.

[13] E. Storms and C. Talcott-Storms, The effect of hydriding on the physical structure of palladium and on the release of contained tritium, *Fusion Technol.* **20** (1991) 246.

[14] E. Storms, A study of those properties of palladium that influence excess energy production by the Pons–Fleischmann effect, *Infinite Energy* **2** (1996) 50.

[15] E. Storms, How the explanation of LENR can be made consistent with observed behaviour and natural laws, *Current Science* **108** (2015) 531–534.

[16] E. Storms, Explaining cold fusion, *J. Cond. Matter Nucl. Sci.* **15** (2015) 295–304.

[17] E. Storms, Some thoughts on the nature of the nuclear-active regions in palladium, in *Sixth Int. Conf. on Cold Fusion*, Progress in New Hydrogen Energy, M. Okamoto (Ed.), New Energy and Industrial Technology Development Organization, Tokyo Institute of Technology, Tokyo, Japan, Lake Toya, Hokkaido, Japan, 1996, vol. 1, p. 105.

[18] E. Storms, The nature of the energy-active state in Pd–D, *Infinite Energy* Issue Nos. 5,6 (1995) 77.

[19] R. Feenstra, R. Griessen and D.G. de Groot, Hydrogen induced lattice expansion and effective H–H interaction in single phase PdH, *J. Phys. F., Met. Phys.* **16** (1986) 1933.

[20] J.F. Lynch, J.D. Clewley and T.B. Flanagan, The formation of voids in palladium metal by the introduction and removal of interstital hydrogen, *Phil. Mag.* **28** (1973) 1415.

[21] W. Krause and L. Kahlenberg, On palladium–hydrogen, *Trans. Electrochem. Soc.* **68** (1935) 449.

[22] S. Pons and M. Fleischmann, Heat after death, in *Fourth Int. Conf. on Cold Fusion,* T.O. Passell (Ed.), Electric Power Research Institute, 3412 Hillview Ave., Palo Alto, CA 94304, Lahaina, Maui, 1993), Vol. 2, p. 8.

[23] T. Mizuno, *Nuclear Transmutation: The Reality of Cold Fusion*, Infinite Energy Press, Concord, NH, 1998, pp. 151.

[24] S.I. Smedley, S. Crouch-Baker, M.C.H. McKubre and F.L. Tanzella, The January 2, 1992, explosion in a deuterium/palladium electrolytic system at SRI International, in *Third Int. Conf. on Cold Fusion*, Frontiers of Cold Fusion, H. Ikegami (Ed.), Universal Academy Press, Tokyo, Japan, Nagoya, Japan, 1992, p. 139.

[25] M.C.H. McKubre, S. Crouch-Baker, A.M. Riley, S.I. Smedley and F.L. Tanzella, Excess power observations in electrochem-

ical studies of the D/Pd system; the influence of loading, in *Third Int. Conf. on Cold Fusion*, Frontiers of Cold Fusion, H. Ikegami (Ed.), Universal Academy Press, Tokyo, Japan, Held at: Nagoya Japan, 1992, p. 5.

[26] E. Storms, Some characteristics of heat production using the "cold fusion" effect, *Trans. Fusion Technol.* **26** (1994) 96.

[27] S. Majorowski and B. Baranowski, Diffusion coefficients of hydrogen and deiterium in highly concentrated palladium hydride and deuteride phases, *J. Phys. Chem. Solid.* **43** (1982) 1119.

[28] M.C.H. McKubre, S. Crouch-Baker, A.K. Hauser, S.I. Smedley, F.L. Tanzella, M.S. Williams and S.S. Wing, Concerning reproducibility of excess power production, in *5th Int. Conf. on Cold Fusion*, S. Pons (Ed.), IMRA Europe, Sophia Antipolis Cedex, France, Monte-Carlo, Monaco, 1995, p. 17.

[29] M. Fleischmann and S. Pons, Calorimetry of the Pd–D$_2$O system: From simplicity via complications to simplicity, in *Third Int. Conf. on Cold Fusion*, Frontiers of Cold Fusion, H. Ikegami (Ed.), Universal Academy Press, Tokyo, Japan, Nagoya Japan, 1992, p. 47.

[30] M. Fleischmann and S. Pons, Calorimetry of the Pd–D$_2$O system: from simplicity via complications to simplicity, *Phys. Lett. A* **176** (1993) 118.

[31] P.L. Hagelstein and I.U. Chaudhary, Phonon models for anomalies in condensed matter nuclear science, *Current Science* **108** (2015), 507–513.

[32] M.C. McKubre, F. Tanzella, I. Dardik, A. El Boher, T. Zilov, E. Greenspan, C. Sibilia and V. Violante, Replication of condensed matter heat production, in *ACS Symposium Series 998, Low-Energy Nuclear Reactions Sourcebook,* J. Marwan, S.B. Krivit (Eds.), American Chemical Society, Washington, DC, 2008, pp. 219.

[33] V. Violante, E. Castagna, S. Lecci, F. Sarto, M. Sansovini, T.D. Makris, A. Torre, D.L. Knies, D.A. Kidwell, K.S. Grabowski, D.D. Dominguez, G.K. Hubler, R. Duncan, A. El Boher, O. Azizi, M.C.H. McKubre and A. La Gatta, Excess of Power during Electrochemical Loading: Materials, Electrochemical Conditions and Techniques, *J. Cond. Matter Nucl. Sci.* **15** (2015) 44–54.

Research Article

How Basic Behavior of LENR can Guide
A Search for an Explanation

Edmund Storms*

LENRGY LLC, Santa Fe, NM 87501, USA

Abstract

The LENR effect was identified 27 years ago by Profs. Fleischmann and Pons as production of extra energy in a normal chemical structure, in this case PdD. Over a thousand published papers now support the discovery and the energy is shown to result from fusion of hydrogen isotopes without the need to apply energy and without energetic radiation being produced. By conventional standards, the claims are impossible. Nevertheless, a new phenomenon has been discovered requiring acceptance and understanding. The major behaviors and their present understanding are described in this paper and are used to suggest how an effective explanation might be constructed. Once again, science has been forced to either reject the obvious or accept the impossible. In this case, the normal skepticism needs to be ignored in order to determine if this promised energy source is real and can provide the ideal energy so critically needed.
© 2016 ISCMNS. All rights reserved. ISSN 2227-3123

1. Introduction

Low Energy Nuclear Reaction (LENR) or Cold Fusion was introduced to the world 27 years ago by Fleischmann and Pons [1], University of Utah, with expectation of great benefit to mankind. Instead, their claim for a new kind of fusion was quickly rejected [2], an attitude that continues even today. Over the years, several thousand papers addressed the subject with a large fraction supporting the claim [3]. Mastery of about 1000 papers is now required to understand the effect. A description of all the known behaviors and all proposed explanations would require much more than a single review paper. Here, the behaviors the author considers important are examined first and then used to form the major structure of the proposed explanation.

Limits will be set using this observed behavior in order to evaluate a few proposed explanations including the one described in this paper. The new kind of nuclear interaction needed to explain LENR is expected to fall within these limits. In other words, boundaries need to be identified to keep the imagination from running wild. These limits are also based on the assumption that the LENR effect is consistent with all rules normally applied to conventional chemical and

---

nuclear behavior. Nevertheless, a novel mechanism is clearly operating in addition to these well understood behaviors. In other words, LENR does not conflict with conventional understanding, but instead has revealed a new, overlooked phenomenon.

Many conditions needing consideration are not quantitative or lend themselves to mathematical analysis. While frustrating to conventional scientists, these unique behaviors must be made part of a successful explanation. Quantitative behaviors can be used to expand understanding once the basic process is understood.

An effective explanation needs to solve several difficult problems. The Coulomb barrier needs to be overcome without using more energy than is normally available in a chemical structure at room temperature. Neutron formation, which has been suggested by several theoreticians [4,5], is prohibited because the required energy of 0.78 MeV and the required neutrino cannot be expected to be available at the same site at the same time.[a] Once fusion has occurred, the mechanism must then dissipate the huge nuclear energy released by the process without producing local destruction of the chemical structure or energetic radiation. The mechanism must also account for various transmutation reactions known to occur. Failure to combine these events in a way that is consistent with known chemical and nuclear behavior dooms most efforts to explain the process. In contrast, a single mechanism is proposed in this paper to cause all observed behavior while being consistent with known chemical and nuclear behavior.

This paper has two parts, with the first describing the important observations on which an explanation must be based. The second part uses a few assumptions combined with these chosen behaviors to provide an explanation about how LENR can be initiated using a proposed mechanism. This mechanism is clearly much different from that causing the conventional hot fusion process. Ironically, this conflict is used to reject the claims for LENR rather than guiding a search for the cause of the difference. Consequently, this difference must be clearly understood before the novel features of LENR can be explored.

Unlike hot fusion, LENR takes place in and requires a chemical structure to operate. The role of this structure must be understood before physics is applied to understanding subsequent nuclear process. Clearly, a unique and rare condition must form in the structure in which a nuclear process can function. The nature of this condition is discussed following the discussion of hot fusion.

1.1. The nature of the hot fusion mechanism

The hot fusion mechanism uses high energy applied to plasma to overcome the Coulomb barrier by brute force. The resulting energy is dissipated as kinetic energy of the nuclear products, which are ^{3}He, tritium, proton, and neutron in equal amounts when deuterium is fused. This large applied energy changes the fusion rate in plasma as shown by the log-log plot in Fig. 1. The hot fusion rate is essentially zero at room temperature while the cold fusion rate can exceed 10^{12} events/s under conditions when no more than 1 eV of energy is available.

Hot fusion can also be initiated by bombarding a material by energetic deuterons. In this case, the fusion rate is slightly greater at low applied energy compared to when the same energy is applied to plasma, as can be seen in Fig. 2. Nevertheless, the fusion rate decreases as applied energy is reduced. In other words, the effective shielding of the Coulomb barrier does not increase as applied energy is reduced, even when the hot-fusion reaction takes place in a material.

Apparently the electron charge in a material can slightly lower the Coulomb barrier at the random encounters between the deuterium in the lattice and the bombarding deuteron when the applied energy is sufficiently low. While the electrons clearly help lower the barrier to achieve hot fusion, this effect alone would seem too small to explain

---

[a] A neutrino needs to be supplied because neither an electron nor a proton contains a neutrino. Consequently, this particle needs to be supplied at the time of the reaction so that when the neutron decays later by emitting an electron and neutrino (or antineutrino), the required neutrino would be available.
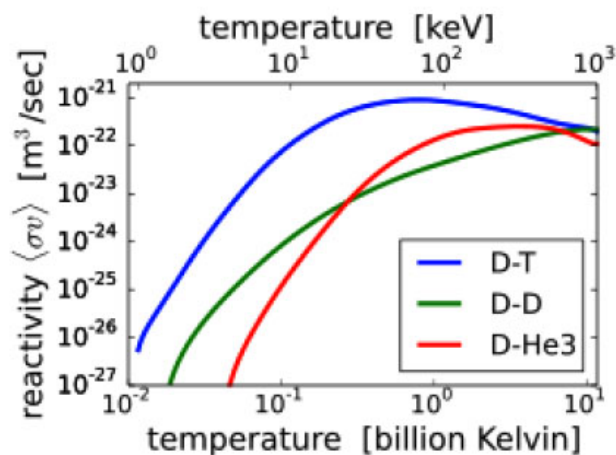
Figure 1. Effect of energy on the fusion rate in plasma for different combinations of hydrogen isotopes as result of the hot fusion process (Wikipedia).

the LENR process, although it might make a small contribution. In any case, the measured shielding effect applies only to the hot fusion mechanism. Perhaps more effective shielding during LENR might be expected if the shielding electrons were contained in a unique nuclear-active environment rather than having a random and low concentration in
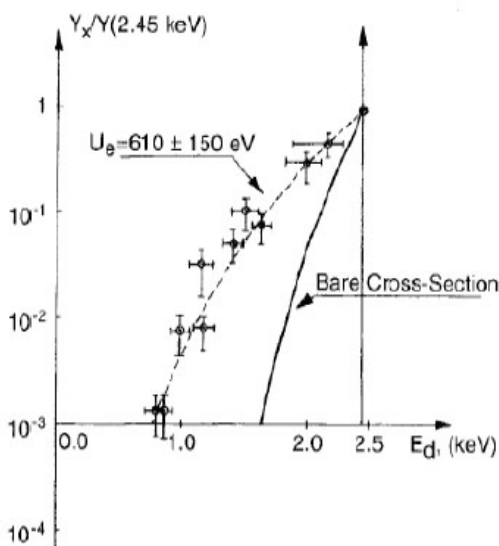
Figure 2. Comparison between the fusion rate in plasma (Bare Cross-Section) and when fusion occurs in a solid material as the result of applying energy to the bombarding D^+ ions, as shown by the X-axis. A value of unity occurs when the rate in plasma is equal to the rate using a target material [6].

the general structure where hot fusion interaction takes place. Consequently, LENR cannot be viewed as an extension of hot fusion. Instead, the process requires it own unique condition in the lattice in which a process operates that can lower the barrier without requiring extra energy.

Once the nuclei of deuterium have fused by hot fusion, the assembly breaks into fragments, which dissipate the excess mass–energy as kinetic energy. Easily detected energetic neutrons, tritium, protons, and He^3 are produced in equal amounts. This process is understood and is consistent with conventional expectations. A similar result occurs when muons are used to bring the nuclei close enough to cause fusion. In other words, no matter whether energy is used to overcome the Coulomb barrier by brute force or the separation is reduced by using the heavy muon [7–10], the same energy dissipation process results. No other method for energy dissipation as result of a fusion reaction was known to occur in nature until "cold fusion" was discovered. Clearly, the mechanisms causing hot fusion and cold fusion are significantly different because LENR does not lead to fragmentation of the nuclear products and the resulting energetic radiation.

This difference has caused much skepticism about the reality of LENR. After all, experience and teaching deny any possibility of spontaneous fusion taking place in an ordinary chemical structure without the need to apply significant energy. This apparent contradiction is resolved by proposing the cold fusion process takes place in a unique structure, called the nuclear-active-environment (NAE) where a novel mechanism might operate without conflicting with the laws that apply to the general structure. Questions about how this structure forms, where in the chemical structure this formation takes place, the nature of the unique conditions at the NAE, and the nuclear mechanism operating therein are explored later in this paper. But first, the nature of the general chemical structure is examined.

1.2. Role of chemical structure

General concepts will be explored first followed in later sections by detailed evaluation.

Because the LENR process takes place within a chemical structure, it must play by the rules such a structure imposes. This conclusion is critical to understanding the LENR process. These rules include the laws of thermodynamics and the phase rule. Local energy cannot spontaneously increase without violating the second law of thermodynamics and the local concentration of ambient energy is limited by how much energy the chemical bonds can tolerate before melting or decomposition results. Simply stated, energy cannot go up hill and its density cannot exceed the strength of the container. While these rules can be violated by random events at the quantum level, a process such as cold fusion that occurs at rates in excess of 10^{12} times/s must be consistent with the overall average behavior to which the laws apply.

If a novel mechanism is proposed to concentrate energy in order to cause nuclear fusion, why it is not found to affect chemical reactions? After all, if such a process were possible, it would be expected to operate in normal chemicals and cause chemical effects before the local energy had increased enough to cause a nuclear reaction. For example, the mechanism of energy transfer to electrons proposed by Widom and Larsen [11,12] would be expected to make many normal chemical compounds unstable. Furthermore, how such a proposed violation of the second law of thermodynamics can function in PdD needs to be justified. Similar conflicts with the laws of thermodynamics and normal chemical behavior create a similar weakness in many explanations now being proposed.

Normally, nuclear reactions of any kind are not affected by the chemical environment because the energy states are too different and local energy density cannot be increased according to the second law of thermodynamics. Apparently, the Coulomb barrier needs to be overcome by a process that does not require significant energy. This realization directs attention to the role of electron charge at the site of the fusion process. Nevertheless, the extra electron charge has to be consistent with limitations imposed by the local chemical conditions at the site.

Once fusion occurs, the structure must convert the excess mass–energy to heat without causing local melting. After all, local destruction of the active site would stop further heat production and severely limit the amount of energy

produced by LENR, which is not experienced. Once started, heat production is normally sustained for significant time. Although local melting is occasionally seen, it is not sufficient to limit the amount of power or its stability over time. Thus, the generated energy has to be dissipated well away from the fusion event and into the surrounding atomic structure as low-level heat energy. This requirement limits the form this energy release process takes and the energy of the emitted radiation.

Several different chemical structures have been found to support LENR, with PdD given the most attention. Consequently, PdD is the focus of further discussion.

1.3. The Nature of PdD

Palladium deuteride has attracted interest for about the last 100 years [13] during which time it has been studied extensively. Although the beta phase can acquire hydrogen up to about β-PdD$_{0.98\pm0.02}$, nothing about its overall behavior would suggest an ability to host a fusion reaction. The structure is face-centered-cubic (fcc) and exists in two slightly different forms having the same crystal structure based on the Pd sublattice. The alpha phase occurs between pure Pd and about PdD$_{0.05}$, and the beta phase forms near PdD$_{0.6}$ when 1 atm of D$_2$ pressure is applied at 20°C. A two-phase region exists between these two compositions. The beta phase continues to acquire D atoms at random sites in the fcc sublattice as pressure is increased, finally reaching the upper limit of the fcc phase. Figure 3 shows the structure when all lattice sites are fully filled by deuterium. Another phase is expected to form and grow in amount as the overall D/Pd ratio increases beyond the upper limit to the beta phase, similar to the behavior of other metallic hydrides [14,15]. In other words, any composition in excess of PdD$_{0.98}$ would be expected to be a two-phase mixture of the fcc and another phase having a different structure and increased stoichiometry. In the absence of the rare double occupancy [16,17] of normal lattice sites, the deuterium nuclei are too far apart to fuse. Achieving close approach without violating the rules of chemistry and without producing the fragmentation typical of hot fusion once fusion occurs remains a serious challenge.

Identifying where the NAE is located and what form it takes in the material has created a problem for many proposed explanations. Many explanations assume the fusion process takes place in a modification of the fcc structure when the D/Pd ratio is large. Formation of such a structure can be identified in the PdD structure because its formation would cause changes in its various properties. A search for the expected change can be made by examining several known properties, such as resistivity and lattice parameter as a function of D/Pd. The lattice parameter can be seen to have a linear [18–21] relationship to composition with no indication of a two-phase region forming within the limits of the beta phase. Both the pressure and resistivity [22] also show no sign of a change in crystal structure [23] over the composition range of interest. In every way, all properties are consistent with a normal fcc structure being present within the composition range in which LENR is found to occur.

On the other hand, Fukai [24] reported formation of a new phase when high pressure is applied at high temperature to PdH. This structure is proposed to also form under normal conditions during electrodeposition [25]. A similar structure change is proposed to be caused by deformation induced vacancies [26]. Such structures might also occur when repeated loading and unloading of PdD causes the structure to expand, producing what Storms [27] calls excess volume. Nevertheless, this condition does not explain LENR because the presence of excess volume over about 2% is found to inhibit LENR [28] rather than aid the reaction as would be expected if formation of metal atom vacancies were required to support LENR. In addition, no evidence for the Fukai phase forming when LENR is detected has been reported.

When a piece of Pd is found to be nuclear active, most of the entire batch is also found to be nuclear active. In addition, once the sample is made nuclear active, the LENR process using that piece becomes reproducible and robust. Obviously, the initial treatment of the entire batch creates stable conditions in which the LENR process can be initiated and then supported for extended times. Unfortunately, these conditions are seldom produced because their unique
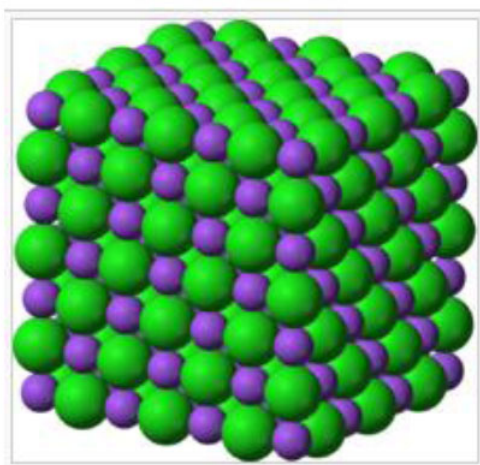
Figure 3.   Crystal structure of the fcc PdD when all deuterium sites (*small purple*) are filled (Wikipedia).

characteristic is unknown and rarely formed by chance. Even when these required initial conditions are present, an additional special treatment is required before the nuclear process will start. These observations are important because they show that a treatment is possible to make large amounts of palladium nuclear active. A suggested combination of conditions is described later in this paper.

Initially, the LENR reaction was thought to take place anywhere in the PdD structure. Later studies reveal both helium [29,30] and tritium [31] form only very near the surface and not within the bulk material or on the surface where nanoparticles might be present. Transmutation products are also detected mainly in the surface region. Based on the known behavior of helium in PdH [32,33], the nuclear reactions apparently take place within a region perhaps no more than 10 μm wide, extending from the surface into the bulk. We now need to discover the nature of the unique condition forming within this narrow band. The condition does not appear to involve a phase change, creation of vacancies in the hydride structure, creation of nanoparticles on the surface, nor does it require a high concentration of deuterium. Formation of the NAE would appear to require a unique condition present only within the surface region, which further limits the proposed nature of the NAE.

2. Important Observed Behavior

2.1. Formation of the NAE

In order for fusion to take place, the reacting nuclei must obviously be in the same place at the same time and with a critical distance between the nuclei. Normally, the D atoms are located at too great a distance to fuse. For the atoms to assemble with less distance between them, Gibbs energy must be released while the material achieves a different stable state. Generally, the atoms in a chemical structure are already close to their equilibrium condition and do not contain excess energy or have the ability to form another crystal structure unless the conditions are significantly changed. Simply increasing the D/Pd ratio does not create sufficient energy to change the structure in order to initiate the LENR process. Furthermore, for the process to be as rare and as difficult to initiate as is observed, the conditions for releasing this energy must be equally rare and difficult to create. To make the problem even more challenging, once the NAE is formed, LENR must operate at a significant rate without a further change in conditions. These conditions immediately place an important limit on any proposed condition in which LENR can take place.

Most samples of PdD do not host the LENR process regardless of the deuterium content presumably because the unique NAE is not initially present in the material. This conclusion suggests the NAE is not related to any of the features normally found in a chemical structure, such as vacancies, dislocations, and occupancy of unusual lattice sites. After all, if the NAE were related to these common features, the effect would be initiated more easily and more often. Multiple occupancy of the normal deuterium-atom vacancy must also be rejected based on this conclusion because, if such occupancy were possible, it would be present in all material under normal conditions and cause LENR with greater frequency. Nevertheless, a rare condition must form as result of some kind of treatment in order to account for occasional success. Failure to initiate LENR simply means this treatment was not successful in producing the required NAE. Once produced, the NAE appears to be stable and relatively constant in amount as indicated by production of relatively constant power.

Experience reveals another important behavior. When part of a batch of palladium can be made nuclear active, the remainder of the batch is found to be active. This activation treatment does not simply involve reaction with D but also requires extended electrolysis and/or repeated deloading and loading with D. This behavior is important because it reveals that the NAE can be created throughout an entire batch of Pd as result of a common treatment. In other words, the physical treatment of the palladium metal before reacting with deuterium affects later initiation of LENR.

Once the nuclei are assembled in the NAE, a unique process must reduce the Coulomb barrier, perhaps by a tunneling mechanism without using energy beyond that which is normally available at room temperature. Immediately, we are confronted by a problem. Normal chemical structures are known not to support nuclear reactions without significant energy being applied to bombarding ions. After all, the Coulomb barrier keeps nuclei separated and allows chemical structures to form in the first place by interaction between the electrons. The energy required to force the nuclei close enough to fuse is well in excess of the energy holding the atoms in the structure and in excess of the electron energy. This well-known and accepted behavior suggests a need to form a novel arrangement between the nuclei in the NAE designed to avoid this limitation.

In summary, two separate processes have to be considered. The first is creation of the NAE. The second is formation of a structure of H and/or D within the NAE having the ability to fuse. This nuclear process is separate from the structure of the NAE, but needs to be consistent with it. A description of the fusion process is a job for physics while identification of the NAE is a job for chemistry. Thus, we are forced to acknowledge an uncomfortable marriage between two normally independent branches of science, with chemistry being applied first to identify the NAE.

2.2. Nature of the NAE

Two different kinds of NAE have been suggested. Many researchers place the LENR process in the normal crystal structure where vacancies or dislocations might be present. Other people identify the NAE as being nanoparticles or other active sites located on the surface of the structure. These structures and flaws are normal variations in a material that for some reason becomes nuclear active.

In contrast, Storms [34] places the NAE in cracks having a critically small gap, which are separate from and chemically independent of the crystal structure. Such an environment can have properties much different from a crystal structure, including a high negative charge. Resolving this fundamental difference in proposed location of the NAE is critical to understanding the LENR process because the chosen location sets the logic on a particular path. A choice of the wrong path will result in arriving at the wrong understanding.

In order to contrast these two proposed conditions, the well documented suggestion by Hagelstein et al. [35] is explored. Hagelstein's idea is based on formation of a new phase in the normal fcc structure, such as suggested by Fukai and Okuma [36]. This phase is proposed to form on occasion after the deuterium content has exceeded D/Pd = 0.95 in a co-deposited material, thereby causing formation of palladium atom vacancies. Deuterium atoms fill the vacant sites and form a structure in which fusion is proposed to occur. The resulting mass–energy is dissipated by

phonons. Evidence for this proposed phase change can be obtained by searching for a discontinuity in the various physical or chemical properties. As noted above, such a search reveals no evidence for a phase change within the composition range of the beta phase. In addition, X-ray and neutron diffraction studies of the fcc structure reveal no phase change in this composition range. No evidence supports a co-deposited structure being present on the surface and helium release is not consistent with its source being so near the surface.

The NAE is apparently a feature outside of the thermodynamic behavior and its presence does not affect the measured physical properties. This conclusion is important to correctly identify the NAE.

The author, in several previous papers [37–39], identifies the NAE as residing in nano-cracks resulting from stress relief. As is required, these gaps exist outside of the chemical properties and are not influenced by limitations imposed by the chemical structure. As long as a gap having a critically small width is created, deuterons are proposed to enter the gap and to form a structure. This structure then experiences fusion by a novel mechanism. The required gap width is rarely created because most cracks would quickly become too wide to host the required hydrogen structure. Consequently, success in creating the NAE involves applying modest stress to a structure containing many weak regions having a similar ability to form small cracks. This condition might be created by accident as result of various intended and accidental treatments, thus accounting for occasional success that might even be attributed to other effects.

Although large cracks are often seen when LENR occurs, the cracks having the ability to act as the NAE are too small to be easily detected and can be overlooked. In fact, unless these structures are sought using high magnification, they would be impossible to detect. Experience shows the critical initial condition can also be created in an entire batch of material by a yet to be identified pretreatment. This realization encourages search for such a treatment.

Deciding which explanation should be explored is important because they each propose entirely different treatments to cause the LENR process. The wrong choice of explanation can lead a researcher down the wrong path with much wasted effort.

2.3. Power production

The LENR effect was first identified by its ability to produce energy in amounts greater than would be possible by any chemical reaction. The first reported success resulted when Pd was used as the cathode in an electrolytic cell containing an electrolyte consisting of D_2O + LiOD. When a Pd cathode is initially subjected to this treatment, the deuterium concentration in the Pd increases while energy is absorbed by the reaction, as shown in Fig. 4. Energy is absorbed because the energy used to decompose the D_2O into D_2 and O_2 is greater than is recovered when the resulting D_2 reacts with Pd, thereby causing an overall endothermic reaction.

The enthalpy of formation for deuterium can be calculated using the data in Fig. 4. For this purpose, the total amount of D reacted every six minutes is divided by the amount of energy absorbed during this time, from which the amount of energy used to decompose the D_2O is subtracted. As can be seen in Fig. 5, the electrolytic method applied to a solid piece of Pd gives values for the partial enthalpy of formation similar to the values obtained when D_2 is reacted directly with Pd nano-powder. Both reactions show that chemical energy is released when Pd reacts with D_2 and the amount decreases as the D/Pd ratio increases.

The equilibrium deuterium activity, presented as pressure, is also plotted to show the large range in values being applied to the material by the electrolytic process. The deviation from ideal behavior, called fugacity, is not taken into account.

Additional treatment was later required to start the LENR process. No additional phase forms in this composition range, such as proposed by Fukai, as indicated by the smooth unbroken variation of ΔH and pressure. Also, the smooth unbroken change in resistivity observed by McKubre et al. [22] while LENR took place is also consistent with this conclusion.

In summary, no evidence supports the claim for the NAE to result from a phase change or vacancy formation within
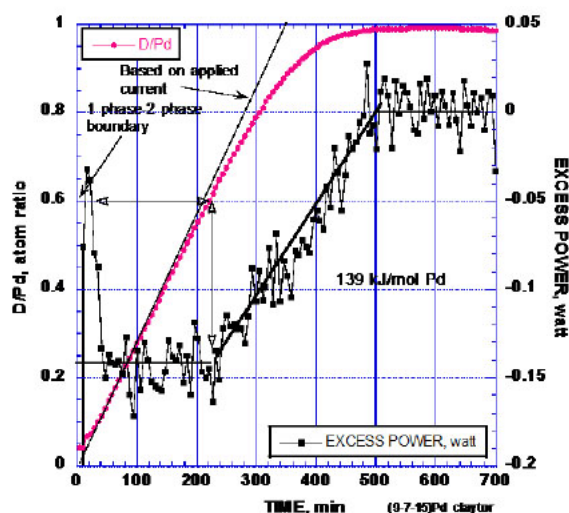
Figure 4. The D/Pd ratio and resulting power when Pd is reacted with D_2O using the electrolytic method. All D made available by the applied current initially reacts with the Pd. The amount reacted is reduced only gradually as the upper limit is reached. No excess energy is produced even after the average D/Pd ratio becomes very large. The total amount of energy/mole Pd absorbed by the process is noted. (Storms, www.LENRexplained.com).

the composition range in which excess energy production is found to occur.

The effect of temperature on power production for various D/Pd ratios is compared in Fig. 6. Samples having D/Pd = 0.80 and 0.48 produce the same amount of power at the same temperature. Removal of all deuterium stops power production. Clearly, power is not as sensitive to the deuterium content as previous studies suggest [42]. Nevertheless, some D is required for LENR to function.

The Arrhenius plot (Fig. 7), using the data in Fig. 6 (D/Pd = 0.8), shows the activation energy for the LENR process to be nearly equal to the value for diffusion of D in PdD. In other words, the rate of the fusion process is sensitive to the rate at which D can get to the site where fusion takes place and it is not sensitive to the concentration of D in the surrounding lattice. The fusion process can be proposed to rapidly convert deuterium in the NAE to fusion products, after which new D has to move relatively slowly from the surrounding lattice in order to supply additional fuel to the active sites. The rate of energy production is determined by the rate at which D can get to the NAE, not by the rate of the fusion event itself. A buildup of helium around the NAE could slow the reaction, as suggested by Hagelstein, if the diffusion rate of D+ were reduced by helium occupying sites the D+ needed for diffusion to occur. By analogy, this is similar to the speed of a car being determined by how fast gas is delivered to the engine and not related to the amount of gas in the tank or the reaction rate within each cylinder.

The resulting equation allows the power to be predicted when temperature is increased. Clearly, simply increasing temperature can produce significant power. Removing an active sample from the electrolytic cell and exposing it to D_2 gas at increased temperature would be expected to result in significantly more power than can be achieved within the 100°C limit imposed by the electrolytic cell.

2.4. Probability of forming the NAE

Figure 8 compares power produced by 157 studies reported before 2007. Notice that most studies produce power at relative low levels. On a few occasions, a large amount of power is observed with the number of reports rapidly
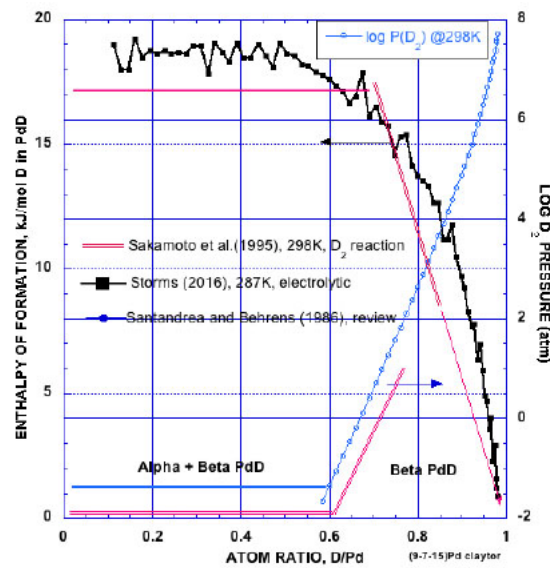
Figure 5. Enthalpy of formation calculated using the data shown in Fig. 4 based on the amount of D reacted every 6 min, the amount of power measured during this time, and the amount of energy used to decompose the D_2O from which the D results. The reaction of D_2 with Pd is exothermic. The Sakamoto et al. [40 line is obtained using their reported linear equation, which is then extrapolated from D/Pd = 0.85 to 0.98, and their reported D_2 pressure. The pressure of D_2 is also obtained from the review by Santandrea and Behrens [41] (Storms, www.LENRexplained.com).

decreasing as the reported power increases. Although various size samples are used, the behavior does not seem to be related to area or volume. The concentration of the NAE seems to be the important variable, which is uniquely determined by the nature of the Pd and its treatment.

The number of reports, shown in Fig. 8 can be compared to predicted behavior based on an assumed probability of causing increased power once power production is possible. In other words, the probability of forming additional NAE once the conditions allow some NAE to form can be estimated and compared to the behavior to see if the assumption of random formation fits.

If the average power is assumed to be related only to the concentration of NAE, if 300 attempts are made to initiate LENR and the probability of producing 10 W is 0.3, the probability of producing 20 W would be 0.3×0.3, and the probability of producing 30 W would be $0.3 \times 0.3 \times 0.3$, etc. The dashed line shows the number of predicted successful observations at each power level. The relatively good fit to the observed behavior suggests the power is caused by an increasing number of active sites whose creation is caused by a random process, with more power resulting as the number of NAE sites is increased by a process having low probability. The probability of producing any power at all would be expected to be much less than production of additional power once conditions allow some NAE to form. The data do not allow determination of the probability to form the initial NAE.

2.5. Helium production

Helium formation is the main source of power produced by LENR when deuterium is used and provides much information about the nature of the nuclear process. Sixteen measurements of the helium/energy ratio have been published. These values are compared as a histogram and plotted using log He/energy in Fig. 9. D + D fusion is proposed as the source because no other nuclear reaction forming helium releases the amount of energy required to be consistent with
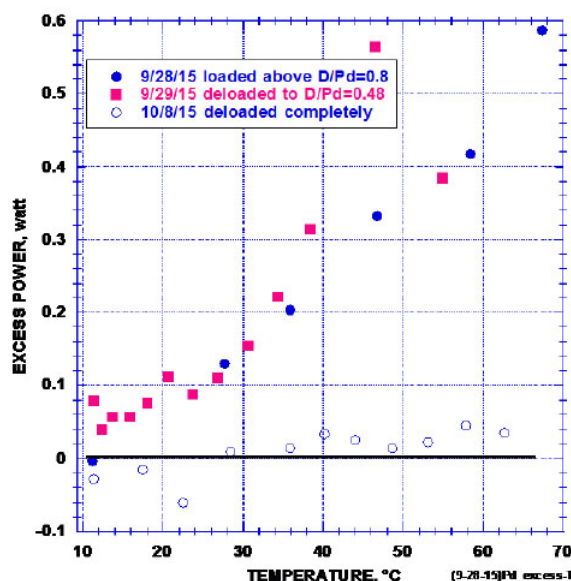
Figure 6. Effect of temperature on power production when three different amounts of deuterium are present in the sample (Storms, www.LENRexplained.com).

the measurements. Nevertheless, two reactions occurring at the same time with always the same ratio of energy and helium might account for the value. If so, one might wonder how such a combination of independent reactions just happened to give a consistent ratio nearly equal to the value produced by the D + D fusion reaction.

For the helium to be detected in the gas produced by electrolysis, the source must be very near the surface. Otherwise, the helium would be retained by the PdD [32,33, 44–46]. The amount of retained He has not been determined. Nevertheless, when efforts are made to coax helium out of the metal, the total amount of helium is found to be very near the amount expected to result from the D+D fusion reaction [47,48].

2.6. Tritium production

Tritium is occasionally detected when LENR is initiated by either the electrolytic or gas discharge method. Formation of this radioactive isotope of hydrogen once again demonstrates the occurrence of a very unusual nuclear process. On some occasions, the neutron flux produced by the process is also measured, which is shown as the tritium/neutron (T/n) ratio in Fig. 10. The ratio frequently reported near 10^6 suggests tritium and neutron production are correlated in a general way. As an example of possible correlation, Storms [34] suggests the neutrons result from D+e+T fusion, a reaction that would increase as the concentration of tritium increased in the material, thereby creating an apparent correlation between tritium and neutron formation. The energy of the resulting neutrons would be predicted to be less that those known to result from D+T fusion by the hot-fusion mechanism.

In contrast, the conventional hot fusion reaction produces a T/n ratio of 1, or zero when plotted as the log. Clearly, the ratio resulting from the LENR process does result from the hot fusion-type reaction.

The detected tritium has been shown to result from a nuclear process occurring very near the surface of the cathode when the electrolytic cell is used [31]. The rate of tritium production is also sensitive to the H/D ratio in the material [49] and Claytor (private communication) and to the nature of the material in which production takes place. Apparently,
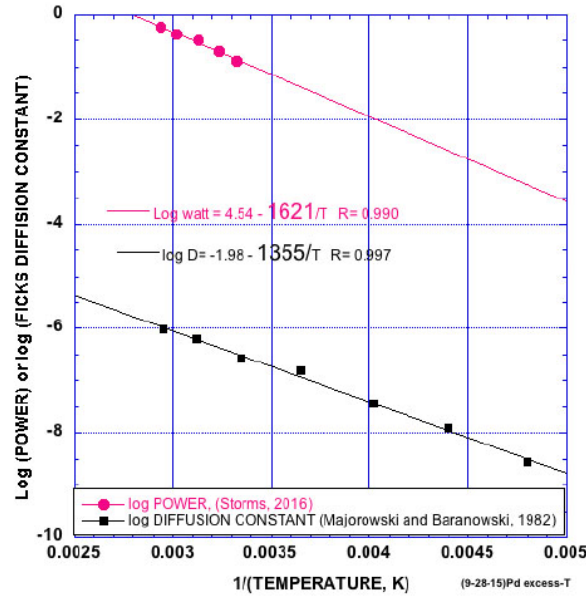
Figure 7. Comparison between the rate of diffusion of D in PdD and production of LENR power as a function of $1/T$. The similar slopes created by the data suggest both processes are affected by the same mechanism, i.e. diffusion of D though PdD [43].

production of He and tritium occur at the same location in the active material and both reactions appear to involve isotopes of hydrogen.

2.7. Transmutation production

Transmutation in the context of this paper is a process during which light nuclei, frequently isotopes of hydrogen, enter the nucleus of a much heavier atom, thereby producing energy and one or more nuclear products. Two kinds of transmutation are observed. The first is found to add various numbers of ^{4}He to the target without fragmentation of final nucleus and the second to result in fragmentation of the target after addition of some protium.

Iwamura et al. [50–52], working at Mitsubishi Heavy Industries Ltd in Japan, have studied the first type of transmutation by allowing D_2 to diffuse through a sandwich consisting of alternate layers of Pd and CaO, with the presence of CaO being important to success. The transmutation reactions occur on the surface of palladium where target nuclei have been deposited before D_2 is applied. Using X-ray florescence to determine the amount of material, they followed the loss of target material from the surface along with increase in the nuclear product. Examples of the various transmutation reactions are listed in Eqs. (1)–(7).

A successful explanation must show how the considerable Coulomb barrier is overcome, how excess energy resulting from the reaction is dissipated, why transmutation of Pd is not observed, and how more than one helium nucleus can be added to the target at the same time. The explanation must also show why the CaO layer can have an effect on a nuclear reaction occurring on the surface when it is separated from the surface by 40 nm of Pd. Equations (1)–(7) show the summary of the transmutation reactions reported by Iwamura et al. [50].

$$^{133}_{55}\text{Cs} \xrightarrow{4\text{d}(2\alpha)} {}^{141}_{59}\text{Pr}, \tag{1}$$

$$\ce{^{88}_{38}Sr ->[4d(2\alpha)] ^{96}_{42}Mo,} \tag{2}$$

$$\ce{^{138}_{56}Ba ->[6d(3\alpha)] ^{150}_{62}Sm,} \tag{3}$$

$$\ce{^{137}_{56}Ba ->[6d(3\alpha)] ^{149}_{62}Sm,} \tag{4}$$

$$\ce{^{44}_{20}Ca ->[2d(\alpha)] ^{48}_{22}Ti,} \tag{5}$$

$$\ce{^{184}_{74}W ->[2d(\alpha)] ^{188}_{76}Os,} \tag{6}$$

$$\ce{^{182}_{74}W ->[4d(2\alpha)] ^{190}_{78}Pt.} \tag{7}$$

Miley and Patterson [53], Miley [54] as well as Srinivasan [55] report finding fragmentation products resulting from transmutation of palladium when palladium is used as the cathode in an electrolytic cell containing D_2O and/or H_2O. As can be seen in Fig 11, the Pd cathode apparently fragments into two parts in addition to experiencing addition of ^{4}He to the target nucleus. The platinum impurity on the cathode surface also shows evidence for similar transmutation
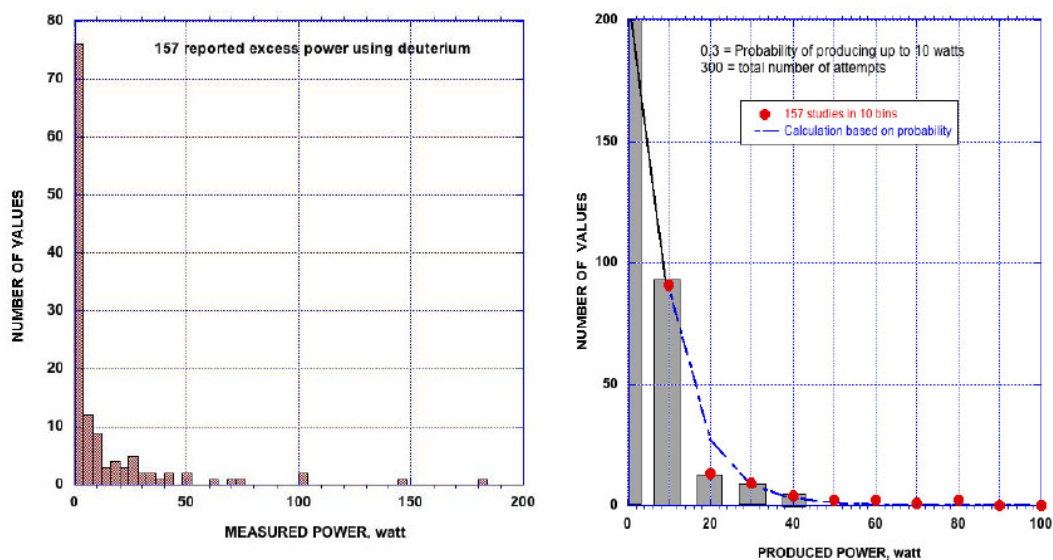
Figure 8. Histogram of power production vs. the number of reported values. A probability function, shown as the dashed line, is used to fit the data to bins at 10 W intervals.
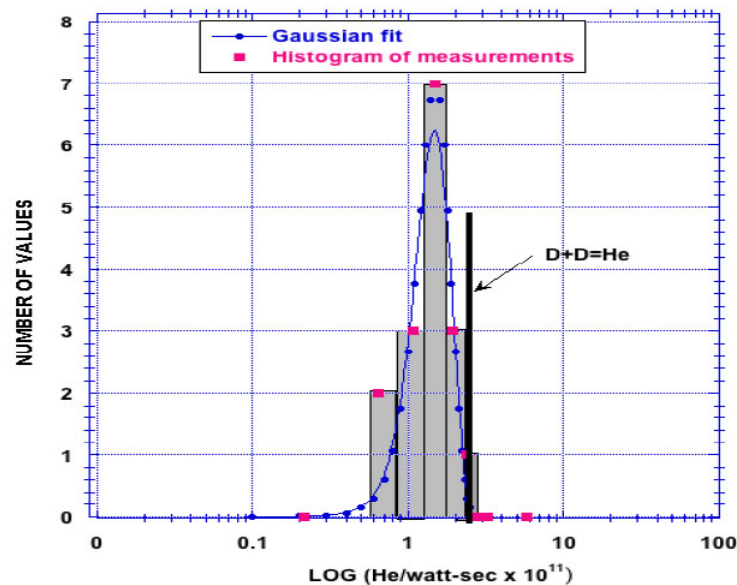
Figure 9. Histogram of reported values as a function of the log He/energy ratio as listed by Storms [30]. Many results showing no power along with no helium would fall at zero on this plot. The expected ratio produced by the D+D = He fusion reaction is shown by the vertical line. A Gaussian error function is fit to the values, which gives a center value of 1.5×10^{11} He/J with uncertainty of $\pm 0.9 \times 10^{11}$ He/J.

reactions. Once again, how the large Coulomb barrier can be overcome must be explained. In this case, explaining the dissipation of energy is not a problem because it is carried by the fragments, as is expected.

2.8. Radiation production

Production of energetic radiation is a necessary result of nuclear reactions as the resulting energy is dissipated into the surrounding material. Each type of radiation responds differently to its passage through material. Photons, also called gamma rays when they are emitted by a nucleus, are reduced in number but their energy does not change as they pass through matter. Particles, such as electrons (beta rays), ^{4}He (alpha particles), neutrons, and hydrogen nuclei all change energy as they pass though matter. In the process, their energy is converted to heat while most of the particles are quickly stopped by the material. If the energy is large, secondary radiation may be produced as the particles interact with electrons in the absorber [56–59]. Evidence for each type of radiation has been reported to result from LENR. The flux ranges from being trivial to being significant, but never sufficient to account for the energy being produced at the time. Clearly, the methods of energy dissipation are complex and handicapped by being largely hidden by being absorbed in the material surrounding the process.

In any case, the amount of radiation exposure experienced by a researcher or by commercial application is not a threat. This advantage is in sharp contrast to the situation when energy is created by hot fusion.

3. Summary of Behavior

Creating an explanation is like doing a jigsaw puzzle with some pieces missing. Nevertheless, the pieces in hand need to be fit together in the proper way in order to reveal the shape of the missing pieces. The greater the number of

successful fits, the better the missing pieces can be imagined and the more effective the search becomes. In addition, limits need to be placed on the imagination when attempts are made to describe the shape of the missing pieces. As with a jigsaw puzzle, each piece has to be consistent with other pieces and cannot be described in isolation. In other words, all the observed properties have to show consistency in their interaction and cause. The shape of the pieces now in hand can be described as follows:

(1) The LENR reaction does not take place in a conventional chemical structure no matter how large the hydrogen content. Features normally present in conventional structures, such as vacancies of any type, dislocations, large cracks, nanoparticles, or impurities, do not host the LENR process. Instead, a unique condition called the nuclear active environment (NAE) must form. The LENR process takes place only in this unique feature and the rate of the nuclear processes is related to the number of NAE sites present.

(2) PdD does not appear to form phases or structures besides the fcc crystal structure within the temperature, pressure, and composition range used to cause LENR.

(3) The NAE is not normally present in a material but needs to be created by various treatments. The probability of forming the initial NAE is presently very small. Once the NAE can form, adding to the amount becomes increasingly difficult as attempts are made to increase the amount.

(4) When an individual piece of palladium is found to form NAE and host LENR, most of the batch from which
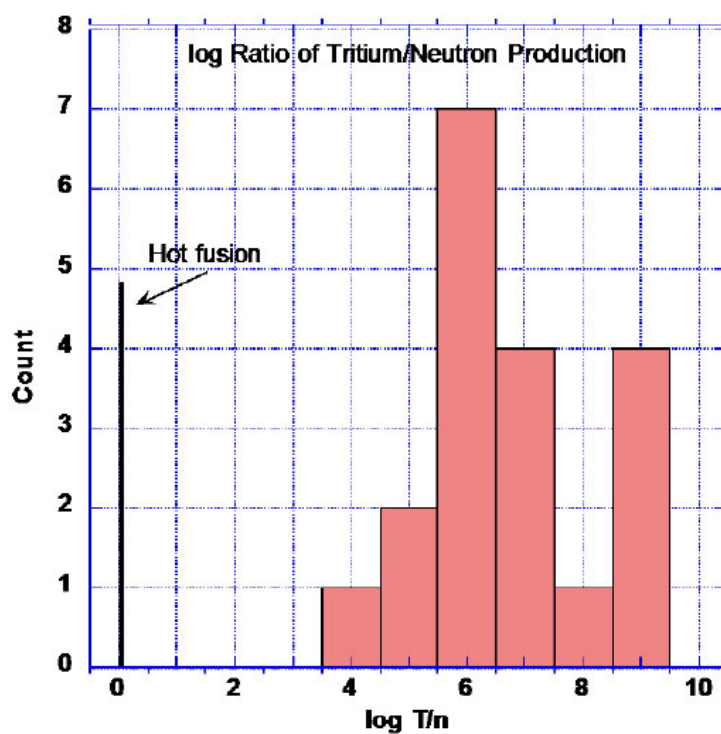
Figure 10. Histogram of the log tritium/neutron ratio resulting from the LENR process. The value for the hot fusion reaction is also shown. The spread in values is justified by the large error expected to result when the small neutron flux is measured. The source of the values is the book by Storms [3].
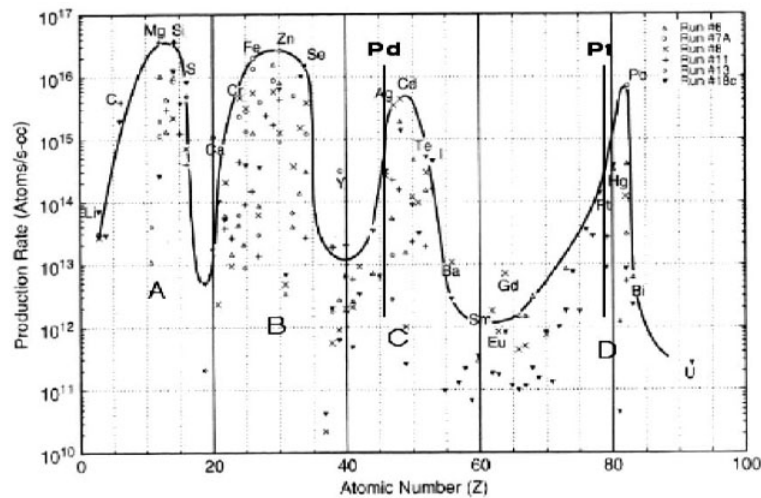
Figure 11. Spectrum of transmutation products reported by Miley and Patterson [53] and Miley [54] based on samples exposed to H_2O and/or D_2O during electrolysis. Some of the elements are expected to result from contamination, which can be ignored without changing the basic shape of the elemental distribution. The atomic number of the two major elements on the surface are noted.

    the piece is obtained is also found to be nuclear active, thereby revealing the presence of a common condition and treatment being important to cause the LENR process.

(5) Once the NAE forms, the hydrogen fuel must spontaneously assemble in the NAE by a conventional chemical process.

(6) When electrolysis is used, the NAE forms in the material near the cathode surface where stress is concentrated and cracks are observed to form.

(7) A process operating within the NAE lowers the Coulomb barrier and, at the same time, dissipates the excess mass–energy without fragmentation of the fusion products.

(8) Production of at least helium-4, tritium with T/n ratio of about 10^6, and two different types of transmutation take place in the NAE. Apparently, transmutation can also take place in biological systems [60]. Whether fusion takes place as part of this transmutation process is unknown but important to consider.

(9) Radiation consisting of neutrons, energetic ions, photons, and electrons are produced. Most radiation has too little energy to escape from the apparatus. In each case, the detected flux intensity outside the apparatus is not correlated with energy production and is very small compared to the generated energy.

(10) The effect of temperature on power production appears to be related to the rate of diffusion of deuterium in the material.

(11) The effect of the D/Pd ratio on power production seems to be small.

(12) LENR can be initiated in several different kinds of chemical structures while using different methods to initiate the process. This behavior indicates a process having universal characteristics may operate.

    Each of these behaviors severely limits how imagination can be applied to finding an explanation. Each general behavior must be accounted for and be consistent with the proposed NAE and the nuclear mechanism. While many conditions and mechanisms can be and have been suggested, the search for the correct explanation requires all observed behavior to be considered, not just behavior that supports the proposed explanation. Likewise, behaviors expected but not reported also must be considered.

A theory of LENR, like a successful jigsaw puzzle, requires all the behaviors be used without forcing a fit. The missing behaviors can be identified only after their correct position in the puzzle is identified. At this stage in the search, the process is less like physics and more like solving a crime.

4. Creating a Theory

An explanation can be used to guide research and help to understand the resulting behavior. In addition, predictions can be suggested to test various assumptions. As much as possible, the explanation needs to be made consistent with all observed behavior and with the laws governing chemical behavior. Nevertheless, some assumptions must be made, which are best kept as simple as possible.

The LENR effect presents three major problems for an explanation. We need to explain how LENR works based on its observed behavior; we need to know why it works by using known physics; and we need to know how to make it work on demand by using the science of metallurgy. Each of these problems requires different kinds of information to which different approaches are applied. For example, the calculations using quantum physics have no hope of revealing how to make the effect work using real materials. The metallurgy needed to design a nuclear active material has no role in showing how the nuclear physics of the process needs to be described. The observed behavior can be used to guide the physics and metallurgy, but only when the important features are accepted as being real and meaningful. Somehow, the discussion has to address these issues as independent subjects and then combine them into a universal process. This paper focuses mainly on the logical consistency between observed behaviors using conventional chemistry and on physics to which are applied several plausible assumptions. Finally, the conclusions are applied to suggest a treatment that can cause the LENR effect.

It is important to consider LENR as a new kind of nuclear interaction. Whether a new kind of physics is required is not clear. Because the conditions and results are not consistent with experience, the LENR process defies understanding when attempts are made to apply conventional knowledge. This conflict forces consideration of new and completely novel mechanisms about how hydrogen nuclei can interact in a chemical structure. The conflict does not justify rejection of LENR.

Rather than using theory and experience based on conventional nuclear interaction or the esoteric concepts common in physics, this paper adopts a different approach [34,37,38]. No effort is made at this stage to create a mathematical description based on quantum mechanics, as is common practice. Acceptance or rejection must flow only from the plausibility of certain assumptions and the logical consequence of their application.

Think of this approach as the creation of a map based on individual reports of various explorers. A few assumptions are made about the basic topography of the land, but the details come only from a logical interpretation of available reports. The goal is to provide aid for future explorers in their search for the expected buried gold. The better the map, the fewer false paths are taken. The details of how the gold got to its location by some complex chemical and geological process is not initially important to explorers and their map. A map seeks only to show the features present on the landscape, not why they formed. Once the map is accepted, physics can be applied to understand how the process works.

5. Assumptions

Assembling the various observed LENR behaviors into a consistent picture requires several assumptions. These assumptions can be justified but not proven. They should be judged only on their plausibility. The assumptions chosen here address mainly the result, with less emphasis on the cause. Nevertheless, the result shows where the cause might be sought.

The nuclear mechanism involving LENR is unknown but it can be assumed to have certain characteristics and

consequences. Listed below are the assumptions on which its overall description is based along with reasons why these assumptions were chosen.

(1) Creation of the NAE is assumed to follow the rules of conventional chemistry, i.e. the laws of thermodynamics apply to its formation and action. Nevertheless, its eventual role in causing a nuclear reaction would not be anticipated based only on its structure. It is important to realize, this later event is a lucky consequence made possible only because the chemical structure happens to have several unique properties.

Justification: In contrast to hot fusion and other nuclear processes, LENR requires a chemical structure in which to function. No other nuclear process has this requirement. Any change in a chemical structure, such as creation of the unique condition required of a NAE, would involve a chemical process, which in turn must follow the rules known to affect chemical reactions. Therefore, before LENR can occur, chemistry must be involved, to which the laws of thermodynamics apply. The amount of power produced is critically dependent on the amount of NAE present in the material, which at the present time is highly variable and caused by an unknown and seemingly random process (see Fig. 8).

(2) The NAE is assumed to be a gap in the crystal structure created as a crack begins to form as result of stress relief, with a critical width near 1 nm. The gap stops being a NAE when the gap width grows too large.

Justification: The common conditions normally present in a crystal structure, such as vacancies and dislocation, are not consistent with the rare nature of LENR and its required unique characteristics. Yet, the NAE must form under a variety of conditions in a variety of materials. These requirements eliminate most features known to exist in a normal material. The nano-crack remains as a plausible possibility in which a linear molecule of hydrogen might form, as described next. Of course, only nano-cracks having access to hydrogen would become nuclear active, which would be rare under most conditions. In other words, both the NAE (in the proposed form of a nano-crack) and hydrogen isotopes must be present simultaneously in a material for the proposed nuclear process to happen.

This gap might form in any material, such as $SrCeO_3$ when it is used as a proton conductor [61], $AlLaO_3$ [62] or in the chemical support of a chemical catalyst such as when Pd is deposited on carbon [63]. A particle of Pd, regardless of its size, is not considered able to be made nuclear active when it is too small to form stress cracks.

(3) The hydrogen atoms prior to fusion are assumed to assemble and form a chemical structure located within the NAE. The proposed structure is assumed to have the form of a linear molecule called the Hydroton. This structure has the ability to host fusion of the hydrogen atoms contained therein by a unique and unknown process.

Justification: The NAE is part of a chemical structure. As such, it must play by the same rules the surrounding structure obeys. Assembly of hydrogen atoms in the NAE would involve a chemical process. For this process to be spontaneous, Gibbs energy would have to be released as the hydrogen ions move from their location in the surrounding lattice and into the NAE. In other words, the formation of a crack creates a chemical environment in which the hydrogen atom has a lower Gibbs energy than in the surrounding lattice. For the sake of this discussion, the resulting structure, called a Hydroton, is assumed to have covalent-metallic bonding in which all the atoms share the bonding electrons. These electrons along with those contributed by the surrounding Pd atoms are expected to play a role in reducing the Coulomb barrier by electron screening.

(4) Regardless of which hydrogen isotope is present or the nature of the surrounding material, the same mechanism is assumed to cause fusion between hydrogen nuclei and dissipate the resulting excess mass–energy. Only the nuclear products are different for a different combination of hydrogen isotopes.

Justification: A phenomenon having such unique behavior and rarity would not be expected to have more than one cause. In addition, Nature is known to use as few causes as possible. For these reasons, search for

a single universal mechanism and NAE is a safe first step.

(5) The hydrogen nuclei are assumed to fuse with an electron, as proposed by Romodanov et al. [64] This assumption is applied here to all isotopes of hydrogen. As a result, the following nuclear products and released energy are created, where d represents the deuteron, p the proton, t the triton, e the electron, and n the neutron. The amount of energy released by each reaction is noted.

d+e+d → H^4 = He^4+ beta + 23.8 MeV,
d+e+p → t + 4.9 MeV,
p+e+p → d + 1.9 MeV,
d+e+t → He^4+ n + e + 19.2 MeV,
p+e+t → He^4+ e + 21.3 MeV.
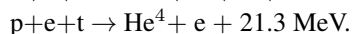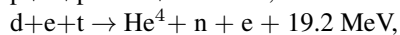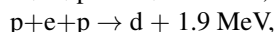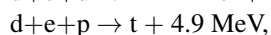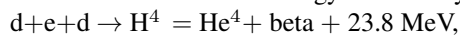
Justification: Tritium is produced without significant neutron emission. The only fusion reaction able to produce this behavior requires addition of an electron when d and p fuse. Assumption #4 requires this process to create all the nuclear products regardless of which isotope of hydrogen is used. Possible involvement of the neutrino is ignored for the present. The electron (e) is captured because it is present along with the nuclei as the source of chemical bonding. As such, it is part of the energy state involved in the fusion process.

(6) The extra mass–energy is assumed to leave gradually from each nucleus as photon radiation. This release process is ongoing and continuous after a group of hydrogen nuclei has assembled in the NAE and continues until all excess mass–energy has been lost and fusion between all the nuclei in the Hydroton is complete. While this behavior is listed as an assumption, this important idea is expanded in greater detail in Sections 6.10 and 6.11.

Justification: Somehow the excess mass–energy must be converted to heat energy. This process can be imagined to happen either before, during, or after the nuclei fuses into the predicted nuclear products. If this energy-loss process is assumed to take place during or after fusion, absence of the hot fusion products must be explained. This problem is avoided by assuming the excess mass–energy is converted gradually to heat by weak photon emission before the nuclei have become a single nucleus. The unique "magic" revealed by LENR involves this process.

(7) Fusion is assumed to occur between adjacent nuclei when enough nuclear energy is released to form a nuclear product without additional release of mass–energy being required. This process is explained in Section 6.4.

Justification: To explain the absence of hot fusion and its energetic radiation, enough excess mass–energy must be lost from the combining nuclei to avoid fragmentation of the final nucleus. To avoid some energy remaining in the final product, this loss process is assumed to continue until the final nucleus would contain no excess mass–energy, whereupon the two nuclei would combine to form a single nucleus without release of additional energy. Failure to follow a strict equal loss from each nucleus would be unacceptable because some nuclei might end with too little or too much mass energy. Some of the extra energy expected to reside in the normally unstable ^4H might be lost as photon emission before the ^4H forms, thereby avoiding the expected decay by neutron emission. The emitted electron is proposed to have too little energy to be easily detected.

(8) Two kinds of transmutations occur during LENR, but at a low rate [55,65]. Both kinds of transmutations are assumed to result from the fusion process and involve different isotopes of hydrogen. Formation of nuclei having greater atomic number than the target is assumed to result from fusion of d, during which various numbers of ^{4}He nuclei are added to the target [66]. Because this process adds very little energy, the need for the final nucleus to fragment is avoided. Fusion products having a fraction of the target mass are assumed to result from fusion of p, during which one or more of the resulting d are added to the target, causing the nucleus to fragment into two parts to dissipate the resulting large excess mass–energy. This complex process is explained in detail by Storms in a previous publication [34].

Jusification: Transmutation requires a very large Coulomb barrier to be overcome for the hydrogen to

enter the target. A chemical lattice does not contain enough energy in any form to cause transmutation. In addition, reaction with a helium nucleus has an even greater Coulomb barrier. These problems can be eliminated if transmutation involves the same process and mechanism operating when fusion of hydrogen nuclei occurs. In this way, fusion and transmutation would both take place in the NAE and involve the same method for overcoming the Coulomb barrier and release of the excess mass–energy without energetic radiation. Once again, assumption #4 is applied. In other words, fusion of hydrogen isotopes is proposed to be coupled to the transmutation reaction so that the two reactions take place in the same NAE at the same time.

6. Logical Consequences of the Assumptions

By definition, an assumption is a speculation for which justification is provided. The more plausible the justification, the more useful is the assumption. Generally, assumptions are hidden in a mathematical description, which is not the case here. Here, all the assumptions are clearly stated and justified so that the reader can decide whether they are plausible. If the assumption is believed to warrant the effort, a mathematical description favored by physicists can be used.

An assumption can only be proven by its predictions being correct or rejected if it conflicts will be accepted as laws or behavior. An effective assumption addresses many critical aspects of the phenomenon, in contrast to ad hoc assumptions that apply to only a single feature of the explanation; thereby cluttering the discussion with many ideas. Good housekeeping in theory construction favors using as few assumptions as possible.

In the end, the importance of an assumption must be based on how well it explains a significant part of observed behavior. With this understanding in mind, the consequence of the eight assumptions identified above is explored next.

6.1. Creation of the NAE

Of greatest importance is creation of the NAE. As described above, nano-cracks are proposed to be the NAE, based largely on a process of elimination of all other possibilities. Creation of such cracks requires the physical properties of the surface be exactly matched by the stress generated when the material reacts with hydrogen or with other elements. For such cracks to be produced in the surface region, the material must be brittle and contain many equally weak regions near the surface. This condition is apparently created during initial treatment of the entire batch of material.

Reaction with hydrogen creates stress as the lattice expands. The initial expansion does not cause cracks because loading subjects the surface to compression. Instead, cracks form as hydrogen is removed, which can happen by chance, if for example the current supply fails as is common during long studies. Or suitable cracks can be caused on purpose by cycling the applied power or ambient pressure.

This cycling can be initiated during electrolysis simply by stopping the power periodically or by applying a super-wave [107,108]. These treatments have all been found to improve success in causing LENR. Cycling applied gas pressure and/or temperature when gas loading is used would achieve the same result. Control of this process is difficult, but must be achieved before reliable power can be achieved.

The more difficult problem is the creation of the required initial conditions in the material. Electrolysis deposits Li, Si, O, and Pt on the surface, which might create the required conditions after an extended electrolysis without an initial treatment being necessary. As experience has shown, LENR can be caused more quickly if the required conditions were created during manufacture of the Pd or by its treatment before it is reacted with hydrogen. This required treatment has yet to be identified. The same consideration applies to the use of powder when it is exposed to H_2 or D_2. The crack might even be generated in the material on which nanoparticles of Pd or Pt are deposited, such as when a chemical catalyst is created [63]. In this case, the cracks would be present initially in the substrate and only

need to be populated by H ions formed by the particles of Pd or Pt located nearby. In other words, the NAE is not located in the nanoparticles of Pd or Pt as is the common belief. Instead, the cracks might be in the carbon or Zeolite substrates on which Pd is deposited. Consequently, care needs to be used when assumptions are made about the nature of the NAE.

6.2. Role of probability in the successful production of energy

Production of excess power first requires formation of a special condition in the material by a random process, described in general terms as the NAE. Not only does the explanation described here rests on this assumption, but the author believes this assumption is essential to understanding LENR regardless of any other assumptions that might be adopted.

We can describe this event using a probability for its formation. Obviously, the probability of creating the condition is small but the value cannot be determined using available information. On the other hand, the probability of generating various levels of power once the NAE forms can be calculated using the data in Fig. 8.

The amount of NAE determines the amount of power being produced. Therefore, the measured power can be used as a stand-in for the number of active sites. The greater the amount of power, the less likely the required number of NAE would form in a particular sample. In other words, the number of samples producing energy can be expected to be smaller the greater the amount of power because the required larger number of NAE would have a reduced probability of forming. For this limitation to be reduced the exact nature of the NAE needs to be determined and ways need to be found to create it in large amount. Thus, a critical requirement for eventual application of LENR as a commercial source of power is identified. Next, how to accomplish this goal needs to be explored.

6.3. LENR initiation first as a chemical reaction

The following description is so important; repeating the idea in different words is necessary to make sure the concept is clearly understood. No progress can be made in understanding LENR until this conclusion is accepted.

To be initiated, LENR first requires a chemical process to take place during which the ambient chemical structure is modified. After all, the LENR process is not found to take place in a large number of chemical structures when exposed to a wide range of conditions. It is rarely produced even when efforts are made to produce it on purpose. Something very rare and unusual must change in a material for the process to occur. This change must involve the chemical conditions in the structure and take place only at certain special locations in order to agree with observed behavior. In other words, a unique NAE must form.

This important conclusion leads directly to another conclusion. The laws of thermodynamics would apply to how the nuclear-active condition forms and to the process of assembling the hydrogen nuclei in the NAE prior to fusion. In other words, the rules of chemistry must be applied first before the nuclear process starts, after which the rules of nuclear physics come into play. This conclusion severely limits how and where in the material the NAE can form. A spontaneous change must involve release of Gibbs energy.

In keeping with this limitation, the NAE chosen here is assumed to be nano-cracks formed by normal stress relief. Normally, cracks have a range of gap width and random length. Larger cracks are able to pass D_2 gas from the interior of the material to the surface, thereby reducing the local deuterium content. Such wide gaps are not thought to be the NAE. On the other hand, very small gaps perhaps as small as 1 nm, are proposed to form a structure in which hydrogen atoms can fuse. The rarity of LENR results because formation of this critical gap dimension is rare and difficult to control. Conditions in the original Pd and the rate at which stress is applied as the Pd reacts with D and other elements would determine the number of cracks and their gap width. Further complexity is produced by how the stress interacts

with the crystallites in the material.[b]

A linear molecule of hydrogen grows in the crack as Gibbs energy is lost, called here a Hydroton. The Hydroton is unique and not a chemical structure formed in normal material, although it can be described as a form of metallic hydrogen. It can also be described as a classic Rydberg molecule [67]. Details of how this kind of structure can form in a crack will be explored in future papers.

6.4. The nuclear process operating during LENR

Moving on to the nuclear process, we are confronted by several important questions. For example, how can helium and tritium form without large amounts of applied energy being available and without generating significant radiation? After all, both of these requirements are characteristic of conventional nuclear reactions without exception. Clearly, LENR demonstrates the need to provide unconventional answers. In this paper, the answers are based on the above-described assumptions.

During LENR, helium production clearly provides the bulk of measured energy when deuterium is used; but what role does the commonly observed tritium play? Is tritium produced by the same mechanism as helium or is it produced by a side reaction? If it is produced by the same mechanism, why is the amount so small? The additional question of how energy is produced when pure protium is used has yet to be answered by experiment. To be consistent with Assumption # 4, the reaction product would be deuterium.

According to Assumption #4, a single mechanism is proposed to operate in the Hydroton during LENR. This single mechanism is assumed to involve fusion of two nuclei of hydrogen along with an electron (Assumption #5). Consequently, tritium results from fusion between p, d, and e. How this happens is not the issue just yet. We are only exploring the consequence of these two assumptions to see how far they can take us toward an explanation of all observed behavior. Figure 12 shows the series of events expected to flow from these assumptions, as explained below. The concentration of p and d in the initial mixture of hydrogen isotopes determines the amount of energy produced and the amount of each nuclear product. The role of transmutation is not discussed here.

The initial Hydroton structure is assumed to consist of a large collection of d and p arranged in a random linear sequence. First, two of the p next to each other fuse to produce d as soon as 0.95 MeV has been lost from each nucleus by process not described here. Further energy loss allows tritium to form where a p and d are next to each other after each nucleus has lost 2.45 MeV. Finally, loss of 11.8 MeV allows the remaining d to fuse to produce H^4. In this way, each fusion reaction takes place in sequence with the reaction requiring the smallest loss of energy occurring first. The resulting d or t might leave the Hydroton or remain to experience further fusion. The final nuclear product of H^4 is radioactive and loses additional energy by emission of beta radiation to form helium, shown as the final event in the sequence, and as described below.

As the hydrogen in a Hydroton fuse, new hydrogen nuclei assemble in the same site and repeat the process as the hydrogen fuel diffuses to the active sites. Millions of Hydrotons are proposed to be in various stages of this process during LENR, with the measured energy being the sum of the energy contributed by each fusion event. Because the concentration of NAE is very non-uniform, some sites at the surface are hotter than others. In fact, most of the energy might result from only a few sites. A search for the NAE on the surface must consider this expectation.

Of course, if only d is present in the Hydroton, only helium can form. In contrast, a Hydroton containing only p will form only d until enough d has accumulated to produce helium and tritium. This logic predicts the use of p would

---

[b]Various conditions including metal and nonmetal atom vacancies, nano-particles, dislocations, and the cage in the Zeolite structure have been proposed as the NAE by other writers, each with different advantages and deficiencies. The reader can decide which is more plausible compared to the nano-crack proposed here. Regardless of the conclusion, a NAE is required and must be identified before LENR can be understood.

produce an unstable amount of power and product considerable tritium, a potentially dangerous radioactive product, as explained below.

6.5. Role of ^{4}H formation

Formation of the ^{4}H isotope would not be expected because it is unstable [68] and is proposed to emit a neutron when it is created using high energy. Beta decay has not been detected when it is formed under these conditions. Even if beta emission did occur, the lower limit to the beta energy, estimated as 17.06 MeV, would produce secondary radiation that is not detected during LENR.

For the assumptions used in this paper to be valid, the ^{4}H would have to form during LENR with a lower mass–energy than expected, decay with a short half-life by beta emission, and then emit the electron with much less energy than given by the above estimate. These requirements might be realized if the ^{4}H created by LENR had less mass than when it is created using high-applied energy. In other words, the process proposed to dissipate excess mass–energy prior to fusion is proposed to carry away some mass–energy from the H^4, leaving less for later beta decay and with no need to emit a neutron.

6.6. Consequence of LENR using a mixture of d and p

Figure 13 shows how the reaction rates for d, He, and t formation are predicted to change as the relative amounts of d and p in the NAE change. The rate of each fusion reaction is assumed influenced only by the atom fraction of d and p in the NAE. Of course, the intrinsic reaction rate of each hydrogen isotope and especially the mixture might be different. In addition, the concentration of the isotopic ratio in the NAE will be different from that in the surrounding gas, but these details are not important at this level of analysis.

Starting first on the right-hand side of Fig. 13, the figure shows production of only helium as long as no p is present. When a small amount of p is added, some tritium and additional deuterium are proposed to form. The rate of tritium formation would be initially proportional to the atom fraction of p and then follow the dotted line in Fig. 13 until formation of deuterium becomes important. However, as the relative amount of p increases, two p would be
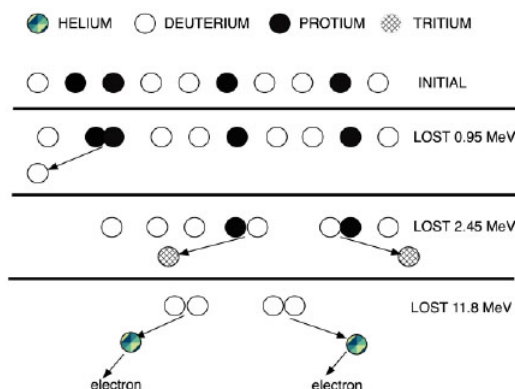
Figure 12. Sequence of events as energy is lost from the Hydroton by photon emission. The final reaction produces ^{4}H that rapidly decays by electron emission to ^{4}He. The process causing transmutation is not shown. The bonding electrons captured into the fusion product and any involvement of the neutrino are not shown. Once fusion occurs, the product might leave the Hydroton structure and join atoms in the surrounding lattice or it might remain and be fused with other hydrogen isotopes when the nuclear product is an isotope of hydrogen.
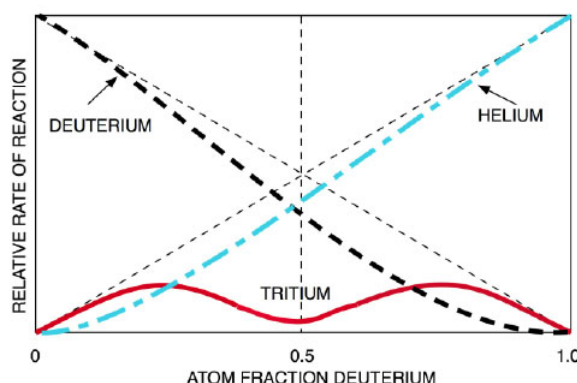
Figure 13. Relative rates of formation for deuterium, helium, and tritium as a function of d/(p+d) in the NAE. The figure approximates ideal behavior when the concentration of NAE and temperature are constant. Unknown influences are expected to slightly modify the relationship. The concentration of p is 100% in the metal on the left side of the figure and d has a concentration of 100% on the right side.

increasingly found adjacent to each other, whereupon deuterium can form instead of tritium. This additional reaction would reduce the rate at which tritium forms as the d/p ratio in the NAE approaches 1.

Because fusion between two p requires loss of only 0.95 MeV from each nucleus, this fusion reaction will be completed before enough energy has been lost from the adjacent d and p for them to form tritium. Thus, the rate of formation of tritium first increases as p is added, then is reduced as the atom fraction of p in the hydrogen mixture approaches 0.5 where the deuterium and helium formation reactions dominate.

Once tritium forms, some of it would fuse with d or p (Assumption #5). When fusion takes place between t and d, a neutron is emitted, thereby accounting for the occasional detected neutron when tritium forms. This reaction will reduce the net amount of tritium, as has been occasionally claimed.

As noted previously, the resulting power is not expected to be stable when protium is used. Power will change as the deuterium concentration in the NAE builds up, allowing tritium to form followed by helium. Total power results from the sum of energy from each reaction, with formation of each He releasing 27.8 MeV[c], each tritium generating 4.9 MeV and finally each deuterium adding 1.9 MeV. The number of each nuclear reaction taking place at any time depends the amount of each hydrogen isotope present in the NAE, which is determined by how much total energy was produced up to that time by the generator. In other words, the observed behavior is expected to be influenced by the previous experience of the material.

Of the nuclear products, only tritium poses a danger, which grows as the generator continues to produce excess energy. A generator making 1 MW for one year is predicted to make as much as 20 g of tritium. This large amount would be dangerous if released into the environment, would be illegal to produce without a permit, and would have great value if captured and sold. The LENR effect would appear to be the easiest and cheapest way to make tritium for civilian and military use while also making useful energy.

This model predicts the total amount of power is influenced by the amount of NAE present, the amount of energy applied to the NAE in any form including temperature, and the isotopic composition of the hydrogen in the NAE. Further change in observed power would result if the amount of NAE and applied energy did not remain constant. Consequently, control of the process in order to generate constant and reliable energy is expected to involve significant

---

[c]For example, helium forms by a series of reactions that combine 4 p with 2 e. This overall process involves a mass change of 0.02979 that is equivalent to 27.75 MeV. Tritium production combines 3 p + 2e that produce a mass change of 0.00852 and 7.94 MeV.

difficulties, especially when light hydrogen is used.

6.7. Transmutation

Transmutation is the black sheep of the LENR family of nuclear products. This process involves adding one or more isotopes of hydrogen to a large target nucleus. Because transmutation is difficult to explain, the mechanism is generally ignored. Claims by Miley using PdH and Rossi [69,70] using Ni+ H_2 have focused attention on the transmutation reaction between protium and various isotopes of Pd, Ni, and lithium. Studies reported by Iwamura et al. have directed attention to transmutation when PdD is used. Two different kinds of transmutation are reported to result from use of the different hydrogen isotopes.

Normally, transmutation cannot be initiated without applying a great deal of energy in order to overcome the very high Coulomb barrier. For example, the barrier between ^{4}He and Pd is 92 charge units and addition of a proton to Ni involves a barrier of 28 charge units. In contrast, fusion between hydrogen only involves a barrier of 1 unit. Even this single charge unit requires application of many keV to cause significant nuclear interaction under ordinary conditions. To add further difficulty to our understanding, we would expect a mechanism that is able to reduce the barrier would first operate to cause hydrogen fusion long before it would reach a level required to cause the more difficult transmutation. In fact as expected, when LENR occurs in PdD, fusion products are the major result with only a small amount of transmutation being detected. In contrast, Rossi has claimed the opposite behavior when NiH is used, with transmutation being the major source of energy production. This conflict points to a potential flaw in the understanding of the two systems.

A further challenge is created by having to dissipate the excess mass energy to avoid emitting energetic radiation, which is not detected. The simplest assumption to explain how the barrier is overcome, how the energy is dissipated, and how two different kinds of transmutation take place involves using the same mechanism proposed to produce fusion of hydrogen. In other words, transmutation is proposed to be a consequence of fusion and takes place as result of the fusion process. This assumption solves both problems by using the mechanism and energy involved in the fusion process to overcome the large Coulomb barrier while the same process dissipates the excess mass energy. In this way, both kinds of transmutation as well as the observed fusion products can form at the same time in the NAE. This proposed process is explained in detail by Storms in previous publications [34,37,71].

6.8. How does the fusion process work?

Now that the general landscape has been described, the next challenge is to examine the details of the fusion process. We have two problems to solve. The Coulomb barrier has to be overcome at a significant rate even though very little energy is available in the material to do the job. The second problem is to dissipate the resulting excess energy without fragmenting the resulting nucleus and without producing significant energetic radiation. These two processes have to work together in the NAE to produce all the observed nuclear products. This is a lot to ask of any known process. To simplify the description below, fusion of two D to create helium is used as an example of how the proposed process might operate, starting with the fusion mechanism.

6.9. Reduction of Coulomb barrier

Even though high energy can overcome the Coulomb barrier without any help from electron screening, the screening electrons come increasingly into play as applied energy is reduced, as can be concluded from the behavior shown in Fig 14. As applied

energy is reduced, the fusion rate increases above that measured using plasma where extra electron charge is not present. The presence of lithium [72,73] in the metal has an especially large effect on this type of enhanced fusion.

Extrapolation of the values in Fig. 14 to the amount of energy available during a typical LENR event (<0.1 eV) reveals that significant electron screening might be possible in a metal environment at low applied energy. This screening process is examined mathematically by Sinha and Hagelstein [74,75] following the work of Ichimaru [76].

How can this behavior be applied to LENR? A high electron concentration can be imagined to exist in a nano-crack, with the resulting negative charge allowing two deuterium nuclei to get close enough to fuse. Unfortunately, the fusion process is expected to quickly go to completion and release the nuclear energy by fragmentation (hot fusion) of the combined nucleus, as bombardment by the D+ ions demonstrates [72, 77–82]. Why does this fragmentation not happen during LENR?

Ion bombardment is not like LENR because the fusion reaction is triggered at random locations in the lattice structure when the energetic ion happens to encounter a stationary ion in the lattice. In contrast, LENR takes place in rare and isolated sites where the conditions are much different from the general lattice. These sites are expected to have a much larger amount of potential electron screening along with the ability to dissipate energy in unusual ways. Such conditions would be very different from those affecting fusion during ion bombardment. Consequently, the behavior during ion bombardment only gives a hint about how electrons might reduce the barrier, but not the full story. The full story requires the NAE be identified so that its unique characteristics can be included in the description. Nevertheless, these ion bombardment studies provide evidence for significant and unexpected electron screening being available in an ordinary chemical environment.

After electron enhanced tunneling has reduced the Coulomb barrier, how can the resulting energy be dissipated without involving the normal fragmentation process?

6.10. Dissipation of excess mass energy

To answer this question, the kind of radiation carrying the excess energy needs to be identified, along with limits to its energy, and the time duration for its release. Normal nuclear reactions release the excess nuclear energy by photon emission, with a delay determined by the half-life of the process. A single photon then carries away all the excess energy stored in single a nucleus as a single event, sometimes combined with other kinds of emissions.

The LENR process is different from normal behavior. The excess energy in the nuclear product can be as high as 23.8 MeV and measurements show that the emitted photons have much less energy than this value. Consequently, we have to assume the energy is released gradually rather than being emitted as a single event after fusion has occurred. Apparently, small quanta of energy are emitted while the fusion process is underway. In other words, the LENR process can be viewed as slow fusion while the hot fusion process can be called fast fusion. This is an important conclusion that contrasts sharply with how energy is released from the hot fusion process and with the energy release process used by other kinds of nuclear reactions. A mechanism proposed to explain cold fusion needs include this slow energy release process and show how the 23.8 MeV can be broken into energy quanta that are generally too small to escape the apparatus, yet do not result in the heat energy being so concentrated to cause local melting.

This concept is so unique and important to understanding cold fusion; a more detailed description is worth considering. Apparently, a new kind of nuclear interaction can dissipate energy while the nuclear process is underway. The process can be visualized as emission of energy from a gradually forming product nucleus in which the nuclear energy states are mixed, but have not yet become characteristic of the final nuclear product. This process would normally not be detected because it would be overwhelmed when high-energy is used to initiate the nuclear process, which is the conventional method. In this case, the fusion process would be so rapid that the small window of time during which energy can be released would be too small to result in detectable energy as fractions of the main emitted energy.

The condition has been described in part by Hagelstein and Chaudhary [84] as a Lossy Spin–boson unstable state. It can also be described as an assembly of overlapping wave functions from which energy is gradually emitted as the wave function approaches that of helium. In any case, a new way for nuclei to interact has been revealed to occur in a

material when high energy is not used to cause the nuclear interaction.

Release of energy from LENR can only involve three possible methods. These are creation of phonons, coupling of energy to the surrounding electrons, or emission of photons. Only these mechanisms can carry energy from the reactants without changing the number of contained neutrons or protons. Energy would then be converted to heat as the phonons or as photons interacted with atoms in nearby material. The exact mechanism by which each of these transport methods does its job does not have to be identified just yet. We first need to understand the general consequence of each idea. Regardless of the method, when energy is released and converted to heat energy, two significant requirements have to be considered. First, the energy has to be distributed into a sufficient number of atoms to avoid causing local melting at the NAE and its subsequent destruction. Second, the energy must not be detectable as energetic radiation, either in the form of primary radiation or as secondary radiation produced when the primary radiation interacts with atoms in the material. These requirements place limits on the energy contained in each quanta of energy. Quanta with too little energy would release energy in the local material too near the source and cause local melting. When too much energy is contained in each released quanta, the radiation would escape the apparatus and be detected as energetic radiation. If too much energy were to leave the apparatus, the amount of measured heat energy would be less than expected. These limits define an energy range into which the quanta must fall.

The source of energy can be visualized as being located at the center of a sphere in which the mass–energy is converted to heat-energy. The goal is to determine the size of the sphere containing enough atoms to prevent the local temperature from rising to a destructive level when the fusion energy is deposited as heat-energy. Figure 15 shows how the number of atoms of $PdD_{0.8}$ would change as the radius of the sphere is changed. Next, the number of atoms that would be melted by a single fusion event and by 25 such events is determined. The values are placed in Fig. 15 to show the radius of a sphere containing this number of atoms. This shows the lower limit to the sphere size above which melting would not be expected as result of this number of fusion reactions. Since the Hydroton can contain an unknown number of deuterons, the true number of fusion events taking place in each of many the Hydrotons is not known. Nevertheless, a useful estimate can be proposed that places a limit of about 0.2 μm on the sphere radius to avoid destruction of the NAE for a plausible number of reactions. This estimate can be used to identify a minimum distance of about 0.4 μm between the NAE in a material hosting d–d–e fusion to avoid destruction of the NAE. If the NAE sites were too close so that the spheres overlap, local melting might occur, as has been observed [85–87] on occasion, which would cause these Hydrotons to be immediately destroyed after which no further energy could be produced at this site. As result, an active material would quickly eliminate sites having too high a concentration of NAE and eventually achieve stable power production.

Because the diameter of the sphere required to acquire energy from d–d–e fusion is much larger than that required when p–p–e fusion occurs, use of light hydrogen would allow a much greater concentration of NAE sites to remain active. If deuterium were added to a material making energy by the p–p–e fusion process, many spheres would now overlap and cause destruction of some energy-producing locations. The reduction in power might be interpreted as poisoning of the process by deuterium. Instead, the reduction might result only from reduction in the number of NAE sites by local melting. Perhaps this is why PdD is found to make less power than the same amount of NiH even though each d–e–d fission event makes more energy than each p–e–p fusion event. Also, a generator using p would be expected to experience increased power as d is formed and increasing amounts of He and tritium are made near the end of its lifetime. A reduction in power would result when this extra energy destroyed some NAE by local melting. Clearly, the process is complex and cannot be interpreted simply by using a constant value for the energy/event

The resulting temperature in the sphere not only depends on the rate at which energy enters the sphere but also on how fast heat-energy can leave. The leaving process takes time and is affected by the temperature of the surrounding material. As observed by Szpak et al. [88], this heating–cooling process occurs in cycles with sudden heat production followed by relatively slow local cooling as the site recharges with hydrogen. During recharging, the local temperature drops as heat energy leaves the site by normal thermal conduction. This process would result in a smaller sphere
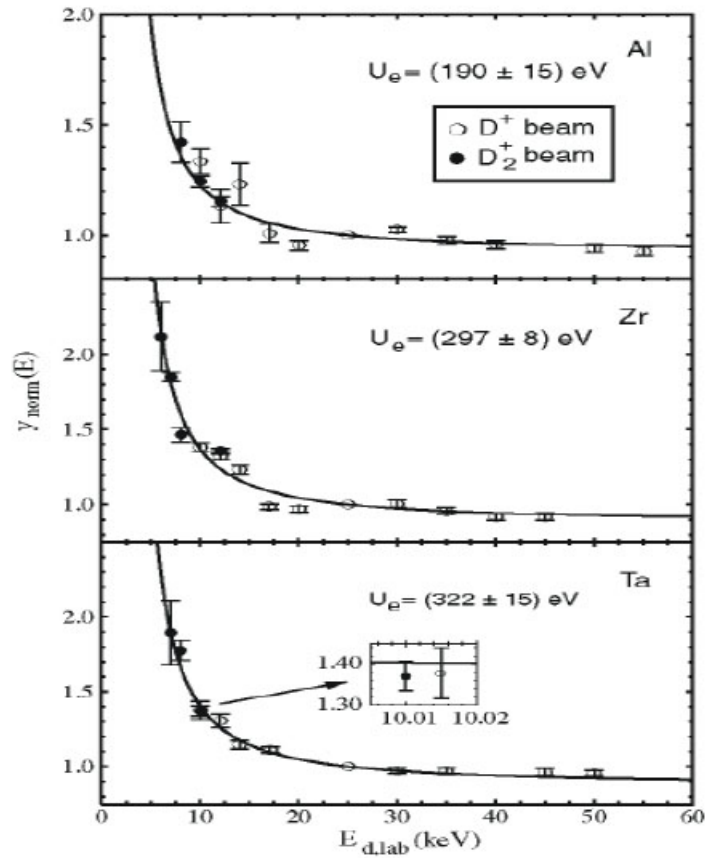
Figure 14. Enhanced fusion resulting from enhanced tunneling as the energy of the D+ ion used to bombard the indicated metal is reduced. A value of $\gamma = 1.0$ means the effect is identical to that produced when plasma is used instead of the solid metal. The rate of fusion decreases as applied energy is reduced, with the enhanced effect causing only a slight increase in the fusion rate within the studied energy range [83]. Nevertheless, the effect of electrons would expected to be significant at the energy present during LENR. The fusion rate is obtained from the measured neutron flux.

of influence with a highly variable value determined by how easily the heat could leave and how many other active Hydrotons were nearby. This observed behavior clearly demonstrates existence of local regions in which LENR creates energy by a cycling process. The total power results from the average of many cycles.

The average energy limit for each quantum released from the fusion process can be estimated from the radius of the sphere using the known absorption behavior of the energy carrier. This calculation is described next.

6.11. Photons as the energy dissipation method

Several methods can be proposed to dissipate the mass–energy. Emission of photons is described first, starting with how they are generated. Photon emission, called gamma, is the normal way energy is lost by all energetic nuclei. Even helium formed by the hot fusion process emits a 23 MeV gamma on a few occasions rather than fragmenting. Because this very energetic gamma is not detected during LENR, we are forced to consider any photon emitted during LENR
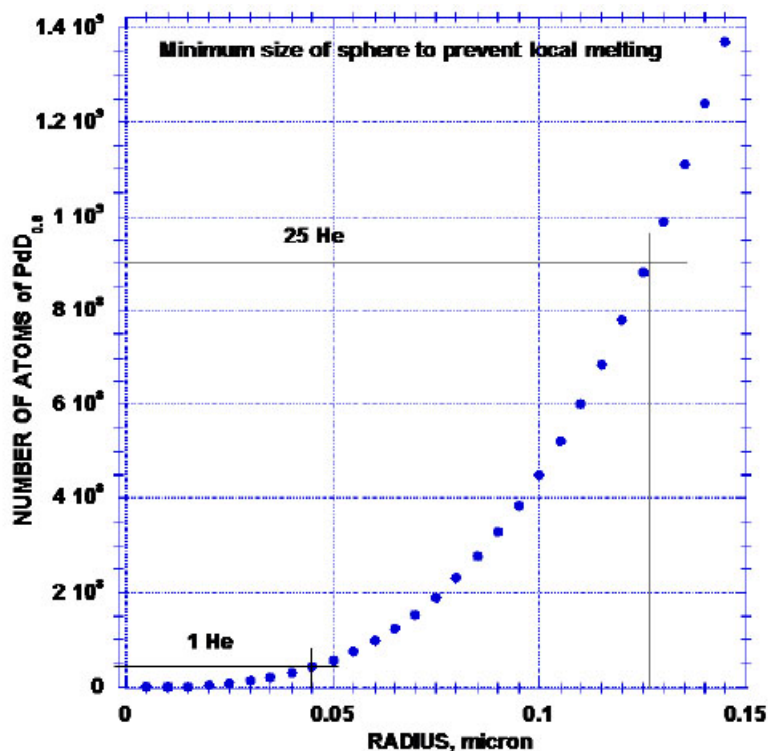
Figure 15. Estimation of the sphere of influence based on a unit cell dimension of 4.06 Å with 7.2 atoms/unit cell for $PdD_{0.8}$. The energy to melt is estimated as 1×10^{-19} J/atom when each fusion releases 23.8 MeV/event.

to result from a different process. What process might be the source?

When a photon is emitted from a nucleus, spin and momentum must be conserved. With this requirement in mind, the process is proposed to involve simultaneous emission of two photons, one from each fusing deuteron with opposite spin and momentum. Because the two nuclei are coupled or entangled by the interaction, the two photons can be thought of as being emitted from the same entity. A continuous series of such pairs would be emitted until all the excess mass energy has been lost from the entity and the resulting ^4H nuclei could form with very little extra mass energy [34]. Eventual decay would result in formation of ^4He. This proposed behavior is based on applying Assumption #4 consistently and does not affect the proposed mechanism for dissipation of the nuclear energy. The proposed mechanism for energy release would be worth considering even if ^4He were formed directly without ^4H being produced. Nevertheless, search for beta radiation resulting from ^4H decay would be worth undertaking.

Photons can never be completely stopped by absorption. Instead, added absorber reduces the number of photons until the number becomes too small to measure. Thus, success in detecting photons requires use of a sensitive detector. For example, X-ray film would have a much higher sensitivity than would a GM detector, hence would be able to detect a much lower emission rate. In fact, numerous studies have detected photon emission using film placed within the apparatus [89–93]. Gozzi et al. [92] detected photon emission from small spots and placed the energy near 89 keV. Violante et al. [93] detected photon radiation between 2 and 12 keV emitted from thin films of Pd and Ni during electrolysis by using a HPGe detector. An upper limit to the photon energy of about 50 keV can be estimated based on

significant radiation not being normally detected outside the apparatus when significant energy is produced.

If each photon had energy of 50 keV, the flux of photons when 1 W was released by d–d–e fusion would be about 10^{14} photons/s at the source. Absorption by the surrounding Pyrex and the D_2O contained in the electrolytic cell combined with low efficiency of the detector would normally reduce detection to a few photons/s. The distance between the source and detector would further reduce the detectable flux. Lower photon energy would result in higher flux and greater heating at the source but fewer photons being detected outside the apparatus. These two effects place upper and lower limits on the predicted energy of any photon resulting from the nuclear process.

Because of these limitations in measuring emitted photons, we must not conclude that the LENR process produces no radiation. The process might generate considerable radiation, but at too low energy to detect using the present methods.

6.12. Electrons as the energy dissipation method

The electrons that promote tunneling through the Coulomb barrier can be proposed to acquire kinetic energy from the fusing atoms and leave the local region at high velocity. These energetic electrons carry the energy from the fusion process to the surround lattice where it is converted to heat energy. This process would generate Bremsstrahlung and X-rays. In this case, we again have to evaluate two different energy limits in order to satisfy two different requirements.

Once again, the energy dissipation process has to result in a local temperature below the melting point of the material in which the NAE is formed, resulting in a lower limit to the deposited energy density. In addition, the generated secondary photon radiation has to have an energy below a critical value to avoid being detected, resulting in upper limit to the electron energy. In other words, electron energy has to fall between two critical values to be consistent with the requirements.

The estimated radius of 0.2 μm, as discussed above, has the stopping power of 0.3 mg/cm^2 when the absorber is PdD. Based on range measurements, electrons with energy of about 10 keV would be completely stopped by this amount of material. To avoid melting the local NAE, the energy-carrying electrons would have to have energy greater than this amount.

The upper limit to electron energy is related to secondary photon production. As electrons lose energy, they generate photon emission called Bremsstrahlung. The photon energy ranges in values below the electron energy and has a maximum flux at about 1/3 this value. These X-rays would have to have an average energy below about 50 keV to avoid being detected outside the apparatus. This requirement places an upper limit to the electron energy of about 150 keV. Consequently, to satisfy the requirements, the average energy of the energy dissipating electrons would have to fall between about 10 and 150 keV. Explaining how the electron energy of proposed electron emission would remain in this range is a challenge for any explanation.

In addition, if each electron carried 10 keV of energy, 2.4×10^6 electrons would be required to carry energy from each fusion event. Given that production of 1 W requires 2×10^{11} fusion/s, an increasing large number of electrons would be affected as power production continued. These electrons would create a current flow between the region in which the NAE is located and the surrounding lattice of about 4×10^{17} electrons/s when one watt is produced. This total current of 0.07 A would produce a small local voltage gradient and magnetic field, both of which might be detected if this proposed process were to actually occur. If the energy were generated in individual particles, such as in a powder, the local charge on individual grains would increase and become obvious.

6.13. Phonons as the energy dissipation method

The term "phonon" is used to identify coherent energy carried by the vibration of atoms and electrons in a physical structure. This energy becomes heat when the vibrations become random. When molecules or crystals acquire enough

phonon energy, the bonds holding them together break and melting occurs. This process limits the amount of energy carried by a phonon as it transports energy from the fusion process. This limit can be estimated as about 1 eV, based on the energy known to hold the PdD lattice together. Thus, at least 23.8×10^6 phonons having no more than 1 eV each would have to be generated over a short period of time as two fusing deuterons approach each other and release their excess mass–energy. Even though each individual phonon would not destroy the structure, the total of so many phonons generated in a very small space would surely cause melting in a local region, thereby stopping the process at this site after a single fusion event. Consequently, this method for energy dissipation would not be consistent with observed behavior. This expectation forces rejection of the proposal by Hagelstein [94], during which the energy is proposed to be dissipated by phonon production.

6.14. Effect of laser radiation

Application of laser radiation has been reported by Letts to stimulate energy production, while the effect is sensitive to the wavelength, to the polarization angle, and perhaps to a magnetic field. A coating of gold on the cathode surface seems to be required in some cases [95–98]. Other success using laser stimulation has also been reported without the need for a gold coating [99–102].

The laser effect is explained here by assuming the light energy enters the active gap and stimulates the reaction by increasing the local temperature in each active gap. The angle of polarization is important because the wave front has to align with the gap in order for it to enter. Because stress relief caused the cracks, they are generally aligned in the same direction within the surface. The frequency is important because the wave-length must match a multiple of the gap width for the energy to enter a gap with maximum efficiency. Otherwise, the energy causes local heating in proportion to the energy being applied to the surface. An especially large effect might be produced when a location containing a high concentration of NAE is heated. In other words, because the concentration of NAE is not uniform, the exact location of the laser spot is important. Indeed, the laser spot might be used to locate where the largest amount of NAE is located, which would allow the nature of the NAE to be explored using analytical methods applied to the identified spot.

The required coating of gold is proposed to contain the active nano-cracks that are generated as the underlying PdD expands as it reacts with deuterium. In this case, the NAE is not proposed to be in the PdD.

Energy entering the gap is expected to be more effective in causing increased energy production than when energy is applied only to the surface. This is why a single laser [95,96,103] can increase energy production while a laser tuned to a gap width can cause a greater effect, thus producing the peaks in power found by Letts [98] and Letts et al. [104,105] In other words, the peaks result when the gap width and a whole fraction of the wave-length match. In this case, the matching wave-length result from a beat frequency generated as the two frequencies interact. A larger effect would be predicted when a match is achieved with the primary frequency. Consequently, use of a tunable laser is recommended as a way to determine the gap width and to explore where the NAE is located on the surface.

7. Testable Predictions

The eight assumptions described in Section 5 can be tested by the following predictions.

(1) As shown in Fig. 13, the relative amount of deuterium, tritium, and helium produced by the LENR process is sensitive to the ratio of d/p in the material. The predicted shape of this relationship can be tested. This test must take into account the molecular form assumed by each of these reaction products in the gas phase where they are measured. Molecules of D_2, DH, H_2, DT, or TH can form and appear in the gas phase. The amount of each can be predicted to depend on the relative concentration of each isotope on the surface where the gas molecule forms.

Because formation of the gas is not an equilibrium process, a random probability exists for an atom finding another atom with which to combine on the surface of the material. As result, the molecular form can be highly variable and not directly related to the isotope concentration.

Because the amount of tritium is also related to the total amount of fusion taking place and to the resulting amount of energy produced, a large amount of tritium is predicted to be present after a large amount of energy is produced using protium. This tritium can be used to test the predictions while being potentially dangerous if it is not properly handled.

(2) Addition of H_2O to D_2O is predicted to reduce the amount of power because p–p–e fusion produces much less energy than d–d–e fusion. This prediction can be tested by measuring the change in power while using various mixtures of d and p. The local concentration of p in the material will be higher than in the electrolyte or gas, which adds complexity to the measurement.

Use of protium initially is expected to result in the least amount of potential power compared to any other isotope of hydrogen or combination thereof. As the LENR process continues, deuterium forms and fuses with the p to produce tritium and increased power. Eventually, enough deuterium will form to produce helium and more power. Consequently, use of protium can be expected to result in a steady increase in power production as tritium and helium accumulate and generate some neutrons. This prediction can be tested using the behavior of the Ni–H_2 system.

(3) When deuterium is used, the few transmutation products are expected to have a greater mass than the nuclei present in the material. When protium is used, each transmutation product will have a mass equal to only a fraction of the target nucleus because the nucleus will fragment. A mixture of p and d is predicted to produce a combination of these two kinds of transmutation products. In no case is transmutation expected to be rapid enough to generate significant energy. This prediction conflicts with the claims now being made about the behavior of NiH by Rossi.

A small amount of slightly lighter than normal proton and deuteron is predicted to exist in nature. The potential for such variable mass being possible is discussed by Davidson [106].

(4) Successful replication requires gaining control over the stress in the material. Gaps formed by stress relief typically have a V shape with the gap widening as the surface of the material is approached. The dimension proposed to be nuclear active is close to the tip of the V. The nuclear active region is expected to be located at an unknown but small distance from the surface. Removal of increasing depths of material from the surface until the LENR process stops could be used to identify the location of the nuclear process and be used to test this description of the required condition.

(5) A magnetic field is expected to change the rate of LENR by changing the frequency of resonance in the Hydroton. Application of laser energy is predicted to change the reaction rate of LENR by adding energy to the Hydroton in proportion to the laser frequency and to its effectiveness in being able to couple to the dimension of the nano-crack. Neither of these changes is expected to initiate the LENR effect.

Each of these predictions can be easily tested and used to evaluate the assumptions and conclusions made in this paper. In the process, this description of the LENR process can be used to guide research from which other insights can be expected to result.

8. Discussion

The LENR process consists of several unique behaviors all combined to produce a result in conflict with how nuclear reactions are normally observed to function. Eventually, each of these behaviors needs to be described using conventional mathematical methods based on quantum mechanics. Meanwhile, a model in which each process operates in

harmony with the others is required. This paper proposes such a model to which mathematical analysis will be applied in later papers.

The well documented and accepted fact that nuclear reactions cannot be initiated in a chemical environment at ambient energy needs to be acknowledged. This conflict between well-accepted expectation and observed behavior requires a unique condition be identified within the material where the observed nuclear reactions can occur, called here the NAE. Such a rare and unique site must exist outside of the normal limitations created by the chemical structure. Nevertheless, this site must form by a normal process in which a collection of hydrogen nuclei can assemble by normal chemical processes. Once assembled, these nuclei fuse without creating easily detected radiation. The unique "magic" of LENR takes place during this final phase of the process. The many observed behaviors can then be used to create a logically consistent description of the process based on these restrictions, as this paper attempts to accomplish.

The rare success in initiating LENR is consistent with there being a small probability for formation of the NAE. Experience reveals that once such sites are formed, LENR can be initiated without restrictions at high rate. This small probability makes a failed attempt the most likely outcome of a study. Success can only be improved by increasing the probability of NAE formation.

A model must start with the unique conditions in which LENR takes place. Regardless of how the NAE is proposed to form and function, its chemical characteristics would have a large effect on how the nuclear process proceeds. Consequently, LENR forces a marriage between chemistry and physics, with chemistry leading the way to understand the initial condition. This initial condition must obey the rules governing chemical behavior and be consistent with observed behavior. Only later does physics need to be applied to explain the nuclear process. Too many proposed theories start with the nuclear process and ignore the environment in which the fusion process must function. This approach has failed to help make the LENR process more reproducible.

A chemical lattice restricts the localized energy to an amount less than would break chemical bonds. This condition is not like plasma in which the energy can be increased without limit. In addition, if super heavy electrons are proposed to form [5,109,110] or if electrons were proposed to seek an orbit closer to the nucleus [111–113] as a way to reduce the Coulomb barrier, these processes would be expected to first produce changes in the chemical structure, which are not detected. Consequently, we are forced to consider only processes that would not interact with the surrounding structure, a requirement that places severe limits on a proposed process for causing LENR.

Ordinary nuclear reactions dissipate the excess mass–energy either at the time the nuclear product is formed or when extra energy is released by radioactive decay after the initial nuclear event. Apparently, the LENR process uses neither method. The nuclear product does not fragment, as is the case during hot fusion. Because the ^{4}H and tritium retain very little of the initial nuclear energy, they do not need to be considered as part of the main dissipation process. Instead, we are encouraged to explore a dissipation process that takes place before the fusion process is fully completed. For this unique dissipation process to be understood, the assembly of hydrogen proceeding fusion must be described in a special way. For this purpose, the assembly of nuclei is called a Hydroton. This structure might also be described as involving a Lossy Spin-boson according to Hagelstein and Chaudhary [84], a Rydberg molecule as suggested by Holmlid [67], coherent correlated states proposed to Vysotskii [114], metallic hydrogen according to Storms [34], discrete breathers suggested by Dubinko [115], Bose–Einstein Condensates as favored by Kim [116], or nuclear threads as proposed by Ivlev [117]. In addition, the hydrogen nuclei might be said to be entangled or be in a super nucleus that is gradually losing energy by complex radioactive decay, the result of which would eventually be a stable nucleus of helium, tritium, or deuterium.

Each of these descriptions, while plausible, addresses only one aspect of the problem. These proposals need to be combined and applied to the entire LENR process. Regardless of how the assembly is described at this time, a collection of nuclei must first form at a unique location in the material. The combination must experience a unique process that can lower the Coulomb barrier while dissipating the excess mass–energy as weak photon radiation. An effective theory must combine these basic requirements into a logically consistent explanation. The problem can be

reduced to two basic choices; reject the obvious or accept what appears to be impossible.

The description provided here uses the well-known behaviors of LENR to create a logically consistent mechanism based on eight assumptions. This combination of assumptions and logical consequences is like a finely tuned machine; with each assumption playing a role without which the machine could not function. The purpose is to provide a platform from which to interpret future behavior and guide research. Only lacking are the mathematical descriptions from which quantitative predictions can be obtained and from which the relationship to conventional physics can be derived. The next step requires the novel process to be explored using the mathematical tools of modern physics and for the phenomenon to take its place among the great discoveries.

When these behaviors are combined to form a unified and logical relationship, a proposed mechanism based on the behavior is forced to have only a small number of possibilities. The challenge is to identify the boundaries of this parameter space and focus on what is consistent with conventional knowledge about chemical systems and nuclear physics. Use of imagination and ad hoc explanation are only useful when all else fails.

In view of the obvious potential of LENR to produce clean, cheap, and easily available energy, the usual skepticism is best put aside until the claims are further explored. Energy of this kind is desperately needed to reduce CO_2 emissions, to purify water, and to remove the role of oil in causing international conflict. The promise can only be tested by obtaining more information about the process and by using this knowledge to create commercial energy generators. Humankind cannot afford to reject such an important gift just because it is not easy to explain or cause.

9. Summary

The LENR process produces energy as result of several nuclear reactions, all taking place in what appear to be ordinary materials under ordinary conditions. The process occurs only after a rarely formed and unique condition is created in the material. Although the process can be initiated under ambient conditions, application of additional energy, such as by increased temperature, application of laser radiation, or electric discharge can increase the rate even though these conditions do not initiate the process. All isotopes of hydrogen appear to be able to produce energy by a fusion process in a variety of materials. Transmutation also occurs and results in nuclear products that depend on the target nucleus and the hydrogen isotope present.

Once the mechanisms is understood, LENR has the potential to be the ideal source of energy required to save the world from the effects of excess CO_2, from the dangers of nuclear fission, and from the uncertain supply inherent in the other sources of energy. LENR also would be the required source of energy to make extended manned space travel possible. Let us hope these many advantages will stimulate interest in solving the difficult problems to understand and apply this source of energy.

Acknowledgement

References

[1] M. Fleischmann, S. Pons and M. Hawkins, Electrochemically induced nuclear fusion of deuterium, *J. Electroanal. Chem.* **261** (301–308) and errata in **263** (1989) 187–188.

[2] J. R. Huizenga, *Cold fusion: The Scientific Fiasco of the Century,* Second edn., Oxford University Press, New York, 1993, pp. 319.

[3] E.K. Storms, *The Science of Low Energy Nuclear Reaction,* World Scientific, Singapore, 2007, 312 pages.

[4] R.E. Godes, The quantum fusion hypothesis, *Infinite Energy* **14** (2008) 15–23.

[5] A. Widom and L. Larsen, Ultra low momentum neutron catalyzed nuclear reactions on metallic hydride surfaces, *Eur. Phys. J.* C **46** (2006) 107.

[6] A.G. Lipson, A.S. Roussetski, A.B. Karabut and G.H. Miley, Strong enhancement of DD-reaction accompanied by X-ray generation in a pulsed low voltage high-current deuterium glow discharge with a titanuim cathode, in *Tenth Int. Conf. on Cold Fusion*, P.L. Hagelstein and S.R. Chubb (Eds.), World Scientific, Cambridge, MA, 2003, pp. 635–656.

[7] D.V. Balin, E.M. Maev, V.I. Medvedev, G.G. Semenchuk, Y.V. Smirenin, A.A. Vorobyov, A.A. Vorobyov and Y.K. Zalite, Experimental investigation of the muon catalyzed d–d fusion, *Phys. Lett.* B **141** (1984) 173.

[8] S.E. Jones, Muon-catalysed fusion revisited, *Nature* (London) **321** (1986) 327.

[9] H.E. Rafelski, D. Harley, G.R. Shin and J. Rafelski, Cold fusion: muon-catalyzed fusion, *J. Phys.* B **24** (1991) 1469.

[10] J. Read, Muons, deuterium, and cold fusion. *Phys. Today* **63**, 10 (2010).

[11] A. Widom, L. Larsen, Nuclear abundances in metallic hydride electrodes of electrolytic chemical cells. *arXiv:cond-mat/062472 v1*, (2006).

[12] A. Widom and L. Larsen, Theoretical standard model rates of proton to neutron conversions near metallic hydride surfaces. *arXiv:cnucl-th/0608059v2*, (2007).

[13] R. P. Santandrea and R.G. Behrens, A review of the thermodynamics and phase relationships in the palladium–hydrogen, palladium–deuterium and palladium–tritium systems, *High Temp. Materials Processes* **7** (1986) 149.

[14] A.C. Switendick, Influence of the electronic structure on the titanium–vanadium–hydrogen phase diagram, *J. Less-Common Metals* **49** (1976) 283–290.

[15] N. Boes and H. Zuchner, Electrochemical methods for studying diffusion, permeation and solubility of hydrogen in metals, *J. Less-Common Metals* **49** (1976) 223–240.

[16] O.Y. Vekilova, D.I. Bazhanov, S.I. Simak and I.A. Abrikosov, First-principles study of vacancy–hydrogen interaction in Pd, *Phys. Rev.* B **80** (2009) 024101–024106.

[17] A.C. Switendick, Electronic structure and stability of palladium hydrogen (deuterium) systems, PdH(D)n, $1 \leq n \leq 3$. *J. less-Common Metals* **172–174** (1991) 1363.

[18] H. Peisl, *The Metal–Hydrogen System*. G. Alefeld and J. Volkl (Eds.), Springer Series in Materials Science, Springer, Berlin, http://link.springer.com/chapter/10.1007/3-540-28883-X_5, 2005), Vol. 21.

[19] N. Asami, T. Senjuh, T. Uehara, M. Sumi, H. Kamimura, S. Miyashita and K. Matsui, Material behavior of highly deuterated palladium, Presented at the *The Ninth Int. Conf. on Cold Fusion*, Beijing, China, Tsinghua University, 2002.

[20] R. Feenstra, R. Griessen and D.G. de Groot, Hydrogen induced lattice expansion and effective H–H interaction in single phase PdH, *J. Phys. F., Met. Phys.* **16** (1986) 1933.

[21] D.L. Knies, V. Violante, K.S. Grabowski, J.Z. Hu, D.D. Dominguez, J.H. He, S.B. Qadri and G.K. Hubler, In-situ synchrotron energy-dispersive X-ray diffraction study of thin Pd foils with Pd: D and Pd: H concentrations up to 1:1, *J. Appl. Phys.* **112** (2012) 083510.

[22] M.C. McKubre and F. Tanzella, Using resistivity to measure H/Pd and D/Pd loading: Method and significance, in *Condensed Matter Nuclear Science, ICCF-12*, Yokohama, Japan, A. Takahashi, K. Ota, Y. Iwamura (Eds.), World Scientific, Singapore, 2005, p. 392.

[23] B. Baranowski, S. Majchrzak and T.B. Flanagan, The volume increase of fcc metals and alloys due to interstitial hydrogen over a wide range of hydrogen contents, *J. Phys. F: Met. Phys.* (1971) 258.

[24] Y. Fukai and N. Okuma, Formation of superabundant vacancies in Pd hydride under high hydrogen pressures, *Phys. Rev. Lett.* **73** (1994) 1640–1643.

[25] Y. Fukai, M. Mizutani, S. Yokota, M. Kanazawa, Y. Miura and T. Watanabe, Superabundant vacancy–hydrogen clusters in electrodeposited Ni and Cu, *J. Alloys and Compd.* **356–357** (2003) 270–273.

[26] M. Krystian, D. Setman, B. Mingler, G. Krexner and M. J. Zehetbauer, Formation of superabundant vacancies in nano-Pd–H generated by high-pressure torsion, *Scripta Materialia* **62** (2010) 49–52.

[27] E.K. Storms, Measurements of excess heat from a Pons–Fleischmann-type electrolytic cell using palladium sheet, *Fusion Technol.* **23** (1993) 230.

[28] E.K. Storms, Anomalous heat generated by electrolysis using a palladium cathode and heavy water, Presented at the American

Physical Society, Atlanta, GA, 1999.

[29] M. Miles, B.F. Bush, J.J. Lagowski, Anomalous effects involving excess power, radiation, and helium production during D_2O electrolysis using palladium cathodes, *Fusion Technol.* **25** (1994) 478.

[30] E.K. Storms, The status of cold fusion (2010), *Naturwissenschaften* **97** (2010) 861.

[31] E.K. Storms and C. Talcott-Storms, The effect of hydriding on the physical structure of palladium and on the release of contained tritium, *Fusion Technol.* **20** (1991) 246.

[32] G.C. Abell, L.K. Matson, R.H. Steinmeyer, R.C. Bowman Jr. and B.M. Oliver, Helium release from aged palladium tritide, *Phys. Rev. B: Mater. Phys.* **41** (1990) 1220.

[33] W.J. Camp, Helium detrapping and release from metal tritides, *J. Vac. Sci. Technol.* **14** (1977) 514–517.

[34] E.K. Storms, *The Explanation of Low Energy Nuclear Reaction,* Infinite Energy Press, Concord, NH, 2014, 365 pages (up-dated e-version available at Amazon.com).

[35] P.L. Hagelstein and I.U. Chaudhary, Phonon models for anomalies in condensed matter nuclear science, *Current Science* **108** (2015) 507–513.

[36] Y. Fukai and N. Okuma, Evidence of copious vacancy formation in Ni and Pd under a high hydrogen pressure, *Jpn. J. Appl. Phys.* **32** (1993) L1256–1259.

[37] E. Storms, Explaining cold fusion, *J. Cond. Matter Nucl. Sci.* **15** (2015) 295–304.

[38] E. Storms, How the explanation of LENR can be made consistent with observed behaviour and natural laws, *Current Science* **108** (2015) 531–534.

[39] E.K. Storms, A theory of LENR based on crack formation, *Infinite Energy* **19** (2013) 24–27.

[40] Y. Sakamoto, M. Imoto, K. Takai, T. Yanaru and K. Ohshima, Calorimetric enthalpies for palladium–hydrogen (deuterium) systems at H(D) contents up to about [H]([D])/[Pd] = 0.86, *J. Phys.: Condens. Mater.* **8** (1996) 3229.

[41] R.P. Santandrea and R.G. Behrens, Thermodynamic properties of alloys used in focused ion beam sources, (LANL, 1985).

[42] M.C.H. McKubre, S. Crouch-Baker, A.M. Riley, S.I. Smedley and F.L. Tanzella, Excess power observations in electrochem-ical studies of the D/Pd system; the influence of loading, in *Third Int. Conf. on Cold Fusion*, Frontiers of Cold Fusion, H. Ikegami (ED.), Universal Academy Press, Tokyo, Japan, Held at: Nagoya Japan, 1992, p. 5.

[43] S. Majorowski and B. Baranowski, Diffusion coefficients of hydrogen and deiterium in highly concentrated palladium hydride and deuteride phases, *J. Phys. Chem. Solid.* **43** (1982) 1119.

[44] P. Jung (Ed.), *Diffusion and Clustering of Helium in Noble Metals*, Plenum Press, NY, 1991, p. 59.

[45] A.N. Zhiganov and A.Y. Kupryazhkin (Eds.), *Grain-Boundary Diffusion of Helium in Palladium with Submicron-Grained Structure*, Am. Inst. Phys., 2003.

[46] J. Xia, W. Hu, J. Yang, B. Ao and X. Wang, A comparative study of helium atom diffusion via an interstitial mechanism in nickel and palladium, *Phys. Stat. Sol.* B **243B** (2006) 579–583.

[47] M.C.H. McKubre and F.L. Tanzella, Results of initial experiment conducted with Pd on C hydrogenation catalyst materials, 1999, private communication.

[48] M.C.H. McKubre, Review of experimental measurements involving dd reactions, *PowerPoint slides, in Tenth Int. Conf. on Cold Fusion*, P.L. Hagelstein and S.R. Chubb (Eds.), World Scientific, Cambridge, MA, 2003.

[49] V. A. Romodanov, V.I. Savin, Y.B. Skuratnik and V.N. Majorov, The nuclear reactions in condensed media for interaction of charge particles in energy region is forming by maximum elastic losses, in *Sixth Int. Conf. on Cold Fusion, Progress in New Hydrogen Energy*, M. Okamoto (Ed.), New Energy and Industrial Technology Development Organization, Tokyo Institute of Technology, Tokyo, Japan, Lake Toya, Hokkaido, Japan, Vol. 1, 1996, p. 340.

[50] Y. Iwamura, T. Itoh, N. Yamazaki, H. Yonemura, K. Fukutani and D. Sekiba, Recent advances in deuterium permeation transmutation experiments, *J. Cond. Matter Nucl. Sci.* **10** (2013) 63–71.

[51] Y. Iwamura, S. Tsuruga and T. Itoh, Increase of transmutation products in deuterium permeation induced transmutation, *in Proc. JCF13*, A. Kitamura (Ed.), Japan CF-Research Soc, WincAichi, Japan, 2012, Vol. http://jcfrs.org/proc_jcf.html, 196-213.

[52] Y. Iwamura, T. Itoh, N. Gotoh and I. Toyoda, Detection of anomalous elements, X-ray, and excess heat in a D_2–Pd system and its interpretation by the electron-induced nuclear reaction model, *Fusion Technol.* **33** (1998) 476.

[53] G.H. Miley and J.A. Patterson, Nuclear transmutations in thin-film nickel coatings undergoing electrolysis, *J. New Energy* (1996) 5.

[54] G. Miley, Characteristics of reaction product patterns in thin metallic films experiments, in *Asti Workshop on Anomalies in*

Hydrogen/Deuterium Loaded Metals, W.J.M.F. Collis (Ed.), Italian Phys. Soc., Villa Riccardi, Rocca d'Arazzo, Italy, 1997, pp. 77–87.

[55] M. Srinivasan, Introduction to isotopic shifts and transmutations observed in LENR experiments, *Current Science* **108** (2015) 624–627.

[56] P.L. Hagelstein, Neutron yield for energetic deuterons in PdD and in D$_2$O, *J. Cond. Matter Nucl. Sci.* **3** (2010) 35–40.

[57] P.L. Hagelstein, Simple parameterizations of the peuteron–peuteron fusion cross sections, *J. Cond. Matter Nucl. Sci.* **3** (2010) 31–34.

[58] P.L. Hagelstein, On the connection between Ka X-rays and energetic alpha particles in Fleischmann–Pons experiments, *J. Cond. Matter Nucl. Sci.* **3** (2010) 50–58.

[59] P.L. Hagelstein, Secondary neutron yield in the presence of energetic alpha particles in PdD, *J. Cond. Matter Nucl. Sci.* **3** (2010) 41–49.

[60] J.-P. Biberian, Biological transmutations, *Current Science* **108** (2015) 633–635.

[61] T. Mizuno, M. Enyo, T. Akimoto and K. Azumi, Anomalous heat evolution from SrCeO$_3$-type proton conductors during absorption/desorption in alternate electric field, in *Fourth Int. Conf. on Cold Fusion*, T.O. Passell (Ed.), Electric Power Research Institute, 3412 Hillview Ave., Palo Alto, CA 94304, Lahaina, Maui, Vols. 2, 14, 1993.

[62] J.-P. Biberian, Excess heat measurements in AlLaO$_3$ doped with deuterium, in *5th Int. Conf. on Cold Fusion*, S. Pons (Ed.), IMRA Europe, Sophia Antipolis Cedex, France, Monte-Carlo, Monaco, Vol. 49, 1995.

[63] L.C. Case, Catalytic fusion of deuterium into helium-4, in *The Seventh Int. Conf. on Cold Fusion*, F. Jaeger (Ed.), ENECO, Salt Lake City, UT, Vancouver, Canada, Vol. 48, 1998.

[64] V.A. Romodanov, Tritium generation during the interaction of plasma glow discharge with metals and a magnetic field, in *Tenth Int. Conf. on Cold Fusion*, P.L. Hagelstein and S.R. Chubb (Ed.), World Scientific, Cambridge, MA, 2003, pp. 325–352.

[65] M. Srinivasan, G. Miley and E.K. Storms, Low-energy nuclear reactions: Transmutations, in *Nuclear Energy Encyclopedia: Science, Technology, and Applications,* S. Krivit, J. H. Lehr and T.B. Kingery (Eds.), Wiley, Hoboken, NJ, 2011, pp. 503–539.

[66] Y. Iwamura, T. Itoh, N. Yamazaki, J. Kasagi, Y. Terada, T. Ishikawa, D. Sekiba, H. Yonemura and K. Fukutani, Observation of low energy nuclear transmutation reactions induced by deuterium permeation through multilayer Pd and CaO thin film, *J. Cond. Matter Nucl. Sci.* **4** (2011) 132–144.

[67] L. Holmlid, Nanometer interatomic distances in Rydberg Matter clusters confirmed by phase-delay spectroscopy, *J. Nanopart. Res.* **12** (2010) on line.

[68] D.R. Tilley and H.R. Weller, Energy levels of light nuclei, $A = 4$, *Nucl. Phys.* A **541** (1992) 1.

[69] A. Rossi, *J. Nucl. Phys.,* http://www.journal-of-nuclear-physics.com/ (2012).

[70] A. Rossi, Method and apparatus for carrying out nickel and hydrogen exothermal reaction, EU, Patent #: WO20110005506, 2011.

[71] E.K. Storms, Explaining cold fusion, *J. Cond. Matter Nucl. Sci.* **15** (2015) 295–304. .

[72] J. Kasagi, H. Yuki, T. Baba, T. Noda, J. Taguchi and W. Galster, Strongly enhanced Li + D reaction in Pd observed in deuteron bombardment on PdLi$_x$ with energies between 30 and 75 keV, *J. Phys. Soc. Japan* **73** (1998) 608–612.

[73] J. Kasagi, Screening potential for nuclear reactions in condensed matter, in *14th Int. Conf. on Condensed Matter Nuclear Science*, D.L. Nagel and M.E. Melich (Ed.), www.LENR.org, Washington, DC, Vol. 1, 2008, pp. 318–325.

[74] K.P. Sinha and P.L. Hagelstein, Electron screening in metal deuterides, *Trans. Am. Nucl. Soc.* **83** (2000) 368.

[75] K.P. Sinha and P.L. Hagelstein, Electron screening in metal deuterides, in *8th Int. Conf. on Cold Fusion*, F. Scaramuzzi (Ed.), Italian Physical Society, Bologna, Italy, Lerici (La Spezia), Italy, 2000, p. 369.

[76] S. Ichimaru, Nuclear fusion in dense plasmas, *Rev. Mod. Phys.* **65** (1993) 255–299.

[77] R.J. Beuhler, G. Friedlander and L. Friedman, Cluster-impact fusion, *Phys. Rev. Lett.* **63** (1989) 1292.

[78] F.E. Cecil, H. Liu and J.S. Yan, Measurements of branching ratios of low energy deuteron-induced nuclear reactions on 2H, 6Li, and 10B, *Phys. Rev. C: Nucl. Phys.* **47** (1993) 1178.

[79] J. Kasagi, T. Murakami, T. Yajima, S. Kobayashi and M. Ogawa, Measurements of the D + D reaction in Ti metal with incident energies between 4.7 and 18 keV, *J. Phys. Soc. Japan* **64** (1995) 608–612.

[80] A. Takahashi, K. Maruta, K. Ochiai and H. Miyamaru, Detection of three-body deuteron fusion in titanium deuteride under the stimulation by a deuteron beam, *Phys. Lett.* A **255** (1999) 89.

[81] K. Czerski, A. Huke, P. Heide and G. Ruprecht, The ^{2}H(d,p)^{3}H reaction in metallic media at very low energies, *Europhys.*

Lett. **68** (2004) 363.

[82] E.N. Tsyganov, Cold nuclear fusion, *Phys. Atomic Nuclei* **75** (2011) 153–159.

[83] K. Czerski, New evidence of the cold nuclear fusion – accelerator experiments at very low energies, Presented at the New Advances on the Fleischmann–Pons Effect, European Parliament, Brussels, 2013.

[84] P.L. Hagelstein and I.U. Chaudhary, Lossy spin–boson model with an unstable upper state and extension to N-level systems, *J. Cond. Matter Nucl. Sci.* **11** (2013) 59–92.

[85] J. Ruer, Simulation of crater formation on LENR cathodes surfaces, *J. Cond. Matter Nucl. Sci.* **12** (2013) 54–68.

[86] D.S. Silver, J. Dash and P.S. Keefe, Surface topography of a palladium cathode after electrolysis in heavy water, *Fusion Technol.* **24** (1993) 423.

[87] A. DeNinno, A. Frattolillo, A. Rizzo, E. Del Giudice and G. Preparata, Experimental evidence of ^{4}He production in a cold fusion experiment, ENEA - Unita Tecnico Scientfica Fusione Centro Ricerche Frascati, Roma, 2002, RT/2002/41/FUS.

[88] S. Szpak, P.A. Mosier-Boss, J. Dea and F. Gordon, Polarized D+/Pd–D_2O system: hot spots and "mini-explosions", in *Tenth Int. Conf. on Cold Fusion*, P.L. Hagelstein and S.R. Chubb (Ed.), World Scientific, Cambridge, MA, 2003, p. 13.

[89] R.K. Rout, A. Shyam, M. Srinivasan and A. Bansal, Copious low energy emissions from palladium loaded with hydrogen or deuterium, *Indian J. Technol.* **29** (1991) 571.

[90] S. Szpak, P.A. Mosier-Boss and J.J. Smith, On the behavior of Pd deposited in the presence of evolving deuterium, *J. Electroanal. Chem.* **302** (1991) 255.

[91] M. Miles and B.F. Bush, Search for anomalous effects involving excess power and helium during D_2O electrolysis using palladium cathodes, in *Third Int. Conf. on Cold Fusion*, Frontiers of Cold Fusion, H. Ikegami (Ed.), Universal Academy Press, Tokyo, Japan, Nagoya Japan, 1992, pp. 189–199.

[92] D. Gozzi, F. Cellucci, P. L. Cignini, G. Gigli, M. Tomellini, E. Cisbani, S. Frullani and G.M. Urciuoli, X-ray, heat excess and ^{4}He in the D/Pd system, *J. Electroanal. Chem.* **452** (1998) 251–271.

[93] V. Violante, P. Tripodi, D. Di Gioacchino, R. Borelli, L. Bettinali, E. Santoro, A. Rosada, F. Sarto, A. Pizzuto, M.C H. McKubre and F. Tanzella, X-ray emission during electrolysis of light water on palladium and nickel thin films, in The *9th Int. Conf. on Cold Fusion, Condensed Matter Nuclear Science*, X.Z. Li (Ed.), Tsinghua Univ. Press, Tsinghua Univ., Beijing, China, 2002, pp. 376–382.

[94] P.L. Hagelstein, On the phonon model in cold fusion/LENR, *Infinite Energy* **19** (2013) 12–17.

[95] D. Letts and D. Cravens, Laser stimulation of deuterated palladium: past and present, in *Tenth Int. Conf. on Cold Fusion*, P.L. Hagelstein and S.R. Chubb (Eds.), World Scientific, Cambridge, MA, 2003, pp. 159–170.

[96] E.K. Storms, Use of a very sensitive Seebeck calorimeter to study the Pons–Fleischmann and Letts effects, in *Tenth Int. Conf. on Cold Fusion*, P.L. Hagelstein and S.R. Chubb (Eds.), World Scientific, Cambridge, MA, 2003, pp. 183–197.

[97] D. Letts and P.L. Hagelstein, Simulation of optical phonons in deuterated palladium, in *14th Int. Conf. on Condensed Matter Nuclear Science*, D.L. Nagel and M.E. Melich (Eds.), Vol. 1, Washington, DC, 2008, pp. 333–337.

[98] D. Letts, Highly reproducible LENR experiments using dual laser stimulation, *Current Science* **108** (2015) 559–561.

[99] J. Tian, L.H. Jin, B.J. Shen, Z.K. Weng and X. Lu, Excess heat triggering by 532 nm laser in a D/Pd gas loading system, in *ICCF-14 Int. Conf. on Condensed Matter Nuclear Science*, D.L. Nagel and M.E. Melich (Eds.), Vol. 1, Washington, DC, 2008, pp. 328–332.

[100] M. Apicella, E. Castagna, L. Capobianco, L. D'Aulerio, G. Mazzitelli, F. Sarto, A. Rosada, E. Santoro, V. Violante, M.C. McKubre, F. Tanzella and C. Sibilia, Some recent results at ENEA, in Condensed Matter Nuclear Science*, ICCF-12*, A. Takahashi, K. Ota, Y. Iwamura (Eds.), World Scientific, Yokohama, Japan, 2005, pp. 117–132.

[101] V. Nassisi, Experimental studies of a XeCl laser having UV preionization perpendicular and parallel to the electrode surfaces, *Appl. Phys.* B **53** (1991) 14–18.

[102] V. Nassisi and M.R. Perrone, Double XeCl laser and lateral UV preionization, *Appl. Phys. B* **51**, 254 (1990).

[103] D. Letts and D. Cravens, Laser stimulation of deuterated palladium, *Infinite Energy* **9** (2003) 10.

[104] D. Letts, D. Cravens and P.L. Hagelstein, Dual laser stimulation and optical phonons in palladium deuteride, in *Low-Energy Nuclear Reactions Sourcebook*, Vol. 2, J. Marwan and S. Krivit (Eds.), Oxford University Press, Oxford, 2009.

[105] D. Letts, D. Cravens, P. L. Hagelstein, Thermal changes in palladium deuteride induced by laser beat frequencies, in *ACS Symposium Series 998, Low-Energy Nuclear Reactions Sourcebook,* J. Marwan and S.B. Krivit (Eds.), American Chemical Society, Washington, DC, 2008, pp. 337.

[106] M. Davidson, Theories of variable mass particles and low energy nuclear phenomena, *Found. Phys.* **44** (2014) 144–174.

[107] I. Dardik, H. Branover, A. El-Boher, D. Gazit, E. Golbreich, E. Greenspan, A. Kapusta, B. Khachatorov, V. Krakov, S. Lesin, B. Michailovitch, G. Shani and T. Zilov, Intensification of low energy nuclear reactions using superwave excitation, in *Tenth Int. Conf. on Cold Fusion*, P.L. Hagelstein and S.R. Chubb (Ed.), World Scientific, Cambridge, MA, 2003, p. 61.

[108] O. Azizi, A. El-Boher, J.-H. He, G.K. Hubler, D. Pease, W. Isaacson, V. Violante and S. Gangopadhyay, Progress towards understanding anomalous heat effect in metal deuterides, *Current Science* **108** (2015) 565–573.

[109] D. Das and M.K.S. Ray, Fusion in condensed matter – a likely scenario, *Fusion Technol.* **24** (1993) 115.

[110] F. Parmigiani and P.G. Sona, Theoretical considerations on the cold nuclear fusion in condensed matter, *Nuovo Cimento Soc. Ital. Fis.* D **11** (1989) 913.

[111] N.V. Samsonenko, D.V. Tahti and F. Ndahayo, On the Barut–Vigier model of the hydrogen atom, *Phys. Lett.* A **220** (1996) 297.

[112] R.L. Mills and W.R. Good, Fractional quantum energy levels of hydrogen, *Fusion Technol.* **28** (1995) 1697.

[113] K.P. Sinha and A. Meulenberg Jr., Lochon catalyzed D–D fusion in deuterated palladium in the solid state, *National Acad. Sci. Lett.* **30** (2007) 243.

[114] V.I. Vysotskii and M.V. Vysotskyy, Coherent correlated states of interacting particles – the possible key to paradoxes and features of LENR, *Current Science* **108** (2015) 524–530.

[115] V.I. Dubinko, Low-energy nuclear reactions driven by discrete breathers, *J. Cond. Matter Nucl. Sci.* **14** (2014) 87–107.

[116] Y.E. Kim, Bose–Einstein condensate theory of deuteron fusion in metal, *J. Cond. Matter Nucl. Sci.* **4** (2011) 188–201.

[117] B. Ivlev, Nuclear threads. *arXiv:1312.6561* (2014).
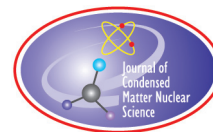
Research Article

Quantum Composites: A Review, and New Results for Models for Condensed Matter Nuclear Science

Peter L. Hagelstein[*]

Massachusetts Institute of Technology, Cambridge, MA, USA

Abstract

A composite is made up of constituent particles; the center of mass dynamics is that of a single particle, and the composite can have many internal states and degrees of freedom. The notion of a quantum composite is foundational to atomic, molecular, nuclear and particle physics; in our view it is also foundational to condensed matter nuclear science. It comes as a surprise that there do not appear to be review papers that discuss quantum composites. Here we first consider elementary particles models, which are used to model composites; the most widely used example is that of the Dirac phenomenology for protons and neutrons. Quantum composite models can be developed from many-particle models, in some cases simply by rewriting in terms of center of mass and relative operators, and in other cases through a reduction or transformation. We have proposed models for anomalies in condensed matter nuclear science which rely heavily on the notion of a relativistic quantum composite. In the nonrelativistic case there is a clean separation of center of mass and internal degrees of freedom, so that any coupling between them must occur through external field interactions. The relativistic composite has a sizeable coupling between the center of mass motion and internal degrees of freedom, which we have proposed is responsible for the anomalies in condensed matter nuclear science. We have developed a new model in which the center of mass dynamics is modeled as nonrelativistic, but the internal structure is kept relativistic; this kind of model is much better adapted to problems in condensed matter nuclear science. Our approach has been strongly criticized, since in a Poincaré invariant theory the center of mass motion separates from the internal degrees of freedom in free space. We are able to rotate out the strongest part of this coupling in free space, consistent with Poincaré invariance. However, in the lattice the problem is in general much more complicated, and more powerful tools are required to diagonalize this relativistic coupling. The spin-boson type of models that we have considered previously for this are the simplest idealized models that can be diagonalized; they describe rich dynamics not present in the free-space version of the problem.

© 2016 ISCMNS. All rights reserved. ISSN 2227-3123

Keywords: Center of mass, Foldy–Wouthuysen transformation, Phonon–nuclear coupling, Quantum composite

1. Introduction

Ever since the announcement by Fleischmann and Pons of the observation of excess heat in a heavy water electro-chemical experiment involving the loading of deuterium into Pd [1,2], people working in the resulting field have been

[*]E-mail: plh@mit.edu

interested in understanding how such an effect might occur. The development of condensed matter physics and nuclear physics over the previous century led to basic theories for each discipline independently, and in neither case was there any basis for understanding how nuclear energy might be released cleanly in an electrochemistry experiment. Although it is possible for a condensed matter environment to provide additional screening between deuterons not present in molecular D_2, it is hard to see how other atoms on an atomic scale might lead to unexpected interactions on a much smaller nuclear scale. And in nuclear physics there are simply no previous experimental observations that suggest a large nuclear energy quantum might result in measurable thermal energy in the absence of commensurate energetic nuclear radiation. The many subsequent experimental observations of anomalies has largely supported the claims of Fleischmann and Pons, and in addition continues to contribute to a growing list of anomalies (low-level nuclear emissions, elemental anomalies, collimated X-ray emission) suggesting that there is a major problem with our understanding of how the world works. Mainstream science has to date not been interested, sympathetic, or supportive of this line of inquiry; consequently the field has largely been decimated over the past quarter century.

In our view there are two basic theoretical issues to be faced in the development of a theory for the anomalies. The first concerns what happens to the large nuclear quanta when energy is generated, such that no commensurate energetic products are seen. If this large quantum can be down-converted, then this part of the theoretical problem can be resolved. Cold fusion theories that have been put forth for the most part over the years have not addressed this issue, instead focusing on other parts of the problem. We have found a relatively simple mechanism implemented in a model involving equivalent two-level systems, a highly excited oscillator, and loss, which appears to be capable of coherent energy exchange under conditions of massive up-conversion and down-conversion [3,4]. However, for this mechanism to work there needs to be a reasonably strong coupling between vibrations (or plasmons or magnons) and the internal nuclear degrees of freedom, much stronger than conventional indirect electric and magnetic dipole interactions.

This brings us to the second of the basic theoretical issues to be faced, which involves whether there can be some new mechanism that allows for a substantial interaction between the condensed matter system on the atomic and macroscopic scales, and the internal nuclear system on the fermi scale. The strongest argument against such an effect is the absence of such an interaction in the literature in either condensed matter physics, or nuclear physics; fields which are considered at this point to be mature, and hence well-studied. The chances that such a substantial interaction has gone unnoticed over the tens of thousands of studies in the literature is epsilonic.

Nevertheless, we have proposed that such an interaction not only exists, but is required in a relativistic model based on a many-particle Dirac Hamiltonian [5]. It may be useful here to review the basic argument initially associated with the proposal. In the nonrelativistic problem there is a clean separation between the center of mass and relative degrees of freedom in free space, and the weak coupling that comes about in the presence of external fields is insufficient. In the relativistic version of the problem when the many-particle Dirac model is written in terms of center of mass and relative operators then there is an explicit coupling. The intuition at the time was that there are (relativistic) changes in the nucleus itself associated with the motion, which can be described by a superposition of rest frame states; consequently, one should expect there to be a coupling between the center of mass motion and the internal states required to modify the nuclear states to be consistent with relativity.

If so, then this solves the problem. The interaction between the center of mass and internal degrees of freedom in this relativistic interaction is much stronger than (conventional) electric or magnetic dipole coupling. Moreover, the associated phonon exchange matrix element for a $D_2/^4He$ transition based on this coupling is sufficiently large that it is consistent with the experimentally observed rate of excess heat production in the Fleischmann-Pons experiment, in a model where the down-conversion of the large quantum is not limiting the reaction rate.

This approach generally has received a large amount of criticism over the years. For example, it is generally not accepted that a large quantum can be fractionated as the models predict. It has been argued that such a down-conversion process must be of very high order so that the rate in perturbation theory is vanishingly small. Other arguments have been made that the incoherent decay involves reaction products moving away near the speed of light, which must make

the incoherent channels much faster than the proposed coherent ones.

The proposal for a strong relativistic coupling has been met with a particularly devastating criticism. In this case the argument is that the proposed coupling itself doesn't exist; since in a Poincaré invariant theory the center of mass and relative degrees of freedom separate in the sense that the free space Hamiltonian can be written in the form

$$\hat{H} \;=\; \sqrt{(\hat{M}c^2)^2 + c^2|\hat{\mathbf{P}}|^2},\tag{1}$$

where $\hat{\mathbf{P}}$ is the center of mass momentum operator, and where $\hat{M}$ is the mass operator that depends on internal degrees of freedom. According to this line of thought, there is no anomalously strong coupling as proposed, and the resulting theory is simply (and obviously) in error [6].

The original plan for the study reported in this work was to examine simple models for composites, and to make the case for the relativistic model that we have been using; there was no plan initially to respond to this devastating argument. In the process of documenting the work it seemed like a good idea to begin making a connection with the relevant literature. A colleague had suggested that it would be helpful to note that finite basis models for composites something like what we have proposed are used in the particle physics literature [6]. Since our models rely so heavily on the notion of a quantum composite, we presumed that there would be standard reviews and references that we could make use of. After some effort tracking down the relevant literature it became clear that the notion of a quantum composite is foundational to atomic, molecular, nuclear and particle physics; however, there are no review papers and no universally accepted standard references. This came as a surprise.

Consequently, it seemed to be useful to attempt to develop a systematic discussion of quantum composites. The simplest models used for composites are elementary particle models, perhaps with modifications. The most widely used model of this kind is the Dirac phenomenology for protons and neutrons. However, more complicated elementary particle models are also used, and these are certainly related to the models we have been working with.

Composite models with realistic internal structure can be developed based on many-particle Hamiltonians. In the simplest case this involves simply writing the model in terms of center of mass and relative operators; in more complicated cases reductions or transformations are involved. In retrospect the development of a systematic review for composites seems like an obvious thing to do; the resulting composite models discussed in what follows are in a sense "simple," even when they involve lots of terms.

There is a strong connection between the coupling terms we have used (for coupling between vibrations and internal nuclear degrees of freedom), and the spin–orbit interaction; this motivated us to see whether others had noticed the same coupling terms, and perhaps provide support for our approach. As it turns out quite a lot has been written about the center of mass coupling terms, but these terms have been treated differently from other interactions in the literature. Most of the papers which include a discussion of these terms are interested in the issue of Poincaré invariance, which perhaps should have been expected. Consequently, our study was expanded to include this additional topic, and associated arguments. It became clear that the coupling terms that we have focused on are present in the models as a requirement of Poincaré invariance.

What we did not expect was to be able to address the above-mentioned devastating criticism. It is clear from the literature that the coupling term we have been working with can be rotated out in free space, and we are able to construct a rotation that does this for a reasonably general potential model. However, it is not clear at all that the generalization of the rotation for nuclei in a condensed matter environment will always be helpful. Instead, the lattice problem is much harder than the free space problem, and in general will need to be analyzed with more powerful tools. The models that we have studied which show coherent energy exchange under conditions of massive up-conversion and down-conversion are idealized and simplified versions of the more general analysis that is needed.

There are quite a few other kinds of models that have used for composite systems as well; including models based on Majorana infinite component wave functions, on many-time formalisms, on a proper time formalism, and based

on the Bethe-Salpeter equation. We have included a brief survey of some of these approaches. There are a very large number of works which treat composites based on field theory; in order to keep this review within a manageable scope, and also to try to make it more accessible to the diverse audience of our condensed matter nuclear science community, we have included only a minimal set of comments concerning this large body of work.

We have found it useful to exploit the finite basis approximation for detailed calculations, so this approach is described as well.

Several hundred papers have been cited in this review, which might seem to be excessive. However, as remarked above quantum composite models are fundamental to many fields and consequently widely used, which means that a large number of papers have been written which are relevant to the topics and issues discussed in this work. A more complete review of quantum composites and associated issues could easily include between one and two thousand references. In the course of writing things up, it seemed useful to cite a few of the most relevant papers, and more in the case of issues that are potentially contentious. As a result, there is much more relevant literature than what is included in the references; however, if a reader is interested in a particular topic it should be possible to track down more papers with modern search tools on a particular topic given the references included.

2. Dirac's Spin 1/2 Model and Electrons

Dirac's equation [7] was developed initially for modeling relativistic electrons, and often appears as a standard topic in textbooks. Our interest in it here is because it is widely used to model relativistic composites, specifically the proton and neutron (to be discussed subsequently). Our purpose here is both to provide a brief introduction to the model, and to examine some of the lowest-order relativistic effects.

2.1. Hamiltonian in free space

In free space we can write

$$\hat{H} = \beta mc^2 + \boldsymbol{\alpha} \cdot c\hat{\mathbf{p}}, \tag{2}$$

where β is a 4×4 matrix, and $\boldsymbol{\alpha}$ is a vector ($\boldsymbol{\alpha} = \hat{\mathbf{i}}_x \alpha_x + \hat{\mathbf{i}}_y \alpha_y + \hat{\mathbf{i}}_z \alpha_z$) of 4×4 matrices

$$\beta = \begin{bmatrix} \mathbf{I} & \mathbf{0} \\ \mathbf{0} & -\mathbf{I} \end{bmatrix} = \begin{bmatrix} 1 & 0 & 0 & 0 \\ 0 & 1 & 0 & 0 \\ 0 & 0 & -1 & 0 \\ 0 & 0 & 0 & -1 \end{bmatrix}, \qquad \alpha_x = \begin{bmatrix} \mathbf{0} & \sigma_x \\ \sigma_x & \mathbf{0} \end{bmatrix} = \begin{bmatrix} 0 & 0 & 0 & 1 \\ 0 & 0 & 1 & 0 \\ 0 & 1 & 0 & 0 \\ 1 & 0 & 0 & 0 \end{bmatrix},$$

$$\alpha_y = \begin{bmatrix} \mathbf{0} & \sigma_y \\ \sigma_y & \mathbf{0} \end{bmatrix} = \begin{bmatrix} 0 & 0 & 0 & -i \\ 0 & 0 & i & 0 \\ 0 & -i & 0 & 0 \\ i & 0 & 0 & 0 \end{bmatrix}, \qquad \alpha_z = \begin{bmatrix} \mathbf{0} & \sigma_z \\ \sigma_z & \mathbf{0} \end{bmatrix} = \begin{bmatrix} 0 & 0 & 1 & 0 \\ 0 & 0 & 0 & -1 \\ 1 & 0 & 0 & 0 \\ 0 & -1 & 0 & 0 \end{bmatrix}. \tag{3}$$

2.2. Relativistic energy and momentum relation

The time-independent Dirac equation in free space is

$$E\psi = \beta mc^2 \psi + \boldsymbol{\alpha} \cdot c\hat{\mathbf{p}}\psi, \tag{4}$$

where the wave function ψ is a 4-component vector

$$\psi = \begin{bmatrix} \psi_1 \\ \psi_2 \\ \psi_3 \\ \psi_4 \end{bmatrix}. \tag{5}$$

We can square the energy on the left and square the Hamiltonian operator on the right to obtain

$$E^2\psi = \left[(\beta mc^2)^2 + (\beta mc^2)(\boldsymbol{\alpha} \cdot c\hat{\mathbf{p}}) + (\boldsymbol{\alpha} \cdot c\hat{\mathbf{p}})(\beta mc^2) + (\boldsymbol{\alpha} \cdot c\hat{\mathbf{p}})^2 \right]\psi. \tag{6}$$

In free space the relativistic energy momentum relation of a free electron satisfies

$$E = \sqrt{(mc^2)^2 + c^2|\mathbf{p}|^2}. \tag{7}$$

For consistency we would like

$$\beta^2 = \mathbf{I}, \qquad \boldsymbol{\alpha}\beta + \beta\boldsymbol{\alpha} = 0, \qquad (\boldsymbol{\alpha} \cdot c\hat{\mathbf{p}})^2 = c^2|\hat{\mathbf{p}}|^2. \tag{8}$$

Dirac arrived at the expressions given above as a solution for these consistency relations. In Dirac's spin 1/2 model these relations are satisfied algebraically (we will find this is not the case in other models to be discussed).

2.3. Minimal coupling

Dirac proposed that the electromagnetic field could be included through the replacement

$$p_\mu \;\rightarrow\; p_\mu + eA_\mu = p_\mu - qA_\mu, \tag{9}$$

which began to be referred to as minimal coupling in the 1960s. The charge q for an electron is negative with a value of $-e$. We can rewrite this in connection with the energy and vector momentum operators as

$$\hat{E} = i\hbar\frac{\partial}{\partial t} \;\rightarrow\; \hat{E} - q\Phi = i\hbar\frac{\partial}{\partial t} - q\Phi,$$

$$\hat{\mathbf{p}} = -i\hbar\nabla \;\rightarrow\; \hat{\mathbf{p}} - q\mathbf{A} = -i\hbar\nabla - q\mathbf{A}, \tag{10}$$

where Φ is the scalar electric potential and $\mathbf{A}$ is the vector potential which in the Coulomb gauge satisfies

$$\mathbf{E} = -\nabla\Phi - \frac{\partial}{\partial t}\mathbf{A},$$

$$\mu_0\mathbf{H} = \nabla \times \mathbf{A}. \tag{11}$$

The Dirac Hamiltonian including interactions with the electromagnetic field becomes

$$\hat{H} = \beta mc^2 + \boldsymbol{\alpha} \cdot c(\hat{\mathbf{p}} - q\mathbf{A}) + q\Phi. \tag{12}$$

2.4. Positive and negative energy sectors

Next we consider the time-independent Dirac equation for a particle in a static electric and magnetic field

$$E\psi = \beta mc^2\psi + \boldsymbol{\alpha} \cdot c(\hat{\mathbf{p}} - q\mathbf{A})\psi + q\Phi\psi. \tag{13}$$

This eigenvalue equation describes two different energy channels that are coupled. This can be seen by expressing the 4-component wave function as

$$\psi = \begin{bmatrix} u \\ v \end{bmatrix} = \begin{bmatrix} u_\uparrow \\ u_\downarrow \\ v_\uparrow \\ v_\downarrow \end{bmatrix}, \tag{14}$$

where u and v are 2-component spinors. Plugging into the Dirac equation leads to two coupled equations

$$Eu = mc^2 u + \boldsymbol{\sigma} \cdot c(\hat{\mathbf{p}} - q\mathbf{A})v + q\Phi u,$$

$$Ev = -mc^2 v + \boldsymbol{\sigma} \cdot c(\hat{\mathbf{p}} - q\mathbf{A})u + q\Phi v. \tag{15}$$

The first of these appears to describe a particle in states with positive energy mc^2, the second describes a particle in states with negative energy $-mc^2$, with coupling between the two.

2.5. Pauli reduction and nonrelativistic limit

We are interested in examining some of the lowest-order relativistic corrections of the Dirac model for the electron to the nonrelativistic limit. The spinor v associated with the negative energy sector can be written in terms of the spinor u associated with the positive energy sector according to

$$v = \frac{1}{E + mc^2 - V} \boldsymbol{\sigma} \cdot c(\hat{\mathbf{p}} - q\mathbf{A})u. \tag{16}$$

We can use this to write a single more complicated equation for the positive energy channel alone as

$$Eu = mc^2 u + [\boldsymbol{\sigma} \cdot c(\hat{\mathbf{p}} - q\mathbf{A})]\frac{1}{E + mc^2 - q\Phi}[\boldsymbol{\sigma} \cdot c(\hat{\mathbf{p}} - q\mathbf{A})]u + q\Phi u. \tag{17}$$

If the potential is small compared to the mass energy we might expand the sandwiched term according to

$$\frac{1}{E + mc^2 - q\Phi} \rightarrow \frac{1}{E + mc^2} + \frac{q\Phi}{(E + mc^2)^2} + \cdots \tag{18}$$

If the energy eigenvalue is not very different from mc^2 then we might approximate further

$$\frac{1}{E + mc^2 - q\Phi} \rightarrow \frac{1}{2mc^2} + \frac{q\Phi}{4(mc^2)^2} + \cdots \tag{19}$$

With this approximation the eigenvalue equation for the positive energy channel reduces to

$$Eu = mc^2 u + [\boldsymbol{\sigma} \cdot c(\hat{\mathbf{p}} - q\mathbf{A})]\left[\frac{1}{2mc^2} + \frac{q\Phi}{4(mc^2)^2} + \cdots\right][\boldsymbol{\sigma} \cdot c(\hat{\mathbf{p}} - q\mathbf{A})]u + q\Phi u. \tag{20}$$

This can be simplified to

$$(E - mc^2)u = \left\{\frac{|\hat{\mathbf{p}}|^2}{2m} + \left(q\Phi + \frac{q^2|\hat{\mathbf{A}}|^2}{2m}\right) - \frac{q}{2m}\left(\hat{\mathbf{p}} \cdot \mathbf{A} + \mathbf{A} \cdot \hat{\mathbf{p}}\right) - i\frac{(\hat{\mathbf{p}} \times q\mathbf{A} + q\mathbf{A} \times \hat{\mathbf{p}}) \cdot \sigma}{2m}\right\}u$$
$$+ [\boldsymbol{\sigma} \cdot c(\hat{\mathbf{p}} - q\mathbf{A})]\left[\frac{q\Phi}{4(mc^2)^2} + \cdots\right][\boldsymbol{\sigma} \cdot c(\hat{\mathbf{p}} - q\mathbf{A})]u. \tag{21}$$

On the right hand side we recognize the nonrelativistic kinetic energy operator $|\hat{\mathbf{p}}|^2/2m$ as well as terms corresponding to the electrostatic potential $q\Phi$ and ponderomotive potential $q^2|\hat{\mathbf{A}}|^2/2m$. We see a term normally used for the interaction with the transvere electromagnetic radiation field

$$\hat{H}_{\text{int}} = -\frac{q}{2m}\left(\hat{\mathbf{p}} \cdot \mathbf{A} + \mathbf{A} \cdot \hat{\mathbf{p}}\right). \tag{22}$$

2.6. Magnetic dipole interaction

The next term accounts for the magnetic dipole interaction

$$-i\frac{(\hat{\mathbf{p}} \times q\mathbf{A} + q\mathbf{A} \times \hat{\mathbf{p}}) \cdot \sigma}{2m} = -\frac{\hbar q}{2m}\sigma \cdot \nabla \times \mathbf{A} = -\hat{\boldsymbol{\mu}}_s \cdot \mathbf{B}, \tag{23}$$

where the magnetic dipole operator in Dirac's model is

$$\hat{\boldsymbol{\mu}}_s = \frac{\hbar q}{2m}\boldsymbol{\sigma} = \frac{q}{m}\hat{\mathbf{s}} = -\frac{e}{m}\hat{\mathbf{s}}. \tag{24}$$

Dirac's model for the electron yields a magnetic dipole interaction which is very close to experiment; we can write

$$\hat{\boldsymbol{\mu}}_s = -g_s\frac{e}{2m}\hat{\mathbf{s}}, \tag{25}$$

where from Dirac's mode $g_s = 2$ and from the NIST reference on fundamental constants

$$g_s = 2.00231930436182. \tag{26}$$

We regard the magnetic dipole interaction in this discussion as the lowest-order relativistic effect involving the vector potential not included in $\hat{H}_{\text{int}}$. If we are interested in how well a relativistic model describes a particle or composite, the magnetic dipole interaction provides a good test.

2.7. Spin–orbit interaction

The reduction of the terms in the second line of Eq. (21) produces a great many terms and corresponding effects; one of them is the spin–orbit term in a central field potential

$$\hat{H}_{\text{SO}} = \frac{q}{2m^2c^2} \frac{1}{r} \frac{d\Phi}{dr} \hat{\mathbf{L}} \cdot \hat{\mathbf{s}} \tag{27}$$

with $q = -e$. Our interest in this discussion is focused on this term as one of the lowest-order relativistic effects involving the scalar potential.

3. Dirac Spin 1/2 Models for the Proton and Neutron

The proton and neutron are composite particles with spin 1/2; however, the Dirac equation is routinely used to model them both. This seems useful to us for a variety of reasons: both composites are well studied; corrections to the Dirac model are recognized; the structure of the nucleon as a composite has been studied.

3.1. Magnetic dipole interaction

Both the proton and neutron have magnetic moments that differ from the Dirac model. For the proton we can write

$$\hat{\boldsymbol{\mu}}_s = \frac{g_{\text{p}} e}{2 M_{\text{p}}} \hat{\mathbf{s}} \tag{28}$$

with the NIST listed value of $g_{\text{p}} = 5.585694702$ (the Dirac model would predict a value of 2). For the neutron we have

$$\hat{\boldsymbol{\mu}}_s = \frac{g_{\text{n}} e}{2 M_{\text{n}}} \hat{\mathbf{s}} \tag{29}$$

with the NIST listed value of $g_{\text{n}} = -3.82608545$ (the Dirac model would predict a value of 0).

The lowest-order relativistic effect involving the transverse electromagnetic field is the magnetic dipole interaction. For both the proton and neutron the basic Dirac spin 1/2 model results in a magnetic dipole interaction which is not in good agreement with experiment.

3.2. Pauli interaction Hamiltonian

Pauli proposed a covariant interaction that describes coupling between an anomalous magnetic moment and the radiation field [8,9], which has been widely used subsequently in addition to minimal coupling to describe proton interactions with photons [10–13]. The associated interaction Hamiltonian can be written as

$$\begin{aligned}
\hat{H}_{\text{Pauli}} &= \left(\frac{g_{\text{p}}}{2} - 1 \right) \frac{e\hbar}{2M_{\text{p}}} \begin{bmatrix} -(\boldsymbol{\sigma} \cdot \mathbf{B}) & i(\boldsymbol{\sigma} \cdot \mathbf{E}) \\ -i(\boldsymbol{\sigma} \cdot \mathbf{E}) & (\boldsymbol{\sigma} \cdot \mathbf{B}) \end{bmatrix} \\
&= -\left(\frac{g_{\text{p}}}{2} - 1 \right) \frac{e\hbar}{2M_{\text{p}}} \beta \left(\boldsymbol{\sigma} \cdot \mathbf{B} - i\boldsymbol{\alpha} \cdot \mathbf{E} \right).
\end{aligned} \tag{30}$$

In the nonrelativistic limit this model results in a magnetic dipole interaction that agrees with experiment, and a spin–orbit coupling term with the proton magnetic moment

$$\hat{H}_{\text{SO}} = \frac{(g_{\text{p}} - 1)e}{2m^2c^2} \frac{1}{r} \frac{\text{d}\Phi}{\text{d}r} \hat{\mathbf{L}} \cdot \hat{s}. \tag{31}$$

The Lagrangian associated with the Pauli interaction appears in many papers [14,15].

3.3. Dirac–Pauli Hamiltonian for the proton

The resulting Dirac–Pauli Hamiltonian is

$$\hat{H} = \beta M_{\text{p}}c^2 + \boldsymbol{\alpha} \cdot c(\hat{\mathbf{p}} - e\mathbf{A}) - \left(\frac{g_{\text{p}}}{2} - 1\right) \frac{e\hbar}{2M_{\text{p}}} \beta \left(\boldsymbol{\sigma} \cdot \mathbf{B} - i\boldsymbol{\alpha} \cdot \mathbf{E} \right). \tag{32}$$

This model describes a spin 1/2 particle with an additional (anomalous) magnetic dipole moment, and coupling to the electromagnetic field through minimal (Dirac) coupling and through the Pauli interaction. The anomalous spin in this model is an added magnetic dipole unconnected with the relativistic kinetic energy part of the Hamiltonian, while there is a magnetic dipole moment in addition present due to the spin 1/2 that is a consequence of the relativistic kinetic energy part of the Hamiltonian.

Nonrelativistic Hamiltonians derived from the Dirac–Pauli Hamiltonian have been discussed in [16–18].

3.4. Proton Compton scattering below the pion threshold

The interaction of light with protons can be studied experimentally in scattering experiments with gamma rays. Elastic scattering of gammas and protons occurs below the threshold for pion production ($m_{\pi^\pm}c^2 = 139.57$ MeV, and $m_{\pi^0}c^2 = 134.98$ MeV), which is very closely related to elastic scattering between gammas and electrons below the pair production threshold [19]. In this case it is possible to use standard diagrammatic methods to compute the scattering cross section, leading to results algebraically similar at low order to those obtained in electron Compton scattering. Proton Compton scattering has been frequently reviewed [20–22].

In early proton Compton experiments that explored the dependence of the cross section on the scattering angle, minor deviations were found relative to predictions based on Dirac (minimal coupling) and Pauli interactions [23]; these were attributed to the polarizability of the proton. It is possible to extract accurate estimates for the polarizability of the proton from experiment [24–27], which can be compared to theoretical models [28–30] and nucleon models [31–33].

At higher energy an additional correction to the Dirac and Pauli interactions needs to be included to take into account the fact that the proton is not a point particle. This is done through the introduction of form factors [34,35].

The situation becomes more complicated above the pion threshold, where additional physics is required to model pion production. At even higher energies excitation of the proton to internal excited states is possible, which complicates things further.

The good agreement between the Dirac spin 1/2 model (with relatively minor corrections) for the proton in connection with proton Compton scattering below the pion threshold provides confidence in the model.

3.5. Dirac–Pauli equation for the neutron

The Dirac equation is widely used to model neutrons as well. Since the neutron has no net electric charge, there is no Dirac minimal coupling present. Since the neutron has an anomalous magnetic moment, it would be appropriate to include the Pauli interaction. The resulting Dirac equation is [36–38]

$$\hat{H} = \boldsymbol{\alpha} \cdot c\hat{\mathbf{p}} + \beta M_{\mathrm{n}}c^2 - \left(\frac{g_{\mathrm{n}}}{2}\right)\frac{e\hbar}{2M_{\mathrm{n}}}\beta\left(\boldsymbol{\sigma} \cdot \mathbf{B} - i\boldsymbol{\alpha} \cdot \mathbf{E}\right). \tag{33}$$

Li et al. [15] have discussed a neutron Dirac equation that models an electric dipole moment; however, experiments so far have not detected one [39,40].

3.6. Dirac phenomenology for nuclear models

A major application of Dirac spin 1/2 models for neutrons and protons is for the computation of nuclear structure and reaction processes [41–44]. These models have proven to be very successful when combined with modern nucleon–nucleon interaction models [45].

4. Higher Spin Models

In this section we are interested in relativistic models for elementary particles with a spin greater than 1/2, and the application of these models to composite systems (higher spin baryons). There is a very substantial associated literature, most of which is not well known outside of particle physics. Our purpose here is not to provide a systematic review; instead we would like to focus on a small number of basic issues appropriate to an introduction for the nonspecialist, and discuss briefly the application to composite systems. We will focus mostly on the spin 3/2 case since this is more interesting, and there are more papers; but we will point out some applications of a spin 1 model.

4.1. Spin 3/2 model of Dirac

Dirac was one of the first to consider the development of wave equations for higher spin systems [46]. He argued that such equations could be constructed from wave equations much like the spin 1/2 case, but with more indices. In the spin 3/2 case the resulting wave equation is written in a form probably not appropriate for the discussion; however, with some work we can write it in the much less elegant form

$$i\hbar\frac{\partial}{\partial t}\begin{bmatrix} A_{1\lambda}^{\dot{\beta}} \\ A_{2\lambda}^{\dot{\beta}} \\ B_{\lambda}^{\dot{1}\dot{\beta}} \\ B_{\lambda}^{\dot{2}\dot{\beta}} \end{bmatrix} = mc^2\begin{bmatrix} 0\ 0\ 1\ 0 \\ 0\ 0\ 0\ 1 \\ 1\ 0\ 0\ 0 \\ 0\ 1\ 0\ 0 \end{bmatrix}\begin{bmatrix} A_{1\lambda}^{\dot{\beta}} \\ A_{2\lambda}^{\dot{\beta}} \\ B_{\lambda}^{\dot{1}\dot{\beta}} \\ B_{\lambda}^{\dot{2}\dot{\beta}} \end{bmatrix} + c\begin{bmatrix} \hat{p}_z & \hat{p}_x + i\hat{p}_y & 0 & 0 \\ \hat{p}_x - i\hat{p}_y & -\hat{p}_z & 0 & 0 \\ 0 & 0 & -\hat{p}_z & -(\hat{p}_x + i\hat{p}_y) \\ 0 & 0 & -(\hat{p}_x - i\hat{p}_y) & \hat{p}_z \end{bmatrix}\begin{bmatrix} A_{1\lambda}^{\dot{\beta}} \\ A_{2\lambda}^{\dot{\beta}} \\ B_{\lambda}^{\dot{1}\dot{\beta}} \\ B_{\lambda}^{\dot{2}\dot{\beta}} \end{bmatrix}. \tag{34}$$

The appearance of dotted indices is important to the notation used by Dirac, which helps to keep track of which indices are raised in the different components. The indices $\dot{\beta}$ and λ each go between 1 and 2, so this wave equation is for a 16-component system. The eigenvalues for the associated Hamiltonian are

$$E = \pm\sqrt{(2mc^2)^2 + c^2|\hat{\mathbf{p}}|^2}. \tag{35}$$

Dirac argued that by imposing a symmetry condition on the components such that $A_{12}^{\dot{\beta}} = A_{21}^{\dot{\beta}}$ and $B_{\lambda}^{\dot{1}\dot{2}} = B_{\lambda}^{\dot{2}\dot{1}}$, it was possible to obtain a 12-component wave equation for a spin 3/2 system.

Dirac proposed to make use of minimal coupling to include interactions with the radiation field.

4.2. Dirac–Fierz–Pauli spin 3/2 model in free space

This was pursued by Fierz and Pauli [47], who considered both spin 3/2 and spin 2 wave equations. In the spin 3/2 case the free-space Hamiltonian was written in a compact notation that we have avoided, which with some effort we can rewrite in the form

$$\hat{H} = mc^2\beta + \boldsymbol{\alpha} \cdot c\hat{\mathbf{p}} \tag{36}$$

with the following definitions for the 12×12 $\boldsymbol{\alpha}$ and β matrices

$$
\beta = \left[\begin{array}{cccccc|cccccc}
0 & 0 & 0 & 0 & 0 & 0 & 1 & 0 & 0 & 0 & 0 & 0 \\
0 & 0 & 0 & 0 & 0 & 0 & 0 & -1 & 2 & 0 & 0 & 0 \\
0 & 0 & 0 & 0 & 0 & 0 & 0 & 1 & 0 & 0 & 0 & 0 \\
0 & 0 & 0 & 0 & 0 & 0 & 0 & 0 & 0 & 0 & 1 & 0 \\
0 & 0 & 0 & 0 & 0 & 0 & 0 & 0 & 0 & 2 & -1 & 0 \\
0 & 0 & 0 & 0 & 0 & 0 & 0 & 0 & 0 & 0 & 0 & 1 \\
\hline
1 & 0 & 0 & 0 & 0 & 0 & 0 & 0 & 0 & 0 & 0 & 0 \\
0 & -1 & 2 & 0 & 0 & 0 & 0 & 0 & 0 & 0 & 0 & 0 \\
0 & 1 & 0 & 0 & 0 & 0 & 0 & 0 & 0 & 0 & 0 & 0 \\
0 & 0 & 0 & 0 & 1 & 0 & 0 & 0 & 0 & 0 & 0 & 0 \\
0 & 0 & 0 & 2 & -1 & 0 & 0 & 0 & 0 & 0 & 0 & 0 \\
0 & 0 & 0 & 0 & 0 & 1 & 0 & 0 & 0 & 0 & 0 & 0
\end{array}\right],\quad
\alpha_x = \left[\begin{array}{cccccc|cccccc}
0 & 0 & -1 & 0 & 0 & 0 & 0 & 0 & 0 & 0 & 0 & 0 \\
-1 & 0 & 0 & -1 & 1 & 0 & 0 & 0 & 0 & 0 & 0 & 0 \\
0 & 0 & 0 & 0 & -1 & 0 & 0 & 0 & 0 & 0 & 0 & 0 \\
0 & -1 & 0 & 0 & 0 & 0 & 0 & 0 & 0 & 0 & 0 & 0 \\
0 & 1 & -1 & 0 & 0 & -1 & 0 & 0 & 0 & 0 & 0 & 0 \\
0 & 0 & 0 & -1 & 0 & 0 & 0 & 0 & 0 & 0 & 0 & 0 \\
\hline
0 & 0 & 0 & 0 & 0 & 0 & 0 & 0 & 1 & 0 & 0 & 0 \\
0 & 0 & 0 & 0 & 0 & 0 & 1 & 0 & 0 & 1 & -1 & 0 \\
0 & 0 & 0 & 0 & 0 & 0 & 0 & 0 & 0 & 0 & 1 & 0 \\
0 & 0 & 0 & 0 & 0 & 0 & 0 & 1 & 0 & 0 & 0 & 0 \\
0 & 0 & 0 & 0 & 0 & 0 & 0 & -1 & 1 & 0 & 0 & 1 \\
0 & 0 & 0 & 0 & 0 & 0 & 0 & 0 & 0 & 1 & 0 & 0
\end{array}\right],
$$

$$
\alpha_y = i\left[\begin{array}{cccccc|cccccc}
0 & 0 & -1 & 0 & 0 & 0 & 0 & 0 & 0 & 0 & 0 & 0 \\
1 & 0 & 0 & -1 & 1 & 0 & 0 & 0 & 0 & 0 & 0 & 0 \\
0 & 0 & 0 & 0 & -1 & 0 & 0 & 0 & 0 & 0 & 0 & 0 \\
0 & 1 & 0 & 0 & 0 & 0 & 0 & 0 & 0 & 0 & 0 & 0 \\
0 & -1 & 1 & 0 & 0 & -1 & 0 & 0 & 0 & 0 & 0 & 0 \\
0 & 0 & 0 & -1 & 0 & 0 & 0 & 0 & 0 & 0 & 0 & 0 \\
\hline
0 & 0 & 0 & 0 & 0 & 0 & 0 & 0 & 1 & 0 & 0 & 0 \\
0 & 0 & 0 & 0 & 0 & 0 & 1 & 0 & 0 & 1 & -1 & 0 \\
0 & 0 & 0 & 0 & 0 & 0 & 0 & 0 & 0 & 0 & 1 & 0 \\
0 & 0 & 0 & 0 & 0 & 0 & 0 & 1 & 0 & 0 & 0 & 0 \\
0 & 0 & 0 & 0 & 0 & 0 & 0 & -1 & 1 & 0 & 0 & 1 \\
0 & 0 & 0 & 0 & 0 & 0 & 0 & 0 & 0 & 1 & 0 & 0
\end{array}\right],\quad
\alpha_z = \left[\begin{array}{cccccc|cccccc}
-1 & 0 & 0 & 0 & 0 & 0 & 0 & 0 & 0 & 0 & 0 & 0 \\
0 & -1 & 2 & 0 & 0 & 0 & 0 & 0 & 0 & 0 & 0 & 0 \\
0 & 0 & -1 & 0 & 0 & 0 & 0 & 0 & 0 & 0 & 0 & 0 \\
0 & 0 & 0 & 1 & 0 & 0 & 0 & 0 & 0 & 0 & 0 & 0 \\
0 & 0 & 0 & -2 & 1 & 0 & 0 & 0 & 0 & 0 & 0 & 0 \\
0 & 0 & 0 & 0 & 0 & 1 & 0 & 0 & 0 & 0 & 0 & 0 \\
\hline
0 & 0 & 0 & 0 & 0 & 0 & 1 & 0 & 0 & 0 & 0 & 0 \\
0 & 0 & 0 & 0 & 0 & 0 & 0 & 1 & -2 & 0 & 0 & 0 \\
0 & 0 & 0 & 0 & 0 & 0 & 0 & 0 & 1 & 0 & 0 & 0 \\
0 & 0 & 0 & 0 & 0 & 0 & 0 & 0 & 0 & -1 & 0 & 0 \\
0 & 0 & 0 & 0 & 0 & 0 & 0 & 0 & 0 & 2 & -1 & 0 \\
0 & 0 & 0 & 0 & 0 & 0 & 0 & 0 & 0 & 0 & 0 & -1
\end{array}\right]
\tag{37}
$$

in connection with a wave function of the form

$$\psi = \begin{bmatrix} a_{11}^{\dot{1}} \\ a_{11}^{\dot{2}} \\ a_{12}^{\dot{1}} \\ a_{12}^{\dot{2}} \\ a_{22}^{\dot{1}} \\ a_{22}^{\dot{2}} \\ b_1^{\dot{1}\dot{1}} \\ b_2^{\dot{1}\dot{1}} \\ b_1^{\dot{1}\dot{2}} \\ b_2^{\dot{1}\dot{2}} \\ b_1^{\dot{2}\dot{2}} \\ b_2^{\dot{2}\dot{2}} \end{bmatrix}, \tag{38}$$

where the $a_{\rho\gamma}^{\dot{\alpha}}$ and $b_{\beta}^{\dot{\rho}\dot{\gamma}}$ components correspond to the definitions of Fierz and Pauli. The Dirac–Fierz–Pauli spin 3/2 model is not written out in this form explicitly in the literature, in part because this form is not useful for understanding the important properties of the model; however, it is useful in the context of our discussion since we can see what the model looks like; and because it provides and example of a many-component Dirac equation that is of a form somewhat similar to what we will encounter much later in this paper when we discuss the finite basis approximation for more complicated composites.

The eigenvalues of this Hamiltonian are

$$E = \pm\sqrt{(mc^2)^2 + c^2|\mathbf{p}|^2}, \pm\sqrt{(2mc^2)^2 + c^2|\mathbf{p}|^2}. \tag{39}$$

There are eight eigenvalues with mass $\pm m$ and four with mass $\pm 2m$. The set of eight are connected with a spin 3/2 particle, and the other set of four describe a spin 1/2 particle; to describe a spin 3/2 particle with mass m the part of the solution that is for the mass $2m$ spin 1/2 particle must be eliminated. This is accomplished through compact constraints (which eliminate antisymmetric solutions) that Fierz and Pauli found; which we can rewrite in the form

$$i\hbar\frac{\partial}{\partial t} \begin{bmatrix} 0 & 0 & 0 & 0 & 0 & 0 \\ 0 & 0 & 0 & 0 & 0 & 0 \\ 0 & -1 & 1 & 0 & 0 & 0 \\ 0 & 0 & 0 & -1 & 1 & 0 \\ 0 & 0 & 0 & 0 & 0 & 0 \\ 0 & 0 & 0 & 0 & 0 & 0 \end{bmatrix} \begin{bmatrix} a_{11}^{\dot{1}} \\ a_{11}^{\dot{2}} \\ a_{12}^{\dot{1}} \\ a_{12}^{\dot{2}} \\ a_{22}^{\dot{1}} \\ a_{22}^{\dot{2}} \end{bmatrix} = -c \begin{bmatrix} 0 & 0 & 0 & 0 & 0 & 0 \\ 0 & 0 & 0 & 0 & 0 & 0 \\ -(p_x - ip_y) & p_z & p_z & p_x + ip_y & 0 & 0 \\ 0 & 0 & -(p_x - ip_y) & p_z & p_z & p_x + ip_y \\ 0 & 0 & 0 & 0 & 0 & 0 \\ 0 & 0 & 0 & 0 & 0 & 0 \end{bmatrix} \begin{bmatrix} a_{11}^{\dot{1}} \\ a_{11}^{\dot{2}} \\ a_{12}^{\dot{1}} \\ a_{12}^{\dot{2}} \\ a_{22}^{\dot{1}} \\ a_{22}^{\dot{2}} \end{bmatrix}, \tag{40}$$

$$i\hbar\frac{\partial}{\partial t} \begin{bmatrix} 0 & 0 & 0 & 0 & 0 & 0 \\ 0 & 1 & -1 & 0 & 0 & 0 \\ 0 & 0 & 0 & 0 & 0 & 0 \\ 0 & 0 & 0 & 1 & -1 & 0 \\ 0 & 0 & 0 & 0 & 0 & 0 \\ 0 & 0 & 0 & 0 & 0 & 0 \end{bmatrix} \begin{bmatrix} b_1^{\dot{1}\dot{1}} \\ b_2^{\dot{1}\dot{1}} \\ b_1^{\dot{1}\dot{2}} \\ b_2^{\dot{1}\dot{2}} \\ b_1^{\dot{2}\dot{2}} \\ b_2^{\dot{2}\dot{2}} \end{bmatrix} = -c \begin{bmatrix} 0 & 0 & 0 & 0 & 0 & 0 \\ -(p_x - ip_y) & p_z & p_z & p_x + ip_y & 0 & 0 \\ 0 & 0 & 0 & 0 & 0 & 0 \\ 0 & 0 & -(p_x - ip_y) & p_z & p_z & p_x + ip_y \\ 0 & 0 & 0 & 0 & 0 & 0 \\ 0 & 0 & 0 & 0 & 0 & 0 \end{bmatrix} \begin{bmatrix} b_1^{\dot{1}\dot{1}} \\ b_2^{\dot{1}\dot{1}} \\ b_1^{\dot{1}\dot{2}} \\ b_2^{\dot{1}\dot{2}} \\ b_1^{\dot{2}\dot{2}} \\ b_2^{\dot{2}\dot{2}} \end{bmatrix}. \tag{41}$$

A further discussion of this model can be found in [48].

4.3. Coupling with the electromagnetic field

Dirac proposed that minimal coupling could be used to describe interactions with the electromagnetic field [46]. This implies a higher-spin Hamiltonian of the form

$$\hat{H} = mc^2\beta + \boldsymbol{\alpha} \cdot c(\hat{\mathbf{p}} - q\mathbf{A}) + q\Phi. \tag{42}$$

Pauli and Fierz showed that adding minimal coupling in this way led to an inconsistency. The resolution of this involved adding additional fields (two simple spinor fields c_α and $d^{\dot{\beta}}$) to develop a Lagrangian, from which wave equations and constraints could be developed; both without an electromagnetic field present (in which case the additional fields are constrained to vanish), and also with an electromagnetic field present (where they do not). In this case minimal coupling with the electromagnetic field requires additional degrees of freedom to be added to the wave equation for the model to be consistent.

4.4. Rarita–Schwinger spin 3/2 model in free space

Rarita and Schwinger developed a Lagrangian for a spin 3/2 elementary particle [49], from which follows the wave equation

$$i\hbar\frac{\partial}{\partial t}\Psi_\mu = \beta mc^2\Psi_\mu + \boldsymbol{\alpha} \cdot c\hat{\mathbf{p}}\Psi_\mu, \tag{43}$$

where Ψ_μ is a 4-vector made up of spinors, so that there are 16 complex elements (the μ index refers to the 4-vector construction, and the spinor index is suppressed). The β and $\boldsymbol{\alpha}$ matrices in this equation operate on the (suppressed) spinor indices, so that this equation implies four sets of 4×4 matrix equations, or 16 equations in all.

We can think of this as a direct product of a spin 1/2 spinor and a vector with spin 0 and spin 1, which we would expect to lead to spin 1/2 and spin 3/2 components; we might write for the rest frame [50]

$$\frac{1}{2} \otimes (0 + 1) = \frac{1}{2} + \frac{1}{2} + \frac{3}{2}. \tag{44}$$

The Rarita–Schwinger wave function has 16 elements (and hence 16 degrees of freedom in this context); only eight degrees of freedom are required for the spin 3/2 part of Ψ_μ, and consequently eight constraints are needed to eliminate the two spin 1/2 degrees of freedom. These constraints follow from their Lagrangian, and are usually written compactly as [51]

$$\gamma^\mu\Psi_\mu = 0, \tag{45}$$

$$\partial^\mu\Psi_\mu = 0. \tag{46}$$

4.5. Free-space Hamiltonian with eight degrees of freedom

A free-space Hamiltonian for an 8-component wavefunction specific to the spin 3/2 degrees of freedom (associated with the Rarita–Schwinger model, and also the Dirac–Pauli–Fierz model) was constructed by Moldauer and Case [52]; this Hamiltonian is nonlinear in the momentum. It can be written as

$$\hat{H} = mc^2 \begin{bmatrix} \mathbf{I} & \mathbf{0} \\ \mathbf{0} & -\mathbf{I} \end{bmatrix} \left(1 + \frac{1}{2} \frac{|\hat{\mathbf{p}}|^2 - (\mathbf{\Sigma}_{3/2} \cdot \hat{\mathbf{p}})^2}{\frac{4}{9}|\hat{\mathbf{p}}|^2 + (mc)^2} \right) + \begin{bmatrix} \mathbf{0} & \mathbf{\Sigma}_{3/2} \cdot c\hat{\mathbf{p}} \\ \mathbf{\Sigma}_{3/2} \cdot c\hat{\mathbf{p}} & \mathbf{0} \end{bmatrix} \left(1 + \frac{|\hat{\mathbf{p}}|^2 - (\mathbf{\Sigma}_{3/2} \cdot \hat{\mathbf{p}})^2}{\frac{4}{9}|\hat{\mathbf{p}}|^2 + (mc)^2} \right) \tag{47}$$

with

$$(\Sigma_{3/2})_x = \begin{bmatrix} 0 & \frac{1}{\sqrt{3}} & 0 & 0 \\ \frac{1}{\sqrt{3}} & 0 & \frac{2}{3} & 0 \\ 0 & \frac{2}{3} & 0 & \frac{1}{\sqrt{3}} \\ 0 & 0 & \frac{1}{\sqrt{3}} & 0 \end{bmatrix}, \quad (\Sigma_{3/2})_y = i \begin{bmatrix} 0 & -\frac{1}{\sqrt{3}} & 0 & 0 \\ \frac{1}{\sqrt{3}} & 0 & -\frac{2}{3} & 0 \\ 0 & \frac{2}{3} & 0 & -\frac{1}{\sqrt{3}} \\ 0 & 0 & \frac{1}{\sqrt{3}} & 0 \end{bmatrix}, \quad (\Sigma_{3/2})_z = \begin{bmatrix} 1 & 0 & 0 & 0 \\ 0 & \frac{1}{3} & 0 & 0 \\ 0 & 0 & -\frac{1}{3} & 0 \\ 0 & 0 & 0 & -1 \end{bmatrix}, \tag{48}$$

where the $\mathbf{\Sigma}_{3/2}$ matrices here are recognized as spin 3/2 generalizations of the $\boldsymbol{\sigma}$ matrices. The eigenvalues are

$$E = \pm\sqrt{(mc^2)^2 + c^2|\mathbf{p}|^2}. \tag{49}$$

We can see from this an interesting feature of the Rarita–Schwinger model. When all 16 degrees of freedom are included the associated Hamiltonian is linear in the momentum; however, the implementation of constraints that remove the spin 1/2 degrees of freedom lead to a more complicated model for the degrees of freedom that remain.

4.6. Minimal coupling

Minimal coupling is often used in connection with the Rarita–Schwinger model, which is implemented using a higher-spin wave equation of the form

$$i\hbar \frac{\partial}{\partial t} \Psi_\mu = \beta mc^2 \Psi_\mu + \boldsymbol{\alpha} \cdot c(\hat{\mathbf{p}} - q\mathbf{A})\Psi_\mu + q\Phi\Psi_\mu. \tag{50}$$

The nonrelativistic limit of the model is discussed by Moldauer and Case, and also in [53]; the Foldy–Wouthuysen transformation is considered in [54].

Massive higher-spin models in general seem to suffer from all kinds of maladies. Johnson and Sudarshan showed that an inconsistency in the commutation relations appeared when higher spin models are quantized [55]. Velo and Zwanziger showed that wave propagation faster than the speed of light occurs for the coupled electromagnetic and Rarita–Schwinger system [56]. There are issues with causality associated with the constraints [57]. Further discussion of these issues can be found in [58–62]. There has been much interest in the possibility of developing an acceptable field theory for spin 3/2 models that continues up to the present day [63–66]. In a recent paper by Adler [67] it is suggested that a suitable field theory for the massless case can be constructed, and that mass can be brought in afterward through a Higgs coupling.

4.7. Higher spin models used for modeling composites

Our interest in these models in this section is motivated by their application to physical composite systems. For example, the Rarita–Schwinger model has been used early on for excited states of the nucleon [68–70], for the $\Delta(1232)$ and other baryon resonances [71–73]. Elementary spin 1 models have been used for modeling the deuteron as a composite in collisions with heavier nuclei [74–76].

5. Bargmann–Wigner Models and Applications

Following the introduction of the quark model in 1964 [77] there was great interest in developing simple models for mesons and baryons based on collinear propagating quarks. These early models were based a the Bargmann–Wigner construction, which was developed to describe elementary particles with higher spin. Consistent with the discussion in Section 4, this provides us with examples of models for composite systems based on wave equations for elementary particles.

5.1. Simple product wave function model

Since our discussion here is introductory, the place to start may be with a simple product approximation (which is very much not what Bargmann and Wigner started with). Consider the construction of a simple product wave function written as

$$\Psi_{\mu_1,\ldots,\mu_N}(\mathbf{r}_1, t_1, \ldots, \mathbf{r}_N, t_N) = \psi_{\mu_1}(\mathbf{r}_1, t_1) \cdots \psi_{\mu_N}(\mathbf{r}_N, t_N),\tag{51}$$

where each single particle wave function satisfies

$$i\hbar \frac{\partial}{\partial t} \psi(\mathbf{r}, t) = \beta mc^2 \psi(\mathbf{r}, t) + \boldsymbol{\alpha} \cdot c\hat{\mathbf{p}} \psi(\mathbf{r}, t).\tag{52}$$

The subscripts μ_j are spinor subscripts associated with particle j, with associated space-time coordinates $\mathbf{r}_j, t_j$. It would follow that the product wave function satisfies a set of wave equations of the form

$$\left[i\hbar \frac{\partial}{\partial t_1} - \beta mc^2 - \boldsymbol{\alpha} \cdot c\hat{\mathbf{p}}_1 \right]_{\mu_1, \nu_1} \Psi_{\nu_1, \cdots, \mu_N}(\mathbf{r}_1, t_1, \ldots, \mathbf{r}_N, t_N) = 0,$$

$$\vdots$$

$$\left[i\hbar \frac{\partial}{\partial t_N} - \beta mc^2 - \boldsymbol{\alpha} \cdot c\hat{\mathbf{p}}_N \right]_{\mu_N, \nu_N} \Psi_{\mu_1, \cdots, \nu_N}(\mathbf{r}_1, t_1, \ldots, \mathbf{r}_N, t_N) = 0.\tag{53}$$

We might think of this as a Dirac equation for each particle individually, with all of the other particle wave functions simply multiplying the one acted upon by the Dirac operator.

5.2. Bargmann–Wigner model

If we start with the simple model above, and then require that spatial coordinates of all of the particles are the same

$$\mathbf{r}_1 \rightarrow \mathbf{r} \quad \cdots \quad \mathbf{r}_N \rightarrow \mathbf{r}\tag{54}$$

and similarly for the time coordinates

$$t_1 \rightarrow t \quad \cdots \quad t_N \rightarrow t,\tag{55}$$

we would end up with a model that describes noninteracting particles that travel together. The wave function in this case would satisfy a set of wave equations of the form

$$\left[i\hbar\frac{\partial}{\partial t} - \beta mc^2 - \boldsymbol{\alpha}\cdot c\hat{\mathbf{p}}\right]_{\mu_1,\nu_1} \Psi_{\nu_1,\ldots,\mu_N}(\mathbf{r},t) = 0,$$

$$\vdots$$

$$\left[i\hbar\frac{\partial}{\partial t} - \beta mc^2 - \boldsymbol{\alpha}\cdot c\hat{\mathbf{p}}\right]_{\mu_N,\nu_N} \Psi_{\mu_1,\ldots,\nu_N}(\mathbf{r},t) = 0. \tag{56}$$

This provides a nonrigorous argument for the Bargmann–Wigner model.

It is possible to add additional structure to the model. For example, if the particles are identical then we would adopt initially an anti-symmetric wave function

$$\Psi_{\mu_1,\ldots,\mu_N}(\mathbf{r}_1,t_1,\ldots,\mathbf{r}_N,t_N) = \mathcal{A}\left\{\psi_{\mu_1}(\mathbf{r}_1,t_1)\cdots\psi_{\mu_N}(\mathbf{r}_N,t_N)\right\} \tag{57}$$

Doing so leads to a Bargmann–Wigner wave function that is antisymmetric in the spinor indices

$$\Psi_{\ldots,\mu_r,\ldots,\mu_s,\ldots}(\mathbf{r},t) = -\Psi_{\ldots,\mu_s,\ldots,\mu_r,\ldots}(\mathbf{r},t). \tag{58}$$

We might also be interested in a superposition of product wave functions in order to describe some group of interest; doing so leads to an imposition of the same group structure in the Bargmann–Wigner wave function.

5.3. Application to SU(6)

Perhaps the most important application of the Bargmann–Wigner model was in connection with QCD when first developed. Bargmann–Wigner wave functions adapted to SU(6) were proposed to for simple models describing mesons and baryons as collinear noninteracting quarks [79–81] following the development of the quark model. These were used with success to describe interactions between baryons and mesons [82]

5.4. Bargmann–Wigner Hamiltonian

Because of the need for a covariant description in particle physics generally, one does not often encounter a Hamiltonian for the Bargmann–Wigner model. Nevertheless, the associated arguments are straightforward, and it is of interest in this discussion to pursue the issue. We might consider a wave function made up of a product of single particle wave functions in a Hamiltonian type of model according to

$$\Psi_{\mu_1,\ldots,\mu_N}(\mathbf{r}_1,\ldots,\mathbf{r}_N,t) = \psi_{\mu_1}(\mathbf{r}_1,t)\cdots\psi_{\mu_N}(\mathbf{r}_N,t), \tag{59}$$

where the single particle wave functions satisfy

$$i\hbar\frac{\partial}{\partial t}\psi(\mathbf{r},t) = \beta mc^2\psi(\mathbf{r},t) + \boldsymbol{\alpha}\cdot c\hat{\mathbf{p}}\psi(\mathbf{r},t). \tag{60}$$

Associated with the many-particle product wave function above is a separable free space Hamiltonian of the form

$$\hat{H} = \beta_1 mc^2 + \boldsymbol{\alpha}_1 \cdot c\hat{\mathbf{p}}_1 + \cdots + \beta_N mc^2 + \boldsymbol{\alpha}_N \cdot c\hat{\mathbf{p}}_N. \tag{61}$$

We can define the total momentum

$$\hat{\mathbf{P}} = \hat{\mathbf{p}}_1 + \cdots + \hat{\mathbf{p}}_N \tag{62}$$

and relative momenta defined according to

$$\hat{\boldsymbol{\pi}}_1 = \hat{\mathbf{p}}_1 - \frac{\hat{\mathbf{P}}}{N} \quad \cdots \quad \hat{\boldsymbol{\pi}}_N = \hat{\mathbf{p}}_N - \frac{\hat{\mathbf{P}}}{N}. \tag{63}$$

Although we have defined N relative momenta here, there are only $N-1$ independent operators since

$$\hat{\boldsymbol{\pi}}_1 + \cdots + \hat{\boldsymbol{\pi}}_N = 0. \tag{64}$$

The free space Hamiltonian above can then be written as

$$\hat{H} = (\beta_1 + \cdots + \beta_N)mc^2 + \frac{1}{N}(\boldsymbol{\alpha}_1 + \cdots + \boldsymbol{\alpha}_N) \cdot c\hat{\mathbf{P}} + \boldsymbol{\alpha}_1 \cdot c\hat{\boldsymbol{\pi}}_1 + \cdots + \boldsymbol{\alpha}_N \cdot c\hat{\boldsymbol{\pi}}_N. \tag{65}$$

Now if we presume collinear propagation, such that the relative momenta can be neglected

$$\hat{\boldsymbol{\pi}}_j \rightarrow 0, \tag{66}$$

we end up with

$$\hat{H} = (\beta_1 + \cdots + \beta_N)mc^2 + \frac{1}{N}(\boldsymbol{\alpha}_1 + \cdots + \boldsymbol{\alpha}_N) \cdot c\hat{\mathbf{P}}. \tag{67}$$

This we recognize as a Hamiltonian for the Bargmann–Wigner model. This kind of Hamiltonian has been used in recent years for the high-spin Dirac oscillator [83] and applications [84,85]. The eigenvalues of this Hamiltonian are

$$E = \begin{cases} \sqrt{(Mc^2)^2 + c^2|\mathbf{P}|^2}, \\ \dfrac{N-2}{N}\sqrt{(Mc^2)^2 + c^2|\mathbf{P}|^2}, \\ \qquad\qquad \vdots \\ -\sqrt{(Mc^2)^2 + c^2|\mathbf{P}|^2}. \end{cases} \tag{68}$$

This is understood simply as a consequence of each constituent particle having the possibility of being in the positive energy sector or negative energy sector.

5.5. Square of the Hamiltonian

We recall that the square of the spin 1/2 Dirac Hamiltonian satisfies

$$\left(\beta mc^2 + \boldsymbol{\alpha} \cdot c\hat{\mathbf{p}}\right)^2 = (mc^2)^2 + c^2|\hat{\mathbf{p}}|^2 \tag{69}$$

as an algebraic identity. We are interested in whether the many-particle Hamiltonian above satisfies a similar relation. We might write the associated Hamiltonian in the form

$$\hat{H} = \mathbf{M}c^2 + \mathbf{a} \cdot c\hat{\mathbf{P}} \tag{70}$$

with

$$\mathbf{M}c^2 = (\beta_1 + \cdots + \beta_N)mc^2, \tag{71}$$

$$\mathbf{a} \cdot c\hat{\mathbf{P}} = \frac{1}{N}(\boldsymbol{\alpha}_1 + \cdots + \boldsymbol{\alpha}_N) \cdot c\hat{\mathbf{P}}. \tag{72}$$

The square of the Hamiltonian is

$$\hat{H} = (\mathbf{M}c^2)^2 + (\mathbf{M}c^2)(\mathbf{a} \cdot c\hat{\mathbf{P}}) + (\mathbf{a} \cdot c\hat{\mathbf{P}})(\mathbf{M}c^2) + (\mathbf{a} \cdot c\hat{\mathbf{P}})^2. \tag{73}$$

It can be verified that

$$\mathbf{M}\mathbf{a} + \mathbf{a}\mathbf{M} \neq 0 \tag{74}$$

and

$$(\mathbf{a} \cdot c\hat{\mathbf{P}})^2 \neq c^2|\hat{\mathbf{P}}|^2. \tag{75}$$

This is in contrast to what we had proposed previously [5]. Instead, the eigenfunctions $\Psi_{\mathbf{P}}$ of the Hamiltonian with momentum $\mathbf{P}$ satisfy

$$\left(\mathbf{M}\mathbf{a} + \mathbf{a}\mathbf{M}\right)\Psi_{\mathbf{P}} = 0. \tag{76}$$

$$(\mathbf{a} \cdot c\hat{\mathbf{P}})^2\Psi_{\mathbf{P}} = c^2|\hat{\mathbf{P}}|^2\Psi_{\mathbf{P}}. \tag{77}$$

5.6. A 20-component free space model for nucleons

The proton and neutron are made up of three quarks, so the models outline above could be relevant in the case of $N = 3$, where the free space wave function would have $4^3 = 64$ components. However, it is possible to isolate the part of the symmetric group that is relevant, which leads to a 20-component wave function. We consider first the basic symmetric group construction for an anti-symmetric three-particle state with spatial (R), flavor (F), spin (S) and color (C) degrees of freedom; the antisymmetric wavefunction can be written in terms of Yamanouchi symbols as [86,87]

$$[3\ 2\ 1]_{\text{RFSC}} = [1\ 1\ 1]_{\text{R}}[1\ 1\ 1]_{\text{FS}}[3\ 2\ 1]_{\text{C}}. \tag{78}$$

We would expect the lowest energy spatial wavefunction of a three quark system to be fully symmetric ($[1\ 1\ 1]_{\text{R}}$); and the nucleon as a three-quark system is modeled as a color singlet [88] ($[3\ 2\ 1]_{\text{C}}$). Consequently the flavor and spin function must be fully symmetric ($[1\ 1\ 1]_{\text{FS}}$). Since there are no strange quarks involved, we are able to use a construction of the flavor part of the problem in SU(2). This can be expanded out as

$$[1\ 1\ 1]_{\text{FS}} = \frac{1}{\sqrt{2}}([1\ 2\ 1]_{\text{F}}[1\ 2\ 1]_{\text{S}} + [2\ 1\ 1]_{\text{F}}[2\ 1\ 1]_{\text{S}}), \tag{79}$$

which is consistent with [89]. Note that it would be possible mathematically to form $[1\ 1\ 1]_{\text{FS}}$ according to

$$[1\ 1\ 1]_{\text{FS}} = [1\ 1\ 1]_{\text{F}}[1\ 1\ 1]_{\text{S}} \tag{80}$$

but this in inconsistent with protons and neutrons as the associated spin would be 3/2 (neutron and proton spins are 1/2), and would lead to flavor quartet states (neutrons and protons are flavor doublets). In the end we can write

$$[3\ 2\ 1]_{\text{RFSC}} = [1\ 1\ 1]_{\text{R}} \left(\frac{[1\ 2\ 1]_{\text{F}}[1\ 2\ 1]_{\text{S}} + [2\ 1\ 1]_{\text{F}}[2\ 1\ 1]_{\text{S}}}{\sqrt{2}} \right) [3\ 2\ 1]_{\text{C}}. \tag{81}$$

We can identify two spins for a single Dirac free particle wave function, as well as positive and negative energy components. The spin degree of freedom is described by SU(2). However, in what follows we are going to be interested in the positive and negative energy degrees of freedom as well, which can also be modeled using SU(2). The generalization of the construction above to include the different energy sectors is straightforward; we may write

$$[3\ 2\ 1]_{\text{RFSTC}} = [1\ 1\ 1]_{\text{R}} \left(\frac{[1\ 2\ 1]_{\text{F}}[1\ 2\ 1]_{\text{ST}} + [2\ 1\ 1]_{\text{F}}[2\ 1\ 1]_{\text{ST}}}{\sqrt{2}} \right) [3\ 2\ 1]_{\text{C}}, \tag{82}$$

where T refers to positive or negative energy sector.

Although this construction looks to be a completely straightforward generalization of the basic symmetric group construction above, there are some issues which are worth thinking about. At issue is what happens when the center of mass moves, or is accelerated. There can be no change in the color or flavor from a boost, so we expect the corresponding parts of the wavefunction to remain invariant. Less obvious is what happens to the spatial part of the wavefunction. After some thought, we recognize that in the simple model under construction there is no modification of the relative part of the problem when the center of mass moves since the free space Hamiltonian is totally symmetric ($[1\ 1\ 1]$). Hence if the relative spatial wavefunction is initially in a fully symmetric state, it remains in a fully symmetric states in the different energy sectors in this model.

Consequently, the only thing that happens is that there is a coupling between the spin degrees of freedom, and the positive and negative energy state degree of freedom.

The relevant Hamiltonian for the three noninteracting quarks of the model is

$$\hat{H} = \left(\beta_1 + \beta_2 + \beta_3 \right) mc^2 + \left(\frac{\boldsymbol{\alpha}_1 + \boldsymbol{\alpha}_2 + \boldsymbol{\alpha}_3}{3} \right) \cdot c\hat{\mathbf{P}}. \tag{83}$$

We would like to construct a reduced Hamiltonian appropriate for the mixed symmetry basis states of the quark system. This construction can be written symbolically as

$$
\begin{aligned}
\langle [3\ 2\ 1]_{\text{RFSTC}} | \hat{H} | [3\ 2\ 1]_{\text{RFSTC}} \rangle =& \langle [1\ 1\ 1]_{\text{R}} | [1\ 1\ 1]_{\text{R}} \rangle \langle [3\ 2\ 1]_{\text{C}} | [3\ 2\ 1]_{\text{C}} \rangle \\
& \left\{ \frac{1}{2} \langle [1\ 2\ 1]_{\text{F}} | [1\ 2\ 1]_{\text{F}} \rangle \langle [1\ 2\ 1]_{\text{ST}} | \hat{H} | [1\ 2\ 1]_{\text{ST}} \rangle \right. \\
& \left. + \frac{1}{2} \langle [2\ 1\ 1]_{\text{F}} | [2\ 1\ 1]_{\text{F}} \rangle \langle [2\ 1\ 1]_{\text{ST}} | \hat{H} | [2\ 1\ 1]_{\text{ST}} \rangle \right\} \\
=& \frac{1}{2} \langle [1\ 2\ 1]_{\text{ST}} | \hat{H} | [1\ 2\ 1]_{\text{ST}} \rangle + \frac{1}{2} \langle [2\ 1\ 1]_{\text{ST}} | \hat{H} | [2\ 1\ 1]_{\text{ST}} \rangle,
\end{aligned} \tag{84}
$$

where R in this refers to the relative spatial degrees of freedom. Ultimately the appropriate Hamiltonian is one that averages over the two mixed symmetry basis states. This suggests that we can write the nucleon Hamiltonian in this free-space collinear quark model as

$$
\begin{aligned}
\hat{H}_{\text{nuc}} =& |[3\ 2\ 1]_{\text{C}}\rangle |[1\ 2\ 1]_{\text{F}}\rangle \hat{H}_{[1\ 2\ 1]} \langle [1\ 2\ 1]_{\text{F}} | \langle [3\ 2\ 1]_{\text{C}} | \\
& + |[3\ 2\ 1]_{\text{C}}\rangle |[2\ 1\ 1]_{\text{F}}\rangle \hat{H}_{[2\ 1\ 1]} \langle [2\ 1\ 1]_{\text{F}} | \langle [3\ 2\ 1]_{\text{C}} |,
\end{aligned} \tag{85}
$$

where the subscript for the Hamiltonian here refers the the symmetric group for flavor. The [1 2 1] part of the Hamiltonian can be written

$$\hat{H}_{[1\ 2\ 1]} = \mathbf{M}c^2 + \mathbf{a} \cdot c\mathbf{P}, \tag{86}$$

where $\mathbf{M}$ and $\mathbf{a}$ are 20×20 matrices, which are given explicitly in Appendix A. The matrices are different for the [2 1 1] case (since the basis states are different); however, we have found that it is possible to arrange for the basis states to be ordered so as to lead to identical matrices.

5.7. Issues with minimal coupling

We might think to apply minimal coupling directly with our Bargmann–Wigner model. For example, if we begin with

$$\hat{H} = \mathbf{M}c^2 + \mathbf{a} \cdot c\hat{\mathbf{P}},$$

then including the electromagnetic field would lead to

$$\hat{H} \rightarrow \mathbf{M}c^2 + \mathbf{a} \cdot c[\hat{\mathbf{P}} - Q\mathbf{A}(\mathbf{R})] + Q\Phi(\mathbf{R}), \tag{87}$$

where Q is the total charge

$$Q = q_1 + \cdots + q_N. \tag{88}$$

This is in essence the argument discussed briefly in [90]. However, there are issues associated with this.

Suppose that the charges of the constituent particles differ, as is the case for quarks in nucleons, and is also the case for a Dirac model for protons and neutrons in nuclei. Minimal coupling leads to a Hamiltonian of the form

$$\hat{H} = \beta_1 mc^2 + \boldsymbol{\alpha}_1 \cdot c[\hat{\mathbf{p}}_1 - q_1 \mathbf{A}(\mathbf{r}_1)] + \cdots + \beta_N mc^2 + \boldsymbol{\alpha}_N \cdot c[\hat{\mathbf{p}}_N - q_N \mathbf{A}(\mathbf{r}_N)] + \sum_j q_j \Phi(\mathbf{r}_j). \tag{89}$$

The Bargmann–Wigner type of Hamiltonian that results is

$$\hat{H} = (\beta_1 + \cdots + \beta_N)mc^2 + \frac{1}{N}(\boldsymbol{\alpha}_1 + \cdots + \boldsymbol{\alpha}_N) \cdot c\hat{\mathbf{P}} + (q_1 \boldsymbol{\alpha}_1 + \cdots + q_N \boldsymbol{\alpha}_N) \cdot c\mathbf{A}(\mathbf{R}) + Q\Phi(\mathbf{R}). \tag{90}$$

In matrix form we can write

$$\hat{H} = \mathbf{M}c^2 + \mathbf{a} \cdot c\hat{\mathbf{P}} - Q\mathbf{a}_Q \cdot c\mathbf{A}(\mathbf{R}) + Q\Phi(\mathbf{R}) \tag{91}$$

with

$$\mathbf{a}_Q = \frac{q_1 \boldsymbol{\alpha}_1 + \cdots + q_N \boldsymbol{\alpha}_N}{Q}. \tag{92}$$

If the charges are all the same, then $\mathbf{a}_Q = \mathbf{a}$; otherwise $\mathbf{a}_Q \neq \mathbf{a}$ and minimal coupling is inconsistent. This was noted in [5].

A possible resolution to these issues is to write the model instead as

$$\hat{H} = (\beta_1 + \cdots + \beta_N)mc^2 + \frac{1}{N}(\boldsymbol{\alpha}_1 + \cdots + \boldsymbol{\alpha}_N) \cdot c[\hat{\mathbf{P}} - Q\mathbf{A}(\mathbf{R})] + Q\Phi(\mathbf{R})$$
$$- \left[\left(q_1 - \frac{Q}{N}\right)\boldsymbol{\alpha}_1 + \cdots + \left(q_N - \frac{Q}{N}\right)\boldsymbol{\alpha}_N\right] \cdot c\mathbf{A}(\mathbf{R}), \tag{93}$$

where the terms on the first line can be associated with center of mass dynamics, and where terms on the second line involve internal transitions. In matrix form this is

$$\hat{H} = \mathbf{M}c^2 + \mathbf{a} \cdot c[\hat{\mathbf{P}} - Q\mathbf{A}(\mathbf{R})] + Q\Phi(\mathbf{R}) - (\mathbf{a}_Q - \mathbf{a}) \cdot cQ\mathbf{A}(\mathbf{R}). \tag{94}$$

These issues are perhaps more important in the case that include a realistic internal structure.

Different issues with minimal coupling for the Bargmann–Wigner model have been discussed in the literature [91,92].

6. Models for Nonrelativistic Composites

The nonrelativistic composite model is straightforward, both conceptually as well as mathematically. A big issue is the clean separation between center of mass and relative mass degrees of freedom, and there is no coupling between the total momentum and internal degrees of freedom except through external field interactions.

6.1. Equal mass model

One of the simplest models of this kind relevant to us is an equal mass Hamiltonian, which we focus on in the rest of the paper. Consider a Hamiltonian of the form

$$\hat{H} = \sum_j \frac{|\hat{\mathbf{p}}_j|^2}{2m} - \sum_j \frac{q_j}{2m}\left[\mathbf{A}(\mathbf{r}_j) \cdot \hat{\mathbf{p}}_j + \hat{\mathbf{p}}_j \cdot \mathbf{A}(\mathbf{r}_j)\right] + \sum_{j<k} \hat{V}_{jk}(\mathbf{r}_j - \mathbf{r}_k) + \sum_j q_j\Phi(\mathbf{r}_j), \tag{95}$$

where for simplicity we have not included the ponderomotive potential. The two-particle potential terms $\hat{V}_{jk}$ are intended to include both the strong force and Coulomb/electromagnetic coupling. Some years ago people worked with empirical nuclear potentials optimized against scattering data and few nucleon bound state properties [93–100]. More recently people have moved to nucleon interaction models derived from an effective chiral field theory [45,101–103]. We note that in these models there occur interactions between three or more nucleons which are used in calculations; in what follows the interaction will be written as a two-particle potential (in an effort to simplify the equations that result) with the understanding that the same arguments apply to the higher-order terms as well.

6.2. Relative and center of mass separation

We introduce relative and center of mass coordinates according to

$$\mathbf{R} = \frac{1}{N}\sum_j \mathbf{r}_j, \qquad \hat{\mathbf{P}} = \sum_j \hat{\mathbf{p}}_j, \tag{96}$$

$$\boldsymbol{\xi}_j = \mathbf{r}_j - \mathbf{R}, \qquad \hat{\boldsymbol{\pi}}_j = \hat{\mathbf{p}}_j - \frac{\hat{\mathbf{P}}}{N}, \tag{97}$$

where N is the total number of particles. With these definitions we have the relations

$$\sum_j \boldsymbol{\xi}_j = 0, \qquad \sum_j \hat{\boldsymbol{\pi}}_j = 0. \tag{98}$$

We can make use of these to separate the Hamiltonian according to

$$\hat{H} = \hat{H}_{\boldsymbol{\xi}} + \hat{H}_{\mathbf{R}} + \hat{H}_{\text{int}}, \tag{99}$$

where $\hat{H}_{\boldsymbol{\xi}}$ is the Hamiltonian for the relative system

$$\hat{H}_{\boldsymbol{\xi}} = \sum_j \frac{|\hat{\boldsymbol{\pi}}_j|^2}{2m} + \sum_{j<k} \hat{V}_{jk}(\boldsymbol{\xi}_j - \boldsymbol{\xi}_k). \tag{100}$$

The Hamiltonian for the center of mass system $\hat{H}_{\mathbf{R}}$ is

$$\hat{H}_{\mathbf{R}} = \frac{|\hat{\mathbf{P}}|^2}{2M}, \tag{101}$$

where M is the total mass

$$M = Nm \tag{102}$$

and the interaction with the external longitudinal and transverse fields are described by the Hamiltonian $\hat{H}_{\text{int}}$

$$\begin{aligned}
\hat{H}_{\text{int}} = &\sum_j \frac{q_j}{2m} \left[\mathbf{A}(\boldsymbol{\xi}_j + \mathbf{R}) \cdot \frac{\hat{\mathbf{P}}}{N} + \frac{\hat{\mathbf{P}}}{N} \cdot \mathbf{A}(\boldsymbol{\xi}_j + \mathbf{R}) \right] \\
&+ \sum_j \frac{q_j}{2m} \left[\mathbf{A}(\boldsymbol{\xi}_j + \mathbf{R}) \cdot \hat{\boldsymbol{\pi}}_j + \hat{\boldsymbol{\pi}}_j \cdot \mathbf{A}(\boldsymbol{\xi}_j + \mathbf{R}) \right] + \sum_j q_j \Phi(\boldsymbol{\xi}_j + \mathbf{R}).
\end{aligned} \tag{103}$$

In the Coulomb gauge $\nabla \cdot \mathbf{A} = 0$ (hence $\hat{\mathbf{p}}_j \cdot \mathbf{A}(\mathbf{r}_j) = 0$), so that in this special case we could write

$$\hat{H}_{\text{int}} = \sum_j \frac{q_j}{m} \mathbf{A}(\boldsymbol{\xi}_j + \mathbf{R}) \cdot \left(\frac{\hat{\mathbf{P}}}{N} + \hat{\boldsymbol{\pi}}_j \right) + \sum_j q_j \Phi(\boldsymbol{\xi}_j + \mathbf{R}). \tag{104}$$

6.3. Interaction with the external scalar potential

We might assume that the potential is slowly varying in the vicinity of the center of mass, and use a Taylor series approximation

$$\Phi(\mathbf{r}_j) = \Phi(\boldsymbol{\xi}_j + \mathbf{R}) = \Phi(\mathbf{R}) + \boldsymbol{\xi}_j \cdot (\nabla\Phi)_{\mathbf{R}} + \cdots \tag{105}$$

This allows us to write

$$\begin{aligned}
\sum_j q_j \Phi(\boldsymbol{\xi}_j + \mathbf{R}) &= \sum_j q_j \left[\Phi(\mathbf{R}) + \boldsymbol{\xi}_j \cdot (\nabla\Phi)_{\mathbf{R}} + \cdots \right] \\
&= Q\Phi(\mathbf{R}) + \sum_j q_j \boldsymbol{\xi}_j \cdot (\nabla\Phi) + \cdots \\
&= Q\Phi(\mathbf{R}) - \mathbf{d} \cdot \mathbf{E}_{\mathrm{L}}(\mathbf{R}) + \cdots,
\end{aligned} \tag{106}$$

where Q is the total charge $\sum_j q_j$, and where $\mathbf{d}$ is the (relative) dipole operator

$$\mathbf{d} = \sum_j q_j \boldsymbol{\xi}_j. \tag{107}$$

The longitudinal electric field is related to the potential through

$$\mathbf{E}_{\mathrm{L}} = -\nabla\Phi. \tag{108}$$

Here and in what follows, the field variables without an explicit associated position are presumed to be evaluated at the composite center of mass

$$\mathbf{E}_{\mathrm{L}}(\mathbf{R}) \rightarrow \mathbf{E}_{\mathrm{L}}, \qquad \Phi(\mathbf{R}) \rightarrow \Phi. \tag{109}$$

The scalar potential interacts with the composite as a whole through the potential at the center of mass position; there is a dipole interaction which mediates transitions between the basis states of the relative problem due to coupling with the longitudinal electric field; and the $\cdots$ indicates quadrupole and higher-order multipole longitudinal field interactions.

6.4. Interaction with the external vector potential

A similar approach can be used in connection with the vector potential. We can use a Taylor series expansion and write

$$\mathbf{A}(\mathbf{r}_j) = \mathbf{A}(\boldsymbol{\xi}_j + \mathbf{R}) = \mathbf{A}(\mathbf{R}) + [(\boldsymbol{\xi}_j \cdot \nabla)\mathbf{A}] + \cdots \tag{110}$$

To make progress we write

$$-\sum_j \frac{q_j}{2m}\left[\mathbf{A}(\mathbf{r}_j)\cdot\hat{\mathbf{p}}_j + \hat{\mathbf{p}}_j\cdot\mathbf{A}(\mathbf{r}_j)\right] = -\frac{Q}{2M}\left[\mathbf{A}\cdot\hat{\mathbf{P}} + \hat{\mathbf{P}}\cdot\mathbf{A}\right] - \left[\sum_j\left(q_j - \frac{Q}{N}\right)\frac{\hat{\boldsymbol{\pi}}_j}{m}\right]\cdot\mathbf{A}$$

$$-\sum_j\frac{q_j}{2m}[(\boldsymbol{\xi}_j\cdot\nabla)\mathbf{A}]\cdot\frac{\hat{\mathbf{P}}}{N} - \frac{\hat{\mathbf{P}}}{N}\cdot\sum_j\frac{q_j}{2m}[(\boldsymbol{\xi}_j\cdot\nabla)\mathbf{A}]$$

$$-\sum_j\frac{q_j}{2m}[(\boldsymbol{\xi}_j\cdot\nabla)\mathbf{A}]\cdot\hat{\boldsymbol{\pi}}_j - \sum_j\frac{q_j}{2m}\hat{\boldsymbol{\pi}}_j\cdot[(\boldsymbol{\xi}_j\cdot\nabla)\mathbf{A}] + \cdots \quad (111)$$

The first term on the right hand side describes the interaction of the composite as a whole with the vector potential, and the second term gives rise to dipole transitions coupling to the transverse electric field. The terms in the next two lines give rise to magnetic dipole interactions and second-order interactions with the transverse electric field; in the case of center of mass coupling (second line) and relative coupling (third line).

The magnetic dipole interaction is normally isolated making use of a specific vector potential for a uniform magnetic field, such as [104]

$$\mathbf{A}(\mathbf{r}) = \frac{1}{2}\mathbf{B}(\mathbf{r})\times\mathbf{r}. \quad (112)$$

However, we would prefer a more general treatment if possible. We know that $(\boldsymbol{\xi}\cdot\nabla)\mathbf{A}$ generates terms connected with the magnetic dipole interaction, as well as others. It is possible to isolate the magnetic interactions by using

$$(\boldsymbol{\xi}\cdot\nabla)\mathbf{A} = -\frac{1}{2}\boldsymbol{\xi}\times\mathbf{B} + \frac{1}{2}\left[(\boldsymbol{\xi}\cdot\nabla)\mathbf{A} + \nabla(\boldsymbol{\xi}\cdot\mathbf{A})\right], \quad (113)$$

where it ends up that the first term can be associated with the magnetic interactions. If we make use of this we obtain

$$-\sum_j\frac{q_j}{2m}\left[\mathbf{A}(\mathbf{r}_j)\cdot\hat{\mathbf{p}}_j + \hat{\mathbf{p}}_j\cdot\mathbf{A}(\mathbf{r}_j)\right] = -\frac{Q}{2M}\left(\mathbf{A}\cdot\hat{\mathbf{P}} + \hat{\mathbf{P}}\cdot\mathbf{A}\right) - \left[\sum_j\left(q_j - \frac{Q}{N}\right)\frac{\hat{\boldsymbol{\pi}}_j}{m}\right]\cdot\mathbf{A}$$

$$-\frac{1}{2}\left(\sum_j q_j\boldsymbol{\xi}_j\right)\times\frac{\hat{\mathbf{P}}}{M}\cdot\mathbf{B} - \left(\sum_j\frac{q_j}{2m}\boldsymbol{\xi}_j\times\hat{\boldsymbol{\pi}}_j\right)\cdot\mathbf{B} + \cdots \quad (114)$$

The third term on the right hand side is the contribution of the relative angular momentum to the magnetic dipole interaction, followed by the contribution to the magnetic dipole interaction due to center of mass motion.
We can rewrite this more simply as

$$-\frac{q}{2m}\sum_j\left[\mathbf{A}(\mathbf{r}_j)\cdot\hat{\mathbf{p}}_j + \hat{\mathbf{p}}_j\cdot\mathbf{A}(\mathbf{r}_j)\right] = -\frac{Q}{2M}\left(\mathbf{A}\cdot\hat{\mathbf{P}} + \hat{\mathbf{P}}\cdot\mathbf{A}\right) - \hat{\mathbf{j}}\cdot\mathbf{A} - \hat{\boldsymbol{\mu}}_l\cdot\mathbf{B}$$

$$-\frac{1}{2}\mathbf{d}\times\frac{\hat{\mathbf{P}}}{M}\cdot\mathbf{B} + \cdots, \quad (115)$$

where we recall that $\mathbf{d}$ is the relative dipole operator $\sum_j q_j \boldsymbol{\xi}_j$, and where

$$\hat{\mathbf{j}} = \sum_j \left(q_j - \frac{Q}{N} \right) \frac{\hat{\boldsymbol{\pi}}_j}{m} \tag{116}$$

is the relative current operator, and

$$\hat{\boldsymbol{\mu}}_l = \sum_j \frac{q_j}{2m} \boldsymbol{\xi}_j \times \hat{\boldsymbol{\pi}}_j \tag{117}$$

is the relative angular momentum contribution to the magnetic dipole moment.

6.5. Resulting Hamiltonian for a nonrelativistic composite

We can assemble the results above and write

$$\begin{aligned}
\hat{H} = &\frac{|\hat{\mathbf{P}}|^2}{2M} + Q\Phi - \frac{Q}{2M} \left(\mathbf{A} \cdot \hat{\mathbf{P}} + \hat{\mathbf{P}} \cdot \mathbf{A} \right) \\
&+ \sum_j \frac{|\hat{\boldsymbol{\pi}}_j|^2}{2m} + \sum_{j<k} \hat{V}_{jk}(|\boldsymbol{\xi}_j - \boldsymbol{\xi}_k|) \\
&- \mathbf{d} \cdot \mathbf{E}_L - \hat{\mathbf{j}} \cdot \mathbf{A} - \hat{\boldsymbol{\mu}}_l \cdot \mathbf{B} - \frac{1}{2} \mathbf{d} \times \frac{\hat{\mathbf{P}}}{M} \cdot \mathbf{B} + \cdots
\end{aligned} \tag{118}$$

In the first line we have terms describing the composite as a particle interacting with external fields; in the second line we see terms that describe the internal structure of the composite in terms of relative degrees of freedom. Terms that appear on the third line describes coupling between the internal degrees of freedom and the longitudinal and transverse electric fields separately, and with the magnetic field. In the last line is a term that accounts for the center of mass contribution to the magnetic dipole interaction, which couples the center of mass with internal degrees of freedom in a magnetic field.

7. Composite Model from a Many-particle Dirac Formalism

In this section we extend the development of a model for a composite particle to the many-particle Dirac formalism. This approach has the disadvantage that it is not covariant, so that the resulting relativistic composite model will not be covariant. On the other hand, we are able to carry out a construction systematically with this model, which is less straightforward with a covariant formalism. We note that in spite of its shortcomings, the Dirac formalism is widely used for atomic, molecular and nuclear physics.

7.1. Relativistic equal mass model

We consider a model based on the many-particle Dirac Hamiltonian

$$\hat{H} = \sum_j \beta_j mc^2 + \sum_j \boldsymbol{\alpha}_j \cdot c[\hat{\mathbf{p}}_j - q_j \mathbf{A}(\mathbf{r}_j)] + \sum_{j<k} \hat{V}_{jk}(\mathbf{r}_j - \mathbf{r}_k) + \sum_j q_j \Phi(\mathbf{r}_j). \tag{119}$$

This kind of model has been of interest since the earliest efforts to develop a relativistic description of quantum systems with two or more particles [105–110]. Keep in mind that in this kind of model there is the possibility of both positive energy and negative energy solutions, so that bound states dissolve into the associated continuum (Brown–Ravenhall disease); in models derived from field theory, this issue is resolved through the appearance of projection operators [111–116]. In the majority of the subsequent literature the projection operators are not written out explicitly; in what follows we will also suppress the projection operators.

We are interested here in composite models for nuclei based on a Dirac phenomenology for nucleons. Consequently, it would be reasonable to use equal masses for the nucleons, and the interaction potential $\hat{V}_{jk}$ includes contributions from both the strong force and electromagnetic interactions.

7.2. Relative and center of mass variables

Relative and center of mass variables are defined once again according to

$$\mathbf{R} = \frac{1}{N} \sum_j \mathbf{r}_j, \qquad \hat{\mathbf{P}} = \sum_j \hat{\mathbf{p}}_j,$$

$$\boldsymbol{\xi}_j = \mathbf{r}_j - \mathbf{R}, \qquad \hat{\boldsymbol{\pi}}_j = \hat{\mathbf{p}}_j - \frac{\hat{\mathbf{P}}}{N}.$$

The Hamiltonian written in terms of these variables is

$$
\begin{aligned}
\hat{H} = & \frac{1}{N} \boldsymbol{\alpha}_j \cdot c[\hat{\mathbf{P}} - Q\mathbf{A}(\mathbf{R})] + \sum_j \beta_j mc^2 + \sum_j \boldsymbol{\alpha}_j \cdot c\hat{\boldsymbol{\pi}}_j + \sum_{j<k} \hat{V}_{jk}(\boldsymbol{\xi}_j - \boldsymbol{\xi}_k) \\
& + \sum_j q_j \Phi(\mathbf{R} + \boldsymbol{\xi}_j) - \sum_j \boldsymbol{\alpha}_j \cdot c \left[q_j \mathbf{A}(\mathbf{R} + \boldsymbol{\xi}_j) - \frac{Q}{N} \mathbf{A}(\mathbf{R}) \right].
\end{aligned}
\tag{120}
$$

If we use Taylor series expansions of the potentials around the center of mass position, we can write for the relativistic composite a model of the form

$$
\begin{aligned}
\hat{H} = & \sum_j \beta_j mc^2 + \frac{1}{N} \sum_j \boldsymbol{\alpha}_j \cdot c(\hat{\mathbf{P}} - Q\mathbf{A}) + Q\Phi + \sum_j \boldsymbol{\alpha}_j \cdot c\hat{\boldsymbol{\pi}}_j + \sum_{j<k} \hat{V}_{jk} \\
& + \left(\sum_j q_j \boldsymbol{\xi}_j \right) \cdot \nabla\Phi - \sum_j \boldsymbol{\alpha}_j \cdot c \left(q_j - \frac{Q}{N} \right) \mathbf{A} - \sum_j \boldsymbol{\alpha}_j \cdot c q_j (\boldsymbol{\xi}_j \cdot \nabla) \mathbf{A} + \cdots
\end{aligned}
\tag{121}
$$

In the first line we see a relativistic description of the composite interacting with external fields, and also a relativistic description of the internal problem; however, both of these models share the same mass terms. In the second line we see in the first term an electric dipole interaction with the longitudinal electric field; we see next the electric dipole interaction with the transverse electric field; and higher-order interactions are included in the terms that follow.

7.3. Rest frame model

The many-particle Dirac model above is widely used; however, from the discussion above it seems clear that for the internal relative problem in the absence of external fields we should be interested in the relative Hamiltonian

$$\hat{H} = \sum_j \beta_j mc^2 + \sum_j \boldsymbol{\alpha}_j \cdot c\hat{\boldsymbol{\pi}}_j + \sum_{j<k} \hat{V}_{jk}. \tag{122}$$

This model is less widely used; however, there are papers where it has been considered. In the case of the two-body problem (without external field coupling) this would be considered as a Kemmer–Fermi–Yang Hamiltonian [117,118]. This kind of model has been widely used over the years; in the case of equal mass models, to describe positronium [119–121], the deuteron and two-nucleon models [122–126], and to describe mesons [127–131]. Models of this kind with nonequal masses have been used to describe the hydrogen atom [132–136]. Three-body problems Dirac models have been studied in connection with quark models for baryons [125–141]. We draw attention to the Dirac phenomenology for nuclear structure [41–44] where the rest frame is assumed, and in most cases the center of mass contributions are removed approximately at the end of the calculation.

7.4. Dirac–Pauli models

In the event that our original model includes Pauli terms, we would start out with

$$\hat{H} = \sum_j \beta_j mc^2 + \sum_j \boldsymbol{\alpha}_j \cdot c[\hat{\mathbf{p}}_j - q_j \mathbf{A}(\mathbf{r}_j)] + \sum_{j<k} \hat{V}_{jk} + \sum_j q_j \Phi(\mathbf{r}_j)$$
$$- \frac{e\hbar}{2m} \sum_j \lambda_j \beta_j \left(\boldsymbol{\Sigma}_j \cdot \mathbf{B}(\mathbf{r}_j) - i\boldsymbol{\alpha}_j \cdot \mathbf{E}(\mathbf{r}_j) \right), \tag{123}$$

where

$$\lambda_j = \begin{cases} \dfrac{g_p}{2} - 1 & \text{protons} \\[2mm] \dfrac{g_n}{2} & \text{neutrons} \end{cases} \tag{124}$$

approximating the proton and neutron masses as being equal. We recall that

$$\boldsymbol{\Sigma} = \begin{bmatrix} \mathbf{0} & \boldsymbol{\sigma} \\ \boldsymbol{\sigma} & \mathbf{0} \end{bmatrix}.$$

The Pauli interaction includes an anomalous magnetic dipole interaction along with the corresponding correction to the spin–orbit interaction.

Of interest here is the composite model that results; we may write

$$\hat{H} = \sum_j \beta_j mc^2 + \frac{1}{N} \sum_j \boldsymbol{\alpha}_j \cdot c(\hat{\mathbf{P}} - Q\mathbf{A}) + Q\Phi + \sum_j \boldsymbol{\alpha}_j \cdot c\hat{\boldsymbol{\pi}}_j + \sum_{j<k} \hat{V}_{jk}$$
$$- \mathbf{d} \cdot \mathbf{E}_L - \hat{\boldsymbol{\mu}}_a \cdot \mathbf{B} - \hat{\mathbf{j}} \cdot \mathbf{A} + i\frac{e\hbar}{2m} \sum_j \lambda_j \beta_j \boldsymbol{\alpha}_j \cdot \mathbf{E} - \sum_j \boldsymbol{\alpha}_j \cdot cq_j(\boldsymbol{\xi}_j \cdot \nabla)\mathbf{A} + \cdots, \qquad (125)$$

where the relativistic relative current operator is

$$\hat{\mathbf{j}} = \sum_j \left(q_j - \frac{Q}{N} \right) c\boldsymbol{\alpha}_j \qquad (126)$$

and where the anomalous magnetic dipole moment operator is

$$\hat{\boldsymbol{\mu}}_a = \frac{e\hbar}{2m} \sum_j \lambda_j \beta_j \boldsymbol{\Sigma}_j. \qquad (127)$$

8. Composite Model from Elimination of Negative Energy States

In this section we consider low-order relativistic corrections based on the elimination of negative energy states (or sometimes called Pauli reduction) from a Dirac model. We are interested in this approach since it is the simplest and most direct approximation possible which results in a model that is close to being nonrelativistic. Such an approach was used early on by Darwin [142], Breit [105], and Gaunt [143]; and it has been made use of many times subsequently [106,107,109,122–124,144–156].

8.1. Elimination of negative energy states

To make progress, we begin with the eigenvalue equation for the many-particle eigenvalue equation

$$E\Psi = \left\{ \sum_j \beta_j mc^2 + \sum_j \boldsymbol{\alpha}_j \cdot c[\hat{\mathbf{p}}_j - q_j \mathbf{A}(\mathbf{r}_j)] + \sum_{j<k} \hat{V}_{jk}(\mathbf{r}_j - \mathbf{r}_k) + \sum_j q_j \Phi(\mathbf{r}_j) \right\} \Psi. \qquad (128)$$

The relativistic wavefunction Ψ in this case has 4^N components, which provides motivation for us to consider a nonrelativistic approximation with fewer components.

The issue we face in this discussion is that there are different sectors in which both positive energy components and negative energy components occur, and we need to keep track of them. The nonrelativistic sector is then the one containing all positive energy components; the associated part of the wave function will be denoted by $\Psi_{+\cdots+}$, where the $+$ signs are associated with different positive energy pieces associated with the different particles.

We can use this kind of notation to write coupled eigenvalue equations of the form [157]

$$E\Psi_{+\cdots+} = \left[Nmc^2 + \sum_{j<k} \hat{V}_{jk} + \sum_j q_j \Phi \right] \Psi_{+\cdots+} + \boldsymbol{\sigma}_1 \cdot c(\hat{\mathbf{p}}_1 - q_1 \mathbf{A})\Psi_{-+\cdots+}$$

$$+ \cdots + \boldsymbol{\sigma}_N \cdot c(\hat{\mathbf{p}}_N - q_N \mathbf{A})\Psi_{+\cdots+-}$$

$$E\Psi_{-+\cdots+} = \left[(N-2)mc^2 + \sum_{j<k} \hat{V}_{jk} + \sum_j q_j \Phi \right] \Psi_{-+\cdots+} + \boldsymbol{\sigma}_1 \cdot c(\hat{\mathbf{p}}_1 - q_1 \mathbf{A})\Psi_{++\cdots+}$$

$$+ \boldsymbol{\sigma}_2 \cdot c(\hat{\mathbf{p}}_2 - q_2 \mathbf{A})\Psi_{--+\cdots+} + \cdots + \boldsymbol{\sigma}_N \cdot c(\hat{\mathbf{p}}_N - q_N \mathbf{A})\Psi_{-\cdots+-}$$

$$\vdots \tag{129}$$

The mass energy decreases by $2mc^2$ with each increase in the number of $-$, since we lose one positive energy particle and gain a negative energy one. Two-body versions of this approach are discussed in [122,158]. In this discussion the interaction has been taken to be the same for positive energy and negative energy sectors; modifications in the case of other potential models is straightforward.

If the problem is not overly relativistic then the channels with two or more negative energy components should have sufficiently small occupation that we might neglect them. We can develop an approximate solution for channels with a single negative energy sector according to

$$\left[E - (N-2)mc^2 + \sum_{j<k} \hat{V}_{jk} + \sum_j q_j \Phi \right] \Psi_{-+\cdots+} \;\rightarrow\; \boldsymbol{\sigma}_1 \cdot c(\hat{\mathbf{p}}_1 - q_1 \mathbf{A})\Psi_{++\cdots+} \tag{130}$$

with similar expressions for other channels. Substituting back leads to

$$E\Psi_{+\cdots+} \approx \left[Nmc^2 + \sum_{j<k} \hat{V}_{jk} + \sum_j q_j \Phi \right] \Psi_{+\cdots+}$$

$$+ \boldsymbol{\sigma}_1 \cdot c(\hat{\mathbf{p}}_1 - q_1 \mathbf{A}) \left[E - (N-2)mc^2 + \sum_{j<k} \hat{V}_{jk} + \sum_j q_j \Phi \right]^{-1} \boldsymbol{\sigma}_1 \cdot c(\hat{\mathbf{p}}_1 - q_1 \mathbf{A})\Psi_{++\cdots+}$$

$$\vdots$$

$$+ \boldsymbol{\sigma}_N \cdot c(\hat{\mathbf{p}}_N - q_N \mathbf{A}) \left[E - (N-2)mc^2 + \sum_{j<k} \hat{V}_{jk} + \sum_j q_j \Phi \right]^{-1} \boldsymbol{\sigma}_N \cdot c(\hat{\mathbf{p}}_N - q_N \mathbf{A})\Psi_{++\cdots+}$$

$$\tag{131}$$

If we take $E - (N-2)mc^2$ to be $2mc^2$, then the approximate nonrelativistic Hamiltonian is

$$
\hat{H} = Mc^2 + \sum_j \frac{\left(\boldsymbol{\sigma}_j \cdot [\hat{\mathbf{p}}_j - q_j \mathbf{A}(\mathbf{r}_j)]\right)^2}{2m} + \sum_{j<k} \hat{V}_{jk}(\mathbf{r}_j - \mathbf{r}_k) + \sum_j q_j \Phi(\mathbf{r}_j)
$$

$$
- \frac{1}{(2mc^2)^2} \sum_l \boldsymbol{\sigma}_l \cdot [\hat{\mathbf{p}}_l - q_l \mathbf{A}(\mathbf{r}_l)] \left(\sum_{j<k} \hat{V}_{jk}(\mathbf{r}_j - \mathbf{r}_k) + \sum_j q_j \Phi(\mathbf{r}_j) \right) \boldsymbol{\sigma}_l \cdot [\hat{\mathbf{p}}_l - q_l \mathbf{A}(\mathbf{r}_l)] + \cdots \quad (132)
$$

In the first line we see terms similar to those encountered in the last section where we discussed the nonrelativistic composite, and in what follows we will see that the spin contribution to the magnetic dipole interaction is now included. Spin–orbit and other relativistic corrections result from the new terms in the second line.

8.2. Keeping the Hermitian part

If we work with this model as is we encounter terms which are nonHermitian [159,160]; this is one of the reasons that this general approach is not more widely used. This problem is discussed at some length in [149]. People tend to prefer the Foldy–Wouthuysen transformation [160] instead since this issue does not arise; the F–W transformation has other advantages that will be evident later on.

If we follow the arguments of [149] we arrive at a Hamiltonian of the form

$$
\hat{H} \;\to\; Mc^2 + \sum_j \frac{\left(\boldsymbol{\sigma}_j \cdot [\hat{\mathbf{p}}_j - q_j \mathbf{A}(\mathbf{r}_j)]\right)^2}{2m} + \sum_{j<k} \hat{V}_{jk}(\mathbf{r}_j - \mathbf{r}_k) + \sum_j q_j \Phi(\mathbf{r}_j)
$$

$$
- \frac{1}{8m^3c^2} \left(\sum_j \left| \boldsymbol{\sigma}_j \cdot [\hat{\mathbf{p}}_j - q_j \mathbf{A}(\mathbf{r}_j)] \right|^2 \right) \left(\sum_k \left| \boldsymbol{\sigma}_k \cdot [\hat{\mathbf{p}}_k - q_k \mathbf{A}(\mathbf{r}_k)] \right|^2 \right)
$$

$$
- \frac{1}{8m^2c^2} \sum_l \left| \boldsymbol{\sigma}_l \cdot [\hat{\mathbf{p}}_l - q_l \mathbf{A}(\mathbf{r}_l)] \right|^2 \left(\sum_{j<k} \hat{V}_{jk}(\mathbf{r}_j - \mathbf{r}_k) + \sum_j q_j \Phi(\mathbf{r}_j) \right)
$$

$$
+ \frac{1}{4m^2c^2} \sum_l \boldsymbol{\sigma}_l \cdot [\hat{\mathbf{p}}_l - q_l \mathbf{A}(\mathbf{r}_l)] \left(\sum_{j<k} \hat{V}_{jk}(\mathbf{r}_j - \mathbf{r}_k) + \sum_j q_j \Phi(\mathbf{r}_j) \right) \boldsymbol{\sigma}_l \cdot [\hat{\mathbf{p}}_l - q_l \mathbf{A}(\mathbf{r}_l)]
$$

$$
- \frac{1}{8m^2c^2} \sum_l \left(\sum_{j<k} \hat{V}_{jk}(\mathbf{r}_j - \mathbf{r}_k) + \sum_j q_j \Phi(\mathbf{r}_j) \right) \left| \boldsymbol{\sigma}_l \cdot [\hat{\mathbf{p}}_l - q_l \mathbf{A}(\mathbf{r}_l)] \right|^2. \quad (133)
$$

In this model we have a nonrelativistic composite model augmented with low-order relativistic corrections; however, we have some work to do to reduce it in what follows to a more standard form.

8.3. Spin magnetic dipole interaction

We can make use of the identity

$$(\boldsymbol{\sigma} \cdot \mathbf{a})(\boldsymbol{\sigma} \cdot \mathbf{a}) = \mathbf{a} \cdot \mathbf{b} + i\boldsymbol{\sigma} \cdot \mathbf{a} \times \mathbf{b} \tag{134}$$

to expand

$$\sum_j \frac{\left(\boldsymbol{\sigma}_j \cdot [\hat{\mathbf{p}}_j - q_j\mathbf{A}(\mathbf{r}_j)]\right)^2}{2m} = \sum_j \frac{\left|\hat{\mathbf{p}}_j - q_j\mathbf{A}(\mathbf{r}_j)\right|^2}{2m} - i\sum_j q_j\left(\boldsymbol{\sigma}_j \cdot \hat{\mathbf{p}}_j \times \mathbf{A}(\mathbf{r}_j) + \boldsymbol{\sigma}_j \cdot \mathbf{A}(\mathbf{r}_j) \times \hat{\mathbf{p}}_j\right)$$

$$= \sum_j \frac{\left|\hat{\mathbf{p}}_j - q_j\mathbf{A}(\mathbf{r}_j)\right|^2}{2m} - \boldsymbol{\mu}_s \cdot \mathbf{B}(\mathbf{r}_j), \tag{135}$$

where

$$\boldsymbol{\mu}_s = \sum_j \frac{\hbar q_j}{2m}\boldsymbol{\sigma}_j. \tag{136}$$

8.4. Terms involving the external electrostatic potential

We can collect together higher-order terms involving the electrostatic potential Φ and write

$$-\frac{1}{8m^2c^2}\sum_l \left|\boldsymbol{\sigma}_l \cdot [\hat{\mathbf{p}}_l - q_l\mathbf{A}(\mathbf{r}_l)]\right|^2 \left(\sum_j q_j\Phi(\mathbf{r}_j)\right)$$

$$+\frac{1}{4m^2c^2}\sum_l \boldsymbol{\sigma}_l \cdot [\hat{\mathbf{p}}_l - q_l\mathbf{A}(\mathbf{r}_l)]\left(\sum_j q_j\Phi(\mathbf{r}_j)\right)\boldsymbol{\sigma}_l \cdot [\hat{\mathbf{p}}_l - q_l\mathbf{A}(\mathbf{r}_l)]$$

$$-\frac{1}{8m^2c^2}\sum_l \left(\sum_j q_j\Phi(\mathbf{r}_j)\right)\left|\boldsymbol{\sigma}_l \cdot [\hat{\mathbf{p}}_l - q_l\mathbf{A}(\mathbf{r}_l)]\right|^2$$

$$= -\frac{1}{8m^2c^2}\sum_l\sum_j \left[\boldsymbol{\sigma}_l \cdot [\hat{\mathbf{p}}_l - q_l\mathbf{A}(\mathbf{r}_l)], \left[\boldsymbol{\sigma}_l \cdot [\hat{\mathbf{p}}_l - q_l\mathbf{A}(\mathbf{r}_l)], q_j\Phi(\mathbf{r}_j)\right]\right]$$

$$= -i\frac{\hbar}{8m^2c^2}\sum_j q_j\left[\boldsymbol{\sigma}_j \cdot [\hat{\mathbf{p}}_j - q_l\mathbf{A}(\mathbf{r}_j)], \boldsymbol{\sigma}_j \cdot \mathbf{E}_L(\mathbf{r}_j)\right]$$

$$= -\frac{\hbar^2}{8m^2c^2}\sum_j q_j\nabla_j \cdot \mathbf{E}_L(\mathbf{r}_j)$$

$$+\frac{\hbar}{8m^2c^2}\sum_j q_j\boldsymbol{\sigma}_j \cdot \left([\hat{\mathbf{p}}_j - q_j\mathbf{A}(\mathbf{r}_j)] \times \mathbf{E}_L(\mathbf{r}_j) - \mathbf{E}_L(\mathbf{r}_j) \times [\hat{\mathbf{p}}_j - q_j\mathbf{A}(\mathbf{r}_j)]\right). \tag{137}$$

We can express this in terms of center of mass and relative variables according to

$$-i\frac{\hbar}{8m^2c^2}\sum_j q_j \left[\boldsymbol{\sigma}_j \cdot [\hat{\mathbf{p}}_j - q_j\mathbf{A}(\mathbf{r}_j)], \boldsymbol{\sigma}_j \cdot \mathbf{E}_L(\mathbf{r}_j) \right]$$

$$= -i\frac{\hbar}{8Mmc^2}\sum_j q_j \left[\boldsymbol{\sigma}_j \cdot [\hat{\mathbf{P}} - Q\mathbf{A}(\mathbf{R})], \boldsymbol{\sigma}_j \cdot [\mathbf{E}_L(\mathbf{R}) + (\boldsymbol{\xi}_j \cdot \nabla)\mathbf{E} + \cdots] \right]$$

$$\quad -i\frac{\hbar}{8m^2c^2}\sum_j q_j \left[\boldsymbol{\sigma}_j \cdot \left(\hat{\boldsymbol{\pi}}_j - q_j\mathbf{A}(\mathbf{R} + \boldsymbol{\xi}_j) + \frac{Q}{N}\mathbf{A}(\mathbf{R}) \right), \boldsymbol{\sigma}_j \cdot [\mathbf{E}_L(\mathbf{R}) + (\boldsymbol{\xi}_j \cdot \nabla)\mathbf{E} + \cdots] \right]$$

$$= -\frac{\hbar^2 Q}{8Mmc^2}\nabla \cdot \mathbf{E}_L + \frac{\hbar}{8Mmc^2}\sum_j q_j\boldsymbol{\sigma}_j \cdot \left((\hat{\mathbf{P}} - Q\mathbf{A}) \times \mathbf{E}_L - \mathbf{E}_L \times (\hat{\mathbf{P}} - Q\mathbf{A}) \right)$$

$$\quad + \frac{\hbar}{8m^2c^2}\sum_j q_j\boldsymbol{\sigma}_j \cdot \left[\left(\hat{\boldsymbol{\pi}}_j - q_j\mathbf{A}(\mathbf{R} + \boldsymbol{\xi}_j) + \frac{Q}{N}\mathbf{A} \right) \mathbf{E}_L(\mathbf{R}) - \mathbf{E}_L(\mathbf{R}) \times \left(\hat{\boldsymbol{\pi}}_j - q_j\mathbf{A}(\mathbf{R} + \boldsymbol{\xi}_j) + \frac{Q}{N}\mathbf{A} \right) \right]$$

$$\quad + \cdots \tag{138}$$

8.5. Terms involving the particle–particle interaction

Higher-order terms involving the interaction can be collected to give

$$-\frac{1}{8m^2c^2}\sum_l \left| \boldsymbol{\sigma}_l \cdot [\hat{\mathbf{p}}_l - q_l\mathbf{A}(\mathbf{r}_l)] \right|^2 \left(\sum_{j<k} \hat{V}_{jk}(\mathbf{r}_j - \mathbf{r}_k) \right)$$

$$+\frac{1}{4m^2c^2}\sum_l \boldsymbol{\sigma}_l \cdot [\hat{\mathbf{p}}_l - q_l\mathbf{A}(\mathbf{r}_l)] \left(\sum_{j<k} \hat{V}_{jk}(\mathbf{r}_j - \mathbf{r}_k) \right) \boldsymbol{\sigma}_l \cdot [\hat{\mathbf{p}}_l - q_l\mathbf{A}(\mathbf{r}_l)]$$

$$-\frac{1}{8m^2c^2}\sum_l \left(\sum_{j<k} \hat{V}_{jk}(\mathbf{r}_j - \mathbf{r}_k) \right) \left| \boldsymbol{\sigma}_l \cdot [\hat{\mathbf{p}}_l - q_l\mathbf{A}(\mathbf{r}_l)] \right|^2$$

$$= -\frac{1}{8m^2c^2}\sum_{j<k}\sum_{l=j,k} \left[\boldsymbol{\sigma}_l \cdot [\hat{\mathbf{p}}_l - q_l\mathbf{A}(\mathbf{r}_l)], \left[\boldsymbol{\sigma}_l \cdot [\hat{\mathbf{p}}_l - q_l\mathbf{A}(\mathbf{r}_l)], \hat{V}_{jk}(\mathbf{r}_j - \mathbf{r}_k) \right] \right]. \tag{139}$$

Since the particle-particle interaction contains spin matrices, in general we cannot carry the development much further. If we express this in terms of center of mass and relative coordinates, we can write

$$-\frac{1}{8m^2c^2}\sum_{j<k}\sum_{l=j,k}\left[\boldsymbol{\sigma}_l\cdot[\hat{\mathbf{p}}_l-q_l\mathbf{A}(\mathbf{r}_l)],\left[\boldsymbol{\sigma}_l\cdot[\hat{\mathbf{p}}_l-q_l\mathbf{A}(\mathbf{r}_l)],\hat{V}_{jk}(\mathbf{r}_j-\mathbf{r}_k)\right]\right]$$

$$=-\frac{1}{8M^2c^2}\sum_{j<k}\sum_{l=j,k}\left[\boldsymbol{\sigma}_l\cdot[\hat{\mathbf{P}}-Q\mathbf{A}(\mathbf{R})],\left[\boldsymbol{\sigma}_l\cdot[\hat{\mathbf{P}}-Q\mathbf{A}(\mathbf{R})],\hat{V}_{jk}(\boldsymbol{\xi}_j-\boldsymbol{\xi}_k)\right]\right]$$

$$-\frac{1}{8Mmc^2}\sum_{j<k}\sum_{l=j,k}\left[\boldsymbol{\sigma}_l\cdot[\hat{\mathbf{P}}-Q\mathbf{A}(\mathbf{R})],\left[\boldsymbol{\sigma}_l\cdot\left(\hat{\boldsymbol{\pi}}_l-q_l\mathbf{A}(\mathbf{R}+\boldsymbol{\xi}_l)+\frac{Q}{N}\mathbf{A}(\mathbf{R})\right),\hat{V}_{jk}(\boldsymbol{\xi}_j-\boldsymbol{\xi}_k)\right]\right]$$

$$-\frac{1}{8Mmc^2}\sum_{j<k}\sum_{l=j,k}\left[\boldsymbol{\sigma}_l\cdot\left(\hat{\boldsymbol{\pi}}_l-q_l\mathbf{A}(\mathbf{R}+\boldsymbol{\xi}_l)+\frac{Q}{N}\mathbf{A}(\mathbf{R})\right),\left[\boldsymbol{\sigma}_l\cdot[\hat{\mathbf{P}}-Q\mathbf{A}(\mathbf{R})],\hat{V}_{jk}(\boldsymbol{\xi}_j-\boldsymbol{\xi}_k)\right]\right]$$

$$-\frac{1}{8m^2c^2}\sum_{j<k}\sum_{l=j,k}\left[\boldsymbol{\sigma}_l\cdot\left(\hat{\boldsymbol{\pi}}_l-q_l\mathbf{A}(\mathbf{R}+\boldsymbol{\xi}_l)+\frac{Q}{N}\mathbf{A}(\mathbf{R})\right),\left[\boldsymbol{\sigma}_l\cdot\left(\hat{\boldsymbol{\pi}}_l-q_l\mathbf{A}(\mathbf{R}+\boldsymbol{\xi}_l)+\frac{Q}{N}\mathbf{A}(\mathbf{R})\right),\right.\right.$$

$$\left.\left.\hat{V}_{jk}(\boldsymbol{\xi}_j-\boldsymbol{\xi}_k)\right]\right]. \tag{140}$$

We see a much larger set of terms present in this case.

Included in this expression are nuclear spin–orbit terms

$$-\frac{1}{8m^2c^2}\sum_{j<k}\sum_{l=j,k}\left[\boldsymbol{\sigma}_l\cdot\hat{\boldsymbol{\pi}}_l,\left[\boldsymbol{\sigma}_l\cdot\hat{\boldsymbol{\pi}}_l,\hat{V}_{jk}(\boldsymbol{\xi}_j-\boldsymbol{\xi}_k)\right]\right], \tag{141}$$

which have long been of interest in the literature [144,145,147,151–154,161,162].

Also present are terms that involve interactions between the relative degrees of freedom and the transverse electromagnetic field

$$-\frac{1}{8m^2c^2}\sum_{l}\sum_{j<k}\left[\boldsymbol{\sigma}_l\hat{\boldsymbol{\pi}}_l,\left[\boldsymbol{\sigma}_l\cdot\left(-q_l\mathbf{A}(\mathbf{R}+\boldsymbol{\xi}_l)+\frac{Q}{N}\mathbf{A}(\mathbf{R})\right),\hat{V}_{jk}(\boldsymbol{\xi}_j-\boldsymbol{\xi}_k)\right]\right]$$

$$-\frac{1}{8m^2c^2}\sum_{l}\sum_{j<k}\left[\boldsymbol{\sigma}_l\cdot\left(-q_l\mathbf{A}(\mathbf{R}+\boldsymbol{\xi}_l)+\frac{Q}{N}\mathbf{A}(\mathbf{R})\right),\left[\boldsymbol{\sigma}_l\cdot\hat{\boldsymbol{\pi}}_l,\hat{V}_{jk}(\boldsymbol{\xi}_j-\boldsymbol{\xi}_k)\right]\right]. \tag{142}$$

These terms can contribute a correction to the magnetic moment, and is included in the analysis of Margenau [163] and subsequent authors [163–165]; and also in other analyses [10,122,158,166]. We note that exchange currents have been of interest in the literature since the observation of Siegert [167] that there should be expected additional contributions from charged meson currents. Contributions from exchange currents are beyond what is included in this formalism (see [168]).

8.6. Terms linear in $\hat{\mathbf{P}}$ with no external fields

We draw attention to terms that include the total momentum and internal nuclear transitions, the lowest order of which are

$$-\frac{1}{8Mmc^2}\sum_l\sum_{j<k}\left[\boldsymbol{\sigma}_l\cdot\hat{\mathbf{P}},\left[\boldsymbol{\sigma}_l\cdot\hat{\boldsymbol{\pi}}_l,\hat{V}_{jk}\right]\right]-\frac{1}{8Mmc^2}\sum_l\sum_{j<k}\left[\boldsymbol{\sigma}_l\cdot\hat{\boldsymbol{\pi}}_l,\left[\boldsymbol{\sigma}_l\cdot\hat{\mathbf{P}},\hat{V}_{jk}\right]\right]. \tag{143}$$

Terms of these kinds are discussed infrequently in the literature; however, a few early (and important) discussions can be found [108,161]. We will follow up on the issues in these works later on. Consequently, the majority of works involving Pauli reduction are carried out in the rest frame, and the Foldy–Wouthuysen transformation is much more widely used.

Our attention has been drawn to terms of this sort recently in connection with the development for a theory for anomalies in condensed matter nuclear science [90]. The issue in this case is that it is in general problematic to develop a sizeable coupling with the internal nuclear degrees of freedom through conventional dipole interactions with external electric and magnetic fields. These terms however provide for a very strong coupling between lattice vibrations, which in a condensed matter setting are represented in the momentum $\hat{\mathbf{P}}$, and internal nuclear states. For this reason this kind of interaction naturally drew our attention. Issues associated with this kind of coupling have ultimately provided motivation for this work.

An effort was made to evaluate numerically coupling matrix elements due to this kind of interaction [90]. Unfortunately these calculations were carried out without taking into account the issues discussed in [149], and may need to be corrected.

We will return to this kind of coupling and the associated physical significance later on in this work when we consider Poincaré invariance.

8.7. Model for a composite

We can assemble the above results and write for a Hamiltonian for a nonrelativistic composite with relativistic corrections in the form

$$\begin{aligned}
\hat{H} = {}& Mc^2 + \sum_j\frac{\left|\hat{\mathbf{p}}_j-q_j\mathbf{A}(\mathbf{r}_j)\right|^2}{2m}+\sum_{j<k}\hat{V}_{jk}(\mathbf{r}_j-\mathbf{r}_k)+\sum_j q_j\Phi(\mathbf{r}_j)\\
&-\sum_j\frac{\hbar q_j}{2m}\boldsymbol{\sigma}_j\cdot\mathbf{B}(\mathbf{r}_j)-\frac{\hbar^2}{8m^2c^2}\sum_j q_j\nabla_j\cdot\mathbf{E}_L(\mathbf{r}_j)\\
&+\frac{\hbar}{8m^2c^2}\sum_j q_j\boldsymbol{\sigma}_j\cdot\left([\hat{\mathbf{p}}_j-q_j\mathbf{A}(\mathbf{r}_j)]\times\mathbf{E}_L(\mathbf{r}_j)-\mathbf{E}_L(\mathbf{r}_j)\times[\hat{\mathbf{p}}_j-q_j\mathbf{A}(\mathbf{r}_j)]\right)\\
&-\frac{1}{8m^2c^2}\sum_l\sum_{j<k}\left[\boldsymbol{\sigma}_l\cdot[\hat{\mathbf{p}}_l-q_l\mathbf{A}(\mathbf{r}_l)],\left[\boldsymbol{\sigma}_l\cdot[\hat{\mathbf{p}}_l-q_l\mathbf{A}(\mathbf{r}_l)],\hat{V}_{jk}(\mathbf{r}_j-\mathbf{r}_k)\right]\right].
\end{aligned}\tag{144}$$

We see the nonrelativistic composite model along with low-order relativistic corrections, all in reasonably standard form.

A feature of this model is that it contains a coupling between the center of mass momentum $\hat{\mathbf{P}}$ and internal degrees of freedom of interest to us on the same footing as the nuclear spin–orbit coupling, and other interactions that are known in the literature. Also, this interaction was derived relatively simply, involving little effort in the elimination of the negative energy sectors.

A disadvantage of the model is that the longitudinal electric field appears in the model differently than the transverse electric field, which should not be the case since we started from a gauge independent model. Although it is possible to remedy this problem within the context of the approach used in this section, it will be more convenient to move on to models based on the Foldy–Wouthuysen transformation where this problem is resolved.

In terms of center of mass and relative variables we can write

$$
\begin{aligned}
\hat{H} =& Mc^2 + \frac{|\hat{\mathbf{P}} - Q\mathbf{A}|^2}{2M} + Q\Phi \\
&+ \sum_j \frac{\left|\hat{\boldsymbol{\pi}}_j - q_j\mathbf{A}(\mathbf{R}+\boldsymbol{\xi}_j) - \frac{Q}{N}\mathbf{A}(\mathbf{R})\right|^2}{2m} + \sum_{j<k}\hat{V}_{jk} - \mathbf{d}\cdot\mathbf{E}_L - \boldsymbol{\mu}_s\cdot\mathbf{B} \\
&- \frac{\hbar^2 Q}{8Mmc^2}\nabla\cdot\mathbf{E}_L + \frac{\hbar}{8Mmc^2}\sum_j q_j\boldsymbol{\sigma}_j\cdot\Big((\hat{\mathbf{P}}-Q\mathbf{A})\times\mathbf{E}_L - \mathbf{E}_L\times(\hat{\mathbf{P}}-Q\mathbf{A})\Big) \\
&+ \frac{\hbar}{8m^2c^2}\sum_j q_j\boldsymbol{\sigma}_j\cdot\left[\left(\hat{\boldsymbol{\pi}}_j - q_l\mathbf{A}(\mathbf{R}+\boldsymbol{\xi}_j) + \frac{Q}{N}\mathbf{A}(\mathbf{R})\right)\times\mathbf{E}_L - \mathbf{E}_L\times\left(\hat{\boldsymbol{\pi}}_j - q_l\mathbf{A}(\mathbf{R}+\boldsymbol{\xi}_j) + \frac{Q}{N}\mathbf{A}(\mathbf{R})\right)\right] \\
&- \frac{1}{8m^2c^2}\sum_l\sum_{j<k}\left[\boldsymbol{\sigma}_l\cdot\left(\hat{\boldsymbol{\pi}}_l - q_l\mathbf{A}(\mathbf{R}+\boldsymbol{\xi}_l) + \frac{Q}{N}\mathbf{A}(\mathbf{R})\right), \left[\boldsymbol{\sigma}_l\cdot\left(\hat{\boldsymbol{\pi}}_l - q_l\mathbf{A}(\mathbf{R}+\boldsymbol{\xi}_l) + \frac{Q}{N}\mathbf{A}(\mathbf{R})\right), \hat{V}_{jk}\right]\right] \\
&- \frac{1}{8Mmc^2}\sum_l\sum_{j<k}\left[\boldsymbol{\sigma}_l\cdot(\hat{\mathbf{P}}-Q\mathbf{A}), \left[\boldsymbol{\sigma}_l\cdot\left(\hat{\boldsymbol{\pi}}_l - q_l\mathbf{A}(\mathbf{R}+\boldsymbol{\xi}_l) + \frac{Q}{N}\mathbf{A}(\mathbf{R})\right), \hat{V}_{jk}\right]\right] \\
&- \frac{1}{8Mmc^2}\sum_l\sum_{j<k}\left[\boldsymbol{\sigma}_l\cdot\left(\hat{\boldsymbol{\pi}}_l - q_l\mathbf{A}(\mathbf{R}+\boldsymbol{\xi}_l) + \frac{Q}{N}\mathbf{A}(\mathbf{R})\right), \left[\boldsymbol{\sigma}_l\cdot(\hat{\mathbf{P}}-Q\mathbf{A}), \hat{V}_{jk}\right]\right] \\
&- \frac{1}{8M^2c^2}\sum_l\sum_{j<k}\left[\boldsymbol{\sigma}_l\cdot(\hat{\mathbf{P}}-Q\mathbf{A}), \left[\boldsymbol{\sigma}_l\cdot(\hat{\mathbf{P}}-Q\mathbf{A}), \hat{V}_{jk}\right]\right] \\
&+ \cdots
\end{aligned}
\tag{145}
$$

Corrected Pauli reduction in this case has led to a reasonably complete model for a nonrelativistic composite with low-order relativistic corrections pretty much in standard form. The issue noted in connection with a lack of gauge invariance due to the presence of the longitudinal field will be corrected when we work with the Foldy–Wouthuysen transformation; however, the correction simply involves the replacement

$$
\mathbf{E}_L \;\rightarrow\; \mathbf{E}
\tag{146}
$$

9. Model based on the Foldy–Wouthuysen Transform

We were interested in the method of elimination of negative energy states due to its simplicity; however, a major disadvantage is that it can produce nonHermitian terms. This motivates us to consider composite models based on the Foldy–Wouthuysen transformation [160] in this section, and also a closely related transform in the following section. This rotation has been very widely used for atomic problems [175–180], as well as for nuclear models [123,150,181–188].

9.1. Foldy–Wouthuysen transform

As with all unitary transformations, the basic idea is to work with a rotated wave function written as

$$\Psi' = e^{i\hat{S}} \Psi. \tag{147}$$

Assuming that $\hat{S}$ is time-dependent, then the system can be modeled with the transformed Hamiltonian

$$\hat{H}' = e^{i\hat{S}} \left[\hat{H} - i\hbar \frac{\partial}{\partial t} \right] e^{-i\hat{S}}. \tag{148}$$

Foldy and Wouthuysen used this approach to develop transformations that allow for a nonrelativistic approximation in the case of a single particle [160,189,190]. In the case of a Dirac particle in an external field, the Dirac Hamiltonian is

$$\hat{H} = \boldsymbol{\alpha} \cdot c(\hat{p} - q\mathbf{A}) + \beta mc^2 + q\Phi. \tag{149}$$

After three successive transforms the lowest-order terms in the transformed (4×4 matrix) Hamiltonian is

$$\hat{H}' \rightarrow \beta \left(mc^2 + \frac{|\hat{\mathbf{p}} - q\mathbf{A}|^2}{2m} - \frac{|\hat{\mathbf{p}} - q\mathbf{A}|^4}{8m^3c^2} \right) + q\Phi - \frac{\hbar q}{2m} \beta \boldsymbol{\Sigma} \cdot \mathbf{B}$$
$$+ \frac{\hbar q}{8m^2c^2} \left[\boldsymbol{\Sigma} \cdot (\hat{\mathbf{p}} - q\mathbf{A}) \times \mathbf{E} - \boldsymbol{\Sigma} \cdot \mathbf{E} \times (\hat{\mathbf{p}} - q\mathbf{A}) \right] - \frac{q\hbar^2}{8m^2c^2} \nabla \cdot \mathbf{E}, \tag{150}$$

where

$$\boldsymbol{\Sigma} = \begin{bmatrix} \boldsymbol{\sigma} & 0 \\ 0 & \boldsymbol{\sigma} \end{bmatrix}. \tag{151}$$

9.2. Many-particle model

There is a long tradition of making use of the Foldy–Wouthuysen transformation on many-particle models. F-W transformations for two interacting Dirac particles have been considered in [176,191–196]; for the many-particle case see [116,177,184,197–199]. Transformations for Hamiltonians that include Pauli interactions for the anomalous magnetic moment have been discussed in [200–204].

We begin with a many-particle model written as

$$\hat{H} = \sum_j \beta_j mc^2 + \sum_j \boldsymbol{\alpha}_j \cdot c[\hat{\mathbf{p}}_j - q_j \mathbf{A}(\mathbf{r}_j)] + \sum_{j<k} \hat{V}_{jk}(\mathbf{r}_j - \mathbf{r}_k) + \sum_j q_j \Phi(\mathbf{r}_j).$$

Foldy–Wouthuysen transformations on each of the particles individually reduce all terms except for the interaction terms. We can write

$$
\begin{aligned}
\hat{H}' \;\to\; & mc^2 \sum_j \beta_j + \sum_j \frac{\left| \hat{\mathbf{p}}_j - q_j \mathbf{A}(\mathbf{r}_j) \right|^2}{2m} \beta_j + \mathrm{e}^{i\hat{S}} \sum_{j<k} \hat{V}_{jk}(\mathbf{r}_j - \mathbf{r}_k) \mathrm{e}^{-i\hat{S}} + \sum_j q_j \Phi(\mathbf{r}_j) \\
& - \sum_j \frac{\hbar q_j}{2m} \beta_j \boldsymbol{\Sigma}_j \cdot \mathbf{B}(\mathbf{r}_j) + \sum_j \frac{\hbar q_j}{8m^2 c^2} \Big[\boldsymbol{\Sigma}_j \cdot [\hat{\mathbf{p}}_j - q\mathbf{A}(\mathbf{r}_j)] \times \mathbf{E}(\mathbf{r}_j) - \boldsymbol{\Sigma}_j \cdot \mathbf{E}(\mathbf{r}_j) \times [\hat{\mathbf{p}}_j - q_j \mathbf{A}(\mathbf{r}_j)] \Big] \\
& - \sum_j \frac{q_j \hbar^2}{8m^2 c^2} \nabla \cdot \mathbf{E}(\mathbf{r}_j).
\end{aligned}
\tag{152}
$$

Since the composite may be in motion, it is best to work in a Foldy–Wouthuysen representation rather than with a nonrelativistic approximation here since additional issues arise in the extraction of the nonrelativistic limit [200]. The Foldy–Wouthuysen transformation of the Breit interaction has been discussed in [116,176,191–196]. A Foldy–Wouthuysen transformation was considered in the case of the Bonn nuclear potential [99] by Amore et al. [208].

9.3. Lowest-order contributions to the transformed potential

We can expand the transformed potential according to

$$
\mathrm{e}^{i\hat{S}} \left(\sum_{j<k} \hat{V}_{jk}(\mathbf{r}_j - \mathbf{r}_k) \right) \mathrm{e}^{-i\hat{S}} = \hat{V}_{jk}(\mathbf{r}_j - \mathbf{r}_k) + i \Big[\hat{S}, \hat{V}_{jk}(\mathbf{r}_j - \mathbf{r}_k) \Big] - \frac{1}{2} \Big[\hat{S}, \Big[\hat{S}, \hat{V}_{jk}(\mathbf{r}_j - \mathbf{r}_k) \Big] \Big] + \cdots
\tag{153}
$$

An expression for the lowest-order correction to the potential can be derived based on

$$
\hat{S} = -i \frac{1}{2mc} \sum_j \beta_j \boldsymbol{\alpha}_j \cdot [\hat{\mathbf{p}}_j - q_j \mathbf{A}(\mathbf{r}_j)].
\tag{154}
$$

We can use this to write

$$
\begin{aligned}
\mathrm{e}^{i\hat{S}} \left(\sum_{j<k} \hat{V}_{jk}(\mathbf{r}_j - \mathbf{r}_k) \right) \mathrm{e}^{-i\hat{S}} \;\to\; & \sum_{j<k} \hat{V}_{jk}(\mathbf{r}_j - \mathbf{r}_k) \\
& + \frac{1}{2mc} \sum_{k<l} \sum_{j=k,l} \Big[\beta_j \boldsymbol{\alpha}_j \cdot [\hat{\mathbf{p}}_j - q_j \mathbf{A}(\mathbf{r}_j)], \hat{V}_{kl}(\mathbf{r}_k - \mathbf{r}_l) \Big].
\end{aligned}
\tag{155}
$$

The transformed Hamiltonian can be approximated by

$$
\hat{H}' \;\to\; mc^2 \sum_j \beta_j + \sum_j \frac{|\hat{\mathbf{p}}_j - q_j \mathbf{A}(\mathbf{r}_j)|^2}{2m}\beta_j + \sum_{j<k} \hat{V}_{jk}(\mathbf{r}_j - \mathbf{r}_k) + \sum_j q_j \Phi(\mathbf{r}_j) - \sum_j \frac{\hbar q_j}{2m}\beta_j \boldsymbol{\Sigma}_j \cdot \mathbf{B}(\mathbf{r}_j)
$$
$$
+ \sum_j \frac{\hbar q_j}{8m^2 c^2}\boldsymbol{\Sigma}_j \cdot \left([\hat{\mathbf{p}}_j - q\mathbf{A}(\mathbf{r}_j)] \times \mathbf{E}(\mathbf{r}_j) - \mathbf{E}(\mathbf{r}_j) \times [\hat{\mathbf{p}}_j - q_j\mathbf{A}(\mathbf{r}_j)] \right) - \sum_j \frac{q_j \hbar^2}{8m^2 c^2}\nabla \cdot \mathbf{E}(\mathbf{r}_j)
$$
$$
+ \frac{1}{2mc}\sum_{k<l}\sum_{j=k,l}\left[\beta_j \boldsymbol{\alpha}_j \cdot [\hat{\mathbf{p}}_j - q_j\mathbf{A}(\mathbf{r}_j)], \hat{V}_{kl}(\mathbf{r}_k - \mathbf{r}_l) \right]. \tag{156}
$$

This model might be viewed as more or less a nonrelativistic composite model (but for a 4^N-component wave function in the F-W representation) with relativistic corrections. As such it is closely related to the composite model developed in the previous section, with the gauge invariance problem now fixed.

9.4. Model in terms of relative and center of mass operators

As before, we can make us of relative and center of mass variables defined according to

$$
\mathbf{R} = \frac{1}{N}\sum_j \mathbf{r}_j, \qquad \hat{\mathbf{P}} = \sum_j \hat{\mathbf{p}}_j,
$$

$$
\boldsymbol{\xi}_j = \mathbf{r}_j - \mathbf{R}, \qquad \hat{\boldsymbol{\pi}}_j = \hat{\mathbf{p}}_j - \frac{\hat{\mathbf{P}}}{N}.
$$

We can use these to write the transformed model as

$$
\begin{aligned}
\hat{H}' \rightarrow\ & mc^2 \sum_j \beta_j + \frac{|\hat{\mathbf{P}} - Q\mathbf{A}|^2}{2M} \frac{1}{N} \sum_j \beta_j + Q\Phi \\
& + \sum_j \frac{\left| \hat{\boldsymbol{\pi}}_j - q_j \mathbf{A}(\mathbf{R} + \boldsymbol{\xi}_j) - \dfrac{Q}{N}\mathbf{A}(\mathbf{R}) \right|^2}{2m} \beta_j + \sum_{j<k} \hat{V}_{jk} - \mathbf{d} \cdot \mathbf{E}_L - \hat{\boldsymbol{\mu}}_s \cdot \mathbf{B} \\
& + \frac{1}{2mc} \sum_{k<l} \sum_{j=k,l} \left[\beta_j \boldsymbol{\alpha}_j \cdot \left(\hat{\boldsymbol{\pi}}_j - q_j \mathbf{A}(\mathbf{R} + \boldsymbol{\xi}_j) - \frac{Q}{N}\mathbf{A}(\mathbf{R}) \right), \hat{V}_{kl} \right] \\
& - \frac{Q\hbar^2}{8m^2c^2} \nabla \cdot \mathbf{E} + \sum_j \frac{\hbar q_j}{8Mmc^2} \boldsymbol{\Sigma}_j \cdot \left[\left(\hat{\mathbf{P}} - Q\mathbf{A} \right) \times \mathbf{E} - \mathbf{E} \times \left(\hat{\mathbf{P}} - Q\mathbf{A} \right) \right] \\
& + \sum_j \frac{\hbar q_j}{8m^2c^2} \boldsymbol{\Sigma}_j \cdot \left[\left(\hat{\boldsymbol{\pi}}_j - q_l \mathbf{A}(\mathbf{R} + \boldsymbol{\xi}_j) + \frac{Q}{N}\mathbf{A}(\mathbf{R}) \right) \times \mathbf{E} - \mathbf{E} \times \left(\hat{\boldsymbol{\pi}}_j - q_l \mathbf{A}(\mathbf{R} + \boldsymbol{\xi}_j) + \frac{Q}{N}\mathbf{A}(\mathbf{R}) \right) \right] \\
& + \sum_j \frac{(\hat{\mathbf{P}} - Q\mathbf{A}) \cdot \left(\hat{\boldsymbol{\pi}}_j - q_j \mathbf{A}(\mathbf{R} + \boldsymbol{\xi}_j) - \dfrac{Q}{N}\mathbf{A}(\mathbf{R}) \right)}{2M} \beta_j \\
& + \sum_j \frac{\left(\hat{\boldsymbol{\pi}}_j - q_j \mathbf{A}(\mathbf{R} + \boldsymbol{\xi}_j) - \dfrac{Q}{N}\mathbf{A}(\mathbf{R}) \right) \cdot (\hat{\mathbf{P}} - Q\mathbf{A})}{2M} \beta_j \\
& + \frac{1}{2Mc} \sum_{k<l} \sum_{j=k,l} \left[\beta_j \boldsymbol{\alpha}_j \cdot (\hat{\mathbf{P}} - Q\mathbf{A}), \hat{V}_{kl} \right] + \cdots
\end{aligned}
\tag{157}
$$

This composite model is more or less in a standard form, and we see the center of mass and relative Hamiltonians, couplings with external fields, electrostatic and nuclear spin–orbit terms, as well as terms that couple the center of mass to the internal degrees of freedom.

9.5. Center of mass coupling with internal degrees of freedom

One of the issues in which we are interested in particular concerns the coupling between the center of mass degrees of freedom and the internal degrees of freedom, so we are motivated to examine the associated terms further.

Since

$$
\sum_j \hat{\boldsymbol{\pi}}_j = 0,
\tag{158}
$$

we can write

$$
\sum_j \frac{\hat{\mathbf{P}} \cdot \hat{\boldsymbol{\pi}}_j}{M} \beta_j = \sum_j \frac{\hat{\mathbf{P}} \cdot \hat{\boldsymbol{\pi}}_j}{M} (\beta_j - \mathbf{I}_j),
\tag{159}
$$

where

$$\mathbf{I}_j = \begin{bmatrix} 1\ 0\ 0\ 0 \\ 0\ 1\ 0\ 0 \\ 0\ 0\ 1\ 0 \\ 0\ 0\ 0\ 1 \end{bmatrix}_j . \tag{160}$$

This suggests that the coupling associated with this kinetic energy term between the center of mass momentum and the internal relative momenta is of higher order in the inverse mass under conditions where the composite momentum is small.

In the absence of external fields there is a coupling between the center of mass momentum and the particle–particle potential

$$\frac{1}{2Mc} \sum_{j<k} \left[(\beta_j \boldsymbol{\alpha}_j + \beta_k \boldsymbol{\alpha}_k) \cdot \hat{\mathbf{P}}, \hat{V}_{jk} \right]. \tag{161}$$

This term is closely related to the nonrelativistic version of the interaction we found when eliminating the contribution of the negative energy sectors above. We will consider this term further later on in this paper.

9.6. Modification in the case of Dirac–Pauli interaction

We noted above that protons and neutrons have anomalous magnetic moments, so that an additional Pauli interaction is sometimes used. In this case we would begin with

$$\hat{H} = \sum_j \left[\beta_j mc^2 + \boldsymbol{\alpha}_j \cdot c[\hat{\mathbf{p}}_j - q_j \mathbf{A}(\mathbf{r}_j)] \right] + \sum_{j<k} \hat{V}_{jk} + \sum_j q_j \Phi(\mathbf{r}_j)$$
$$- \sum_j \lambda_j \frac{e\hbar}{2m} \beta_j \left[\boldsymbol{\sigma}_j \cdot \mathbf{B}(\mathbf{r}_j) - i\boldsymbol{\alpha}_j \cdot \mathbf{E}(\mathbf{r}_j) \right].$$

The nonrelativistic limit of this kind of model has been discussed numerous times in the literature [37,169–174].

If the lowest-order contributions to the magnetic dipole interaction are summed and combined with the anomalous magnetic dipole contribution, then at lowest order we can write

$$-\sum_j \frac{q_j \boldsymbol{\xi}_k \times \hat{\boldsymbol{\pi}}_j}{2m} \cdot \mathbf{B}(\mathbf{R}) - \sum_j \frac{\hbar q_j}{2m} \boldsymbol{\sigma}_j \cdot \mathbf{B}(\mathbf{r}_j) - \sum_j \lambda_j \frac{e\hbar}{2m} \boldsymbol{\sigma}_j \cdot \mathbf{B}(\mathbf{r}_j)$$
$$= -\sum_j \frac{q_j \boldsymbol{\xi}_k \times \hat{\boldsymbol{\pi}}_j}{2m} \cdot \mathbf{B}(\mathbf{R}) - \sum_j g_j \frac{e\hbar}{4m} \boldsymbol{\sigma}_j \cdot \mathbf{B}(\mathbf{r}_j)$$
$$\rightarrow \quad -(\hat{\boldsymbol{\mu}}_l + \boldsymbol{\mu}_s + \boldsymbol{\mu}_a) \cdot \mathbf{B}(\mathbf{R}) = -\sum_j \left(\frac{q_j}{2m} \mathbf{l}_j + \frac{e}{2m} g_j \mathbf{s}_j \right) \cdot \mathbf{B} = -\boldsymbol{\mu} \cdot \mathbf{B}. \tag{162}$$

The magnetic dipole moment in this model is made up of a nonrelativistic contribution due to the internal (relative) angular momentum $\boldsymbol{\mu}_l$, a relativistic contribution due to the nucleon spin $\boldsymbol{\mu}_s$, and an extra component included through the Pauli interaction to account for the anomalous magnetic moment $\boldsymbol{\mu}_a$.

A correction also occurs for the spin–orbit terms involving the electrostatic interaction [203,204]

$$\sum_j \frac{\hbar q_j}{8m^2 c^2} \boldsymbol{\Sigma}_j \cdot \left([\hat{\mathbf{p}}_j - q\mathbf{A}(\mathbf{r}_j)] \times \mathbf{E}(\mathbf{r}_j) - \mathbf{E}(\mathbf{r}_j) \times [\hat{\mathbf{p}}_j - q_j \mathbf{A}(\mathbf{r}_j)] \right) - \sum_j \frac{q_j \hbar^2}{8m^2 c^2} \nabla \cdot \mathbf{E}(\mathbf{r}_j)$$

$$\rightarrow \sum_j \frac{\hbar(q_j + 2e\lambda_j)}{8m^2 c^2} \boldsymbol{\Sigma}_j \cdot \left([\hat{\mathbf{p}}_j - q\mathbf{A}(\mathbf{r}_j)] \times \mathbf{E}(\mathbf{r}_j) - \mathbf{E}(\mathbf{r}_j) \times [\hat{\mathbf{p}}_j - q_j \mathbf{A}(\mathbf{r}_j)] \right)$$

$$- \sum_j \frac{\hbar^2(q_j + 2e\lambda_j)}{8m^2 c^2} \nabla \cdot \mathbf{E}(\mathbf{r}_j). \tag{163}$$

10. A Partial Foldy–Wouthuysen Transformation

The motion of the nuclei in the lattice is very much nonrelativistic; however, it may be that the interior nuclear structure problem may be relativistic. It would be good to have a formulation in which the relative problem is treated relativistically, while at the same time treating the center of mass problem nonrelativistically. In this section we make use of a partial Foldy–Wouthuysen transformation to develop such a formulation.

10.1. Isolation of a center of mass Hamiltonian

We begin with the relativistic model expressed in terms of center of mass and relative variables

$$\hat{H} = \sum_j \beta_j mc^2 + \sum_j \boldsymbol{\alpha}_j \cdot c \left[\frac{\hat{\mathbf{P}}}{N} + \hat{\boldsymbol{\pi}}_j - q_j \mathbf{A}(\mathbf{R} + \boldsymbol{\xi}_j) \right] + \sum_{j<k} \hat{V}_{jk}(\boldsymbol{\xi}_j - \boldsymbol{\xi}_k) + \sum_j q_j \Phi(\mathbf{R} + \boldsymbol{\xi}_j) \tag{164}$$

and rewrite it according to

$$\hat{H} = \hat{H}_{\mathbf{R}} + \hat{H}_{\boldsymbol{\xi}} + \hat{H}_{\text{int}} \tag{165}$$

with

$$\hat{H}_{\mathbf{R}} = \sum_j \beta_j mc^2 + \frac{1}{N} \sum_j \boldsymbol{\alpha}_j \cdot c(\hat{\mathbf{P}} - Q\mathbf{A}) + Q\Phi, \tag{166}$$

$$\hat{H}_{\boldsymbol{\xi}} = \sum_j \boldsymbol{\alpha}_j \cdot c\hat{\boldsymbol{\pi}}_j + \sum_{j<k} \hat{V}_{jk}(\boldsymbol{\xi}_j - \boldsymbol{\xi}_k), \tag{167}$$

$$\hat{H}_{\text{int}} = \sum_j \left[q_j \Phi(\mathbf{R} + \boldsymbol{\xi}_j) - \frac{Q}{N} \Phi(\mathbf{R}) \right] - \sum_j \boldsymbol{\alpha}_j \cdot c \left[q_j \mathbf{A}(\mathbf{R} + \boldsymbol{\xi}_j) - \frac{Q}{N} \mathbf{A}(\mathbf{R}) \right]. \tag{168}$$

We identify $\hat{H}_{\mathbf{R}}$ as a center of mass Hamiltonian, which will be the focus of our partial Foldy–Wouthuysen transform. The remaining terms in the Hamiltonian include $\hat{H}_{\boldsymbol{\xi}}$ which here is an incomplete version of the relative Hamiltonian, and $\hat{H}_{\text{int}}$ which includes the residual interaction with the external electromagnetic field.

10.2. Rotation of the center of mass Hamiltonian

It is possible to carry out a Foldy–Wouthuysen transformation on the center of mass Hamiltonian which leads to a model that will be of interest for us. The transformed center of mass Hamiltonian is

$$\hat{H}'_{\mathbf{R}} = e^{i\hat{S}} \left(\hat{H}_{\mathbf{R}} - i\hbar \frac{\partial}{\partial t} \right) e^{-i\hat{S}}.$$

We work with a transformation based on

$$\hat{S} = -i \frac{1}{2Mc^2} \sum_j \beta_j \boldsymbol{\alpha}_j \cdot c(\hat{\mathbf{P}} - Q\mathbf{A}). \tag{169}$$

The implementation of this rotation is nontrivial, and details are provided in Appendix B. The result can be written as

$$\hat{H}'_{\mathbf{R}} \;\rightarrow\; \sum_j \beta_j mc^2 + \frac{|\hat{\mathbf{P}} - Q\mathbf{A}|^2}{2M} \frac{1}{N} \sum_j \beta_j + Q\Phi - \frac{\hbar Q}{2M} \frac{1}{N} \sum_j \beta_j \boldsymbol{\Sigma}_j \cdot \mathbf{B}$$
$$- \frac{\hbar^2 Q}{8M^2 c^2} \sum_j \nabla \cdot \mathbf{E} + \frac{\hbar Q}{8M^2 c^2} \sum_j \boldsymbol{\Sigma}_j \cdot \left[(\hat{\mathbf{P}} - Q\mathbf{A}) \times \mathbf{E} - \mathbf{E} \times (\hat{\mathbf{P}} - Q\mathbf{A}) \right]. \tag{170}$$

10.3. Transformed Hamiltonian

We can apply the same rotation to the full Hamiltonian according to

$$\hat{H}' = \hat{H}'_{\mathbf{R}} + e^{i\hat{S}} \hat{H}_{\boldsymbol{\xi}} e^{-i\hat{S}} + e^{i\hat{S}} \hat{H}_{\text{int}} e^{-i\hat{S}}. \tag{171}$$

In the event that the external fields are relatively weak then we should be able to work with

$$\hat{H}' \;\rightarrow\; \hat{H}'_{\mathbf{R}} + \hat{H}_{\boldsymbol{\xi}} + \hat{H}_{\text{int}} + i[\hat{S}, \hat{H}_{\boldsymbol{\xi}}]. \tag{172}$$

We can evaluate

$$i[\hat{S}, \hat{H}_{\boldsymbol{\xi}}] = \frac{1}{M} \sum_j \beta_j (\hat{\mathbf{P}} - Q\mathbf{A}) \cdot \hat{\boldsymbol{\pi}}_j + \frac{1}{2Mc} \sum_{k<l} \sum_{j=k,l} \left[\beta_j \boldsymbol{\alpha}_j \cdot (\hat{\mathbf{P}} - Q\mathbf{A}), \hat{V}_{kl} \right]. \tag{173}$$

We can collect terms and write

$$\hat{H}' \;\rightarrow\; \frac{|\hat{\mathbf{P}} - Q\mathbf{A}|^2}{2M}\frac{1}{N}\sum_j \beta_j + Q\Phi - \frac{\hbar Q}{2M}\frac{1}{N}\sum_j \beta_j \mathbf{\Sigma}_j \cdot \mathbf{B} - \frac{\hbar^2 Q}{8M^2 c^2}\nabla \cdot \mathbf{E}$$

$$+ \frac{\hbar Q}{8M^2 c^2}\sum_j \mathbf{\Sigma}_j \cdot \Big[(\hat{\mathbf{P}} - Q\mathbf{A}) \times \mathbf{E} - \mathbf{E} \times (\hat{\mathbf{P}} - Q\mathbf{A}) \Big]$$

$$+ \sum_j \beta_j m c^2 + \sum_j \boldsymbol{\alpha}_j \cdot c\hat{\boldsymbol{\pi}}_j + \sum_{j<k} \hat{V}_{jk}$$

$$+ \sum_j \Big[q_j \Phi(\mathbf{R} + \boldsymbol{\xi}_j) - \frac{Q}{N}\Phi(\mathbf{R}) \Big] - \sum_j \boldsymbol{\alpha}_j \cdot c \Big[q_j \mathbf{A}(\mathbf{R} + \boldsymbol{\xi}_j) - \frac{Q}{N}\mathbf{A}(\mathbf{R}) \Big]$$

$$+ \frac{1}{M}\sum_j \beta_j (\hat{\mathbf{P}} - Q\mathbf{A}) \cdot \hat{\boldsymbol{\pi}}_j + \frac{1}{2Mc}\sum_{j<k} \Big[(\beta_j \boldsymbol{\alpha}_j + \beta_k \boldsymbol{\alpha}_k) \cdot (\hat{\mathbf{P}} - Q\mathbf{A}), \hat{V}_{jk} \Big]. \tag{174}$$

The terms in the first two lines of this rotated Hamiltonian models the center of mass degrees of freedom in a nonrelativistic model interacting with the radiation field; terms in the third line models the field-free relative nuclear problem in the rest frame; terms in the fourth line account for the interaction of the internal degrees of freedom with the external electromagnetic field; and terms in the last line model the interaction of the canonical momentum of the center of mass with the internal degrees of freedom.

11. The Poincaré Group and Composite Models

In our discussions above we have considered models for composites derived from the nonrelativistic many-particle Schrödinger equation and the many-particle Dirac equation. However, the interacting many-particle Dirac model is in general not covariant, and this motivates us to consider the issue of invariance. The basic idea is that if we have a model for a composite at rest, then our model should be invariant if we translate the composite in free space, or if we rotate it, or if it moves with constant velocity [210]. Wigner considered invariance in connection with relativistic quantum mechanics in an early often-cited paper [211], and in some subsequent publications [78,212,213]. These ideas have had a fundamental impact on relativistic quantum mechanics and field theory; our interest in this section is focused only on a number of specific issues that follow from these general considerations which are of interest to us and which have been discussed in the literature.

11.1. Lie algebra of the Lorentz group

Wigner was interested in representations of what he termed the inhomogeneous Lorentz group [211], which appears in more recent literature as the Poincaré group. We are interested in the Lie algebra of the Poincaré group in connection with the discussion to follow. However, it seems worthwhile to begin with the generators and Lie algebra of the Lorentz group first.

Consider generators for infinitesimal rotations and boosts $\hat{\mathbf{J}}$ and $\hat{\mathbf{K}}$, which can be used to implement a rotation according to

$$\Psi' = \exp\left(-i\theta\hat{\mathbf{n}} \cdot \hat{\mathbf{J}} \right)\Psi, \tag{175}$$

where $\hat{\mathbf{n}}$ is the axis of rotation and θ is the rotation angle; the infinitesimal boost operator can be used to implement a finite boost according to

$$\Psi' = \exp\left(i\frac{\mathbf{v}}{c}\cdot\hat{\mathbf{K}}\right)\Psi, \tag{176}$$

where $\mathbf{u}$ is the increase in velocity resulting from the boost. These are the infinitesimal operators of the Lorentz group, which satisfy the Lie algebra

$$[\hat{J}_i, \hat{J}_j] = i\hbar\epsilon_{ijk}\hat{J}_k,$$

$$[\hat{J}_i, \hat{K}_j] = i\hbar\epsilon_{ijk}\hat{K}_k,$$

$$[\hat{K}_i, \hat{K}_j] = -i\hbar\epsilon_{ijk}\frac{1}{c^2}\hat{J}_k, \tag{177}$$

where ϵ_{ijk} is the Levi-Civita symbol

$$\epsilon_{jkl} = \begin{cases} +1 \text{ if } (i,j,k) = (1,2,3),(2,3,1),(3,1,2), \\ -1 \text{ if } (i,j,k) = (3,2,1),(2,1,3),(1,3,2), \\ 0, \quad \text{otherwise.} \end{cases} \tag{178}$$

This Lie algebra is consistent with Ref. [214].

11.2. Lie algebra of the Poincaré group

Wigner understood that infinitesimal generators for translations in spacetime should be considered as well, which takes us from the Lorentz group to the inhomogeneous Lorentz group, or Poincaré group.

The momentum operator $\hat{\mathbf{P}}$ can be used as an infinitesimal generator of displacements in space according to

$$\Psi' = \exp\left(-i\frac{\mathbf{R}_0\cdot\hat{\mathbf{P}}}{\hbar}\right)\Psi, \tag{179}$$

where $\mathbf{R}_0$ is the displacement in position. The Hamiltonian operator is an infinitesimal generator of displacements in time according to

$$\Psi' = \exp\left(it_0\hat{H}\right)\Psi, \tag{180}$$

where t_0 is the displacement in time. The Lie algebra that results is the Lie algebra of the inhomogeneous Lorentz group or Poincaré group [78,215], which we can write as [216–221]

$$[\hat{P}_i, \hat{P}_j] = 0, \quad [\hat{P}_i, \hat{H}] = 0, \quad [\hat{J}_i, \hat{H}] = 0,$$

$$[\hat{J}_i, \hat{J}_j] = i\hbar\epsilon_{ijk}\hat{J}_k, \quad [\hat{J}_i, \hat{P}_j] = i\hbar\epsilon_{ijk}\hat{P}_k, \quad [\hat{J}_i, \hat{K}_j] = i\hbar\epsilon_{ijk}\hat{K}_k,$$

$$[\hat{K}_i, \hat{P}_j] = i\hbar\delta_{ij}\frac{1}{c^2}\hat{H}, \quad [\hat{K}_i, \hat{K}_j] = -i\hbar\epsilon_{ijk}\frac{1}{c^2}\hat{J}_k, \quad [\hat{K}_i, \hat{H}] = i\hbar\hat{P}_i. \tag{181}$$

If one has constructed a relativistic quantum model, one make use of this algebra to verify that it is an acceptable relativistic theory (that it is a representation of the Poincaré group) [78]. Alternatively, this algebra can be used to construct a relativistic model given a rest frame Hamiltonian [222].

11.3. Infinitesimal generators with no interaction

The many-particle Dirac Hamiltonian in the absence of an interaction, and without external fields

$$\hat{H} = \sum_j \boldsymbol{\alpha}_j \cdot c\hat{\mathbf{p}}_j + \beta_j mc^2 \tag{182}$$

is a representation of a Hamiltonian generator of the Poincaré Lie algebra. In this case we can write for the other infinitesimal generators

$$\hat{\mathbf{P}} = \sum_j \hat{\mathbf{p}}_j, \tag{183}$$

$$\hat{\mathbf{J}} = \sum_j \mathbf{r}_j \times \hat{\mathbf{p}}_j + \frac{\hbar}{2}\boldsymbol{\Sigma}_j, \tag{184}$$

$$\hat{\mathbf{K}} = \frac{1}{2c^2}\sum_j \left[\mathbf{r}_j(\boldsymbol{\alpha}_j \cdot c\hat{\mathbf{p}}_j + \beta_j mc^2) + (\boldsymbol{\alpha}_j \cdot c\hat{\mathbf{p}}_j + \beta_j mc^2)\mathbf{r}_j\right]. \tag{185}$$

If a particle-particle interaction is present, then in general the resulting model will not be invariant. An exception occurs when the interaction potential is proporional to a δ-function [223]

11.4. Casimir invariant

A Casimir invariant $\hat{X}$ is an operator which commutes with the 10 Poincaré infinitesimal generators

$$\left[\hat{X}, \hat{H}\right] = 0, \quad \left[\hat{X}, \hat{P}_i\right] = 0, \quad \left[\hat{X}, \hat{J}_i\right] = 0, \quad \left[\hat{X}, \hat{K}_i\right] = 0. \tag{186}$$

With a few lines of commutator algebra it can be demonstrated that

$$\hat{M}^2 c^4 = \hat{H}^2 - c^2|\hat{\mathbf{P}}|^2 \tag{187}$$

is a Casimir invariant, where $\hat{M}$ is a mass operator. This means that the energy momentum dispersion relation in a consistent relativistic model for a positive eigenvalue of a composite with no external fields must be

$$E = \sqrt{(Mc^2)^2 + c^2|\mathbf{P}|^2} \tag{188}$$

simply as a consequence of Poincaré invariance.

11.5. Separability

Poincaré invariance has numerous consequences, one of which is the separability of center of mass and relative degrees of freedom in free space. If the mass operator is a Casimir invariant, then it cannot depend on the momentum. Consequently, it should be possible to write the Hamiltonian for a Poincaré invariant model in the form [219,224]

$$\hat{H} = \sqrt{(\hat{M}c^2)^2 + c^2|\hat{\mathbf{P}}|^2},$$

(189)

where $\hat{M}$ is a mass operator that depends only on relative degrees of freedom.

In the case of a two-particle Dirac model with a Breit interaction, it is possible to construct unitary transforms which separate the center of mass and relative mass terms up to $O(1/c^2)$ [209,224]. Separability in the case of more general potentials was discussed in Refs. [222,225,226]. Studies that focus on the impact on nuclear interaction models have appeared in [227–230].

11.6. Many-particle Dirac model with interaction

Our attention now turns to the issue of separability in the many-particle Dirac model when particle-particle interactions are present. We consider a model for a composite in the absence of external fields described by

$$\hat{H} = \frac{1}{N} \sum_j \boldsymbol{\alpha}_j \cdot c\hat{\mathbf{P}} + \sum_j \beta_j mc^2 + \sum_j \boldsymbol{\alpha}_j \cdot c\hat{\boldsymbol{\pi}}_j + \sum_{j<k} \hat{V}_{jk}(\boldsymbol{\xi}_j - \boldsymbol{\xi}_k).$$

(190)

We make use of the partial Foldy–Wouthuysen transformation of the last section to write a rotated Hamiltonian when no external fields are present

$$\hat{H}' \; \rightarrow \; \frac{|\hat{\mathbf{P}}|^2}{2M} \frac{1}{N} \sum_j \beta_j + \sum_j \beta_j mc^2 + \sum_j \boldsymbol{\alpha}_j \cdot c\hat{\boldsymbol{\pi}}_j + \sum_{j<k} \hat{V}_{jk}$$

$$+ \frac{1}{M} \sum_j \beta_j \hat{\mathbf{P}} \cdot \hat{\boldsymbol{\pi}}_j + \frac{1}{2Mc} \sum_{j<k} \left[(\beta_j \boldsymbol{\alpha}_j + \beta_k \boldsymbol{\alpha}_k) \cdot \hat{\mathbf{P}}, \hat{V}_{jk} \right].$$

(191)

The result of the unitary transformation is a Hamiltonian which contains separated center of mass and relative terms in the first line, and relatively small terms in the second line that provide a coupling between the center of mass and relative degrees of freedom. The coupling in the last term is consistent with the nonrelativistic reduction of a boosted composite Hamiltonian given in [231].

11.7. Interpretation for terms linear in $\hat{\mathbf{P}}$

To understand the significance of the new term we examine an example discussed some time ago in [209] which focused on the special case of the Coulomb plus Breit interaction. If we first consider the rest frame where

$$\hat{\mathbf{P}} \; \rightarrow \; 0$$

(192)

then the many-particle Dirac Hamiltonian with no external field can be written as

$$\hat{H} = \sum_j \beta_j mc^2 + \sum_j \boldsymbol{\alpha}_j \cdot c\hat{\boldsymbol{\pi}}_j + \sum_{j<k} \frac{q_j q_k}{4\pi\epsilon_0} \left\{ \frac{1}{r_{jk}} - \frac{1}{2} \left[\frac{\boldsymbol{\alpha}_j \cdot \boldsymbol{\alpha}_k}{r_{jk}} + \frac{(\boldsymbol{\alpha}_j \cdot \mathbf{r}_{jk})(\boldsymbol{\alpha}_k \cdot \mathbf{r}_{jk})}{r_{jk}^3} \right] \right\}. \tag{193}$$

We consider how this Hamiltonian should be modified if boosted so that the composite has a center of mass momentum $\hat{\mathbf{P}}$. For this argument we identify the $\boldsymbol{\alpha}$ matrices as equivalent normalized velocity operators (as a consequence of Ehrenfest's Theorem applied to the Dirac equation, where $\dfrac{\mathrm{d}}{\mathrm{d}t}\langle\mathbf{r}\rangle = c\langle\boldsymbol{\alpha}\rangle$)

$$\boldsymbol{\alpha} \sim \frac{\hat{\mathbf{v}}}{c}. \tag{194}$$

If so, then from a naive perspective boosting the system should result in

$$\hat{\mathbf{v}} \rightarrow \hat{\mathbf{v}} + \frac{\hat{\mathbf{P}}}{M}. \tag{195}$$

Based on these simple considerations the boosted Hamiltonian should look something like

$$\hat{H} \rightarrow \frac{|\hat{\mathbf{P}}|^2}{2M} + \sum_j \beta_j mc^2 + \sum_j \left(\boldsymbol{\alpha}_j + \frac{\hat{\mathbf{P}}}{Mc} \right) \cdot c\hat{\boldsymbol{\pi}}_j$$
$$+ \sum_{j<k} \frac{q_j q_k}{4\pi\epsilon_0} \left\{ \frac{1}{r_{jk}} - \frac{1}{2} \left[\frac{\left(\boldsymbol{\alpha}_j + \dfrac{\hat{\mathbf{P}}}{Mc}\right) \cdot \left(\boldsymbol{\alpha}_k + \dfrac{\hat{\mathbf{P}}}{Mc}\right)}{r_{jk}} + \frac{\left(\boldsymbol{\alpha}_j + \dfrac{\hat{\mathbf{P}}}{Mc}\right) \cdot \mathbf{r}_{jk} \left(\boldsymbol{\alpha}_k + \dfrac{\hat{\mathbf{P}}}{Mc}\right) \cdot \mathbf{r}_{jk}}{r_{jk}^3} \right] \right\}. \tag{196}$$

We can rewrite this as

$$\hat{H} \rightarrow \frac{|\hat{\mathbf{P}}|^2}{2M} + \sum_j \beta_j mc^2 + \sum_j \boldsymbol{\alpha}_j \cdot c\hat{\boldsymbol{\pi}}_j + \sum_{j<k} \frac{q_j q_k}{4\pi\epsilon_0} \left\{ \frac{1}{r_{jk}} - \frac{1}{2} \left[\frac{\boldsymbol{\alpha}_j \cdot \boldsymbol{\alpha}_k}{r_{jk}} + \frac{(\boldsymbol{\alpha}_j \cdot \mathbf{r}_{jk})(\boldsymbol{\alpha}_k \cdot \mathbf{r}_{jk})}{r_{jk}^3} \right] \right\}$$
$$+ \sum_j \frac{\hat{\mathbf{P}} \cdot \hat{\boldsymbol{\pi}}_j}{M} - \frac{1}{2Mc} \frac{q_j q_k}{4\pi\epsilon_0} \left[\frac{\hat{\mathbf{P}} \cdot \boldsymbol{\alpha}_k}{r_{jk}} + \frac{\boldsymbol{\alpha}_j \cdot \hat{\mathbf{P}}}{r_{jk}} + \frac{(\hat{\mathbf{P}} \cdot \mathbf{r}_{jk})(\boldsymbol{\alpha}_k \cdot \mathbf{r}_{jk})}{r_{jk}^3} + \frac{(\boldsymbol{\alpha}_j \cdot \mathbf{r}_{jk})(\hat{\mathbf{P}} \cdot \mathbf{r}_{jk})}{r_{jk}^3} \right]$$
$$+ \cdots \tag{197}$$

For the Coulomb plus Breit interaction the commutator that we found is evaluated to yield

$$-\frac{1}{4Mc} \frac{q_j q_k}{4\pi\epsilon_0} \sum_{j<k} \left[(\beta_j \boldsymbol{\alpha}_j + \beta_k \boldsymbol{\alpha}_k) \cdot \hat{\mathbf{P}}, \frac{\boldsymbol{\alpha}_j \cdot \boldsymbol{\alpha}_k}{r_{jk}} + \frac{(\boldsymbol{\alpha}_j \cdot \mathbf{r}_{jk})(\boldsymbol{\alpha}_k \cdot \mathbf{r}_{jk})}{r_{jk}^3} \right]$$
$$= -\frac{1}{2Mc} \frac{q_j q_k}{4\pi\epsilon_0} \sum_{j<k} \left[\beta_j \frac{\hat{\mathbf{P}} \cdot \boldsymbol{\alpha}_k}{r_{jk}} + \beta_k \frac{\boldsymbol{\alpha}_j \cdot \hat{\mathbf{P}}}{r_{jk}} + \beta_j \frac{(\hat{\mathbf{P}} \cdot \mathbf{r}_{jk})(\boldsymbol{\alpha}_k \cdot \mathbf{r}_{jk})}{r_{jk}^3} + \beta_k \frac{(\boldsymbol{\alpha}_j \cdot \mathbf{r}_{jk})(\hat{\mathbf{P}} \cdot \mathbf{r}_{jk})}{r_{jk}^3} \right]. \tag{198}$$

In this case the partial Foldy–Wouthuysen transformation gives us

$$
\begin{aligned}
\hat{H}' =& \frac{|\hat{\mathbf{P}}|^2}{2M} \frac{1}{N} \sum_j \beta_j + \sum_j \beta_j mc^2 + \sum_j \boldsymbol{\alpha}_j \cdot c\hat{\boldsymbol{\pi}}_j + \sum_{j<k} \frac{q_j q_k}{4\pi\epsilon_0} \left\{ \frac{1}{r_{jk}} - \frac{1}{2} \left[\frac{\boldsymbol{\alpha}_j \cdot \boldsymbol{\alpha}_k}{r_{jk}} + \frac{(\boldsymbol{\alpha}_j \cdot \mathbf{r}_{jk})(\boldsymbol{\alpha}_k \cdot \mathbf{r}_{jk})}{r_{jk}^3} \right] \right\} \\
&+ \sum_j \beta_j \frac{\hat{\mathbf{P}} \cdot \hat{\boldsymbol{\pi}}_j}{M} - \frac{1}{2Mc} \frac{q_j q_k}{4\pi\epsilon_0} \sum_{j<k} \left[\beta_j \frac{\hat{\mathbf{P}} \cdot \boldsymbol{\alpha}_k}{r_{jk}} + \beta_k \frac{\boldsymbol{\alpha}_j \cdot \hat{\mathbf{P}}}{r_{jk}} + \beta_j \frac{(\hat{\mathbf{P}} \cdot \mathbf{r}_{jk})(\boldsymbol{\alpha}_k \cdot \mathbf{r}_{jk})}{r_{jk}^3} + \beta_k \frac{(\boldsymbol{\alpha}_j \cdot \mathbf{r}_{jk})(\hat{\mathbf{P}} \cdot \mathbf{r}_{jk})}{r_{jk}^3} \right] \\
&+ \cdots
\end{aligned}
\tag{199}
$$

Consequently, we understand the Hamiltonian that results from the partial Foldy–Wouthuysen transformation as generating a correction that accounts for how the interaction changes in a moving frame to first order. We see that β matrices are present in the expression that results from the evaluation of the commutator, and not present in our simple argument above; this of course complicates things, but the basic argument of [209] (and equivalent arguments given earlier by [108,161]) gives us an intuitive way to understand what the partial Foldy–Wouthuysen transformatation in this relativistic case is doing.

11.8. Terms up to second order

The nucleon-nucleon interaction models available in the literature are specified in the rest frame. We have seen that the magnetic interaction is modified in a moving composite, so we expect that parts of the nuclear interaction that are akin to the magnetic interaction will also be modified. In some nuclear physics calculations the empirical nuclear potential is corrected to account for this. For example, in [232–235] one finds

$$
\hat{V}_{jk}(\mathbf{r}) \;\rightarrow\; \hat{V}_{jk}(\mathbf{r}) + \delta\hat{V}_{jk}(\mathbf{r})
\tag{200}
$$

with

$$
\begin{aligned}
\delta\hat{V}_{jk}(\mathbf{r}_{jk}) =& \frac{1}{8m^2c^2} \left[(\boldsymbol{\sigma}_j - \boldsymbol{\sigma}_k) \times \hat{\mathbf{P}} \cdot \hat{\mathbf{p}}_{jk}, \hat{V}_{jk}(\mathbf{r}_{jk}) \right] - \frac{|\hat{\mathbf{P}}|^2}{8m^2c^2} \hat{V}_{jk}(\mathbf{r}_{jk}) \\
&+ i\frac{1}{8m^2c^2} \left[(\hat{\mathbf{P}} \cdot \mathbf{r}_{jk})(\hat{\mathbf{P}} \cdot \hat{\mathbf{p}}_{jk}), \hat{V}_{jk}(\mathbf{r}_{jk}) \right].
\end{aligned}
\tag{201}
$$

The term linear in $\hat{\mathbf{P}}$ is consistent with the first-order term from the partial Foldy–Wouthuysen transformation. The terms quadratic in $\hat{\mathbf{P}}$ are similar to second-order terms associated with

$$
\hat{H}' = \hat{H} + i[\hat{S}, \hat{H}] - \frac{1}{2}[\hat{S}, [\hat{S}, \hat{H}]] + \cdots
\tag{202}
$$

In this case the transformed Hamiltonian in free space is

$$\hat{H}' \rightarrow \frac{|\hat{\mathbf{P}}|^2}{2M} \frac{1}{N} \sum_j \beta_j + \sum_j \beta_j mc^2 + \sum_j \boldsymbol{\alpha}_j \cdot c\hat{\boldsymbol{\pi}}_j + \sum_{j<k} \hat{V}_{jk}$$

$$+ \frac{1}{M} \sum_j \beta_j \hat{\mathbf{P}} \cdot \hat{\boldsymbol{\pi}}_j + \frac{1}{2Mc} \sum_{j<k} \left[(\beta_j \boldsymbol{\alpha}_j + \beta_k \boldsymbol{\alpha}_k) \cdot \hat{\mathbf{P}}, \hat{V}_{jk} \right]$$

$$+ \frac{1}{8(Mc)^2} \sum_{j<k} \left[(\boldsymbol{\alpha}_j + \boldsymbol{\alpha}_k) \cdot \hat{\mathbf{P}}, \left[(\beta_j \boldsymbol{\alpha}_j + \beta_k \boldsymbol{\alpha}_k) \cdot \hat{\mathbf{P}}, \hat{V}_{jk} \right] \right]. \tag{203}$$

Much effort has gone into the development of chiral effective field theory [101] for the development of accurate nucleon–nucleon potential models [45]. A reduction of the potential based on a relativistic formalism has been considered [236–240], with a modification of the potential due to motion discussed in [241,242].

11.9. Elimination of the larger coupling term

Based on the discussion above a Poincaré invariant model (in free space with no external fields) is separable in the sense of a Hamiltonian with a square root as in Eq. (189); and separable as a conventional Hamiltonian at low order when the square root is linearized. The many-particle Dirac model with interactions is consistent with a separable low-order Hamiltonian in the second sense to $O(1/c^2)$ [224,225].

This suggests that we should be able to rotate out the terms linear in $\hat{\mathbf{P}}$ in $\hat{H}'$; of specific interest here is the elimination of the larger coupling term involving the commutator with the potential. We have found that it is possible to eliminate it using

$$\hat{S}' = -i \frac{1}{8Mmc^3} \sum_{j<k} \left[\beta_j + \beta_k, \left[(\beta_j \boldsymbol{\alpha}_j + \beta_k \boldsymbol{\alpha}_k) \cdot \hat{\mathbf{P}}, \hat{V}_{jk} \right] \right] \tag{204}$$

in the event that

$$\beta_j \beta_k \hat{V}_{jk} = \hat{V}_{jk} \beta_j \beta_k \tag{205}$$

since (as can be shown with substantial algebra that)

$$i \left[\hat{S}', \sum_j \beta_j mc^2 \right] = -\frac{1}{2Mc} \sum_{j<k} \left[(\beta_j \boldsymbol{\alpha}_j + \beta_k \boldsymbol{\alpha}_k) \cdot \hat{\mathbf{P}}, \hat{V}_{jk} \right]. \tag{206}$$

The success of this rotation supports the suspicion that the many-particle Dirac model with interaction but no external fields in free space approximately separates at low order.

11.10. Impact of separability on external fields

If external fields are present, this rotation will result in terms where the external fields couple to internal states of the composite based on complicated interactions involving the particle-particle interaction. This can be illustrated by considering the lowest order terms generated with the rotation above when an electrostatic potential is present. In this case we can write

$$i\left[\hat{S}', Q\Phi\right] = i\left[-i\frac{1}{8Mmc^3}\sum_{j<k}\left[\beta_j + \beta_k, \left[(\beta_j\boldsymbol{\alpha}_j + \beta_k\boldsymbol{\alpha}_k)\cdot\hat{\mathbf{P}}, \hat{V}_{jk}\right]\right], Q\Phi\right]$$

$$= -i\frac{\hbar Q}{8Mmc^3}\sum_{j<k}(\beta_j + \beta_k)(\beta_j\boldsymbol{\alpha}_j + \beta_k\boldsymbol{\alpha}_k)\cdot\mathbf{E}_L\hat{V}_{jk} - (\beta_j + \beta_k)\hat{V}_{jk}(\beta_j\boldsymbol{\alpha}_j + \beta_k\boldsymbol{\alpha}_k)\cdot\mathbf{E}_L$$

$$- (\beta_j\boldsymbol{\alpha}_j + \beta_k\boldsymbol{\alpha}_k)\cdot\mathbf{E}_L\hat{V}_{jk}(\beta_j + \beta_k) + \hat{V}_{jk}(\beta_j\boldsymbol{\alpha}_j + \beta_k\boldsymbol{\alpha}_k)\cdot\mathbf{E}_L(\beta_j + \beta_k). \tag{207}$$

The coupling that we have rotated out now shows up reduced in magnitude in other parts of the model.

12. Many Nuclei in a Lattice

We are interested in composite models in connection with the development of a theory for anomalies in condensed matter nuclear science, where we consider the situation where many identical nuclei interact with a common highly excited vibrational model. The basis for models that we have studied has consisted of treating the nuclei as composites each with coupling terms linear in $\hat{\mathbf{P}}$, making use of a finite basis approximation, and then diagonalizing the problem that results.

If one were to naively adopt the point of view that the center of mass degrees of freedom separate from the internal degrees of freedom, then the basic program under consideration for this kind of model would be called into question. Since we are able to carry out the rotations that implement the separation, it seems useful to think about these kinds of models in terms of the rotations. Based on the discussion above, it may be best to make use of the partial Foldy–Wouthuysen transformation above in order to work with a nonrelativistic description for the center of mass degrees of freedom. Then we can consider a second rotation to implement low-order separability.

12.1. Many nuclei interacting with a common vibrational mode

Suppose that we consider a simple version of the model in which the nuclei in the lattice interact through screened Coulomb and exchange forces. In this case we could start out with an idealized Hamiltonian of the form

$$\hat{H} = \sum_a\left\{\frac{1}{N_a}\sum_{j_a}\boldsymbol{\alpha}_{j_a}\cdot c\hat{\mathbf{P}}_a + \sum_{j_a}\beta_{j_a}mc^2 + \sum_{j_a}\boldsymbol{\alpha}_{j_a}\cdot c\hat{\boldsymbol{\pi}}_{j_a} + \sum_{j_a<k_a}\hat{V}_{j_ak_a}(\boldsymbol{\xi}_{j_a} - \boldsymbol{\xi}_{k_a})\right\}$$

$$+ \sum_{a<b}\sum_{j_a,k_b}q_{j_a}q_{k_b}U_{ab}(\mathbf{r}_{j_a} - \mathbf{r}_{k_b}), \tag{208}$$

where $U_{ab}(\mathbf{r}_{j_a} - \mathbf{r}_{k_b})$ models the screened Coulomb interaction between nucleons in different nuclei in a Born-Oppenheimer picture. The summation over a indicates summing over the different nuclei; and the index j_a indicates a specific nucleon within nucleus a. For this model we have eliminated other external field interactions in order to simplify the notation.

12.2. First transformation

We consider now a big partial Foldy–Wouthuysen transformation which eliminates the $\boldsymbol{\alpha}_{j_a}\cdot c\hat{\mathbf{P}}_a$ coupling terms.

$$\hat{H}' = \mathrm{e}^{i\hat{S}} \left[\hat{H} - i\hbar \frac{\partial}{\partial t} \right] \mathrm{e}^{-i\hat{S}} \tag{209}$$

with

$$\hat{S} = -i \frac{1}{2mc^2} \sum_a \frac{1}{N_a} \sum_{j_a} \beta_{j_a} \alpha_{j_a} \cdot c\hat{\mathbf{P}}_a. \tag{210}$$

This leads to a transformed Hamiltonian of the form

$$\hat{H}' \rightarrow \sum_a \left\{ \frac{|\hat{\mathbf{P}}_a|^2}{2M_a} \frac{1}{N_a} \sum_{j_a} \beta_{j_a} + \sum_{j_a} \beta_{j_a} mc^2 + \sum_{j_a} \boldsymbol{\alpha}_{j_a} \cdot c\hat{\boldsymbol{\pi}}_{j_a} + \sum_{j_a < k_a} \hat{V}_{j_a k_a} \right.$$
$$\left. + \frac{1}{M_a} \sum_{j_a} \beta_{j_a} \hat{\mathbf{P}}_a \cdot \hat{\boldsymbol{\pi}}_{j_a} + \frac{1}{2M_a c} \sum_{j_a < k_a} \left[(\beta_{j_a} \boldsymbol{\alpha}_{j_a} + \beta_{k_a} \boldsymbol{\alpha}_{k_a}) \cdot \hat{\mathbf{P}}_a, \hat{V}_{j_a k_a} \right] \right\}$$
$$+ \sum_{a<b} Q_a Q_b U_{ab}(\mathbf{R}_a - \mathbf{R}_b) + \sum_{a<b} \sum_{j_a, k_b} \left(q_{j_a} q_{k_b} U_{ab}(\mathbf{r}_{j_a} - \mathbf{r}_{k_b}) - \frac{Q_a}{N_a} \frac{Q_b}{N_b} U_{ab}(\mathbf{R}_a + \boldsymbol{\xi}_{j_a} - \mathbf{R}_b - \boldsymbol{\xi}_{j_b}) \right)$$
$$+ \sum_{b \neq a} \frac{\hbar^2 Q_a Q_b}{8M_a^2 c^2} \nabla^2 U_{ab}(\mathbf{R}_a - \mathbf{R}_b) - \sum_{a \neq b} \frac{\hbar Q_a Q_b}{8M_a^2 c^2} \sum_{j_a} \boldsymbol{\Sigma}_{j_a} \cdot \left[\hat{\mathbf{P}}_a \times (\nabla U_{ab}) - (\nabla U_{ab}) \times \hat{\mathbf{P}}_a \right] + \cdots, \tag{211}$$

where $M_a = N_a m$ is the mass of nucleons in nucleus a. Although this rotated Hamiltonian is more complicated that the single composite equivalent that we encountered previously, we can see familiar terms; including dipole coupling terms to internal states; spin–orbit terms associated with the screened Coulomb and exchange interactions; and other coupling terms. Our inclination at this point is to neglect all minor terms not involved with the effects of immediate interest for the anomalies, and approximate the rotated Hamiltonian as

$$\hat{H}' \approx \sum_a \frac{|\hat{\mathbf{P}}_a|^2}{2M_a} + \sum_{a<b} Q_a Q_b U_{ab}(\mathbf{R}_a - \mathbf{R}_b) + \sum_a \left\{ \sum_{j_a} \beta_{j_a} mc^2 + \sum_{j_a} \boldsymbol{\alpha}_{j_a} \cdot c\hat{\boldsymbol{\pi}}_{j_a} + \sum_{j_a < k_a} \hat{V}_{j_a k_a} \right\}$$
$$+ \sum_a \frac{1}{2M_a c} \sum_{j_a < k_a} \left[(\beta_{j_a} \boldsymbol{\alpha}_{j_a} + \beta_{k_a} \boldsymbol{\alpha}_{k_a}) \cdot \hat{\mathbf{P}}_a, \hat{V}_{j_a k_a} \right]. \tag{212}$$

What remains are center of mass kinetic and potential energy terms for the different nuclei, relative Hamiltonians for the internal nuclear states, and coupling terms which arise due to the modification of the nuclear forces when the nuclei are in motion.

12.3. Second transformation

If the nuclei were not interacting in free space, we would expect to be able to rotate out the coupling terms linear in $\hat{\mathbf{P}}_a$. For nuclei in the lattice the situation is not so clear since the nuclei interact with one another. Nevertheless, we can attempt a second Foldy–Wouthuysen transformation based on

$$\hat{S}' = -i \sum_a \frac{1}{8M_a mc^3} \sum_{j_a < k_a} \left[\beta_{j_a} + \beta_{k_a}, \left[(\beta_{j_a} \boldsymbol{\alpha}_{j_a} + \beta_{k_a} \boldsymbol{\alpha}_{k_a}) \cdot \hat{\mathbf{P}}_a, \hat{V}_{j_a k_a} \right] \right] \tag{213}$$

assuming that

$$\beta_j \beta_k \hat{V}_{jk} = \hat{V}_{jk} \beta_j \beta_k. \tag{214}$$

We can write for the doubly rotated Hamiltonian

$$
\begin{aligned}
\hat{H}'' \;\rightarrow\; & \sum_a \frac{|\hat{\mathbf{P}}_a|^2}{2M_a} + \sum_{a<b} Q_a Q_b U_{ab}(\mathbf{R}_a - \mathbf{R}_b) + \sum_a \left\{ \sum_{j_a} \beta_{j_a} mc^2 + \sum_{j_a} \boldsymbol{\alpha}_{j_a} \cdot c\hat{\boldsymbol{\pi}}_{j_a} + \sum_{j_a < k_a} \hat{V}_{j_a k_a} \right\} \\
& + i \left[\hat{S}', \sum_{a<b} Q_a Q_b U_{ab}(\mathbf{R}_a - \mathbf{R}_b) \right] - \frac{1}{2} \left[\hat{S}', \left[\hat{S}', \sum_{a<b} Q_a Q_b U_{ab}(\mathbf{R}_a - \mathbf{R}_b) \right] \right] + \cdots
\end{aligned}
\tag{215}
$$

To lowest order the coupling term is eliminated, and all that remains is the rotation of the screened Coulomb interaction. In the first line are the lowest-order terms of the separated lattice and nuclear Hamiltonian; in the second line are some of the residual terms that remain.

The apparent simplicity of this doubly rotated Hamiltonian is probably deceptive. Operators that mediate internal transitions of one nucleus get imprinted on the screened Coulomb and exchange interaction of neighboring nuclei at lowest order. At next order these operators propagate to even more nuclei, and there appear many new terms with with products of operators involving internal transitions at different sites. If all of the nuclei are initially in the ground state, and if the lattice is unexcited or thermal then we would not expect any significant consequences associated with the neglect of this exponential explosion of coupling terms. However, this would not be expected to be true in general.

Consider the case of an excitation transfer effect mediated by phonon exchange in a lattice, where second-order coupling terms results in the excitation at one site to be coupled to identical nuclei at a great many other sites. In this case a description of the problem without the additional rotation seems most straightforward. Working with a rotated version of the problem to model excitation transfer is of course possible (since a rotation implements a basis change but otherwise does not change the model), but in this case the unrotated version of the problem would be preferred.

12.4. Connection with spin-boson type models

From these arguments we see that the separability of the free space problem with no interaction between composites does not immediately translate into a guaranteed separability when nuclei are in a lattice. The simple rotation that works cleanly for the free space problem now generates and explosion of terms in the lattice version of the problem. While there are cases where the resulting separated model will be a good approximation for the physical system, there is no reason to believe that this is true universally.

The lattice problem with nuclei interacting through effective forces is much more complicated, and the only way to develop reliable predictions is to work with models for the coupled lattice nucleus problem. In the highly idealized case where the nuclear system is abstracted by equivalent two-level systems, and the multi-mode lattice vibrations are replaced by a single oscillator, then what remains is a spin–boson model [243]. And it is well known that a variety of dynamical effects involving many two-level systems occur in the spin-boson model. We have argued that when the lossy spin-boson model is augmented with loss that efficient coherent energy exchange is possible in the multi-phonon regime [243–248].

13. Relativistic Models for Composites

In the past few sections we have covered some of the more important models and issues that relate to the use of composites for condensed matter nuclear science. What remains are topics which might help to complete our review of models for composites, and which may point to future directions for composite model development for applications.

For example, it would be nice to have a simple few-level Poincaré invariant model that we might adapt for us in the context of a lattice model. In this case we might be able to address concerns about how the coupling with vibrational degrees of freedom work, starting from models easier to understand. Alternatively, it would be nice to have a covariant version of the many-particle Dirac model with interactions, since there might be concerns about the coupling provided by the noncovariant many-particle Dirac model used in the sections above.

These and other issues provide motivation for us to consider other composite models which have been discussed in the literature which might provide a different starting place for constructing new models in the future. For example, there are models which can be viewed as essentially covariant N-level systems; there are a variety of covariant or Poincaré invariant models for composites, as well as other models that are approximately Poincaré invariant. In this section our goal is to provide a survey of some of the alternate approaches.

13.1. Elementary particle models with different spin states

In Section 4 we discussed the Rarita–Schwinger model [49] for a spin 3/2 particle; as was discussed this model includes constraints which eliminate two spin 1/2 states with the same mass. If these constraints were not imposed, then we would be left with the underlying relativistically invariant model which describes a particle with three different available sets of states, all with the same mass. One could imagine making use of this model as a kind of Poincaré invariant equivalent N-level model to in which transitions and relativistically invariant kinematics could be studied.

The Rarita–Schwinger model is not unique in this regard. There are several relativistic wave equations in the literature that include two or more spin configurations, as discussed in [249,250].

13.2. Elementary particle models with different mass states

We also considered in Section 4 the Dirac–Fierz–Pauli model [46,47] for a spin 3/2 particle, which once again involves constraints in order to remove a spin 1/2 state with a different mass. Were we to discard the constraint, the resulting elementary particle model could describe a composite with a spin 1/2 and spin 3/2 states of different masses. This is interesting, as it potentially provides us with a relatively simple Poincaré invariant model with nondegenerate states; however, we would prefer a to work with a model in which we could arbitrarily specify the state energies. Other models with two states are discussed in [251–256].

13.3. Infinite-component wave equations

In an early paper on relativistic wave equations, Majorana proposed possible generalizations of the Dirac equation based on wave functions with an infinite number of components [257] (see also [258,259]). In this study α and β matrices were constructed using relatively simple raising and lowering operators, which allowed for both the construction, and also for the determination of the mass spectrum and associated spins. While the goal was to develop a wave equation without negative energy states applicable to elementary particles with arbitrary spin, this construction pointed the way to a new class of relativistic models for composites in which the internal degrees of freedom are treated algebraically. There have been many studies of this approach, and proposals for specific (solvable) Majorana wave equation constructions [260–270].

Perhaps the most important application of these models is for the construction of infinite component wave equations for baryons; the resulting mass spectrum could be fitted to the observed bayron masses, which allows for the estimation of form factors, magnetic moments, and other observables [271–281].

This approach was also used to construct relativistic equations for the hydrogen atom as a composite, where the center of mass motion is relativistic (and has the correct relativistic dispersion relation), and where the internal dynamics are approximately that of the nonrelativistic hydrogen atom [263,282–292]. In the construction of [288] and subsequent papers, the energy is given by

$$E_n(\mathbf{P}) = \sqrt{(M_n c^2)^2 + c^2 |\mathbf{P}|^2} \tag{216}$$

for the positive energy solutions, where the mass spectrum in general is

$$M_n^2 = m_p^2 + m_e^2 \pm 2 m_p m_e \sqrt{1 - \frac{\alpha^2}{n^2}} \tag{217}$$

and the positive energy mass solutions approximately match those of the nonrelativistic hydrogen atom in the sense

$$M_n \;\rightarrow\; m_p + m_e - \frac{\mu \alpha^2}{2 n^2} + \cdots \tag{218}$$

Infinite component wave equations have been constructed for rotators [293,294] as well as for other systems [295,296].

13.4. Poincaré invariant and approximately invariant approaches

We recall the discussion given in [224] in which a two-body Hamiltonian of the form

$$\hat{H} = \sqrt{(\hat{M} c^2)^2 + c^2 |\hat{\mathbf{P}}|^2} \tag{219}$$

was considered in connection with Poincaré invariance, with the mass operator $\hat{M}$ a function of internal degrees of freedom. One can imagine a many-particle generalization of this with

$$\hat{M} c^2 = N m c^2 + \sum_j \frac{|\hat{\boldsymbol{\pi}}_j|^2}{2m} + \sum_{j<k} \hat{V}_{jk} \tag{220}$$

with spin-dependent (and also isospin-dependent) potentials in connection with a many-particle wave function built up from two-component single particle wave functions. There seem only to be a few papers that make use of this approach [297,298].

One can find models that are approximately Poincaré invariant based on Hamiltonians of the form [194,232,299–301]

$$\hat{H} = \sum_j \sqrt{(m c^2)^2 + c^2 |\hat{\mathbf{p}}|^2} + \sum_{j<k} \hat{V}_{jk}. \tag{221}$$

13.5. Covariant many-time models

A many-time covariant generalization of the many-particle Dirac equation was proposed by Barut in [302]. A simplified version of the covariant two-body equation can be written in the form

$$
\left(i\hbar \frac{\partial}{\partial t_1} - \boldsymbol{\alpha}_1 \cdot c\hat{\mathbf{p}}_1 - \beta_1 mc^2 + i\hbar \frac{\partial}{\partial t_2} - \boldsymbol{\alpha}_2 \cdot c\hat{\mathbf{p}}_2 - \beta_2 mc^2 \right) \Psi(\mathbf{r}_1, t_1, \mathbf{r}_2, t_2)
$$
$$
= \hat{V} \left(\sqrt{|\mathbf{r}_2 - \mathbf{r}_1|^2 + c^2(t_2 - t_1)^2} \right) \Psi(\mathbf{r}_1, t_1, \mathbf{r}_2, t_2). \tag{222}
$$

In the two-body case there is a simplification in connection with the different times, which allows for the construction of solutions; good results are obtained [304–306].

Much earlier a qualitatively different approach was proposed by Tomonaga [307]. A simplified version of this approach for the two-body problem can be written as

$$
\left(i\hbar \frac{\partial}{\partial t_1} - \boldsymbol{\alpha}_1 \cdot c\hat{\mathbf{p}}_1 - \beta_1 mc^2 \right) \Psi(\mathbf{r}_1, t_1, \mathbf{r}_2, t_2) = \hat{V} \left(\sqrt{|\mathbf{r}_2 - \mathbf{r}_1|^2 + c^2(t_2 - t_1)^2} \right) \Psi(\mathbf{r}_1, t_1, \mathbf{r}_2, t_2)
$$
$$
\left(i\hbar \frac{\partial}{\partial t_2} - \boldsymbol{\alpha}_2 \cdot c\hat{\mathbf{p}}_2 - \beta_2 mc^2 \right) \Psi(\mathbf{r}_1, t_1, \mathbf{r}_2, t_2) = \hat{V} \left(\sqrt{|\mathbf{r}_2 - \mathbf{r}_1|^2 + c^2(t_2 - t_1)^2} \right) \Psi(\mathbf{r}_1, t_1, \mathbf{r}_2, t_2). \tag{223}
$$

Some of the technical issues associated with this approach were discussed in subsequent papers [308–310]. The use of a many times approach was discussed by Dirac in (1932) [311]. See [312] for a retrospective of these ideas in connection with the development of quantum electrodynamics.

13.6. Bethe–Salpeter approach

An important covariant two-body model was proposed by Bethe and Salpeter in connection with the development of field theory and quantum electrodynamics [313]. Although not usually written in this way, for the purposes of the discussion in this section we could write a many-time version of it in the form

$$
\left(i\hbar \frac{\partial}{\partial t_1} - \boldsymbol{\alpha}_1 \cdot c\hat{\mathbf{p}}_1 - \beta_1 mc^2 \right) \left(i\hbar \frac{\partial}{\partial t_2} - \boldsymbol{\alpha}_2 \cdot c\hat{\mathbf{p}}_2 - \beta_2 mc^2 \right) \Psi(\mathbf{r}_1, t_1, \mathbf{r}_2, t_2)
$$
$$
= \hat{V} \left(\sqrt{|\mathbf{r}_2 - \mathbf{r}_1|^2 + c^2(t_2 - t_1)^2} \right) \Psi(\mathbf{r}_1, t_1, \mathbf{r}_2, t_2). \tag{224}
$$

Most people work instead with a single-time version. This model has been widely used for two-body bound state problems; for the hydrogen atom [314–317]; for the deuteron [318–322]; for the two-quark system [323–326]; and for the three-quark system [327–329]. There has appeared some discussion of general N-body Bethe–Salpeter models [330,331].

13.7. Proper time models

An alternate approach to the problem was proposed by Stueckelberg [332,333], who proposed making use of a proper time to develop a new kind of relativistic quantum mechanics. Interest in this approach in recent times has been stimulated by Horwitz and Piron [335]; in the following years there has accumulated a substantial body of work on this kind of model [336–345]. A review appears in [343].

A covariant two-body model based on an internal nonrelativistic potential problem can be written in the form

$$
i\hbar\frac{\partial}{\partial\tau}\Psi(\mathbf{r}_1,t_1,\mathbf{r}_2,t_2,\tau) = \left[\frac{|\hat{\mathbf{p}}_1|^2 + \frac{\hbar^2}{c^2}\frac{\partial^2}{\partial t_1^2}}{2M} + \frac{|\hat{\mathbf{p}}_2|^2 + \frac{\hbar^2}{c^2}\frac{\partial^2}{\partial t_2^2}}{2M} + \hat{V}\left(\sqrt{|\mathbf{r}_2 - \mathbf{r}_1|^2 + c^2(t_2 - t_1)^2}\right)\right]
$$
$$
\times\ \Psi(\mathbf{r}_1,t_1,\mathbf{r}_2,t_2,\tau). \tag{225}
$$

One can see that the spacetime position and time variables are treated on the same footing naturally in this kind of model. This approach has been used for detailed calculations for two-body problems with a radial potential with good results [341,344–347]. The general approach is readily adapted to internal relativistic models.

It has been proposed by Davidson that variable rest mass effects in this kind of approach might account for anomalies in condensed matter nuclear science [348,349].

13.8. Approximate separation in the many-particle Dirac model

We have considered yet another approach which involves approximate separation in the many-particle Dirac model [350]. We begin by writing the model in terms of center of mass and relative coordinates according to

$$
\hat{H} = \frac{1}{N}\sum_j \boldsymbol{\alpha}_j \cdot c\hat{\mathbf{P}} + \sum_j \beta_j mc^2 + \sum_j \boldsymbol{\alpha}_j \cdot c\hat{\boldsymbol{\pi}}_j + \sum_{j<k} \hat{V}_{jk}(\boldsymbol{\xi}_j - \boldsymbol{\xi}_k). \tag{226}
$$

As we have remarked above, the center of mass and relative mass parts of the model share the same mass operators. We can rewrite this model as

$$
\hat{H} = \frac{1}{N}\sum_j \boldsymbol{\alpha}_j \cdot c\hat{\mathbf{P}} + \sum_j \beta_j m^*c^2
$$
$$
+ \sum_j \beta_j mc^2 + \sum_j \boldsymbol{\alpha}_j \cdot c\hat{\boldsymbol{\pi}}_j + \sum_{j<k} \hat{V}_{jk}(\boldsymbol{\xi}_j - \boldsymbol{\xi}_k) - \sum_j \beta_j m^*c^2, \tag{227}
$$

where in the first line we have what amounts to a Bargmann–Wigner type of model for noninteracting spin 1/2 particles with a modified mass; in the second line we see a version of the relative Hamiltonian with a counter term.

We consider now the time-independent Schrödinger equation

$$
E\Psi = \hat{H}\Psi. \tag{228}
$$

An approximate product solution for the time-independent Schrödinger equation is proposed according to

$$
\Psi = X(\{\boldsymbol{\xi}\})Y(\mathbf{R}), \tag{229}
$$

where Ψ is a 4^N component wave function, where X is a 4^N component rest frame wave function, and where Y is a $4^N \times 4^N$ matrix. The Schrödinger equation for the product is

$$EXY = \left[\frac{1}{N} \sum_j \boldsymbol{\alpha}_j \cdot c\hat{\mathbf{P}} + \sum_j \beta_j m^* c^2 \right] XY$$

$$+ \left[\sum_j \beta_j mc^2 + \sum_j \boldsymbol{\alpha}_j \cdot c\hat{\boldsymbol{\pi}}_j + \sum_{j<k} \hat{V}_{jk}(\boldsymbol{\xi}_j - \boldsymbol{\xi}_k) - \sum_j \beta_j m^* c^2 \right] XY. \tag{230}$$

We can arrange for approximate separability by requiring X to satisfy a (nonstandard) eigenvalue equation of the form

$$m^* c^2 \sum_j \beta_j X(\{\boldsymbol{\xi}\}) = \left[\sum_j \beta_j mc^2 + \sum_j \boldsymbol{\alpha}_j \cdot c\hat{\boldsymbol{\pi}}_j + \sum_{j<k} \hat{V}_{jk}(\boldsymbol{\xi}_j - \boldsymbol{\xi}_k) \right] X(\{\boldsymbol{\xi}\}). \tag{231}$$

We normally work with rest frame eigenfunctions that satisfy

$$E\psi(\{\boldsymbol{\xi}\}) = \left[\sum_j \beta_j mc^2 + \sum_j \boldsymbol{\alpha}_j \cdot c\hat{\boldsymbol{\pi}}_j + \sum_{j<k} \hat{V}_{jk}(\boldsymbol{\xi}_j - \boldsymbol{\xi}_k) \right] \psi(\{\boldsymbol{\xi}\}), \tag{232}$$

hence the presence of a mass operator in connection with the eigenvalue makes the eigenvalue equation above in this case be nonstandard. However, within this approximation we achieve a measure of separation, and the resulting center of mass equation is

$$EXY = \left[\frac{1}{N} \sum_j \boldsymbol{\alpha}_j \cdot c\hat{\mathbf{P}} + \sum_j \beta_j m^* c^2 \right] XY. \tag{233}$$

In essence the center of mass problem is modeled using a Bargmann–Wigner Hamiltonian based on the mass eigenvalue. We would expect the energy eigenvalue for the rest frame problem to give a better approximation to the mass energy than the mass eigenvalue, so it would of course be possible as an additional approximation to choose m^* to be consistent with the rest frame energy eigenvalue. Solving for the large matrix Y is not so easy in this case; however, the bigger issue here is the connection between the realistic many-particle Dirac model for the relative problem and the covariant Bargmann–Wigner model for the center of mass dynamics. We are not aware of literature on this kind of approximation outside of the proposal of [350].

14. Finite basis Approximation

In a realistic composite model for a multi-nucleon nucleus there are an infinite number of internal states, which is inconvenient for use in a lattice model that involves many nuclei. In this case it is convenient to make use of a finite basis approximation. Such models have been discussed previously for this application [157].

14.1. Matrix elements for a multi-particle Dirac model

In the case of a multi-particle Dirac model we start with a Hamiltonian of the form

$$\hat{H} = \frac{1}{N}\sum_j \boldsymbol{\alpha}_j \cdot c(\hat{\mathbf{P}} - Q\mathbf{A}) + \sum_j \beta_j mc^2 + \sum_j \boldsymbol{\alpha}_j \cdot c\left[\hat{\boldsymbol{\pi}}_j - q_j\mathbf{A}(\mathbf{R} + \boldsymbol{\xi}_j) + \frac{Q}{N}\mathbf{A}(\mathbf{R})\right]$$
$$+ \sum_{j<k}\hat{V}_{jk}(\boldsymbol{\xi}_j - \boldsymbol{\xi}_k) + Q\Phi + \sum_j\left[q_j\Phi(\mathbf{R} + \boldsymbol{\xi}_j) - \frac{Q}{N}\Phi(\mathbf{R})\right]. \tag{234}$$

It is convenient to work with basis states defined in terms of rest frame states that satisfy

$$E_n\phi_n = M_nc^2\phi_n = \left[\sum_j \beta_j mc^2 + \sum_j \boldsymbol{\alpha}_j \cdot c\hat{\boldsymbol{\pi}}_j + \sum_{j<k}\hat{V}_{jk}(\boldsymbol{\xi}_j - \boldsymbol{\xi}_k)\right]\phi_n. \tag{235}$$

Matrix elements of the Hamiltonian in this basis can be written as

$$\langle\phi_n|\hat{H}|\phi_{n'}\rangle = M_nc^2\delta_{n,n'} + \left\langle\phi_n\left|\frac{1}{N}\sum_j \boldsymbol{\alpha}_j\right|\phi_{n'}\right\rangle \cdot c(\hat{\mathbf{P}} - Q\mathbf{A}) + Q\Phi\delta_{n,n'}$$
$$+ \left\langle\phi_n\left|\sum_j\left[q_j\Phi(\mathbf{R} + \boldsymbol{\xi}_j) - \frac{Q}{N}\Phi(\mathbf{R})\right]\right|\phi_m\right\rangle$$
$$- \left\langle\phi_n\left|\sum_j \boldsymbol{\alpha}_j \cdot c\left[q_j\mathbf{A}(\mathbf{R} - \boldsymbol{\xi}_j) + \frac{Q}{N}\mathbf{A}(\mathbf{R})\right]\right|\phi_{n'}\right\rangle. \tag{236}$$

14.2. Finite basis model

Approximate solutions to the time-dependent problem can be constructed keeping only a finite number of basis states; we can write

$$\Psi(\{\boldsymbol{\xi}\}, \mathbf{R}, t) = \sum_n \Psi_n(\mathbf{R}, t)\phi_n(\{\boldsymbol{\xi}\}). \tag{237}$$

We can use this to construct an approximate solution to the time-dependent Schrödinger equation

$$i\hbar\frac{\partial}{\partial t}\Psi(\{\boldsymbol{\xi}\}, \mathbf{R}, t) = \hat{H}\Psi(\{\boldsymbol{\xi}\}, \mathbf{R}, t). \tag{238}$$

Within the finite basis approximation individual channel wave functions satisfy

$$i\hbar\frac{\partial}{\partial t}\Psi_n(\mathbf{R}, t) = \sum_{n'}\langle\phi_n|\hat{H}|\phi_{n'}\rangle\Psi_{n'}(\mathbf{R}, t). \tag{239}$$

This we can expand out in the form

$$
i\hbar\frac{\partial}{\partial t}\Psi_n(\mathbf{R},t) = M_n c^2 \Psi_n(\mathbf{R},t) + \sum_{n'}\left\langle\phi_m\left|\frac{1}{N}\sum_j\boldsymbol{\alpha}_j\right|\phi_n\right\rangle\cdot c(\hat{\mathbf{P}}-Q\mathbf{A})\Psi_{n'}(\mathbf{R},t) + Q\Phi\Psi_n(\mathbf{R},t)
$$

$$
+ \sum_{n'}\left\langle\phi_n\left|\sum_j\left[q_j\Phi(\mathbf{R}+\boldsymbol{\xi}_j)-\frac{Q}{N}\Phi(\mathbf{R})\right]\right|\phi_{n'}\right\rangle\Psi_{n'}(\mathbf{R},t)
$$

$$
- \sum_{n'}\left\langle\phi_n\left|\sum_j\boldsymbol{\alpha}_j\cdot c\left[q_j\mathbf{A}(\mathbf{R}-\boldsymbol{\xi}_j)+\frac{Q}{N}\mathbf{A}(\mathbf{R})\right]\right|\phi_{n'}\right\rangle\Psi_{n'}(\mathbf{R},t). \tag{240}
$$

In terms of vectors and matrices this can be recast as

$$
i\hbar\frac{\partial}{\partial t}\boldsymbol{\Psi}(\mathbf{R},t) = \left[\mathbf{M}c^2 + \mathbf{a}\cdot c(\hat{\mathbf{P}}-Q\mathbf{A})+q\Phi\right]\boldsymbol{\Psi}(\mathbf{R},t)
$$

$$
- \mathbf{d}\cdot\mathbf{E}_L\boldsymbol{\Psi}(\mathbf{R},t)-\mathbf{j}\cdot\mathbf{A}\boldsymbol{\Psi}(\mathbf{R},t)+\cdots \tag{241}
$$

The vector wave function $\boldsymbol{\Psi}(\mathbf{R},t)$ here contains the channel wave functions $\Psi_n(\mathbf{R},t)$, and the matrices are constructed from the different parts of the Hamiltonian matrix elements; for example

$$
\mathbf{a}_{nn'} = \left\langle\phi_m\left|\frac{1}{N}\sum_j\boldsymbol{\alpha}_j\right|\phi_n\right\rangle. \tag{242}
$$

Only the lowest-order dipole interactions between the external field and the internal states have been kept explicitly in the matrix and vector version of the Schrödinger equation.

We have made use of this approach in earlier work on anomalies in condensed matter nuclear science [157].

14.3. Partial Foldy–Wouthuysen transformed model

In the future, we will likely make use of a finite basis approximation in connection with the partial Foldy–Wouthuysen transformation. We were able to make use of a partial F–W transformation in Section 10 to develop a model in which the center of mass degrees of freedom are described in a nonrelativistic type of approximation, and the internal states are treated relativistically. We can write the transformed Hamiltonian as

$$
\begin{aligned}
\hat{H}' =& \frac{|\hat{\mathbf{P}} - Q\mathbf{A}|^2}{2M} + Q\Phi - \frac{\hbar Q}{2M}\frac{1}{N}\sum_j \boldsymbol{\Sigma}_j \cdot \mathbf{B} - \frac{\hbar^2 Q}{8M^2c^2}\nabla \cdot \mathbf{E} \\
&+ \frac{\hbar Q}{8M^2c^2}\sum_j \boldsymbol{\Sigma}_j \cdot \left[(\hat{\mathbf{P}} - Q\mathbf{A}) \times \mathbf{E} - \mathbf{E} \times (\hat{\mathbf{P}} - Q\mathbf{A})\right] \\
&+ \sum_j \beta_j mc^2 + \sum_j \boldsymbol{\alpha}_j \cdot c\hat{\boldsymbol{\pi}}_j + \sum_{j<k} \hat{V}_{jk} \\
&+ \sum_j \left[q_j\Phi(\mathbf{R} + \boldsymbol{\xi}_j) - \frac{Q}{N}\Phi(\mathbf{R})\right] - \sum_j \boldsymbol{\alpha}_j \cdot c\left[q_j\mathbf{A}(\mathbf{R} + \boldsymbol{\xi}_j) - \frac{Q}{N}\mathbf{A}(\mathbf{R})\right] \\
&+ \frac{1}{M}\sum_j \beta_j\hat{\boldsymbol{\pi}}_j \cdot (\hat{\mathbf{P}} - Q\mathbf{A}) + \frac{1}{2Mc}\sum_{j<k}\left[(\beta_j\boldsymbol{\alpha}_j + \beta_k\boldsymbol{\alpha}_k), \hat{V}_{kl}\right] \cdot (\hat{\mathbf{P}} - Q\mathbf{A}) \\
&\frac{|\hat{\mathbf{P}} - Q\mathbf{A}|^2}{2M}\left(\frac{1}{N}\sum_j(\beta_j - \mathbf{I}_j)\right) - \frac{\hbar Q}{2M}\frac{1}{N}\sum_j(\beta_j - \mathbf{I}_j)\boldsymbol{\Sigma}_j \cdot \mathbf{B} + \cdots
\end{aligned} \tag{243}
$$

We can make use of a similar finite basis approximation to write

$$
\begin{aligned}
i\hbar\frac{\partial}{\partial t}\boldsymbol{\Psi}(\mathbf{R}, t) =& \mathbf{M}c^2\boldsymbol{\Psi}(\mathbf{R}, t) + \left(\frac{|\hat{\mathbf{P}} - Q\mathbf{A}|^2}{2M} + Q\Phi - \frac{Q}{NM}\mathbf{S} \cdot \mathbf{B} - \frac{\hbar^2 Q}{8M^2c^2}\nabla \cdot \mathbf{E}\right)\boldsymbol{\Psi}(\mathbf{R}, t) \\
&+ \frac{Q}{4M^2c^2}\mathbf{S} \cdot \left[(\hat{\mathbf{P}} - Q\mathbf{A}) \times \mathbf{E} - \mathbf{E} \times (\hat{\mathbf{P}} - Q\mathbf{A})\right]\boldsymbol{\Psi}(\mathbf{R}, t) - \mathbf{d} \cdot \mathbf{E}\boldsymbol{\Psi}(\mathbf{R}, t) - \mathbf{j} \cdot \mathbf{A}\boldsymbol{\Psi}(\mathbf{R}, t) \\
&+ \mathbf{a} \cdot c(\hat{\mathbf{P}} - Q\mathbf{A})\boldsymbol{\Psi}(\mathbf{R}, t) + \cdots
\end{aligned} \tag{244}
$$

Only a subset of the terms appearing in the rotated Hamiltonian appear explicitly in this matrix and vector version of the finite basis approximation. In this case elements of the $\mathbf{a}$ matrix are

$$
\mathbf{a}_{n,n'} = \left\langle \phi_n \left| \frac{1}{Mc}\sum_j \beta_j\hat{\boldsymbol{\pi}}_j + \frac{1}{2Mc}\sum_{j<k}\left[\beta_j\boldsymbol{\alpha}_j + \beta_k\boldsymbol{\alpha}_k, \hat{V}_{jk}\right] \right| \phi_{n'} \right\rangle. \tag{245}
$$

15. Composites in Field Theory

A reviewer has argued that the most reliable physical models available at this time are field theories (see [351,352]), such as quantum electrodynamics and quantum chromodynamics, and that our discussion should be extended to include some discussion of composites in field theory. The standard model includes QED, QCD and more; it provides the most accurate and comprehensive theory for particles and interactions through the strong, electromagnetic and weak interactions. A field theory to describe gravitational interactions runs into technical difficulties associated with spin two gravitons, for which there is no consistent renormalization scheme. There are many efforts ongoing at present to develop new models based on a generalization of field theory (which models particles as points) to string theory (in which particles are modeled as strings) and M-theory (in which particles are modeled as higher-dimensional objects).

By construction the field theories within the standard model are Poincaré invariant, and are physically and mathematically acceptable relativistic models. These models have been applied to describe composite particles, with great success. A systematic review of models for composites in field theory by itself would be book length; consequently here we will be satisfied with only the briefest outline of some of the issues and problems that have been studied.

15.1. Field theory and many-particle Dirac models

The many-particle Dirac model for electrons is widely used, but is not a correct relativistic theory; while QED is a correct relativistic theory which is less widely used for applications, in part because it is more complicated. It is possible to begin with QED and to derive a many-particle Dirac model, which in a sense references a relativistic quantum mechanical model to its equivalent in field theory. This notion underlies the early studies of Brown and Ravenhall [111] and of Salpeter [353] (see also [176,354]). Subsequently more systematic efforts were made to provide a foundation for many-particle Dirac models in [112–114].

15.2. Field theory and relativistic corrections

Wide use is made of nonrelativistic quantum mechanical models that contain relativistic corrections. Early on corrections were developed from the many-particle Dirac model; however, it has been recognized that a better starting place is from field theory. One widely cited paper where this is done is Douglas and Kroll [355]; see [356] for a discussion of an application of the approach in quantum chemistry.

Earlier in this paper we have made use of the Foldy–Wouthuysen transformation of many-particle Dirac models to obtain nonrelativistic models with relativistic corrections. However, there is no reason that the transformation cannot be applied in the case of QED; this was pursued in [357]. In [358] QED and the standard model is considered in the Foldy–Wouthuysen representation; and in [359] a nonrelativistic version of QED is discussed.

15.3. QED corrections in atomic systems

It is possible to develop good estimates for wave functions and energies based on quantum mechanical models for atomic systems; however, these models do not include a wide variety of higher-order corrections that are present in field theoretical models based on QED. In this case it is possible to isolate corrections that are due to QED and analyze them in detail. These include self-energy corrections, two-photon exchange corrections, and a wide variety of other higher-order effects. Atomic systems are composites in the sense under discussion in this paper, and the QED corrections are small compared to the binding energies since electromagnetic interactions are relatively weak.

The literature on QED corrections is vast. For one-electron systems reviews have been given in [360–364]; and in the case of few-electron systems calculations have been discussed and reviewed in [365–372]. In recent years QED corrections are being calculated systematically for multi-electron atoms and ions [373–375].

In general the agreement between theory and experiment is good. The high accuracy of QED as a physical theory is evident in the determination of the electron anomalous magnetic moment, where the agreement between theory and experiment is impressive (for example, differences appear in the 10th digit in [376]).

However, in recent years the Lamb shift of muonic hydrogen was measured, and found to be in disagreement with theory [377],[378]. This has resulted in consternation, and a revisiting of theoretical models to see whether an understanding of the effect might be found (see e.g. [379]). This discrepancy currently remains unexplained [380].

15.4. Effective field theory for nuclei

The strong force coupling between nucleons in nuclei is very much stronger than the electromagnetic interaction in atoms, so that field theoretical corrections are much more important. For example, the inclusion of two-photon

exchange in atomic hydrogen gives only a minor correction, while the inclusion of two-boson exchange effects is needed to have a reasonably accurate nucleon–nucleon potential for structure or scattering calculations. There are many papers in which three-boson exchange effects are included; and even higher-order models have been considered [45].

Consequently, field theory is much more important in nuclear physics. We have previous commented on Bethe–Salpeter treatments for the deuteron [318–322]; the approach has also been used for the three-nucleon problem [381,382]. In the case of nuclear physics an effective field theory (quantum hadrodynamics) is used, one which relies on nucleons and boson exchange; effective Lagrangians are found in [383–385]. Many-nucleon nuclei as composite particles in some cases are treated analogously to atomic systems, based on self-consistent field calculations but with interactions between nucleons based on the exchange of more than one boson [386,387], and self-energy and other corrections modeled [388,389].

15.5. Quantum field theory for quarks and gluons

In the 1960s there emerged a quantum field theory (quantum chromodynamics) for quarks and gluons, which make up mesons and nucleons as well as a host of other particles. The initial applications of the model were to high-energy scattering problems, where calculations could be done with modest effort and be compared with experiment. The application of QCD to bound state problems came later due to technical difficulties in the calculations. For example, quarks are tightly bound in nucleons, but the interaction due to single gluon exchange is modest in comparison. The headache comes about when quarks become somewhat separated; in this case the fields associated with the color charge are very strong and polarize the vacuum, the more so the larger the separation. Vacuum polarization produces additional quarks and gluons, leading to a much more complicated physical system than occurs for electrons in atoms, or for nucleons in nuclei. A quark and anti-quark pair has zero net color charge, and so can be bound as a meson. Three quarks of the three different colors (red, green, blue) can combine to make a color singlet, which has no net color charge, and so can be bound as a baryon.

Given this situation, quantum mechanical models have been studied (with some success) in which empirical potentials are used to model single gluon exchange and confinement [390,391]. However, it would be much better if one could work with QCD directly in order to model few-quark composites. In recent years a large amount of effort has gone into lattice QCD calculations, in which very time consuming Monte Carlo calculations are done on a set of discrete points, from which masses, expectation values, and hadron properties can be determined. The results for masses are perhaps most easily understood here; by now there have been lattice QCD calculations of hadron masses [392–394] with increasingly good agreement between values extrapolated from the calculations and experimental values. For example, a calculated value of the nucleon mass of 929 MeV is reported in [394] which compares well with the average of the proton and neutron mass which is 938.9 MeV. The mass difference between the neutron and proton is calculated in [395] to be 1.51 MeV, which is comparable to the experimental value 1.293 MeV.

16. Summary and Conclusions

Even though the notion of a quantum composite is in a sense foundational to atomic, molecular, nuclear and particle physics, there has not to our knowledge appeared previously a review.

Elementary particle models are widely used to model composite particles; most notably in the case of protons and neutrons, where the Dirac phenomenology is widely used. For spin 3/2 composite particles the Rarita–Schwinger model is also widely used; and Bargmann–Wigner models have been applied successfully to describe mesons and baryons.

Our interest in this concerns the use of composite models for nuclei in the lattice in connection with modeling anomalies in condensed matter nuclear science. In this case the clean separation between the center of mass and

relative degrees of freedom that occurs in the nonrelativistic problem leads to very weak coupling, probably too weak to lead to the kinds of anomalies (excess heat, low-level nuclear radiation, elemental anomalies, collimated X-ray emission) that have been reported. This motivated us to seek a much stronger coupling in the relativistic version of the problem.

We found some years ago that a much stronger coupling appears in the many-particle Dirac model based on a Pauli reduction involving the elimination of the negative energy sectors, and we subsequently have based our modeling on this interaction. Estimates for the rate of excess heat production in the Fleischmann–Pons experiment based on this interaction appears to be consistent with experiment, under conditions where the weak coupling of the $D_2/^4He$ transitions limit the reaction rate. Attempts to connect theory with experiment without this much stronger coupling seems hopeless based on models that we have worked with so far.

However, this approach generally has been very strongly criticized in recent years, for a variety of reasons. One criticism is that due to Poincaré invariance, the center of mass and relative problems separate, so that there is no coupling between the center of mass and internal degrees of freedom. Another criticism is a more generic one that argues for the impossibility of any exchange between phonons, which are delocalized, and internal nuclear degrees of freedom, which are highly localized. Yet other criticisms have been put forth concerning the impossibility of coherent energy exchange with massive up-conversion and down-conversion. It has even been suggested that the up-conversion of many vibrational quanta is impossible because the system entropy is decreased. The local consensus among colleagues at MIT seems to be that since it is impossible for there to be any anomalies in the first place, all experimental reports of anomalies are simply wrong; and consequently any models that suggest they might have been possible should not have been considered in the first place.

Given the quantity and intensity of the criticism, there is no possibility of any response that would be considered to be satisfactory; hence there is little motivation to try. There are nonetheless a number of specific issues that have been to us of intrinsic interest and that have been clarified to some degree in the discussion above.

One of the most significant results from our perspective come in the form of the composite models that have been developed systematically in Sections 6-10. The nonrelativistic composite is simplest, and from our perspective important; but it does not appear much in the literature. The relativistic composite based on the many-particle Dirac model is also relatively simple, and also fundamental; however, the literature does not contain much discussion of it either. Composites resulting from the Foldy–Wouthuysen approximation appear to have been most widely considered, and a major motivation for this appears to have come from issues associated with the Gerasimov–Drell–Hearn sum rule [396,397].

The partial Foldy–Wouthuysen transformation described in Section 10 is new, and results in composite models where the center of mass is nonrelativistic and the internal degrees of freedom are relativistic; which from our perspective is very interesting. In the future we will focus on this kind of model for the basis of our models for anomalies in condensed matter nuclear science; since it is much easier to include in a model with lattice vibrations; since the coupling of the center of mass to internal degrees of freedom is simpler; and since we are able to rotate out terms involving the commutator with the potential for reasonably general potential models in free space.

Criticisms of our model which pertain to Poincaré invariance have in our view been the most serious to date, since if there is no sizeable interaction between the center of mass motion and the internal degrees of freedom, then it will be nearly impossible to develop a model that can connect with experiment along the lines we have pursued. The absence of such a coupling in free space as a result of Poincaré invariance is a very strong argument, and has been the source of much concern. The arguments resolving this issue are probably more subtle than one would wish, and rely on the fact that the many-particle Dirac model is approximately Poincaré invariant. Because of this, it is possible to construct a rotation that eliminates the strongest part of the interaction between the center of mass and relative degrees of freedom in free space. However, there is no guarantee that the generalization of this same rotation always works in the lattice case to produce the clean free space separation. In our work this was recognized long ago, and we have relied instead

on the diagonalization of the many-nucleus problem when they are interacting (and participating in the vibrations of a highly excited phonon mode). These arguments appear in Sections 11 and 12.

In essence, the free space problem differs from the condensed matter problem since this rotation that eliminates the coupling between center of mass and internal degrees of freedom always works in free space, but conditions can be found for the lattice case where it gives rise to unexpected new effects.

There are other approaches to modeling composites discussed in Section 13, some of which involve models that are covariant or Poincaré invariant, and for which there is the potential of using to model nuclei as composites in a lattice in the future. Relativistic composite models are also interesting intrinsically and have applications in other fields. A brief discussion of more sophisticated composite models in field theory is given in Section 15.

We have relied heavily on the finite basis approximation in connection with models for composites in our models (this does not appear to have been pursued much in other areas). In Section 14 we outline the approach, one which we have made use of previously in the case of the many-particle Dirac model. However, it seems clear that finite basis models based on the transformed Hamiltonian from the partial Foldy–Wouthuysen transformation provide a much better starting place for this kind of modeling, and in the future we expect to make use of this approach.

Appendix A. 20-component Free Space Model for Nucleons

The relevant Hamiltonian for the three noninteracting quarks of the model is

$$\hat{H} = \left(\beta_1 + \beta_2 + \beta_3 \right) mc^2 + \left(\frac{\boldsymbol{\alpha}_1 + \boldsymbol{\alpha}_2 + \boldsymbol{\alpha}_3}{3} \right) \cdot c\hat{\mathbf{P}}. \tag{A.1}$$

We would like to construct a reduced Hamiltonian appropriate for the mixed symmetry basis states of the quark system. As discussed in Section 5 this can be written symbolically as

$$\begin{aligned}
\hat{H}_{nuc} =& |[3\ 2\ 1]_C\rangle |[1\ 2\ 1]_F\rangle \hat{H}_{[1\ 2\ 1]} \langle [1\ 2\ 1]_F| \langle [3\ 2\ 1]_C| \\
&+ |[3\ 2\ 1]_C\rangle |[2\ 1\ 1]_F\rangle \hat{H}_{[2\ 1\ 1]} \langle [2\ 1\ 1]_F| \langle [3\ 2\ 1]_C|.
\end{aligned} \tag{A.2}$$

The [1 2 1] part of the Hamiltonian can be written

$$\hat{H}_{[1\ 2\ 1]} = \mathbf{M}c^2 + \mathbf{a} \cdot c\mathbf{P}, \tag{A.3}$$

where $\mathbf{M}$ and $\mathbf{a}$ are 20×20 matrices. We can write for $\mathbf{M}c^2$

$$
\mathbf{M}c^2 = mc^2
\left(
\begin{array}{cccccccc|cccccccc|cccc}
3 & 0 & 0 & 0 & 0 & 0 & 0 & 0 & 0 & 0 & 0 & 0 & 0 & 0 & 0 & 0 & 0 & 0 & 0 & 0 \\
0 & 3 & 0 & 0 & 0 & 0 & 0 & 0 & 0 & 0 & 0 & 0 & 0 & 0 & 0 & 0 & 0 & 0 & 0 & 0 \\
0 & 0 & 1 & 0 & 0 & 0 & 0 & 0 & 0 & 0 & 0 & 0 & 0 & 0 & 0 & 0 & 0 & 0 & 0 & 0 \\
0 & 0 & 0 & 1 & 0 & 0 & 0 & 0 & 0 & 0 & 0 & 0 & 0 & 0 & 0 & 0 & 0 & 0 & 0 & 0 \\
0 & 0 & 0 & 0 & -1 & 0 & 0 & 0 & 0 & 0 & 0 & 0 & 0 & 0 & 0 & 0 & 0 & 0 & 0 & 0 \\
0 & 0 & 0 & 0 & 0 & -1 & 0 & 0 & 0 & 0 & 0 & 0 & 0 & 0 & 0 & 0 & 0 & 0 & 0 & 0 \\
0 & 0 & 0 & 0 & 0 & 0 & -3 & 0 & 0 & 0 & 0 & 0 & 0 & 0 & 0 & 0 & 0 & 0 & 0 & 0 \\
0 & 0 & 0 & 0 & 0 & 0 & 0 & -3 & 0 & 0 & 0 & 0 & 0 & 0 & 0 & 0 & 0 & 0 & 0 & 0 \\
\hline
0 & 0 & 0 & 0 & 0 & 0 & 0 & 0 & 1 & 0 & 0 & 0 & 0 & 0 & 0 & 0 & 0 & 0 & 0 & 0 \\
0 & 0 & 0 & 0 & 0 & 0 & 0 & 0 & 0 & 1 & 0 & 0 & 0 & 0 & 0 & 0 & 0 & 0 & 0 & 0 \\
0 & 0 & 0 & 0 & 0 & 0 & 0 & 0 & 0 & 0 & 1 & 0 & 0 & 0 & 0 & 0 & 0 & 0 & 0 & 0 \\
0 & 0 & 0 & 0 & 0 & 0 & 0 & 0 & 0 & 0 & 0 & 1 & 0 & 0 & 0 & 0 & 0 & 0 & 0 & 0 \\
0 & 0 & 0 & 0 & 0 & 0 & 0 & 0 & 0 & 0 & 0 & 0 & -1 & 0 & 0 & 0 & 0 & 0 & 0 & 0 \\
0 & 0 & 0 & 0 & 0 & 0 & 0 & 0 & 0 & 0 & 0 & 0 & 0 & -1 & 0 & 0 & 0 & 0 & 0 & 0 \\
0 & 0 & 0 & 0 & 0 & 0 & 0 & 0 & 0 & 0 & 0 & 0 & 0 & 0 & -1 & 0 & 0 & 0 & 0 & 0 \\
0 & 0 & 0 & 0 & 0 & 0 & 0 & 0 & 0 & 0 & 0 & 0 & 0 & 0 & 0 & -1 & 0 & 0 & 0 & 0 \\
\hline
0 & 0 & 0 & 0 & 0 & 0 & 0 & 0 & 0 & 0 & 0 & 0 & 0 & 0 & 0 & 0 & 1 & 0 & 0 & 0 \\
0 & 0 & 0 & 0 & 0 & 0 & 0 & 0 & 0 & 0 & 0 & 0 & 0 & 0 & 0 & 0 & 0 & 1 & 0 & 0 \\
0 & 0 & 0 & 0 & 0 & 0 & 0 & 0 & 0 & 0 & 0 & 0 & 0 & 0 & 0 & 0 & 0 & 0 & -1 & 0 \\
0 & 0 & 0 & 0 & 0 & 0 & 0 & 0 & 0 & 0 & 0 & 0 & 0 & 0 & 0 & 0 & 0 & 0 & 0 & -1
\end{array}
\right).
\tag{A.4}
$$

Written in this form, we see three sets of $[1\ 2\ 1]$ states isolated in blocks. For the $\mathbf{a}_x$ matrix we may write

$$
\mathbf{a}_x =
\left(
\begin{array}{cccccccc|cccccccc|cccc}
0 & 0 & 0 & -\alpha & 0 & 0 & 0 & 0 & 1 & 0 & -\alpha & 0 & 0 & 0 & 0 & 0 & 0 & -\beta & 0 & 0 \\
0 & 0 & -\alpha & 0 & 0 & 0 & 0 & 0 & 0 & -\alpha & 0 & 1 & 0 & 0 & 0 & 0 & -\beta & 0 & 0 & 0 \\
0 & -\alpha & 0 & 0 & 0 & -\delta & 0 & 0 & 0 & 0 & 0 & 0 & -\alpha & 0 & \gamma & 0 & 0 & 0 & 0 & \delta \\
-\alpha & 0 & 0 & 0 & -\delta & 0 & 0 & 0 & 0 & 0 & 0 & 0 & 0 & \gamma & 0 & -\alpha & 0 & 0 & \delta & 0 \\
0 & 0 & 0 & -\delta & 0 & 0 & 0 & -\alpha & -\alpha & 0 & \gamma & 0 & 0 & 0 & 0 & 0 & 0 & \delta & 0 & 0 \\
0 & 0 & -\delta & 0 & 0 & 0 & -\alpha & 0 & 0 & \gamma & 0 & -\alpha & 0 & 0 & 0 & 0 & \delta & 0 & 0 & 0 \\
0 & 0 & 0 & 0 & 0 & -\alpha & 0 & 0 & 0 & 0 & 0 & 0 & 1 & 0 & -\alpha & 0 & 0 & 0 & 0 & -\beta \\
0 & 0 & 0 & 0 & -\alpha & 0 & 0 & 0 & 0 & 0 & 0 & 0 & 0 & -\alpha & 0 & 1 & 0 & 0 & -\beta & 0 \\
\hline
1 & 0 & 0 & 0 & -\alpha & 0 & 0 & 0 & 0 & 0 & 0 & 0 & 0 & -\alpha & 0 & 0 & 0 & 0 & -\beta & 0 \\
0 & -\alpha & 0 & 0 & 0 & \gamma & 0 & 0 & 0 & 0 & 0 & 0 & -\alpha & 0 & -\delta & 0 & 0 & 0 & 0 & \delta \\
-\alpha & 0 & 0 & 0 & \gamma & 0 & 0 & 0 & 0 & 0 & 0 & 0 & 0 & -\delta & 0 & -\alpha & 0 & 0 & \delta & 0 \\
0 & 1 & 0 & 0 & 0 & -\alpha & 0 & 0 & 0 & 0 & 0 & 0 & 0 & 0 & -\alpha & 0 & 0 & 0 & 0 & -\beta \\
0 & 0 & -\alpha & 0 & 0 & 0 & 1 & 0 & 0 & -\alpha & 0 & 0 & 0 & 0 & 0 & 0 & -\beta & 0 & 0 & 0 \\
0 & 0 & 0 & \gamma & 0 & 0 & 0 & -\alpha & -\alpha & 0 & -\delta & 0 & 0 & 0 & 0 & 0 & 0 & \delta & 0 & 0 \\
0 & 0 & \gamma & 0 & 0 & 0 & -\alpha & 0 & 0 & -\delta & 0 & -\alpha & 0 & 0 & 0 & 0 & \delta & 0 & 0 & 0 \\
0 & 0 & 0 & -\alpha & 0 & 0 & 0 & 1 & 0 & 0 & -\alpha & 0 & 0 & 0 & 0 & 0 & 0 & -\beta & 0 & 0 \\
\hline
0 & -\beta & 0 & 0 & 0 & \delta & 0 & 0 & 0 & 0 & 0 & 0 & -\beta & 0 & \delta & 0 & 0 & 0 & 0 & \gamma \\
-\beta & 0 & 0 & 0 & \delta & 0 & 0 & 0 & 0 & 0 & 0 & 0 & 0 & \delta & 0 & -\beta & 0 & 0 & \gamma & 0 \\
0 & 0 & 0 & \delta & 0 & 0 & 0 & -\beta & -\beta & 0 & \delta & 0 & 0 & 0 & 0 & 0 & 0 & \gamma & 0 & 0 \\
0 & 0 & \delta & 0 & 0 & 0 & -\beta & 0 & 0 & \delta & 0 & -\beta & 0 & 0 & 0 & 0 & \gamma & 0 & 0 & 0
\end{array}
\right).
\tag{A.5}
$$

For the $\mathbf{a}_y$ matrix we may write

$$\mathbf{a}_y = i \left(\begin{array}{cccccccc|cccccccc|cccc}
0 & 0 & 0 & \alpha & 0 & 0 & 0 & 0 & 1 & 0 & \alpha & 0 & 0 & 0 & 0 & 0 & 0 & \beta & 0 & 0 \\
0 & 0 & -\alpha & 0 & 0 & 0 & 0 & 0 & 0 & -\alpha & 0 & -1 & 0 & 0 & 0 & 0 & -\beta & 0 & 0 & 0 \\
0 & \alpha & 0 & 0 & 0 & \delta & 0 & 0 & 0 & 0 & 0 & 0 & -\alpha & 0 & -\gamma & 0 & 0 & 0 & 0 & -\delta \\
-\alpha & 0 & 0 & 0 & -\delta & 0 & 0 & 0 & 0 & 0 & 0 & 0 & 0 & \gamma & 0 & \alpha & 0 & 0 & \delta & 0 \\
0 & 0 & 0 & \delta & 0 & 0 & 0 & \alpha & -\alpha & 0 & -\gamma & 0 & 0 & 0 & 0 & 0 & 0 & -\delta & 0 & 0 \\
0 & 0 & -\delta & 0 & 0 & 0 & -\alpha & 0 & 0 & \gamma & 0 & \alpha & 0 & 0 & 0 & 0 & \delta & 0 & 0 & 0 \\
0 & 0 & 0 & 0 & 0 & \alpha & 0 & 0 & 0 & 0 & 0 & 0 & 1 & 0 & \alpha & 0 & 0 & 0 & 0 & \beta \\
0 & 0 & 0 & 0 & -\alpha & 0 & 0 & 0 & 0 & 0 & 0 & 0 & 0 & -\alpha & 0 & -1 & 0 & 0 & -\beta & 0 \\
\hline
-1 & 0 & 0 & 0 & \alpha & 0 & 0 & 0 & 0 & 0 & 0 & 0 & 0 & \alpha & 0 & 0 & 0 & 0 & \beta & 0 \\
0 & \alpha & 0 & 0 & 0 & -\gamma & 0 & 0 & 0 & 0 & 0 & 0 & -\alpha & 0 & \delta & 0 & 0 & 0 & 0 & -\delta \\
-\alpha & 0 & 0 & 0 & \gamma & 0 & 0 & 0 & 0 & 0 & 0 & 0 & 0 & -\delta & 0 & \alpha & 0 & 0 & \delta & 0 \\
0 & 1 & 0 & 0 & 0 & -\alpha & 0 & 0 & 0 & 0 & 0 & 0 & 0 & 0 & -\alpha & 0 & 0 & 0 & 0 & -\beta \\
0 & 0 & \alpha & 0 & 0 & 0 & -1 & 0 & 0 & \alpha & 0 & 0 & 0 & 0 & 0 & 0 & \beta & 0 & 0 & 0 \\
0 & 0 & 0 & -\gamma & 0 & 0 & 0 & \alpha & -\alpha & 0 & \delta & 0 & 0 & 0 & 0 & 0 & 0 & -\delta & 0 & 0 \\
0 & 0 & \gamma & 0 & 0 & 0 & -\alpha & 0 & 0 & -\delta & 0 & \alpha & 0 & 0 & 0 & 0 & \delta & 0 & 0 & 0 \\
0 & 0 & 0 & -\alpha & 0 & 0 & 0 & 1 & 0 & 0 & -\alpha & 0 & 0 & 0 & 0 & 0 & 0 & -\beta & 0 & 0 \\
\hline
0 & \beta & 0 & 0 & 0 & -\delta & 0 & 0 & 0 & 0 & 0 & 0 & -\beta & 0 & -\delta & 0 & 0 & 0 & 0 & -\gamma \\
-\beta & 0 & 0 & 0 & \delta & 0 & 0 & 0 & 0 & 0 & 0 & 0 & 0 & \delta & 0 & \beta & 0 & 0 & \gamma & 0 \\
0 & 0 & 0 & -\delta & 0 & 0 & 0 & \beta & -\beta & 0 & -\delta & 0 & 0 & 0 & 0 & 0 & 0 & -\gamma & 0 & 0 \\
0 & 0 & \delta & 0 & 0 & 0 & -\beta & 0 & 0 & \delta & 0 & \beta & 0 & 0 & 0 & 0 & \gamma & 0 & 0 & 0
\end{array}\right). \tag{A.6}$$

Finally, for the $\mathbf{a}_z$ matrix we may write

$$\mathbf{a}_z = \left(\begin{array}{cccccccc|cccccccc|cccc}
0 & 0 & \alpha & 0 & 0 & 0 & 0 & 0 & 0 & -\beta & 0 & 0 & 0 & 0 & 0 & 0 & \beta & 0 & 0 & 0 \\
0 & 0 & 0 & -\alpha & 0 & 0 & 0 & 0 & 0 & 0 & \beta & 0 & 0 & 0 & 0 & 0 & 0 & -\beta & 0 & 0 \\
\alpha & 0 & 0 & 0 & \delta & 0 & 0 & 0 & 0 & 0 & 0 & 0 & 0 & \delta & 0 & 0 & 0 & 0 & -\delta & 0 \\
0 & -\alpha & 0 & 0 & 0 & -\delta & 0 & 0 & 0 & 0 & 0 & 0 & 0 & 0 & -\delta & 0 & 0 & 0 & 0 & \delta \\
0 & 0 & \delta & 0 & 0 & 0 & \alpha & 0 & 0 & \delta & 0 & 0 & 0 & 0 & 0 & 0 & -\delta & 0 & 0 & 0 \\
0 & 0 & 0 & -\delta & 0 & 0 & 0 & -\alpha & 0 & 0 & -\delta & 0 & 0 & 0 & 0 & 0 & 0 & \delta & 0 & 0 \\
0 & 0 & 0 & 0 & \alpha & 0 & 0 & 0 & 0 & 0 & 0 & 0 & 0 & -\beta & 0 & 0 & 0 & 0 & \beta & 0 \\
0 & 0 & 0 & 0 & 0 & -\alpha & 0 & 0 & 0 & 0 & 0 & 0 & 0 & 0 & \beta & 0 & 0 & 0 & 0 & -\beta \\
\hline
0 & 0 & 0 & 0 & 0 & 0 & 0 & 0 & 0 & 0 & 0 & 0 & -1 & 0 & 0 & 0 & 0 & 0 & 0 & 0 \\
-\beta & 0 & 0 & 0 & \delta & 0 & 0 & 0 & 0 & 0 & 0 & 0 & 0 & -\gamma & 0 & 0 & 0 & 0 & \epsilon & 0 \\
0 & \beta & 0 & 0 & 0 & -\delta & 0 & 0 & 0 & 0 & 0 & 0 & 0 & 0 & \gamma & 0 & 0 & 0 & 0 & -\epsilon \\
0 & 0 & 0 & 0 & 0 & 0 & 0 & 0 & 0 & 0 & 0 & 0 & 0 & 0 & 0 & 1 & 0 & 0 & 0 & 0 \\
0 & 0 & 0 & 0 & 0 & 0 & 0 & 0 & -1 & 0 & 0 & 0 & 0 & 0 & 0 & 0 & 0 & 0 & 0 & 0 \\
0 & 0 & \delta & 0 & 0 & 0 & -\beta & 0 & 0 & -\gamma & 0 & 0 & 0 & 0 & 0 & 0 & \epsilon & 0 & 0 & 0 \\
0 & 0 & 0 & -\delta & 0 & 0 & 0 & \beta & 0 & 0 & \gamma & 0 & 0 & 0 & 0 & 0 & 0 & -\epsilon & 0 & 0 \\
0 & 0 & 0 & 0 & 0 & 0 & 0 & 0 & 0 & 0 & 0 & 1 & 0 & 0 & 0 & 0 & 0 & 0 & 0 & 0 \\
\hline
\beta & 0 & 0 & 0 & -\delta & 0 & 0 & 0 & 0 & 0 & 0 & 0 & 0 & \epsilon & 0 & 0 & 0 & 0 & -\gamma & 0 \\
0 & -\beta & 0 & 0 & 0 & \delta & 0 & 0 & 0 & 0 & 0 & 0 & 0 & 0 & -\epsilon & 0 & 0 & 0 & 0 & \gamma \\
0 & 0 & -\delta & 0 & 0 & 0 & \beta & 0 & 0 & \epsilon & 0 & 0 & 0 & 0 & 0 & 0 & -\gamma & 0 & 0 & 0 \\
0 & 0 & 0 & \delta & 0 & 0 & 0 & -\beta & 0 & 0 & -\epsilon & 0 & 0 & 0 & 0 & 0 & 0 & \gamma & 0 & 0
\end{array}\right). \tag{A.7}$$

For these matrices we have used

$$\alpha = \frac{1}{\sqrt{3}}, \quad \beta = \frac{2}{\sqrt{3}}, \quad \gamma = \frac{1}{3}, \quad \delta = \frac{2}{3}, \quad \epsilon = \frac{4}{3}. \tag{A.8}$$

We have also constructed the [2 1 1] Hamiltonian, which in our construction is identical in form, but involves [2 1 1] basis states instead of [1 2 1] basis states. Strictly speaking this indicates that the Hamiltonian actually involves 40×40 matrices; however, since the form of the constituent 20×20 matrices are the same it should be possible to make do with a reduced 20×20 model.

Appendix B. Implementation of the Partial F–W Transformation

Due to the relative simplicity of the single-particle Dirac equation with external field coupling it is possible to eliminate odd operators in the Hamiltonian to high order [160,190,398,399]. For the partial Foldy–Wouthuysen transformation of the center of mass part of the many-particle Dirac Hamiltonian in Section 10, the operators involved are much more complicated. Because of this our focus in this case needs to be on the development of low-order terms, of which there are many.

B.1. Even and odd operators of the F–W transformation

We are interested in evaluating to low-order the rotation of the center of mass Hamiltonian

$$\hat{H}'_{\mathbf{R}} = e^{i\hat{S}} \left(\hat{H}_{\mathbf{R}} - i\hbar \frac{\partial}{\partial t} \right) e^{-i\hat{S}}$$

and then subsequently rotate the other parts of the overall Hamiltonian The center of mass Hamiltonian can be written in terms of even and odd operators according to

$$\hat{H}_{\mathbf{R}} = \sum_j \beta_j mc^2 + \mathcal{E} + \sum_j \mathcal{O}_j, \tag{B.1}$$

which generalizes the Foldy–Wouthuysen approach a bit (reminiscent of [197]), where the even and odd operators satisfy

$$\beta_j \mathcal{E} = \mathcal{E} \beta_j, \tag{B.2}$$

$$\beta_j \mathcal{O}_j = -\mathcal{O}_j \beta_j,$$
$$\beta_j \mathcal{O}_k = \mathcal{O}_k \beta_j \quad (j \neq k). \tag{B.3}$$

B.2. Calculation of low-order contributions to the transformation

In general we can carry out the F–W transformation using

$$\hat{H}'_{\mathbf{R}} = \hat{H}_{\mathbf{R}} + i[\hat{S}, \hat{H}_{\mathbf{R}}] - \frac{1}{2}[\hat{S}, [\hat{S}, \hat{H}_{\mathbf{R}}]] - \frac{i}{6}[\hat{S}, [\hat{S}, [\hat{S}, \hat{H}_{\mathbf{R}}]]] + \frac{1}{24}[\hat{S}, [\hat{S}, [\hat{S}, [\hat{S}, \hat{H}_{\mathbf{R}}]]]] + \cdots$$
$$- \hbar \frac{\partial \hat{S}}{\partial t} - \frac{i}{2} \left[\hat{S}, \hbar \frac{\partial \hat{S}}{\partial t} \right] + \frac{1}{6} \left[\hat{S}, \left[\hat{S}, \hbar \frac{\partial \hat{S}}{\partial t} \right] \right] + \cdots \tag{B.4}$$

with

$$\hat{S} = -i\frac{1}{2mc^2}\sum_j \beta_j \mathcal{O}_j. \tag{B.5}$$

By direct calculation we obtain

$$i[\hat{S}, \hat{H}_{\mathbf{R}}] = -\sum_j \mathcal{O}_j + \frac{1}{2mc^2}\sum_j \beta_j\left[\mathcal{O}_j, \mathcal{E}\right] + \frac{1}{mc^2}\sum_j \beta_j \mathcal{O}_j^2, \tag{B.6}$$

$$-\frac{1}{2}\left[\hat{S}, \left[\hat{S}, \hat{H}_{\mathbf{R}}\right]\right] = -\frac{1}{2mc^2}\sum_j \beta_j \mathcal{O}_j^2 - \frac{1}{8m^2c^4}\sum_j \left[\mathcal{O}_j, \left[\mathcal{O}_j, \mathcal{E}\right]\right]$$
$$+ \frac{1}{8m^2c^4}\sum_j\sum_{k\neq j} \beta_j\beta_k\left[\mathcal{O}_j, \left[\mathcal{O}_k, \mathcal{E}\right]\right] - \frac{1}{2m^2c^4}\sum_j \mathcal{O}_j^3, \tag{B.7}$$

$$-\frac{i}{6}[\hat{S}, [\hat{S}, [\hat{S}, \hat{H}_{\mathbf{R}}]]] = \frac{1}{6m^2c^4}\sum_j \mathcal{O}_j^3 + \frac{1}{48m^3c^6}\sum_j\sum_k\sum_l \left[\beta_j\mathcal{O}_j, \left[\beta_k\mathcal{O}_k, \beta_l\left[\mathcal{O}_l, \mathcal{E}\right]\right]\right]$$
$$- \frac{1}{6m^3c^6}\sum_j \beta_j \mathcal{O}_j^4, \tag{B.8}$$

$$\frac{1}{24}[\hat{S}, [\hat{S}, [\hat{S}, [\hat{S}, \hat{H}_{\mathbf{R}}]]]] = \frac{1}{24m^3c^6}\sum_j \beta_j \mathcal{O}_j^4$$
$$+ \frac{1}{384m^3c^6}\sum_j\sum_k\sum_l\sum_m \left[\beta_j\mathcal{O}_j, \left[\beta_k\mathcal{O}_k, \left[\beta_l\mathcal{O}_l, \beta_m\left[\mathcal{O}_m, \mathcal{E}\right]\right]\right]\right]$$
$$+ \frac{1}{24m^3c^6}\sum_j \mathcal{O}_j^5, \tag{B.9}$$

$$-\hbar\frac{\partial\hat{S}}{\partial t} = i\frac{\hbar}{2mc^2}\sum_j \beta_j\frac{\partial\mathcal{O}_j}{\partial t}, \tag{B.10}$$

$$-\frac{i}{2}\left[\hat{S}, \hbar\frac{\partial\hat{S}}{\partial t}\right] = -i\frac{\hbar}{8m^2c^4}\sum_j \left[\mathcal{O}_j, \frac{\partial\mathcal{O}_j}{\partial t}\right] + i\frac{\hbar}{8m^2c^4}\sum_j\sum_{k\neq j} \beta_j\beta_k\left[\mathcal{O}_j, \frac{\partial\mathcal{O}_k}{\partial t}\right], \tag{B.11}$$

$$\frac{1}{6}\left[\hat{S}, \left[\hat{S}, \hbar\frac{\partial\hat{S}}{\partial t}\right]\right] = i\frac{\hbar}{48m^3c^6}\sum_j\sum_k\sum_l \left[\beta_j\mathcal{O}_j, \left[\beta_k\mathcal{O}_k, \beta_l\frac{\partial\mathcal{O}_l}{\partial t}\right]\right]. \tag{B.12}$$

We can collect the results above and write

$$\hat{H}'_{\mathbf{R}} = \sum_j \beta_j mc^2 + \mathcal{E} + \frac{1}{2mc^2} \sum_j \beta_j \left[\mathcal{O}_j, \mathcal{E}\right] + \frac{1}{2mc^2} \sum_j \beta_j \mathcal{O}_j^2 - \frac{1}{8m^2c^4} \sum_j \left[\mathcal{O}_j, \left[\mathcal{O}_j, \mathcal{E}\right]\right]$$

$$+ \frac{1}{8m^2c^4} \sum_j \sum_{k \neq j} \beta_j \beta_k \left[\mathcal{O}_j, \left[\mathcal{O}_k, \mathcal{E}\right]\right] - \frac{1}{3m^2c^4} \sum_j \mathcal{O}_j^3$$

$$+ \frac{1}{48m^3c^6} \sum_j \sum_k \sum_l \left[\beta_j \mathcal{O}_j, \left[\beta_k \mathcal{O}_k, \beta_l \left[\mathcal{O}_l, \mathcal{E}\right]\right]\right] - \frac{1}{8m^3c^6} \sum_j \beta_j \mathcal{O}_j^4$$

$$+ \frac{1}{384m^3c^6} \sum_j \sum_k \sum_l \sum_m \left[\beta_j \mathcal{O}_j, \left[\beta_k \mathcal{O}_k, \left[\beta_l \mathcal{O}_l, \beta_m \left[\mathcal{O}_m, \mathcal{E}\right]\right]\right]\right] + \frac{1}{24m^3c^6} \sum_j \mathcal{O}_j^5$$

$$+ i\frac{\hbar}{2mc^2} \sum_j \beta_j \frac{\partial \mathcal{O}_j}{\partial t} - i\frac{\hbar}{8m^2c^4} \sum_j \left[\mathcal{O}_j, \frac{\partial \mathcal{O}_j}{\partial t}\right] + i\frac{\hbar}{8m^2c^4} \sum_j \sum_{k \neq j} \beta_j \beta_k \left[\mathcal{O}_j, \frac{\partial \mathcal{O}_k}{\partial t}\right]$$

$$+ i\frac{\hbar}{48m^3c^6} \sum_j \sum_k \sum_l \left[\beta_j \mathcal{O}_j, \left[\beta_k \mathcal{O}_k, \beta_l \frac{\partial \mathcal{O}_l}{\partial t}\right]\right] + \cdots \tag{B.13}$$

If we retain terms only up to $O(1/m^2)$ this reduces to

$$\hat{H}'_{\mathbf{R}} \rightarrow \sum_j \beta_j mc^2 + \mathcal{E} + \frac{1}{2mc^2} \sum_j \beta_j \left[\mathcal{O}_j, \mathcal{E}\right] + \frac{1}{2mc^2} \sum_j \beta_j \mathcal{O}_j^2 - \frac{1}{8m^2c^4} \sum_j \left[\mathcal{O}_j, \left[\mathcal{O}_j, \mathcal{E}\right]\right]$$

$$+ \frac{1}{8m^2c^4} \sum_j \sum_{k \neq j} \beta_j \beta_k \left[\mathcal{O}_j, \left[\mathcal{O}_k, \mathcal{E}\right]\right] - \frac{1}{2m^2c^4} \sum_j \mathcal{O}_j^3 + \frac{1}{6m^2c^4} \sum_j \mathcal{O}_j^3$$

$$+ i\frac{\hbar}{2mc^2} \sum_j \beta_j \frac{\partial \mathcal{O}_j}{\partial t} - i\frac{\hbar}{8m^2c^4} \sum_j \left[\mathcal{O}_j, \frac{\partial \mathcal{O}_j}{\partial t}\right] + i\frac{\hbar}{8m^2c^4} \sum_j \sum_{k \neq j} \beta_j \beta_k \left[\mathcal{O}_j, \frac{\partial \mathcal{O}_k}{\partial t}\right]. \tag{B.14}$$

B.3. Evaluation of the F-W transformation

We can write for the even and odd operators

$$\mathcal{E} = Q\Phi, \tag{B.15}$$

$$\mathcal{O}_j = \frac{1}{N} \boldsymbol{\alpha}_j \cdot c(\hat{\mathbf{P}} - Q\mathbf{A}). \tag{B.16}$$

We can evaluate

$$\mathcal{O}_j^2 = \frac{c^2}{N^2} |\hat{\mathbf{P}} - Q\mathbf{A}|^2 - \frac{\hbar c^2 Q}{N^2} \boldsymbol{\Sigma}_j \cdot \mathbf{B}, \tag{B.17}$$

$$\left[\mathcal{O}_j, \mathcal{E}\right] = -i\frac{\hbar Qc}{N}\boldsymbol{\alpha}_j \cdot \nabla\Phi, \tag{B.18}$$

$$\left[\mathcal{O}_j, \left[\mathcal{O}_j, \mathcal{E}\right]\right] + i\hbar\left[\mathcal{O}_j, \frac{\partial\mathcal{O}_j}{\partial t}\right] = \frac{\hbar^2 Qc^2}{N^2}\nabla\cdot\mathbf{E} - \frac{\hbar Qc^2}{N^2}\boldsymbol{\Sigma}_j\cdot(\hat{\mathbf{P}} - Q\mathbf{A})\times\mathbf{E}$$
$$+ \frac{\hbar Qc^2}{N^2}\boldsymbol{\Sigma}_j\cdot\mathbf{E}\times(\hat{\mathbf{P}} - Q\mathbf{A}), \tag{B.19}$$

$$\left[\mathcal{O}_j, \left[\mathcal{O}_k, \mathcal{E}\right]\right]_{j\neq k} = -\frac{\hbar^2 c^2 Q}{N^2}\left((\boldsymbol{\alpha}_j\cdot\nabla)(\boldsymbol{\alpha}_k\cdot\nabla)\Phi\right)_{j\neq k}, \tag{B.20}$$

$$\left[\mathcal{O}_j, \frac{\partial\mathcal{O}_j}{\partial t}\right] = i\frac{\hbar c^2 Q}{N^2}\nabla\cdot\frac{\partial\mathbf{A}}{\partial t} - i\frac{c^2 Q}{N^2}\left(\boldsymbol{\Sigma}_j\cdot(\hat{\mathbf{P}} - Q\mathbf{A})\times\frac{\partial\mathbf{A}}{\partial t} - \boldsymbol{\Sigma}_j\cdot\frac{\partial\mathbf{A}}{\partial t}\times(\hat{\mathbf{P}} - Q\mathbf{A})\right), \tag{B.21}$$

$$\left[\mathcal{O}_j, \frac{\partial\mathcal{O}_k}{\partial t}\right]_{j\neq k} = i\frac{\hbar c^2 Q}{N^2}\left[(\boldsymbol{\alpha}_j\cdot\nabla)\left(\boldsymbol{\alpha}_k\cdot\frac{\partial\mathbf{A}}{\partial t}\right)\right]_{j\neq k}. \tag{B.22}$$

We can make use of these results to write

$$\hat{H}'_\mathbf{R} = \sum_j\beta_j mc^2 + \frac{|\hat{\mathbf{P}} - Q\mathbf{A}|^2}{2M}\frac{1}{N}\sum_j\beta_j + Q\Phi - \frac{\hbar Q}{2M}\frac{1}{N}\sum_j\beta_j\boldsymbol{\Sigma}_j\cdot\mathbf{B}$$
$$- \frac{\hbar^2 Q}{8M^2 c^2}\sum_j\nabla\cdot\mathbf{E} + \frac{\hbar Q}{8M^2 c^2}\sum_j\boldsymbol{\Sigma}_j\cdot\left[(\hat{\mathbf{P}} - Q\mathbf{A})\times\mathbf{E} - \mathbf{E}\times(\hat{\mathbf{P}} - Q\mathbf{A})\right]$$
$$+ i\frac{\hbar Qc}{2Mc^2}\sum_j\beta_j\boldsymbol{\alpha}_j\cdot\mathbf{E} - \frac{\hbar^2}{8M^2 c^2}\sum_j\sum_{k\neq j}\beta_j\beta_k\left[(\boldsymbol{\alpha}_j\cdot\nabla)(\boldsymbol{\alpha}_k\cdot\nabla)\Phi\right]$$
$$- \frac{1}{3M^2 c^2}\frac{1}{N}\sum_j\left[|\hat{\mathbf{P}} - Q\mathbf{A}|^2 - \hbar Q\boldsymbol{\Sigma}_j\cdot\mathbf{B}\right]\boldsymbol{\alpha}_j\cdot c(\hat{\mathbf{P}} - Q\mathbf{A})$$
$$- \frac{\hbar^2 Q}{8M^2 c^2}\sum_j\sum_{k\neq j}\beta_j\beta_k\left[(\boldsymbol{\alpha}_j\cdot\nabla)\left(\boldsymbol{\alpha}_k\cdot\frac{\partial\mathbf{A}}{\partial t}\right)\right] + \cdots \tag{B.23}$$

The terms on the last three lines all have odd pieces, so they are smaller and can be removed with further F–W rotations (the discussion in [197] is relevant here). The terms that survive to $O(1/m^2)$ are

$$\hat{H}'_\mathbf{R} \rightarrow \sum_j\beta_j mc^2 + \frac{|\hat{\mathbf{P}} - Q\mathbf{A}|^2}{2M}\frac{1}{N}\sum_j\beta_j + Q\Phi - \frac{\hbar Q}{2M}\frac{1}{N}\sum_j\beta_j\boldsymbol{\Sigma}_j\cdot\mathbf{B}$$
$$- \frac{\hbar^2 Q}{8M^2 c^2}\sum_j\nabla\cdot\mathbf{E} + \frac{\hbar Q}{8M^2 c^2}\sum_j\boldsymbol{\Sigma}_j\cdot\left[(\hat{\mathbf{P}} - Q\mathbf{A})\times\mathbf{E} - \mathbf{E}\times(\hat{\mathbf{P}} - Q\mathbf{A})\right]. \tag{B.24}$$

This provides the generalization of the Foldy–Wouthuysen single particle result to the center of mass degrees of freedom of the composite.

Appendix C. Reviewer Comments

The reviewer has raised a number of issues, most of which were addressed in a significant revision of the paper. However, it seems worth while to consider the remaining issues in this Appendix. One issue has to do with the focus of the paper and conclusions; another issue has to do with other approaches to the problem of anomalies in condensed matter nuclear science.

C.1. Coupling and projection operators

The reviewer wrote:

> It is argued that the many particle Foldy–Wouthuysen theory, projected onto positive energy solutions, might allow some sort of coupling between the center of mass momentum of a composite, and the internal degrees of freedom that might facilitate coupling between nuclear events and phonons or plasmons in a solid, or at least that is how I read it. But the projections onto the positive energy space of Foldy–Wouthuysen transformations are complicated, and a specific reason why they might lead to the coupling that is desired linking internal nuclear degrees of freedom to extended quasi-particles like phonons or plasmons in a solid was not given. Obviously this is an open topic for future work. The hope seems to be that a process of elimination might yield the desired result. Since just about every other source for coupling between the nuclear degrees of freedom and the solid are ruled out, only the complexity of the positive energy projection in the Foldy–Wouthuysen transformation leaves it alone as a possibility. It might be so, but explicit evidence to that effect was not given in this paper, as far as I could tell.

In response, we note that there are a number of different issues raised in this comment, which are probably worth sorting out. One issue has to do with the projection operators, which are required in a relativistic theory in order to cure Brown–Ravenhall disease (coupling to negative energy states) that occurs in the many-particle Dirac model. The majority of relativistic Dirac Hartree–Fock atomic physics calculations that have been done over the years make use of Coulomb plus Breit interactions without explicit projection operators. In this case projection is generally implemented instead through the inclusion of positive energy basis states (in a Furry picture sense), such as in a multi-state eigenvalue calculation, transition calculation or scattering calculation. In a self-consistent calculation the selection of positive energy eigenvalues for individual orbitals ends up restricting the calculation to the positive energy sector. An alternate approach is to make use of some of the "no-pair" formulations that are available, and which are used for relativistic quantum chemistry calculations; negative energy contributions, again in the Furry picture sense, are eliminated by the formalism.

Projection operators arise in the formal development of the nucleon-nucleon interaction (see e.g. [400,401]). In previous years the majority of nuclear calculations were done with nonrelativistic models so that there was no issue. In relativistic models there is a potential issue; however, it is easy to deal with as in the atomic case through a restriction of the basis states used (to positive energy states), or through the selection of positive energy orbitals in a Dirac-Fock type of calculation. In the literature there is no indication that headaches arise when the center of mass coupling is implemented [232–235].

Perhaps a good way to think about the appearance of the projection operators in a many-particle Dirac model is that they are present in order to prevent coupling to (single particle) negative energy states; but otherwise contribute relatively minor corrections (which would be important in a high precision calculation [176]).

A second issue concerns the coupling between lattice degrees of freedom and the internal degrees of freedom in a nucleus. There is no difficulty in finding external field interactions that will provide a weak coupling between

vibrations and internal nuclear transitions; one can see such terms in the composite models described above. The headache is that these terms are weak. The center of mass interaction terms that we have emphasized in this work can mediate a coupling between vibrations and internal nuclear transitions, even though we have found no papers (outside of our own) which consider this possibility. In essence, this coupling is present in many-particle Dirac models, and in Poincaré invariant models more generally, and it can produce an interaction between lattice vibrations and nuclear transitions which has not been previously considered. In coherent models that we have investigated this coupling is sufficiently large to account for $D_2/^4He$ transitions occurring at a rate consistent with experiment, as long as the large nuclear quantum can be down-shifted efficiently. Based on the present work we now have much greater confidence that this interaction must be present in a Poincaré invariant model, and is not a mistake or an artifact.

Finally, it is definitely the case that in our research we tried every other coupling we could think of, and the process of elimination succeeded in eliminating all interactions that we were aware of as being candidates to implement the effects we were interested in. It was not the purpose of this work to argue for, or to attempt to prove, that this interaction is responsible for the anomalies in condensed matter nuclear science. It is true as the reviewer has indicated that external field interactions are sufficiently weak such that we would not expect them to provide much coupling between the lattice and internal nuclear states; hence we would not expect them to be very important in connection with the anomalies under consideration. However, we have already spent some years working with this center of mass interaction in connection with excess heat, and in connection with collimated X-ray emission; and in both cases the center of mass interaction looks very promising (and there seem to be no alternatives). The purpose of this paper in connection with this point is to understand the center of mass interaction in the context of quantum composite models, to understand what relevant literature is available that discusses the interaction, and also to gain some understanding as to what the interaction is. In other works we have considered applications, and in future papers we will revisit calculations of the coupling matrix element as well as applications to conventional physical systems as well as to anomalies in condensed matter nuclear science.

C.2. Nonperturbative effects

The reviewer wrote:

> The author may want to look at and discuss another feature of the standard model and QED, which is the infrared divergence phenomena which was first described by the Bloch–Nordsieck model. This is a nonperturbative feature of QED. It leads to modifications to the particle propagators which have been termed infraparticles (see https://en.wikipedia.org/wiki/Infraparticle). This infra-red phenomenon could lead to the type of nonlocal features the author is looking for in interactions between the nucleus and the solid. It would be nice to add them to the discussion in this paper. These "dressed" particles of QED are not fully understood, especially not in a nonequilibrium condensed matter setting, but they involve infinite numbers of photons interacting with a charged particle, and due to the infrared divergence, they lead to a blurring of the mass of the charged particle. The propagators for the charged particle ends up no longer being a simple pole in the 4-momentum squared. This is hard to interpret in conventional quantum field theory, and so I would say this is an unresolved issue in QED. The behavior of these dressed QED particles in nonequilibrium condensed matter settings are largely unknown. Because they involve an infinite number of photons, and are consequently nonperturbative effects, they might provide the kind of nonlocal coupling between a charged particle and the extended solid that is required in LENR and that the author is seeking. Moreover, as they do not have a fixed mass, they might also provide a basis for off-mass-shell behavior as in Fock–Stueckelberg theory.

Our hope back in 1989 was to find some straightforward bit of physics which would account for the anomalies in a way that could be easily understood. For example, it was clear that we would expect a weak coupling between vibrations and internal nuclear transitions mediated by electric and magnetic fields. Since there was little question as to how lattice vibrations work, or how transitions between nuclear states work, the only issue left seemed to concern what happens when the vibrations are coupled to the transitions. It was clear early on that we might have Dicke enhancement factors showing up, which could serve to amplify the small interaction. However, the big issue then as now was whether it was possible to down-convert a large quantum into lots of small quanta, or vice versa with up-conversion. Over the years we managed to develop models which described the kind of up-conversion and down-conversion required, and we have been successful in quantifying these models under ideal conditions.

Looking back, there have been two "new" components to the models under investigation; one is the new up-conversion mechanism; and the other has been the center of mass coupling. In this study the issue of the coupling has in our view been clarified. We have solid derivations, clean formulas for the interaction, a connection with the literature, and a simple understanding of what the interaction is. What remains is to carry out calculations of the coupling matrix elements for specific transitions of interest. What we need to do is to go back to the up-conversion and down-conversion mechanism, and to see whether we might push them further theoretically, and also see whether we might connect with experiment in an unambiguous way. At present we are attempting to develop some simple experiments that would test these ideas.

I will be the first to agree with the reviewer that there are some subtle effects that emerge in quantum field theory models; that there are unresolved issues in QED; and that there are issues with "dressed" particles in QED and in condensed matter physics which can be very nonintuitive. A measure of my interest level might be the large number of books and papers collected in my office (and in many cases read). An unfortunately reality of our field has been, and continues to be, a relative lack of resources. I can see a potential solution to the puzzle (which are the anomalies) in the approach and in the models I have pursued; and if I can find a way to continue working on the approach I might just be able to clarify whether it is a solution, or whether it is yet another dead end. And if it is to be the dead end, then the suggestions of the reviewer are approaches that might be considered next.

References

[1] M. Fleischmann, S. Pons and M. Hawkins, Electrochemically induced nuclear fusion of deuterium, *J. Electroanal. Chem. Interfacial ElectroChem.* **201** (1989) 301; errata **263** (1990) 187.

[2] M. Fleischmann, S. Pons, M.W. Anderson, L.J. Li and M. Hawkins, Calorimetry of the palladium–deuterium–heavy water system, *J. Electroanal. Chem. and Interfacial ElectroChem.* **287** (1990) 293–348.

[3] P.L. Hagelstein and I.U. Chaudhary, Phonon models for anomalies in condensed matter nuclear science, *Current Science* **108** (2015) 507.

[4] P.L. Hagelstein, Current status of the theory and modeling effort based on fractionation, *J. Condensed Matter Nucl. Sci.,* in press.

[5] P.L. Hagelstein and I.U. Chaudhary, Phonon–nuclear coupling for anomalies in condensed matter Nuclear Science, *J. Condensed Matter Nucl. Sci.* **12** (2013) 105.

[6] M. Davidson, Private communication.

[7] P.A.M. Dirac, The quantum theory of the electron, *Proc. Roy. Soc. London A: Mathematical, Physical and Engineering Sciences* **117** (1928) 610–624.

[8] W. Pauli, *Handbuch der Physik, Part I*, **24** (1933).

[9] W. Pauli and Wolfgang, Relativistic field theories of elementary particles, *Rev. Modern Phys.* **13** (1941) 203.

[10] P. Caldirola, Relativistic correction in calculating the magnetic moment of the deuteron, *Phy. Rev.* **69** (1946) 608.

[11] J.L. Powell, Note on the bremsstrahlung produced by protons, *Phy. Rev.* **75** (1949) 32.

[12] M. Gell-Mann and M.L. Goldberger, Scattering of low energy photons by particles of spin 1/2, *Phy. Rev.* **96** (1954) 1433.

[13] R. Gomez and D. Walecka, Separation of the cross section for scattering of photons by protons into spin-flip and non-spin-flip parts, *Phy. Rev.* **104** (1956) 1479.

[14] S.N. Gupta, Anomalous magnetic moments of nucleons in nucleon–photon interaction, *Phy. Rev.* **107** (1957) 1442.

[15] F. Li, L. Ma and Y.-D. Zhang, Some studies of the neutron's Dirac equation, *Commun. Theoret. Phys.* **23** (1995) 191.

[16] A.Ya. Silenko, Quantum-mechanical description of the electromagnetic interaction of relativistic particles with electric and magnetic dipole moments, *Russian Phys. J.* **48** (2005) 788–792.

[17] T.-W. Chen and D.-W. Chiou, Correspondence between classical and Dirac–Pauli spinors in view of the Foldy–Wouthuysen transformation, *Phy. Rev. A* **89** (2014) 032111.

[18] T.-W. Chen and D.-W. Chiou, High-order Foldy–Wouthuysen transformations of the Dirac and Dirac–Pauli Hamiltonians in the weak-field limit, *Phy. Rev. A* **90** (2014) 012112.

[19] O. Klein and Y. Nishina, The scattering of light by free electrons according to Dirac's new relativistic dynamics, *Nature* **122** (1928) 398–399.

[20] P. Christillin, Nucl. Compton scattering, *J. Phys. G: Nucl. Phys.* **12** (1986) 837.

[21] M.-Th. Hütt, A.I. L'vov, A.I. Milstein and M. Schumacher, Compton scattering by nuclei, *Phys. Reports* **323** (2000) 457–594.

[22] H.W. Griesshammer, J.A. McGovern, D.R. Phillips and G. Feldman, Using effective field theory to analyse low-energy Compton scattering data from protons and light nuclei, *Prog. in Particle and Nucl. Phys.* **67** (2012) 841–897.

[23] V.I. Goldansky, O.A. Karpukhin, A.V. Kutsenko and V.V. Pavlovskaya, Elastic γ-p scattering at 40 to 70 MeV and polarizability of the proton, *Nucl. Phys.* **18** (1960) 473–491.

[24] P. Baranov, G. Buinov, V. Godin, V. Kuznetzova, V. Petrunkin, L. Tatarinskaya, V. Shirthenko, L. Shtarkov, V. Yurtchenko and Yu Yanulis, New experimental data on the proton electromagnetic polarizabilities, *Phys. Lett. B* **52** (1974) 122–124.

[25] F.J. Federspiel, R.A. Eisenstein, M.A. Lucas, B.E. MacGibbon, K. Mellendorf, A.M. Nathan, A. O'Neill and D.P. Wells, Proton Compton effect: A measurement of the electric and magnetic polarizabilities of the proton, *Phy. Rev. Lett.* **67** (1991) 1511.

[26] B.E. MacGibbon, G. Garino, M.A. Lucas, A.M. Nathan, G. Feldman and B. Dolbilkin, Measurement of the electric and magnetic polarizabilities of the proton, *Phy. Rev. C* **52** (1995) 2097.

[27] De León, V. Olmos, F. Wissmann, P. Achenbach, J. Ahrens, H.-J. Arends, R. Beck, P.D. Harty, V. Hejny, P. Jennewein, M. Kotulla and B. Krusche, Low-energy Compton scattering and the polarizabilities of the proton, *Eur. Phys. J. A – Hadrons and Nuclei* **10** (2001) 207–215.

[28] V.S. Barashenkov, H.J. Kaiser, E.E. Kapuscik and J.S. Kwiecinski, A semi-phenomenological description of Compton scattering on spin 1/2 systems, *Nucl. Phys.* **50** (1964) 684–692.

[29] B.R. Holstein, D. Drechsel, B. Pasquini and M. Vanderhaeghen, Higher order polarizabilities of the proton, *Phy. Rev. C* **61** (2000) 034316.

[30] M. Schumacher, Polarizability of the nucleon and Compton scattering, *Prog. Particle and Nucl. Phys.* **55** (2005) 567–646.

[31] P.C. Hecking and G.F. Bertsch, Proton polarizability in the MIT bag model, *Phys. Lett. B* **99** (1981) 237–239.

[32] V. Bernard, N. Kaiser and Ulf-G. Meissner, Chiral expansion of the nucleonŠs electromagnetic polarizabilities, *Phys. Rev. Lett.* **67** (1991) 1515.

[33] T.R. Hemmert, B.R. Holstein, J. Kambor and G. Knöchlein, Compton scattering and the spin structure of the nucleon at low energies, *Phy. Rev. D* **57** (1998) 5746.

[34] D. Drechsel, B. Pasquini and M. Vanderhaeghen, Dispersion relations in real and virtual Compton scattering, *Phys. Reports* **378** (2003) 99–205.

[35] C.E. Hyde-Wright and K.de Jager, Electromagnetic form factors of the nucleon and Compton scattering, *Ann. Rev. Nucl. and Particle Sci.* **54** (2003) 217.

[36] Y.-D. Zhang, On the neutron's Dirac equation, *Il Nuovo Cimento B* **103** (1989) 343–367.

[37] M. Bawin and S.A. Coon, Neutron charge radius and the Dirac equation, *Phy. Rev. C* **60** (1999) 025207.

[38] V.I. Vysotskii and M.V. Vysotskyy, Abnormal features of neutron–nucleus low-energy interaction and the mechanism of inhibition of neutron-induced reactions, *Eur. Phys. J. A* **44** (2010) 279–285.

[39] V.F. Sears, Electromagnetic neutron–atom interactions, *Phys. Reports* **141** (1986) 281–317.

[40] H. Abele, The neutron. Its properties and basic interactions, *Prog. in Particle and Nucl. Phys.* **60** (2008) 1–81.

[41] F.E. Serr and J.D. Walecka, A relativistic quantum field theory of finite nuclei, *Phys. Lett. B* **79** (1978) 10–14.

[42] C.J. Horowitz and B.D. Serot, Self-consistent Hartree description of finite nuclei in a relativistic quantum field theory, *Nucl. Phys. A* **368** (1981) 503–528.

[43] Y. K. Gambhir, P. Ring and A. Thimet, Relativistic mean field theory for finite nuclei, *Ann. Phys.* **198** (1990) 132–179.

[44] E.N.E. Van Dalen and H. Müther, Relativistic description of finite nuclei based on realistic NN interactions, *Phy. Rev. C* **84** (2011) 024320.

[45] R. Machleidt and D.R. Entem, Chiral effective field theory and Nuclear forces, *Phys. Reports* **503** (2011) 1–75.

[46] P.A.M. Dirac, Relativistic wave equations, *Proc. Roy. Soc. of London. Series A, Math. Phy. Sci.* **155** (1936) 447–459.

[47] M. Fierz and W. Pauli, On relativistic wave equations for particles of arbitrary spin in an electromagnetic field, *Proc. Roy. Soc. of London. Series A, Math. Phy. Sci.* **173** (1939) 211–232.

[48] S. Tani, Reformulation of the Dirac–Fierz–Pauli equation for spin 3/2, *Phy. Rev. D* **2** (1970) 980.

[49] W. Rarita and J. Schwinger, On a theory of particles with half-integral spin, *Phy. Rev.* **60** (1941) 61.

[50] T. Pilling, Symmetry of Massive RaritaŰSchwinger fields, *Int. J. Modern Phys. A* **20** (2005) 2715–2741.

[51] A.D. Bryden, Equivalence of manifestly covariant theories for spin 3/2, *Nucl. Phys.* **58** (1964) 314–320.

[52] P.A. Moldauer and K.M. Case, Properties of half-integral spin Dirac–Fierz–Pauli particles, *Phy. Rev.* **102** (1956) 279.

[53] J. Niederle and A.G. Nikitin, Relativistic wave equations for interacting, massive particles with arbitrary half-integer spins, *Phy. Rev. D* **64** (2001) 125013.

[54] A,D, Bryden, A Foldy–Wouthuysen transformation for particles of spin 3/2, *Nucl. Phys.* **53** (1964) 165–173.

[55] K. Johnson and E.C.G. Sudarshan, Inconsistency of the local field theory of charged spin 3/2 particles, *Ann. of Phys.* **13** (1961) 126–145.

[56] G. Velo and D. Zwanziger, Propagation and quantization of Rarita–Schwinger waves in an external electromagnetic potential, *Phy. Rev.* **186** (1969) 1337.

[57] S. Deser, A. Waldron and V. Pascalutsa, Massive spin 3/2 electrodynamics, *Phy. Rev. D* **62** (2000) 105031.

[58] C.R. Hagen, New inconsistencies in the quantization of spin-3/2 fields, *Phy. Rev. D* **4** (1971) 2204.

[59] G.R. Allcock and S.F. Hall, Constraints, positivity, 'obscure' representations and the spin-3/2 problem, *J. Phys. A: Math. General* **11** (1978) 2305.

[60] M. Kobayashi and Y. Takahashi, Rarita–Schwinger paradoxes as a common disease in constrained systems, *Prog. Theoret. Phys.* **75** (1986) 993–995.

[61] M. Kobayashi and Y. Takahashi, The Rarita–Schwinger paradoxes, *J. Phys. A: Math. General* **20** (1987) 6581.

[62] M. Kobayashi and Y. Takahashi, The Rarita–Schwinger paradoxes in the theory with an auxiliary field, *Il Nuovo Cimento B* **104** (1989) 67–79.

[63] S.N. Gupta and W.W. Repko, Quantization of the charged spin-3/2 field, *Phy. Rev.* **177** (1969) 1921.

[64] J.D. Kimel and L.M. Nath, Quantization of the spin-3/2 field in the presence of interactions, *Phy. Rev. D* **6** (1972) 2132.

[65] W. Cox, On the Lagrangian and Hamiltonian constraint algorithms for the Rarita–Schwinger field coupled to an external electromagnetic field, *J. Phys. A: Math. General* **22** (1989) 1599.

[66] S. Dengiz, Faddeev–Jackiw Hamiltonian reduction for free and gauged Rarita–Schwinger theories, *arXiv preprint* arXiv:1602.01018 (2016).

[67] S.L. Adler, Classical gauged massless Rarita–Schwinger fields, *Phy. Rev. D* **92** (2015) 085022.

[68] T. Hamada, Effect of nucleon excited state on magnetic moment anomaly, *Prog. Theoret. Phys.* **10** (1953) 309–322.

[69] Y. Fujii, Isobar model and the S-wave pion–nucleon scattering, *Prog. Theoret. Phys.* **24** (1960) 1013–1032.

[70] D.M. Brudnoy, Isobar model for resonance scattering, *Phy. Rev.* **145** (1966) 1229.

[71] M. Benmerrouche, R.M. Davidson and N.C. Mukhopadhyay, Problems of describing spin-3/2 baryon resonances in the effective Lagrangian theory, *Phy. Rev. C* **39** (1989) 2339.

[72] I. Lovas, K. Sailer and W. Greiner, Generalized Rarita–Schwinger equations for non-strange baryons, *Acta Physica Hungarica, New Series Heavy Ion Phys.* **5** (1997) 85–95.

[73] V. Pascalutsa, Quantization of an interacting spin-3/2 field and the Δ isobar, *Phy. Rev. D* **58** (1998) 096002.

[74] R. E. Kozack, B. C. Clark, S. Hama, V. K. Mishra, G. Kälbermann, R. L. Mercer and L. Ray, Relativistic deuteron–nucleus scattering in the Kemmer–Duffin–Petiau formalism, *Phy. Rev. C* **37** (1988) 2898.

[75] R.E. Kozack, B.C. Clark, S. Hama, V.K. Mishra, R.L. Mercer and L. Ray, Spin-one Kemmer–Duffin–Petiau equations and intermediate–energy deuteron–nucleus scattering, *Phy. Rev. C* **40** (1989) 2181.

[76] V.K. Mishra, S. Hama, B.C. Clark, R.E. Kozack, R.L. Mercer and L. Ray, Implications of various spin-one relativistic wave equations for intermediate-energy deuteron–nucleus scattering, *Phy. Rev. C* **43** (1991) 801.

[77] M. Gell-Mann, A schematic model of baryons and mesons, *Phys. Lett.* **8** (1964) 214–215.

[78] V. Bargmann and E.P. Wigner, Group theoretical discussion of relativistic wave equations, *Proc. National Academy Sci.* **34** (1948) 211–223.

[79] A. Salam, R. Delbourgo and J. Strathdee, The covariant theory of strong interaction symmetries, *Proc. Roy. Soc. London A: Math., Physical and Eng. Sci.* **284** (1965) 146–158.

[80] B. Sakita and K.C. Wali, Relativistic formulation of the SU(6) symmetry scheme, *Phy. Rev.* **139** (1965) B1355.

[81] J.M. Charap and P.T. Matthews, On the covariant extension of SU(6), *Proc. Roy. Soc. London A: Math., Physical and Eng. Sci.* **286** (1965) 300–312.

[82] F. Hussain, J.G. Körner and G. Thompson, Relativistic SU(6) wave functions as the basis of modern approaches to hadronic wave functions, *Ann. Phys.* **206** (1991) 334–367.

[83] M. Moshinsky, A. del Sol Mesa and V. Riquer, Supermultiplicity and the relativistic Coulomb problem with arbitrary spin, *Foundations Phys.* **27** (1997) 1139–1157.

[84] M. Moshinsky, The relativistic many body problem in quantum mechanics, *Symmetries in Science,* Vol. XI, Springer, Netherlands, 2004, pp. 37–43.

[85] E. Sadurní, The Dirac–Moshinsky oscillator: theory and applications, *Latin-American School of Phys.-XL ELAF: Symmetries in Physics*, AIP Publishing, **1334** (2011) 249–290.

[86] Fl. Stancu, *Group Theory in SubNuclear Physics*, Clarendon Press, Oxford, 1996.

[87] I.U. Chaudhary, Applications of group theory to few-body physics, Ph.D. Thesis, Massachusetts Institute of Technology, USA, 2005.

[88] A. De Rujula, H. Georgi and S.L. Glashow, Hadron masses in a gauge theory, *Phy. Rev. D* **12** (1975) 147.

[89] F. Myhrer and J. Wroldsen, The nucleon–nucleon force and the quark degrees of freedom, *Rev. Modern Phys.* **60** (1988) 629.

[90] P.L. Hagelstein and I.U. Chaudhary, Central and tensor contributions to the phonon-exchange matrix element for the $D_2/^4$He transition, *J. Cond. Matter Nucl. Sci.* **11** (2013) 15–58.

[91] S.N. Gupta and W.W. Repko, Electromagnetic interaction of the Bargmann–Wigner field with spin 1/2, *Phy. Rev.* **159** (1967) 1082.

[92] J. Leon, M. Quiros and J. Ramírez Mittelbrunn, Gauge invariance, Lorentz covariance and the electromagnetic properties of elementary systems, *Il Nuovo Cimento B* **54** (1979) 153–170.

[93] T. Hamada and I.D. Johnston, A potential model representation of two-nucleon data below 315 MeV, *Nucl. Phys.* **34** (1962) 382–403.

[94] R.V. Reid, Local phenomenological nucleon–nucleon potentials, *Ann. Phys.* **50** (1968) 411–448.

[95] G. Bertsch, J. Borysowicz, H. McManus and W.G. Love, Interactions for inelastic scattering derived from realistic potentials, *Nucl. Phys. A* **284** (1977) 399–419.

[96] M.M. Nagels, T.A. Rijken and J.J. De Swart, Low-energy nucleon–nucleon potential from Regge-pole theory, *Phy. Rev. D* **17** (1978) 768.

[97] M. Lacombe, B. Loiseau, J.M. Richard, R. Vinh Mau, J. Côté, P. Pires and R. De Tourreil, Parametrization of the Paris N–N potential, *Phy. Rev. C* **21** (1980) 861.

[98] I.E. Lagaris and V.R. Pandharipande, Phenomenological two-nucleon interaction operator, *Nucl. Phys. A* **359** (1981) 331–348.

[99] R. Machleidt, K. Holinde and Ch. Elster, The Bonn meson-exchange model for the nucleonŮ-nucleon interaction, *Phys. Reports* **149** (1987) 1–89.

[100] R.B. Wiringa, V.G.J. Stoks and R. Schiavilla, Accurate nucleon–nucleon potential with charge-independence breaking, *Phy. Rev. C* **51** (1995) 38.

[101] S. Weinberg, Effective chiral Lagrangians for nucleon–pion interactions and Nucl. forces, *Nucl. Phys. B* **363** (1991) 3–18.

[102] D.R. Entem and R. Machleidt, Accurate nucleonŮnucleon potential based upon chiral perturbation theory, *Phys. Lett. B* **524** (2002) 93–98.

[103] D.R. Entem and R. Machleidt, Accurate charge-dependent nucleon–nucleon potential at fourth order of chiral perturbation theory, *Phy. Rev. C* **68** (2003) 041001.

[104] L.D. Landau and E.M. Lifshitz, *Quantum Mechanics – Nonrelativistic Theory*, Pergammon Press, New York, 1975.

[105] G. Breit, The effect of retardation on the interaction of two electrons, *Phy. Rev.* **34** (1929) 553.

[106] G. Breit and F.W. Doermann, The hyperfine structure of S and P terms of two electron atoms with special reference to Li+, *Phy. Rev.* **36** (1930) 1732.

[107] D.R. Inglis, Hyperfine structure as a test of a linear wave equation in the two-body problem, *Phy. Rev.* **37** (1931) 795.

[108] G. Breit, Approximately relativistic equations for nuclear particles, *Phy. Rev.* **51** (1937) 248.

[109] I.S. Lowen, The effect of nuclear motion in the dirac equation, *Phy. Rev.* **51** (1937) 190.

[110] G. Breit, Approximately relativistic equations, *Phy. Rev.* **53** (1938) 153.

[111] G.E. Brown and D.G. Ravenhall, On the interaction of two electrons, *Proc. Roy. Soc. London A: Math., Physical and Eng. Sci.* **208** (1951) 552–559.

[112] M. H. Mittleman, Configuration-space Hamiltonian for heavy atoms and correction to the Breit interaction, *Phy. Rev. A* **5** (1972) 2395.

[113] J. Sucher, Foundations of the relativistic theory of many-electron atoms, *Phy. Rev. A* **22** (1980) 348.

[114] J. Sucher, Foundations of the relativistic theory of many-electron bound states, *Int. J. Quantum Chem.* **25** (1984) 3–21.

[115] G. Hardekopf and J. Sucher, Relativistic wave equations in momentum space, *Phy. Rev. A* **30** (1984) 703.

[116] S.N. Datta and A. Misra, Relativistic dynamics of two spin-half particles in a homogeneous magnetic field, *J. Chemical Phys.* **114** (2001) 1478–1490.

[117] N. Kemmer, Zur theorie der neutron–proton wechselwirkung, *Helv. Phys. Acta* **10** (1937) 48.

[118] E. Fermi and C.-N. Yang, Are mesons elementary particles? *Phy. Rev.* **76** (1949) 1739.

[119] W. Kluzniak, W. Królikowski and J. Rzewuski, Relativistic radial equations for two spin-1/2 particles with a static interaction: part two, *Acta Physica Polonica Series B* **9** (1978) 43–48.

[120] F. Gesztesy, H. Grosse and B. Thaller, Relativistic corrections to bound-state energies for two-fermion systems, *Phy. Rev. D* **30** (1984) 2189.

[121] J.A. McNeil and B.K. Wallin, Search for positronium resonances in the Kemmer–Fermi–Yang model, *Phys. Lett. B* **297** (1992) 223–227.

[122] G. Breit and I. Bloch, Relativistic correction to the magnetic moment of the deuteron, *Phy. Rev.* **72** (1947) 135.

[123] A. E. S. Green and T. Sawada, Meson theoretic N–N interactions for nuclear physics, *Rev. Modern Phys.* **39** (1967) 594.

[124] S. Sato, Nonrelativistic limit of Kemmer–Fermi–Yang equation, *Il Nuovo Cimento A* **82** (1984) 339–350.

[125] A.O. Barut, On the treatment of Möller and Breit-potentials and the covariant two-body equation for positronium and muonium, *Physica Scripta* **36** (1987) 493.

[126] A.P. Galeao, J.A. Castilho Alcarás and P. Leal Ferreira, Two-body Dirac equation approach to the deuteron, *Int. J. Modern Phys. E* **7** (1998) 89–106.

[127] H.M. Moseley and N. Rosen, The meson as a composite particle, *Phy. Rev.* **80** (1950) 177.

[128] R.W. Childers, Two-body Dirac equation for semirelativistic quarks, *Phy. Rev. D* **26** (1982) 2902.

[129] Y. Koide, Exactly solvable model of relativistic wave equations and meson spectra, *Il Nuovo Cimento A* **70** (1982) 411–434.

[130] A.O. Barut and N. Ünal, Radial equations for the relativistic two-Fermion problem with the most general electric and magnetic potentials, *Fortschritte der Physik/Prog. Phys.* **33** (1985) 319–332.

[131] P.L. Ferreira, Two-body Dirac equation with a scalar linear potential, *Phy. Rev. D* **38** (1988) 2648.

[132] G. Breit and R.E. Meyerott, Effect of Nucl. motion of the hyperfine structure of the ground term of hydrogen, *Phy. Rev.* **72** (1947) 1023.

[133] G. Breit, G.E. Brown and G.B. Arfken, The effect of Nucl. motion on the hyperfine structure of hydrogen, *Phy. Rev.* **76** (1949) 1299.

[134] W.E. Lamb, Fine structure of the hydrogen atom–III, *Phy. Rev.* **85** (1952) 259.

[135] W.A. Barker and F.N. Glover, Reduction of relativistic two-particle wave equations to approximate forms–III, *Phy. Rev.* **99** (1955) 317.

[136] M. Malvetti and H. Pilkuhn, Equal-time relativistic two-body equations, *Phys. Reports* **248** (1994) 1–60.

[137] A.O. Barut and G.L. Strobel, Center-of-mass motion of a system of relativistic Dirac particles, *Few-Body Systems* **1** (1986) 167–180.

[138] G.L. Strobel and C.A. Hughes, Analytic solution of the covariant shell model of three Dirac fermions with harmonic forces, *Few-Body Systems* **2** (1987) 155–168.

[139] M. Kaluza and N.M. Borstnik, Leptons as systems of Dirac particles, *Il Nuovo Cimento A* **101** (1989) 71–83.

[140] J. Giammarco and J. Franklin, Relativistic calculation of ground-state baryon masses, *Nucl. Phys. A* **585** (1995) 450–462.

[141] G.L. Strobel, Analytic relativistic three-fermion harmonic-oscillator wave functions, *Few-Body Systems* **21** (1996) 1–23.

[142] C.G. Darwin, The wave equations of the electron, *Proc. Roy. Soc. of London, Series A* **118** (1928) 654–680.

[143] J.A. Gaunt, The triplets of helium, *Philos. Trans. Roy. Soc. London, Series A* **228** (1929) 151–196.

[144] W.H. Furry, On the introduction of nonelectric forces into Dirac's equations, *Phy. Rev.* **50** (1936) 784.

[145] S. Share and G. Breit, Relativistic effects for the deuteron, *Phy. Rev.* **52** (1937) 546.

[146] E.L. Hill and R. Landshoff, The Dirac electron theory, *Rev. Modern Phys.* **10** (1938) 87.

[147] P. Caldirola, Sul moto di una particella di Dirac in un campo coulombiano misto, *Il Nuovo Cimento* **5** (1948) 29–35.

[148] A.P. Stone, Nuclear and relativistic effects in atomic spectra, *Proc. Phy. Soc.* **77** (1961) 786.

[149] E. de Vries and J.E. Jonker, Nonrelativistic approximations of the Dirac Hamitonian, *Nucl. Phys. B* **6** (1968) 213–225.

[150] P. Urban, The Dirac–Foldy–Wouthuysen transformation, *Topics in Applied Quantumelectrodynamics*, Springer, Vienna, 1970, pp. 1–24.

[151] V.A. Krutov and L. N.Savushkin, Relativity and spin–orbit interaction in nuclei, *J. Phys. A: Math., Nucl. General* **6** (1973) 93.

[152] V.A. Krutov, V.N. Fomenko and L.N. Savushkin, Scheme of the approximate relativistic theory of the nucleus I. Calculation of the single-particle basis Hamiltonian from internucleon interactions, *J. Phys. A: Math., Nucl. General* **7** (1974) 372.

[153] L. Armstrong and Serge Feneuille, Relativistic effects in the many-electron atom, *Adv. Atomic and Mol. Phys.* **10** (1974) 1–52.

[154] J.V. Noble, Consistency of nuclear Dirac phenomenology with meson–nucleon interactions, *Nucl. Phys. A* **329** (1979) 354–364.

[155] S. Sato, Two-body Dirac equation for nucleon–nucleon system, *Il Nuovo Cimento A* **103** (1990) 471–486.

[156] J.M. Yao, H. Chen and J. Meng, Time-odd triaxial relativistic mean field approach for nuclear magnetic moments, *Phy. Rev. C* **74** (2006) 024307.

[157] P.L. Hagelstein and I.U. Chaudhary, Including nuclear degrees of freedom in a lattice Hamiltonian, *J. Cond. Matter Nucl. Sci.* **7** (2012) 35–50.

[158] R.G. Sachs, On the magnetic moment of the deuteron, *Phy. Rev.* **72** (1947) 91.

[159] S. T. Ma, Contact and core interactions according to Dirac's relativistic theory of the electron, *Nucl. Phys.* **2** (1956) 347–355.

[160] L.L. Foldy and S.A. Wouthuysen, On the Dirac theory of spin 1/2 particles and its nonrelativistic limit, *Phy. Rev.* **78** (1950) 29.

[161] S.M. Dancoff, spin–orbit Coupling in He^5, *Phy. Rev.* **58** (1940) 326.

[162] H.H. Barschall and Louis Brown, Early estimates of the strength of the nuclear spin–orbit force, *Found. Phys.* **16** (1986) 115–124.

[163] H. Margenau, Relativistic magnetic moment of a charged particle, *Phy. Rev.* **57** (1940) 383.

[164] L.D. Miller, Relativistic single-particle potentials for nuclei, *Ann. Phys.* **91** (1975) 40–57.

[165] M. Bawin, Dirac approach to anomalous magnetic moment calculations, *Phy. Rev. C* **34** (1986) 1487.

[166] G. Breit and R.M. Thaler, Relativistic corrections to the magnetic moments of nuclear particles, *Phy. Rev.* **89** (1953) 1177.

[167] A.J.F. Siegert, Note on the interaction between nuclei and electromagnetic radiation, *Phy. Rev.* **52** (1937) 787.

[168] M. Sugawara, The relativistic and exchange current corrections to the deuteron magnetic moment and the thermal np capture cross section, *Prog. Theoret. Phys.* **14** (1955) 535–550.

[169] L.A. Radicati, L'equazione del secondo ordine per una particella di Dirac–Pauli, *Il Nuovo Cimento* **5** (1948) 173–180.

[170] G. Breit, Electron–neutron interaction, *Proc. National Academy of Sci.* **37** (1951) 837–846.

[171] J.B. Calvert, On the electromagnetic interaction of spin-1/2 particles, Ph.D. dissertation, Montana State University-Bozeman, College of Letters and Science, 1959.

[172] G. Do Dang and N. Van Giai, Quasielastic electron scattering: Effect of relativistic nuclear potentials, *Phy. Rev. C* **30** (1984) 731.

[173] A.Ya. Silenko, Dirac equation in the Foldy–Wouthuysen representation describing the interaction of spin-1/2 relativistic particles with an external electromagnetic field, *Theoret. Math. Phys.* **105** (1995) 1224–1230.

[174] A.J. Silenko, Foldy–Wouthuysen representation in the standard model of electroweak interactions, *Theoret. Math. Phys.* **112** (1997) 922–928.

[175] W.A. Barker and Z.V. Chraplyvy, Conversion of an amplified Dirac equation to an approximately relativistic form, *Phy. Rev.* **89** (1953) 446.

[176] W.A. Barker and F.N. Glover, Reduction of relativistic two-particle wave equations to approximate forms–III, *Phy. Rev.* **99** (1955) 317.

[177] S. Feneuille and L. Armstrong, Additive nature of correlation and relativistic effects in atomic hyperfine structure, *Phy. Rev. A* **8** (1973) 1173.

[178] P. Hafner and W.H.E. Schwarz, Pseudo-potential approach including relativistic effects, *J. Phys. B: Atomic and Mol. Phys.* **11** (1978) 217.

[179] P.T. Leung, M.L. Rustgi and S.A. T. Long, Relativistic corrections to the Bethe sum rule, *Phy. Rev. A* **33** (1986) 2827.

[180] K. Pachucki, Higher-order effective Hamiltonian for light atomic systems, *Phy. Rev. A* **71** (2005) 012503.

[181] H.-P. Duerr, Relativistic effects in nuclear forces, *Phy. Rev.* **103** (1956) 469.

[182] B. Rozsnyai, Self-consistent nuclear model, *Phy. Rev.* **124** (1961) 860.

[183] K.W. McVoy and L. Van Hove, Inelastic electron–nucleus scattering and nucleon–nucleon correlations, *Phy. Rev.* **125** (1962) 1034.

[184] R.A. Krajcik and L.L. Foldy, Electromagnetic interactions with an arbitrary loosely bound system, *Phy. Rev. Lett.* **24** (1970) 545.

[185] M.K. Liou and M.I. Sobel, Relativistic corrections in the nclear-plus-electromagnetic Hamiltonian, *Phy. Rev. C* **7** (1973) 2044.

[186] T. Goldman, Gauge invariance, time-dependent Foldy–Wouthuysen transformations, and the Pauli Hamiltonian, *Phy. Rev. D* **15** (1977) 1063.

[187] K.J. Sebastian, Relativistic corrections to the electric dipole and the magnetic dipole single photon transition amplitudes of a composite system, *Phys. Lett. A* **80** (1980) 109–112.

[188] J. Potvin, A nonrelativistic reduction of the Dirac equation in the free-particle basis, *J. Phys. A: Math. General* **14** (1981) 1117.

[189] L.L. Foldy, The electromagnetic properties of Dirac particles, *Phy. Rev.* **87** (1952) 688.

[190] J.D. Bjorken and S.D. Drell, *Relativistic Quantum Mechanics* McGraw-Hill, New York, 1964.

[191] Z.V. Chraplyvy, Reduction of relativistic two-particle wave equations to approximate forms I, *Phy. Rev.* **91** (1953) 388.

[192] E. Eriksen, Foldy–Wouthuysen transformation. Exact solution with generalization to the two-particle problem, *Phy. Rev.* **111** (1958) 1011.

[193] E. Eriksen, Transformations of relativistic two-particle equations, *Il Nuovo Cimento* **20** (1961) 747–758.

[194] M.K. Liou and M.I. Sobel, Relativistic corrections in the nuclear-plus-electromagnetic Hamiltonian, *Phy. Rev. C* **7** (1973) 2044.

[195] H. Sazdjian, The Foldy–Wouthuysen transformation in the two-particle case, *In Annales de l'Institute Henri Poincaré, Physique théorique* **47** (1087) 39–62.

[196] A. Turovsky, On the Chraplyvy transformation and some features of its application for higher-order expansions, *J. Physical Studies* **18** (2014) 1004.

[197] D.L. Pursey, On generalized Foldy–Wouthuysen transformations, *Nucl. Phys.* **8** (1958) 595–601.

[198] B. Rozsnyai, Self-consistent nuclear model, *Phy. Rev.* **124** (1961) 860.

[199] K. Pachucki, Higher-order effective Hamiltonian for light atomic systems, *Phy. Rev. A* **71** (2005) 012503.

[200] S.J. Brodsky and J.R. Primack, The electromagnetic interactions of composite systems, *Ann. Phys.* **52** (1969) 315–365.

[201] R.A. Hegstrom, Nuclear-mass and anomalous-moment corrections to the Hamiltonian for an atom in a constant external magnetic field, *Phy. Rev. A* **7** (1973) 451.

[202] C. L'Huillier and J.P. Faroux, Hamiltonian of a many-electron atom in an external magnetic field and classical electrodynamics, *J. de Physique* **38** (1977) 747–755.

[203] K. Pachucki, Long-wavelength quantum electrodynamics, *Phy. Rev. A* **69** (2004) 052502.

[204] K. Pachucki, Nuclear mass correction to the magnetic interaction of atomic systems, *Phy. Rev. A* **78** (2008) 012504.

[205] M.M. Sternheim, Second-order effects of nuclear magnetic fields, *Phy. Rev.* **128** (1962) 676.

[206] W. Cencek and W. Kutzelnigg, Accurate relativistic energies of one-and two-electron systems using Gaussian wave functions, *J. Chemical Phys.* **105** (1996) 5878–5885.

[207] J. Seino and M. Hada, Applicability of the lowest-order two-electron Breit–Pauli relativistic correction in many-electron heavy and super-heavy elements, *Chemical Phys. Lett.* **442** (2007) 134–139.

[208] P. Amore, M.B. Barbaro and A. De Pace, Relativistic Hamiltonians in many-body theories, *Phy. Rev. C* **53** (1996) 2801.

[209] H. Grotch and R. A. Hegstrom, Hydrogenic atoms in a magnetic field, *Phy. Rev. A* **4** (1971) 59.

[210] E. Wigner, Invariance in physical theory, *Proc. Amer. Philos. Soc.* **93** (1949) 521–526.

[211] E. Wigner, On unitary representations of the inhomogeneous Lorentz group, *Ann. Math.* **40** (1939) 149–204.

[212] E.P. Wigner, Relativistic invariance in quantum mechanics, *Il Nuovo Cimento* **10** (1956) 517–532.

[213] E.P. Wigner, Unitary representations of the inhomogeneous Lorentz group including reflections, *Group Theoretical Concepts in Elementary Particle Physics*, Gordan and Breach, NY, 1964, 37–80.

[214] V. Bargmann, Irreducible unitary representations of the Lorentz group, *Ann. Math.* **48** (1947) 568–640.

[215] P.A.M. Dirac, Forms of relativistic dynamics, *Rev. Modern Phys.* **21** (1949) 392.

[216] W.E.F. Pauli, Continuous groups in quantum mechanics, *CERN Report No. CERN-56-31*, CERN, 1956.

[217] L.L. Foldy, Synthesis of covariant particle equations, *Phy. Rev.* **102** (1956) 568.

[218] M.A. Melvin, Elementary particles and symmetry principles, *Rev. Modern Phys.* **32** (1960) 477.

[219] L.L. Foldy, Relativistic particle systems with interaction, *Phy. Rev.* **122** (1961) 275.

[220] J.L. Friar, Relativistic effects on the wave function of a moving system, *Phy. Rev. C* **12** (1975) 695.

[221] B. Durand, Properties of three position operators constructed from free spin-1/2 fields, *Phy. Rev. D* **14** (1976) 1554.

[222] R.A. Krajcik and L.L. Foldy, Relativistic center-of-mass variables for composite systems with arbitrary internal interactions, *Phy. Rev. D* **10** (1974) 1777.

[223] W. Glöckle, Y. Nogami and I. Fukui, Structure of a composite system in motion in relativistic quantum mechanics, *Phy. Rev. D* **35** (1987) 584.

[224] F.E. Close and H. Osborn, Relativistic center-of-mass motion and the electromagnetic interaction of systems of charged particles, *Phy. Rev. D* **2** (1970) 2127.

[225] L.L. Foldy and R.A. Krajcik, Separability in directly interacting relativistic particle systems, *Phy. Rev. Lett.* **32** (1974) 1025.

[226] L.L. Foldy and R.A. Krajcik, Separable solutions for directly interacting particle systems, *Phy. Rev. D* **12** (1975) 1700.

[227] W. Glöckle and L. Müller, Relativistic theory of interacting particles, *Phy. Rev. C* **23** (1981) 1183.

[228] M. De Sanctis, R. Mignani and D. Prosperi, Covariance properties of a multifermion Hamiltonian with pairwise, massless vector-boson exchange, *Il Nuovo Cimento A* **102** (1989) 1671–1700.

[229] M. De Sanctis and D. Prosperi, A covariant two-nucleon wave equation with retardation contributions, *Il Nuovo Cimento A* **107** (1994) 611–636.

[230] A. Krüger and W. Glöckle, Approach towards N-nucleon effective generators of the Poincaré group derived from a field theory, *Phy. Rev. C* **59** (1999) 1919.

[231] F.E. Close and Zhenping Li, Photo-and electroproduction of N* in a quark model, *Phy. Rev. D* **42** (1990) 2194.

[232] J.L. Forest, V.R. Pandharipande and J.L. Friar, Relativistic nuclear Hamiltonians, *Phy. Rev. C* **52** (1995) 568.

[233] J.L. Forest, V.R. Pandharipande, J. Carlson and R. Schiavilla, Variational Monte Carlo calculations of ^{3}H and ^{4}He with a relativistic Hamiltonian, *Phy. Rev. C* **52** (1995) 576.

[234] R. Schiavilla, Relativistic nuclear Hamiltonian currents to $(v/c)^2$, *Jefferson National Lab Report* CEBAF-TH-95-0, 1995.

[235] J.L. Forest, V.R. Pandharipande and A. Arriaga, Quantum Monte Carlo studies of relativistic effects in light nuclei, *Phy. Rev. C* **60** (1999) 014002.

[236] C.A. da Rocha and M.R. Robilotta, Two pion exchange nucleon–nucleon potential: The minimal chiral model, *Phy. Rev. C* **49** (1994) 1818.

[237] C.A. Da Rocha and M.R. Robilotta, Chiral background for the two-pion exchange nuclear potential: A parametrized version, *Phy. Rev. C* **52** (1995) 531.

[238] M.R. Robilotta and Carlos A. da Rocha, Two-pion exchange nucleon–nucleon potential; Model independent features, *Nucl. Phys. A* **615** (1997) 391–416.

[239] R. Higa and M.R. Robilotta, Two-pion exchange nucleon–nucleon potential: $O(q^4)$ relativistic chiral expansion, *Phy. Rev. C* **68** (2003) 024004.

[240] R. Higa, M.R. Robilotta and C.A. da Rocha, Relativistic $O(q^4)$ two-pion exchange nucleon–nucleon potential: Configuration space, *Phy. Rev. C* **69** (2004) 034009.

[241] M.R. Robilotta, Nucleon–nucleon potential: Drift effects, *Phy. Rev. C* **74** (2006) 044002.

[242] M.R. Robilotta, Two and three nucleon forces, *Nucl. Phys. A* **790** (2007) 3c–9c.

[243] P.L. Hagelstein and I.U. Chaudhary, Energy exchange in the lossy spin–boson model, *J. Condensed Matter Nucl. Sci.* **5** (2011) 52–71.

[244] P.L. Hagelstein and I.U. Chaudhary, Second-order formulation and scaling in the lossy spin–boson model, *J. Condensed Matter Nucl. Sci.* **5** (2011) 87–101.

[245] P.L. Hagelstein and I.U. Chaudhary, Local approximation for the lossy spin–boson model, *J. Condensed Matter Nucl. Sci.* **5** (2011) 102–115.

[246] P.L. Hagelstein and I.U. Chaudhary, Coherent energy exchange in the strong coupling limit of the lossy spin–boson model, *J. Condensed Matter Nucl. Sci.* **5** (2011) 116–139.

[247] P.L. Hagelstein and I.U. Chaudhary, Errata and comments on a recent set of papers in J. Condensed Matter in Nuclear Science , *J. Condensed Matter Nucl. Sci.* **7** (2012) 1–7.

[248] P.L. Hagelstein and I.U. Chaudhary, Pulse and amplitude approximation for the lossy spin–boson model, *J. Condensed Matter Nucl. Sci.* **9** (2012) 30–49.

[249] M.A.K. Khalil, Barnacle equivalence structure in relativistic wave equations, *Prog. Theoret. Phys.* **60** (1978) 1559–1582.

[250] M.A.K. Khalil, Reducible relativistic wave equations, *J. Phys. A: Math. General* **12** (1979) 649.

[251] H.J. Bhabha, Equations with two distinct masses, *Phil. Mag.* **43** (1952) 33.

[252] H.J. Bhabha, An equation for a particle with two mass states and positive charge density, *London, Edinburgh, and Dublin Philosophical Magazine and J. Sci.* **43** (1952) 33–47.

[253] K.K. Gupta, Bhabha's equation for a particle of two mass states in Rarita–Schwinger form, *Proc. Roy. Soc. London A: Math., Physical Eng. Sci.* **222** (1954) 118–127.

[254] A.O. Barut, The mass of the muon, *Phys. Lett. B* **73** (1978) 310–312.

[255] S.I. Kruglov, On the generalized Dirac equation for fermions with two mass states, it arXiv preprint quant-ph/0408056 (2004).

[256] S.I. Kruglov, On the Hamiltonian form of generalized Dirac equation for fermions with two mass states, *arXiv preprint* hep-ph/0603181 (2006).

[257] E. Majorana, Teoria relativistica di particelle con momento intrinseco arbitrario, *Il Nuovo Cimento* **9** (1932) 335–344.

[258] D. M. Fradkin, Comments on a paper by Majorana concerning elementary particles, *Am. J. Phys.* **34** (1966) 314.

[259] R. Casalbuoni, Majorana and the infinite component wave equations, *Int. Conference – Ettore MajoranaŠs legacy and the Phys. of the XXI century*; and *arXiv preprint* hep-th/0610252 (2006).

[260] Harish-Chandra, Infinite irreducible representations of the Lorentz group, *Proc. Roy. Soc. London. Series A, Math. Phy. Sci.* **189** (1947) 372–401.

[261] I.M.Gelfand and A.M. Yaglom, General relativistic invariant equations and infinite-dimensional representations of the Lorentz group, *Zh. Eksperim. i Teor. Fiz.* **18** (1948) 707–733.

[262] Y. Nambu, Relativistic wave equations for particles with internal structure and mass spectrum, *Prog. Theoret. Phys. Supplement* **37** (1966) 368–382.

[263] Y. Nambu, Infinite-component wave equations with hydrogenlike mass spectra, *Phy. Rev.* **160** (1967) 1171.

[264] Y. Nambu and S.P. Rosen, Magnetic moments and charge radii for states described by an infinite component wave equation, *Prog. of Theoret. Phys.* **40** (1968) 1151–1158.

[265] R. Hermann, General mass formula for the Nambu wave equations, *Phy. Rev.* **167** (1968) 1318.

[266] D. Tz. Stoyanov and I.T. Todorov, Majorana representations of the Lorentz group and infinite-component fields, *J. Math. Phys.* **9** (1968) 2146–2167.

[267] I. Gyuk and H. Umezawa, Finite- and infinite-component wave equations, *Phy. Rev. Lett.* **22** (1969) 972.

[268] C.D. Palev, Finite-and infinite-component fields and equations generated from the Dirac equation, *Il Nuovo Cimento A* **62** (1969) 585–603.

[269] K.C. Tripathy, Generalized wave equations –II, *Phy. Rev. D* **2** (1970) 2955.

[270] M.I. Pavkovic, Infinite-component wave equations in the external electromagnetic field, *Phy. Rev. D* **4** (1971) 2534.

[271] A.O. Barut and H. Kleinert, Dynamical group O(4,2) for baryons and the behavior of form factors, *Phy. Rev.* **161** (1967) 1464.

[272] H. Kleinert, Isoscalar nucleon form factor from O(4,2) dynamics, *Phy. Rev.* **163** (1967) 1807.

[273] A.O. Barut, Pion form factor and mass spectrum of bosons, *Nucl. Phys. B* **4** (1968) 455–461.

[274] A.O. Barut, D. Corrigan and H. Kleinert, Derivation of mass spectrum and magnetic moments from current conservation in relativistic O(3,2) and O(4,2) theories, *Phy. Rev.* **167** (1968) 1527.

[275] A.O. Barut, D. Corrigan and H. Kleinert, Magnetic moments, form factors, and mass spectrum of baryons, *Phy. Rev. Lett.* **20** (1968) 167.

[276] A.O. Barut and S. Malin, Form factor and mass corrections to weak decay amplitudes, *Nucl. Phys. B* **9** (1969) 194–200.

[277] D. Corrigan, B. Hamprecht and H. Kleinert, Form factors of $\Delta(1236)$ from O(4,2) dynamics, *Nucl. Phys. B* **11** (1969) 1–6.

[278] H. Kleinert, Baryon current solving SU(3) charge–current algebra, *Springer Tracts in Modern Phys.* **49** (1969) 90.

[279] A.O. Barut and W.B. Monsma, Infinite-component wave equations and mass splittings within SU(3) and SU(2) multiplets, *Phy. Rev. D* **5** (1972) 2327.

[280] R. Wilson and R.F. Peierls, Proton structure functions in an infinite resonance O(4,2) model, *Ann. Phys.* **81** (1973) 15–48.

[281] A.O. Barut and J. Nagel, Electromagnetic polarizabilities of nucleons, *Phy. Rev. D* **13** (1976) 2075.

[282] A.O. Barut, P. Budini and C. Fronsdal, Two examples of covariant theories with internal symmetries involving spin, *Proc. Roy. Soc. London A: Math., Physical and Eng. Sci.* **291** (1966) 106–112.

[283] C. Fronsdal, Infinite multiplets and the hydrogen atom, *Phy. Rev.* **156** (1967) 1665.

[284] A.O. Barut and H. Kleinert, Current operators and Majorana equation for the hydrogen atom from dynamical groups, *Phy. Rev.* **157** (1967) 1180.

[285] A.O. Barut and H. Kleinert, Transition probabilities of the hydrogen atom from noncompact dynamical groups, *Phy. Rev.* **156** (1967) 1541.

[286] A.O. Barut, D. Corrigan and H. Kleinert, Derivation of mass spectrum and magnetic moments from current conservation in relativistic O(3,2) and O(4,2) theories, *Phy. Rev.* **167** (1968) 1527.

[287] G. Bisiacchi, P. Budini and G. Calucci, Majorana equations for composite systems, *Phy. Rev.* **172** (1968) 1508.

[288] H. Kleinert, Relativistic Current of the H Atom in O(4,2) Dynamics, *Phy. Rev.* **168** (1968) 1827.

[289] A.O. Barut and A. Baiquni, Theory of the relativistic H atom and positronium, *Phy. Rev.* **184** (1969) 1342.

[290] A.O. Barut, and A. Baiquni, Relativistic infinite-component wave equation for H-atom with spin, *Phys. Lett. A* **30** (1969) 352–353.

[291] C. Itzykson, V.G. Kadyshevsky and I.T. Todorov, Three-dimensional formulation of the relativistic two-body problem and infinite-component wave equations, *Phy. Rev. D* **1** (1970) 2823.

[292] A.O. Barut and W. Rasmussen, The hydrogen atom as a relativistic elementary particle I. The wave equation and mass formulae, *J. Phys. B: Atomic Mol. Phys.* **6** (1973) 1695.

[293] T. Takabayasi, Infinite-component wave equation with relativistic rotator mass spectrum, *Prog. Theoret. Phys.* **38** (1967) 285–287.

[294] T. Miyazaki, Composite particles with rotational mass levels, *Prog. Theoret. Phys.* **40** (1968) 427–428.

[295] T. Takabayasi, Dynamical group of relativistic oscillator and linear meson trajectories, *Prog. Theoret. Phys.* **42** (1969) 1210–1212.

[296] T. Miyazaki, How to construct wave equations when mass levels are known? *Prog. Theoret. Phys.* **47** (1972) 1385–1395.

[297] N.D. Son and J. Sucher, Bound states of a relativistic two-body Hamiltonian; Comparison with the Bethe–Salpeter equation, *Phy. Rev.* **153** (1967) 1496.

[298] F. Coester, S.C. Pieper and F.J.D. Serduke, Relativistic effects in phenomenological nucleon–nucleon potentials and nuclear matter, *Phy. Rev. C* **11** (1975) 1.

[299] B. Bakamjian and L.H. Thomas, Relativistic particle dynamics–II, *Phy. Rev.* **92** (1953) 1300.

[300] R.L. Hall, W. Lucha and F.F. Schöberl, Relativistic N-boson systems bound by pair potentials $V(r_{ij}) = g(r_{ij}^2)$, *J. Math. Phys.* **45** (2004) 3086–3094.

[301] R.L. Hall and W. Lucha, Binding energy of semirelativistic N-boson systems, *J. Phys. A: Math. Theoret.* **40** (2007) 6183.

[302] A.O. Barut, The covariant many-body problem in quantum electrodynamics, *J. Math. Phys.* **32** (1991) 1091–1095.

[303] A.O. Barut and N. Ünal, An exactly soluble relativistic quantum two-fermion problem, *J. Math. Phys.* **27** (1986) 3055–3060.

[304] A.O. Barut and N. Ünal, A new approach to bound-state quantum electrodynamics: I. Theory, *Physica A: Statistical Mechanics and its Applications* **142** (1987) 467–487.

[305] A.O. Barut and N. Ünal, A new approach to bound-state quantum electrodynamics–II. Spectra of positronium, muonium and hydrogen, *Physica A: Statistical Mechanics and its Applications* **142** (1987) 488–497.

[306] A.O. Barut, A.J. Bracken, S. Komy and N. Ünal, New approach to the determination of eigenvalues and eigenfunctions for a relativistic two-fermion equation, *J. Math. Phys.* **34** (1993) 2089–2106.

[307] S. Tomonaga, On a relativistically invariant formulation of the quantum theory of wave fields, *Prog. Theoret. Phys.* **1** (1946) 27–42.

[308] S. Tomonaga, Super-many-time formulation of the quantum theory of wave fields, *Prog. Theoret. Phys.* **2** (1947) 100.

[309] Z. Koba, T. Tati and S. Tomonaga, On a reletivistically invariant formulation of the quantum theory of wave fields–II: Case of interacting electromagnetic and electron fields, *Prog. Theoret. Phys.* **2** (1947) 101–116.

[310] Z. Koba, T. Tani and S. Tomonaga, On a relativistically invariant formulation of the quantum theory of wave fields–III, *Prog. Theoret. Phys.* **2** (1947) 198–208.

[311] P.A.M. Dirac, Relativistic quantum mechanics, *Proc. Roy. Soc. London A: Math., Physical and Eng. Sci.* **136** (1932) 453–464.

[312] S. Tomonaga, Development of quantum electrodynamics, *The PhysicistŠs Conception of Nature*, Springer, Netherlands, 1966, pp. 404–412.

[313] E.E. Salpeter and H.A. Bethe, A relativistic equation for bound-state problems, *Phy. Rev.* **84** (1951) 1232.

[314] F.L. Scarf, Spectrum and nonrelativistic limit of a Bethe–Salpeter equation, *Phy. Rev.* **100** (1955) 912.

[315] J.L. Gammel and M.T. Menzel, Bethe–Salpeter equation: Numerical experience with a hydrogenlike atom, *Phy. Rev. A* **7** (1973) 858.

[316] G.T. Bodwin, D.R. Yennie and M.A. Gregorio, Recoil effects in the hyperfine structure of QED bound states, *Rev. Modern Phys.* **57** (1985) 723.

[317] J.H. Connell, QED test of a Bethe–Salpeter solution method, *Phy. Rev. D* **43** (1991) 1393.

[318] E.E. Salpeter and J.S. Goldstein, Momentum space wave functions–II. The deuteron ground state, *Phy. Rev.* **90** (1953) 983.

[319] J.S. Goldstein, Properties of the Salpeter–Bethe two-nucleon equation, *Phy. Rev.* **91** (1953) 1516.

[320] S. Deser and P.C. Martin, A covariant meson–nucleon equation, *Phy. Rev.* **90** (1953) 1075.

[321] H.S. Green and S.N. Biswas, Covariant solutions of the Bethe–Salpeter equation, *Prog. Theoret. Phys.* **18** (1957) 121–138.

[322] M.J. Zuilhof and J.A. Tjon, Relativistic effects in the two-nucleon system, *Phy. Rev. C* **24** (1981) 736.

[323] A.H. Guth, A relativistic quark model for mesons based on numerical solutions of the Bethe–Salpeter equation, *Ann. Phys.* **82** (1974) 407–448.

[324] K.-I. Aoki, T. Kugo and M.G. Mitchard, Meson properties from the ladder Bethe–Salpeter equation, *Phys. Lett. B* **266** (1991) 467–472.

[325] M. Harada, M. Kurachi and K. Yamawaki, Meson masses in large N_f QCD from the Bethe–Salpeter equation, *Phy. Rev. D* **68** (2003) 076001.

[326] M.S. Bhagwat, M.A. Pichowsky and Peter C. Tandy, Confinement phenomenology in the Bethe–Salpeter equation, *Phy. Rev. D* **67** (2003) 054019.

[327] B.H. Kellett, A relativistic quark model for baryons, *Ann. Phys.* **87** (1974) 60–94.

[328] U. Löring, K. Kretzschmar, B.Ch. Metsch and H.R. Petry, Relativistic quark models of baryons with instantaneous forces, *Euro. Phy. J. A – Hadrons and Nuclei* **10** (2001) 309–346.

[329] A. Faessler, Th. Gutsche, M.A. Ivanov, J.G. Körner, V.E. Lyubovitskij, D. Nicmorus and K. Pumsa-Ard, Magnetic moments of heavy baryons in the relativistic three-quark model, *Phy. Rev. D* **73** (2006) 094013.

[330] R.O.A. Robinson, The Bethe–Salpeter equation for many-body systems, *Canadian J. Phys.* **33** (1955) 369–382.

[331] J. Bijtebier, 3D reduction of the N-body Bethe-ŰSalpeter equation, *Nucl. Phys. A* **696** (2001) 581–604.

[332] E.C.G. Stueckelberg, La signification du temps propre en mécanique: ondulatoire, *Helv. Phys. Acta* **14** (1941) 321–322.

[333] E.C.G. Stueckelberg, La mécanique du point matériel en théorie de relativité et en théorie des quanta, *Helv. Phys. Acta* **15** (1942) 23–37.

[334] J.H. Cooke, Proper-time formulation of quantum mechanics, *Phy. Rev.* **166** (1968) 1293.

[335] L.P. Horwitz and C. Piron, Relativistic dynamics, *Helv. Phys. Acta* **46** (1973) 316.

[336] L.P. Horwitz, C. Piron and F. Reuse, Relativistic dynamics for the spin-1/2 particle, *Helv. Phys. Acta* **46** (1973) 316.

[337] L.P. Horwitz and F.C. Rotbart, Nonrelativistic limit of relativistic quantum mechanics, *Phy. Rev. D* **24** (1981) 2127.

[338] L.P. Horwitz and R. Arshansky, On relativistic quantum theory for particles with spin 1/2, *J. Phys. A: Math. General* **15** (1982) L659.

[339] L.P. Horwitz and Y. Lavie, Scattering theory in relativistic quantum mechanics, *Phy. Rev. D* **26** (1982) 819.

[340] J.R. Fanchi, Parametrizing relativistic quantum mechanics, *Phy. Rev. A* **34** (1986) 1677.

[341] R. Arshansky and L.P. Horwitz, The quantum relativistic two-body bound state I. The spectrum, *J. Math. Phys.* **30** (1989) 66–80.

[342] R. Arshansky and L.P. Horwitz, The quantum relativistic two-body bound state–II. The induced representation of SL(2,C), *J. Math. Phys.* **30** (1989) 380–392.

[343] J.R. Fanchi, Review of invariant time formulations of relativistic quantum theories, *Foundations Phys.* **23** (1993) 487–548.

[344] M.C. Land, R.I. Arshansky and L.P. Horwitz, Selection rules for dipole radiation from a relativistic bound state, *Foundations Phys.* **24** (1994) 563–578.

[345] M.C. Land and L.P. Horwitz, The Zeeman effect for the relativistic bound state, *J. Phys. A: Math. General* **28** (1995) 3289.

[346] M.C. Land and L.P. Horwitz, The covariant Stark effect, *Foundations Phys.* **31** (2001) 967–991.

[347] M. Land and L.P. Horwitz, Offshell quantum electrodynamics, *J. Phys.: Conf. Ser.* **437** (2013) 012011.

[348] M. Davidson, Theories of variable mass particles and low energy nuclear phenomena, *Foundations Phys.* **44** (2014) 144–174.

[349] M. Davidson, Variable mass theories in relativistic quantum mechanics as an explanation for anomalous low energy nuclear phenomena, *J. Phys.: Conf. Ser.* **615** (2015) 012016.

[350] P.L. Hagelstein and Irfan U. Chaudhary, Kinematic mass of a composite in the many-particle Dirac model, *arXiv preprint* arXiv:1201.1488 (2012).

[351] C. Itzykson and J.-B. Zuber, *Quantum Field Theory*, McGraw-Hill, New York, 1980.

[352] S. Weinberg, *The Quantum Theory of Fields*, Vols. 1–3, Cambridge University Press, New York, 1996.

[353] E.E. Salpeter, Mass corrections to the fine structure of hydrogen-like atoms, *Phys. Rev.* **87** (1952) 328.

[354] T. Itoh, Derivation of nonrelativistic Hamiltonian for electrons from quantum electrodynamics, *Rev. Modern Phys.* **37** (1965) 159.

[355] M. Douglas and N.M. Kroll, Quantum electrodynamical corrections to the fine structure of helium, *Ann. Phys.* **82** (1974) 89–155.

[356] A. Wolf, M. Reiher and B.A. Hess, The generalized Douglas–Kroll transformation, *J. Chem. Phys.* **117** (2002) 9215–9226.

[357] D.L. Lin, Foldy–Wouthuysen transformation of quantum electrodynamics and relativistic corrections to the transition operator in two-electron systems, *Phy. Rev. A* **15** (1977) 2324.

[358] V.P. Neznamov, On the theory of interacting fields in the Foldy–Wouthuysen representation, *Phys. Particles Nuclei* **37** (2006) 86–103.

[359] P. Labelle, Effective field theories for QED bound states: Extending nonrelativistic QED to study retardation effects, *Phy. Rev. D* **58** (1998) 093013.

[360] G.W. Erickson, Energy levels of one-electron atoms, *J. Phy. Chem. Ref. Data* **6** (1977) 831–870.

[361] G.W.F. Drake, Quantum electrodynamic effects in few-electron atomic systems, *Adv. Atomic Mol. Phys.* **18** (1982) 399–460.

[362] J.R. Sapirstein and D.R. Yennie, Theory of hydrogenic bound states, *Quantum Electrodynamics*, T. Kinoshita (Ed,), World Scientific, New Jersey, 1990, pp. 560–672.

[363] K. Pachucki, D. Leibfried, M. Weitz, A. Huber, W. König, and T.W. Hänsch, Theory of the energy levels and precise two-photon spectroscopy of atomic hydrogen and deuterium, *J. Phys. B: Atomic, Mol. Optical Phys.* **29** (1996) 177.

[364] S.G. Karshenboim, Precision Physics of simple atoms: QED tests, nuclear structure and fundamental constants, *Phys. Reports* **422** (2005) 1–63.

[365] P. Indelicato, O. Gorveix and Jean-Paul Desclaux, Multiconfigurational Dirac–Fock studies of two-electron ions–II. Radiative corrections and comparison with experiment, *J. Phys. B: Atomic and Mol. Phys.* **20** (1987) 651.

[366] J. Sapirstein, QED of high-Z three-electron ions, *Nucl. Instr. Methods Phys. Res. Sect. B: Beam Interactions with Materials Atoms* **31** (1988) 70–78.

[367] P. Indelicato, Recent Progress in the theory of relativistic effects and QED corrections in two and three-electron ions, *J. de Physique Colloques* **50** (1989) C1-239.

[368] P.J. Mohr, Quantum electrodynamics calculations in few-electron systems, *Physica Scripta* **T46** (1993) 44.

[369] P.J. Mohr, QED effects in high-Z few-electron atoms, *Nucl. Instr. Methods Phys. Res. Sect. B: Beam Interactions with Materials and Atoms* **87** (1994) 232–236.

[370] H. Persson, I. Lindgren, L.N. Labzowsky, G. Plunien, T. Beier and G. Soff, Second-order self-energy-vacuum-polarization contributions to the Lamb shift in highly charged few-electron ions, *Phy. Rev. A* **54** (1996) 2805.

[371] V.M. Shabaev, A.N. Artemyev and V.A. Yerokhin, QED and nuclear effects in high-Z few-electron atoms, *Physica Scripta* **T86** (2000) 7.

[372] K.T. Cheng, M.H. Chen and J. Sapirstein, Quantum electrodynamic corrections in high-Z Li-like and Be-like ions, *Phy. Rev. A* **62** (2000) 054501.

[373] S.A. Blundell, Calculations of the screened self-energy and vacuum polarization in Li-like, Na-like, and Cu-like ions, *Phy. Rev. A* **47** (1993) 1790.

[374] J. Sapirstein, Theoret. methods for the relativistic atomic many-body problem, *Rev. Modern Phys.* **70** (1998) 55.

[375] C. Thierfelder and P. Schwerdtfeger, Quantum electrodynamic corrections for the valence shell in heavy many-electron atoms, *Phy. Rev. A* **82** (2010) 062503.

[376] S. Sturm, G. Werth and K. Blaum, Electron g-factor determinations in Penning traps, *Annalen der Physik* **525** (2013) 620–635.

[377] U. D. Jentschura, Lamb shift in muonic hydrogen–I. Verification and update of theoretical predictions, *Ann. Phys.* **326** (2011) 500–515.

[378] U.D. Jentschura, Lamb shift in muonic hydrogen–II. Analysis of the discrepancy of theory and experiment, *Ann. Phys.* **326** (2011) 516–533.

[379] P. Indelicato, Nonperturbative evaluation of some QED contributions to the muonic hydrogen $n = 2$ Lamb shift and hyperfine structure, *Phy. Rev. A* **87** (2013) 022501.

[380] R. Pohl, Laser spectroscopy of muonic hydrogen and the puzzling proton, *J. Phy. Soc. Japan* **85** (2016) 091003.

[381] G. Rupp and J.A. Tjon, Bethe–Salpeter calculation of three-nucleon observables with rank-one separable potentials, *Phy. Rev. C* **37** (1988) 1729.

[382] G. Rupp and J.A. Tjon, Bethe–Salpeter calculation of three-nucleon observables with multirank separable interactions, *Phy. Rev. C* **45** (1992) 2133.

[383] B.D. Serot and J.D. Walecka, Chiral QHD with vector mesons, *Acta Physica Polonica. Ser. B* **23** (1992) 655–679.

[384] S. Typel, T.V. Chossy and H.H. Wolter, Relativistic mean field model with generalized derivative nucleon–meson couplings, *Phy. Rev. C* **67** (2003) 034002.

[385] B.D. Serot, Electromagnetic interactions in a chiral effective Lagrangian for nuclei, *Ann. Phys.* **322** (2007) 2811–2830.

[386] C.E. Price and G.E. Walker, Self-consistent Hartree description of deformed nuclei in a relativistic quantum field theory, *Phy. Rev. C* **36** (1987) 354.

[387] B.D. Serot, Building atomic nuclei with the Dirac equation, *Int. J. Modern Phys. A* **19** (2004) 107–118.

[388] O. Plohl and Christian Fuchs, Relativistic self-energy in nuclear dynamics, *Phy. Rev. C* **74** (2006) 034325.

[389] A. Haga, H. Toki, S. Tamenaga, Y. Horikawa and H.L. Yadav, Self-consistent relativistic random-phase approximation with vacuum polarization, *Phy. Rev. C* **72** (2005) 034301.

[390] J. Vijande, F. Fernández and A. Valcarce, Constituent quark model study of the meson spectra, *J. Phys. G: Nucl. Particle Phys.* **31** (2005) 481.

[391] D. Ebert, R.N. Faustov and V.O. Galkin, Masses of heavy baryons in the relativistic quark model, *Phy. Rev. D* **72** (2005) 034026.

[392] S. Dürr, Z. Fodor, J. Frison, C. Hoelbling, R. Hoffmann, S.D. Katz, S. Krieg, T. Kurth, L. Lellouch, T. Lippert, K.K. Szabo and G. Vulvert, Ab initio determination of light hadron masses, *Science* **322** (2008) 1224–1227.

[393] Z. Fodor and C. Hoelbling, Light hadron masses from lattice QCD, *Rev. Modern Phys.* **84** (2012) 449.

[394] S. Durr, Z. Fodor, C. Hoelbling, S.D. Katz, S. Krieg, L. Lellouch, T. Lippert, T. Metivet, A. Portelli, K.K. Szabo, C. Torrero, B.C. Toth and L. Varnhorst, Lattice computation of the nucleon scalar quark contents at the physical point, *Phy. Rev. Lett.* **116** (2016) 172001.

[395] Sz. Borsanyi, S. Durr, Z. Fodor, C. Hoelbling, S.D. Katz, S. Krieg, L. Lellouch, T. Lippert, A. Portelli, K.K. Szabo and B.C. Toth, Ab initio calculation of the neutron–proton mass difference, *Science* **347** (2015) 1452–1455.

[396] S.B. Gerasimov, A sum rule for magnetic moments and the damping of the nucleon magnetic moment in nuclei, *Sov. J. Nucl. Phys.* **2** (1966) 430.

[397] S.D. Drell and A.C. Hearn, Exact sum rule for nucleon magnetic moments, *Phy. Rev. Lett.* **16** (1966) 908.

[398] X.-S. Mei, S.-M. Zhao and H.-X. Qiao, Calculation of higher-order Foldy–Wouthuysen transformation Hamiltonian, *Chinese Phys. Lett.* **31** (2014) 063102.

[399] A.J. Silenko, General properties of the Foldy–Wouthuysen transformation and applicability of the corrected original Foldy–Wouthuysen method, *Phy. Rev. A* **93** (2016) 022108.

[400] M.H. Partovi and Earle L. Lomon, Field-Theoretical nucleon–nucleon potential, *Phy. Rev. D* **2** (1970) 1999.

[401] A. Gersten, R.H. Thompson and A.E.S. Green, Relativistic calculation of nucleon–nucleon phase parameters, *Phy. Rev. D* **3** (1971) 2076.